AGEM²

ADVANCES IN GEOPHYSICAL AND ENVIRONMENTAL MECHANICS AND MATHEMATICS

Chongbin Zhao · Bruce E. Hobbs · Alison Ord

Convective and Advective Heat Transfer in Geological Systems

Springer

Advances in Geophysical and Environmental Mechanics and Mathematics

Series Editor: Professor Kolumban Hutter

Chongbin Zhao · Bruce E. Hobbs ·
Alison Ord

Convective and Advective Heat Transfer in Geological Systems

Springer

Dr. Chongbin Zhao
Computational Geosciences
Research Centre
Central South University
Changsha, China
Chongbin.zhao@iinet.net.au

Dr. Alison Ord
School of Earth
and Geographical Sciences
The University of Western Australia
Perth, Australia
and CSIRO Division of Exploration
and Mining
Perth, Australia
alison.ord@csiro.au

Dr. Bruce E. Hobbs
School of Earth
and Geographical Sciences
The University of Western Australia
Perth, Australia
Bruce.Hobbs@csiro.au

ISBN: 978-3-540-79510-0 e-ISBN: 978-3-540-79511-7

Advances in Geophysical and Environmental Mechanics and Mathematics

ISSN 1866-8348 e-ISSN 1866-8356

Library of Congress Control Number: 2008927195

© 2008 Springer-Verlag Berlin Heidelberg

This work is subject to copyright. All rights are reserved, whether the whole or part of the material is concerned, specifically the rights of translation, reprinting, reuse of illustrations, recitation, broadcasting, reproduction on microfilm or in any other way, and storage in data banks. Duplication of this publication or parts thereof is permitted only under the provisions of the German Copyright Law of September 9, 1965, in its current version, and permission for use must always be obtained from Springer. Violations are liable to prosecution under the German Copyright Law.

The use of general descriptive names, registered names, trademarks, etc. in this publication does not imply, even in the absence of a specific statement, that such names are exempt from the relevant protective laws and regulations and therefore free for general use.

Cover design: deblik, Berlin

Printed on acid-free paper

9 8 7 6 5 4 3 2 1

springer.com

Preamble

Theoretical understanding of convective and advective heat transfer phenomena in geological systems at the crustal scale is important to the understanding of controlling processes involved in ore body formation and mineralization, hydrocarbon maturation and accumulation, hot spot locations within the Earth's crust, environmental remediation and nuclear waste storage. Such an understanding provides useful analytical and numerical tools for accurate and efficient modeling of many of these important processes within the Earth's crust, but also on the Earth's surface and in the atmosphere, so that the interaction between the lithosphere, hydrosphere and atmosphere of the whole Earth system can be appropriately considered. Towards this end, multidisciplinary collaboration among mathematicians, engineers, chemists, physicists and geoscientists is required.

Although convective and advective heat transfer during fluid flow in porous media have been studied and discussed for many years, a systematic and theoretical treatment of these phenomena in geological systems at the crustal scale is lacking. This monograph aims to provide state-of-the-art theoretical results in this particular research field, based on the authors' own work during the last decade. For this purpose, although some numerical results are provided to complement theoretical ones, the main focus of this monograph is on theoretical aspects of the topic. This means that the theoretical treatment contained in this monograph is also applicable to a wide range of problems of other length scales such as engineering length scales. To broaden the readership of this monograph, common mathematical notations are used to derive the theoretical solutions. This enables this monograph to be used either as a useful textbook for postgraduate students or as a valuable reference book for mathematicians, engineers and geoscientists. In addition, each chapter is written independently so that readers may read the chapter of interest separately.

In this monograph we investigate, both theoretically and numerically, the detailed physical mechanisms related to pore-fluid pressure gradient distributions, the critical conditions required to trigger convective pore-fluid flow and the effects of geological heterogeneities on advective and convective heat transfer in the crust. We also extend the numerical treatment of the convective heat transfer problem to ore

body formation and mineralization problems within the upper crust of the Earth. The related theoretical and numerical results demonstrate that:

(1) For a stable (that is, non-deforming) continental crust, although the entrapped pore-fluid pressure may reach or exceed the lithostatic pressure in an overpressured system consisting of a permeable layer and two adjacent impermeable layers, the pore-fluid pressure gradient cannot be maintained at or exceed the lithostatic pressure gradient, even if thermal effects are neglected in the crust.

(2) Pure heat conduction may influence how pore-fluid pressure is distributed in the lower part of the crust, but it has little influence on the distribution of pore-fluid pressure in the upper part of the crust. Thus, for a fluid-saturated crust with motionless pore-fluid, the pore-fluid pressure gradient is very close to the hydrostatic pressure gradient arising from the constant density of the pore-fluid, even though heat conduction takes place.

(3) In the case of a thin crust, the thermal effect of heat advection on the distribution of the pore-fluid pressure gradient is very limited, but in the case of a thick crust, the thermal effect is significant. Generally, the effect of heat advection on the distribution of the pore-fluid pressure gradient becomes more significant with increased conductive thermal flux at the bottom of the system. For a thin crustal model, the pore-fluid pressure gradient is very close to the lithostatic pressure gradient. However, for a thick crustal model, the pore-fluid pressure gradient clearly departs from the lithostatic pressure gradient, especially in the case where the base has a large conductive thermal flux.

(4) If the Rayleigh number of the system is critical or supercritical, convective pore-fluid flow can take place in the crust when the pore-fluid pressure gradient is close to the hydrostatic pressure gradient. The resulting convective pore-fluid flow has a significant effect on heat transfer, causing temperature localization within the crust.

(5) If the pore-fluid pressure gradient is close to a lithostatic pressure gradient, convective pore-fluid flow cannot take place in a crust that has constant temperature and impermeable boundary conditions at both the top and the bottom of the crust, but it can take place if the crust has a permeable top with constant pressure and temperature, and a base with constant upward pore-fluid velocity and conductive heat flux.

(6) The heterogeneity of both medium permeability and thermal conductivity has a significant effect on convective heat transfer within the system. Material thermoelasticity may also affect heat transfer, depending on the elastic hardness of rock masses comprising the crust. In addition, the effect of temperature-dependent pore-fluid viscosity is to destabilize convective flow in the crust. In other words, convective flow takes place more easily when temperature-dependent pore-fluid viscosity is considered.

(7) In the case of strong pore-fluid inflow from the far field of the surrounding rock, the inflow is highly focused within geological faults. The focused pore-fluid flow can cause significant advective heat transfer within and around faults.

(8) Under certain boundary conditions, convective pore-fluid flow is possible within both vertical and inclined three-dimensional fault zones. This conclusion is

also valid when double-diffusion driven convective instability of pore-fluid flow is considered within three-dimensional fault zones.

(9) Convective pore-fluid flow is very efficient for mixing reactive mineral carrying fluids and, therefore, plays an important role in ore body formation and mineralization within the upper crust of the Earth. Mineralization rates are useful to predict precipitation and dissolution of minerals in convective hydrothermal systems. The locations of both injected reactive fluids and geological structures can significantly affect the distributions of pore-fluid flow and temperature as well as the zonation of minerals within the upper crust of the Earth.

October 18, 2007

Chongbin Zhao
Bruce E. Hobbs
Alison Ord

Acknowledgements

Dr. Chongbin Zhao expresses his sincere thanks to his wife, Ms. Peiying Xu, for her persistent support and encouragement, without which it would be impossible to write this monograph. We are very grateful to the Central South University for financial support while writing this monograph. The monograph was carefully reviewed by Professor K. Hutter, whom we thank for the valuable comments and suggestions that lead to a significant improvement over the early version of the monograph.

Contents

Nomenclature

The following symbols are commonly used with the attached definitions, unless otherwise specified in the monograph.

A	area of a finite element
C	species concentration
$\mathbf{C}$	species concentration vector
C_1	non-zero constant
C_2	arbitrary constant
c_p	specific heat of pore-fluid
D	mass diffusivity
g	acceleration due to gravity
H	reference length
K	medium permeability
K_h	reference medium permeability in the horizontal direction
L	length of a problem domain
Le	Lewis number
P	pressure
$\mathbf{P}$	pressure vector
P_0	hydrostatic pressure
q_C	mass flux on the boundary of a finite element
q_T	heat flux on the boundary of a finite element
Ra	Rayleigh number
$Ra_{critical}$	critical Rayleigh number
S	boundary length of a finite element
T	temperature
$\mathbf{T}$	temperature vector
t	temporal variable
u	Darcy velocity in the x direction
$\mathbf{U}$	Darcy velocity vector
v	Darcy velocity in the y direction
w	Darcy velocity in the z direction

x, y, z	spatial coordinates
λ	thermal conductivity
λ_{e0}	reference thermal conductivity in the horizontal direction
ϕ	porosity
ψ	stream function
$\boldsymbol{\psi}$	shape function vector for the pressure of a finite element
ρ_0	reference density of pore-fluid
μ	dynamic viscosity of pore-fluid
β	thermal volume expansion coefficient of pore-fluid
σ	stress on the boundary of a finite element
$\boldsymbol{\varphi}$	shape function vector for the temperature, species concentration and Darcy velocity of a finite element
η	permeability ratio of the underlying medium to its overlying folded layer
ζ	thermal conductivity ratio of the underlying medium to its overlying folded layer
ε	penalty parameter associated with the penalty finite element approach

Subscripts

f	pertaining to pore-fluid
0	pertaining to reference quantities

Superscripts

e	pertaining to equivalent quantities of a porous medium
e	pertaining to quantities in a finite element level
$*$	pertaining to dimensionless quantities
s	pertaining to solid matrix

Chapter 1
Introduction

The study of heat transfer mechanisms in hydrothermal systems is important for understanding the basic physics behind orebody formation and mineralization in the upper crust (Bickle and Mckenzie 1987; Bjorlykke et al. 1988; Brady 1988; England and Thompson 1989; Hoisch 1991; Connolly 1997). Generally, heat energy may be transferred within the crust in the following forms: conduction, advection (including forced convection) where the heat is carried by a moving mass of rock during deformation or by a moving fluid, convection (i.e., free convection, natural convection, buoyancy driven convection, temperature gradient driven convection) and a combination of these processes. Since advective flow is usually generated by a pore-fluid pressure gradient, heat transfer due to advective flow is largely dependent on the pore-fluid pressure gradient distribution in hydrothermal systems. A typical example of this advective flow is the upward throughflow caused by lithostatic pore-fluid pressure gradients within the lower crust. Extensive studies (Connolly and Ko 1995; Etheridge et al. 1983; England et al. 1987; Fyfe et al. 1978; Walther and Orville 1982; Peacock 1989; Yardley and Bottrell 1992; Hanson 1992; Yardley and Lloyd 1995; Norton and Knapp 1970) have shown that lithostatic pore-fluid pressure can be built up by metamorphic fluids arising from devolatilization and dehydration reactions, if the permeability is low enough to control fluid flow in the lower crust. It is noted that *the advective heat transfer mentioned in this study refers to the contribution of pore-fluid pressure gradient driven flow to heat transfer, whereas convective heat transfer refers to the contribution of pore-fluid buoyancy driven flow to heat transfer in a fluid-saturated porous medium*. Although heat transfer due to both conduction and convective flow arises from a vertical temperature gradient, there are some significant differences between these two heat transfer mechanisms. First, heat transfer due to pure conduction arises from a subcritical temperature gradient, while heat transfer due to convective flow is caused by a critical or supercritical temperature gradient. For a given hydrothermal system, the critical vertical temperature gradient can be evaluated using the critical Rayleigh number, which is directly determinable from classical theory in the field of convective flow in porous media (Horton and Rogers 1945; Lapwood 1948; Nield 1968; Bories and Combarnous 1973; Caltagirone 1975; Phillips 1991; Nield and Bejan 1992; Zhao et al. 1997, 1998a, b, 1999a, b, 2000a, 2001a). The definition and physical implication of both the Rayleigh number and the critical Rayleigh number for a given hydrothermal

C. Zhao et al., *Convective and Advective Heat Transfer in Geological Systems*,

© Springer-Verlag Berlin Heidelberg 2008

system will be addressed in detail later. Second, in the case of heat transfer due to conduction, both the rock mass and the pore-fluid in a porous medium play important roles in transferring heat energy. However, in the case of heat transfer due to convective flow, heat energy is predominantly transferred by the pore-fluid in the porous medium (in the case of large Rayleigh numbers).

Pore-fluid flow in permeable rocks in the upper crust is a very complicated phenomenon. Generally, such flow can be generated by mechanical process, thermal process, chemical process or combinations of these. In the case of mechanical process, pore-fluid flow mainly results from a pressure gradient in the porous medium and, therefore, is called pressure gradient driven flow. This kind of pore-fluid flow can cause advective heat transfer in the porous medium. Pore-fluid flow induced by the uneven topography of a basin and the flow of pore-fluid squeezed out of a sedimentary basin by the shortening of the upper crust are typical examples of pore-fluid pressure gradient driven flow. In the case of thermal process, pore-fluid flow is predominantly caused by a temperature gradient in porous rocks. Thus, it is often called temperature gradient driven flow (Phillips 1991; Nield and Bejan 1992; Zhao et al. 1997, 1998a, b, 1999a, b, 2000a, 2001a). Due to the nature of temperature gradient driven flow, convective heat transfer takes place in the porous medium. In order to generate convective flow in the upper crust with a flat top and bottom, the temperature gradient of the hydrothermal system must be equal to or greater than a critical temperature gradient. Convective pore-fluid flow is important for ore body formation and mineralization in hydrothermal systems from the following three points of view.

(1) Since the pore-fluid flows circularly within convecting hydrothermal systems, consumption of the pore-fluid is a minimum within the system. This enables convective flow to last for relatively long periods of time, if a high temperature at the bottom of the system can be maintained.
(2) Since convective pore-fluid flow comprises a circular flow regime, it is an effective and efficient process for mixing different chemical species within a hydrothermal system.
(3) Convective pore-fluid flow may result in highly localized temperature distributions in the hydrothermal system. This provides a favorable condition under which highly-localized, high-grade, giant hydrothermal ore deposits may be formed.

For these reasons, the study of convective pore-fluid flow instability in geological systems has attracted ever-increasing attention in recent years. In the case of chemical process, a species concentration gradient is the main driving force to trigger pore-fluid flow. This kind of pore-fluid flow may be called chemical concentration gradient driven flow. In particular, if convective pore-fluid flow is driven by a pore-fluid density change due to the diffusion of both heat and chemical species simultaneously, it is called *double-diffusion driven convective flow*, as considered in Chap. 11. Otherwise, *temperature gradient driven convective flow*, which is caused by heat diffusion only, is considered in the rest of this monograph when convective pore-fluid flow is treated.

Although the theoretical basis for convective flow in pore-fluid saturated porous media has been well established in many scientific fields, the occurrence of convective pore-fluid flow in the crust has been debated for many years. The core issue of the debate is the statement that traditional convective flow can only take place in a porous medium, if the pore-fluid pressure gradient is hydrostatic. Strictly speaking, this statement is not true even if pure heat conduction is considered in the porous medium since the fluid density at the base of the system is less than at the top due to thermal expansion. Thus even if the geothermal gradient is subcritical in a single layered homogeneous crust, the buoyancy generated by the geothermal gradient may cause a departure of the pore-fluid pressure gradient from hydrostatic in the traditional geological sense. However, for a multiply layered crust, it is impossible to maintain a pore-fluid pressure gradient at hydrostatic in the whole crust.

There are three major scientific methods, namely the experimental method, the theoretical analysis method and the computer simulation method, which are widely used to solve contemporary scientific and engineering problems. The experimental method is used to produce data for establishing fundamental physical and chemical laws, while theoretical analysis is used to establish the corresponding fundamental physical and chemical laws as well as governing equations for describing inherent characteristics of a problem. In addition, theoretical analysis can produce exact theoretical solutions for some kinds of scientific and engineering problems. Due to the complex and complicated nature of geo-scientific problems, the computer simulation method has found more and more applications. This gradually changes the traditional geoscience from a description-dominated empirical discipline into a computer simulation-dominated scientific discipline. Since computer simulations are usually based on an approximate numerical algorithm, it is necessary to verify and validate the computer simulation method before it is used to solve any new kind of scientific problem. In this regard, it is desirable to derive analytical solutions for typical benchmark problems of simple geometry. Since analytical solutions can be used to investigate the general behavior within the whole parameter space of the system, they result in general conclusions for the problem. However, since it is often impossible to use numerical solutions to investigate the general behaviors within the whole parameter space, which is usually of infinite extent, numerical solutions can only produce some kind of specific conclusion for the problem. Therefore, in order to draw general conclusions for problems associated with convective and advective heat transfer within the crust of the Earth, analytical solutions, if available, are always superior to numerical solutions. As mentioned above, analytical solutions to benchmark problems provide an important and often unique tool for validating and verifying numerical methods and algorithms used to solve problems with complicated geometries, such as convective and advective heat transfer within the heterogeneous crust of the Earth. For those reasons, the main focus of this monograph is on the development of analytical solutions for convective and advective heat transfer problems within pore-fluid saturated porous rocks.

The nature of large scale convective flows of pore-fluids such as water and carbon dioxide within the Earth's crust is not only fundamental for understanding the generation and formation of giant hydrothermal ore and oil deposits, but is also important

for understanding the release of heat and carbon dioxide from the deep Earth into the hydrosphere and atmosphere. Thus, the understanding of such convective flow processes has become closely involved in climate change related issues, such as finding the most efficient ways and places to dispose of captured carbon dioxide, locating and managing groundwater resources sustainably and exploring new geothermal resources that can be used for desalination and to produce electricity. On the nuclear power generation front, the understanding of convective and advective heat transfer processes can help us find the most appropriate places, with stable geology and negligible risk for convective and advective flow, for the safe long-term storage of radioactive materials. Thus, the topic of this monograph is clearly of interest for theoretical understanding in the field of geoscience and for broad applications in many other scientific and engineering fields.

We use both analytical and numerical methods to investigate convective and advective heat transfer in geological systems of the crustal scale. Because the pore-fluid (i.e., water) considered is within the Earth's crust, it is reasonable to assume that the density of the pore-fluid (i.e., water) is a linear function of temperature, which can be described by the Oberbeck-Boussinesq equation. In order to make a systematic investigation of the major issues associated with convective and advective heat transfer in the crust, the conceptual models addressed in this monograph gradually become more complicated. Discrepancies between the conceptual models are clearly stated so that the solutions can be compared with each other in the related chapters. In this regard, the contents of this monograph are arranged as follows. A rigorous analysis of the distribution of pore-fluid pressure gradients in both a homogeneous and layered crust without considering temperature effects is carried out in Chap. 2. In Chap. 3, analytical solutions for both pore-fluid pressure and its gradient are derived for a homogenous crust with the incorporation of heat conduction and advection effects. The solutions presented in this chapter are valid for a crust that is not hot enough to trigger convective pore-fluid flow. In Chap. 4, convective heat transfer within the crust is addressed and, in particular, the concepts of both the Rayleigh number and the critical Rayleigh number are discussed in detail. A significant result in this section is the discussion of the potential occurrence of convective pore-fluid flow in a crust that has a non-hydrostatic pore-fluid pressure gradient. Convective heat transfer in a heterogeneous crust is investigated in Chap. 5. The focus of this chapter is the influence of material anisotropy, thermoelasticity and temperature-dependent viscosity on convective pore-fluid flow. In Chaps. 6 and 7, focusing of pore-fluid flow within two-dimensional faults and cracks of crustal scales is considered without including temperature effects. A complete set of analytical solutions for excessive pore-fluid pressure, pore-fluid velocity and the stream function within and around elliptical faults is derived and presented in both a local elliptical coordinate system and a global Cartesian coordinate system. Based on the theoretical work conducted in Chaps. 6 and 7, numerical models are tested and used to investigate pore-fluid flow focused transient heat transfer within and around two-dimensional faults and cracks of crustal scales in Chap. 8. To examine convective instability of pore-fluid flow within three-dimensional fault zones, theoretical analysis of a vertical three-dimensional fault zone is conducted in Chap. 9,

while the theoretical analysis of an inclined three-dimensional fault zone is carried out in Chap. 10. In Chap. 11, the double-diffusion effect due to both temperature and chemical species is considered theoretically to investigate convective instability of pore-fluid flow within a vertical three-dimensional fault zone. In Chap. 12, convective heat transfer simulation is extended to investigate ore body formation and mineralization within the upper crust of the Earth. The precipitation and dissolution of lead-, zinc- and iron-bearing minerals are considered to demonstrate the important role that convective pore-fluid flow plays in hydrothermal systems. Finally, some conclusions are given at the end of the monograph.

Chapter 2
Distribution of Pore-Fluid Pressure Gradient in the Crust with Temperature Neglected

On the crustal scale, the rock mass of the crust may be treated as a porous material, the pores of which are filled with pore fluid (e.g., water). From the analytical point of view, it is assumed that the whole crust is comprised of layered materials. At this point, it must be pointed out that analytical solutions, which are derived from a purely mathematical analysis, are very important for scientific and engineering problems (Zhao and Steven 1996). First, an analytical solution can be used as a powerful means to gain an understanding of the solution scenarios under some extreme conditions for a given problem. Second, an analytical solution is often a useful, or even in some circumstances, a unique measure in the assessment and verification of any numerical methods. However, most scientific and engineering problems are mathematically described by a set of partial differential equations with complicated geometry and boundary conditions. This makes it extremely difficult to obtain analytical solutions for such problems. Thus, the main purpose of this section is to provide analytical solutions for problems with simple geometry and boundary conditions. In order to enhance the broad readability of the material, simple mathematics is used as much as possible, together with a discussion of the geological implications.

2.1 The Crust Comprised of a Single Homogeneous Layer

In order to demonstrate the concept of pore-fluid pressure gradient, we first consider the simple case of the crust represented as a single homogeneous layer, as shown in Fig. 2.1. We assume that the rock is rigid in this particular case. Under this assumption, the steady-state (i.e., the long-term state in a geological sense) governing equations of the pore-fluid flow in the crust are expressed as (Bear 1972; Scheidegger 1974):

$$\frac{\partial u}{\partial x} + \frac{\partial v}{\partial y} = 0, \tag{2.1}$$

$$u = \frac{K}{\mu}\left(-\frac{\partial P}{\partial x}\right), \tag{2.2}$$

C. Zhao et al., *Convective and Advective Heat Transfer in Geological Systems*,

© Springer-Verlag Berlin Heidelberg 2008

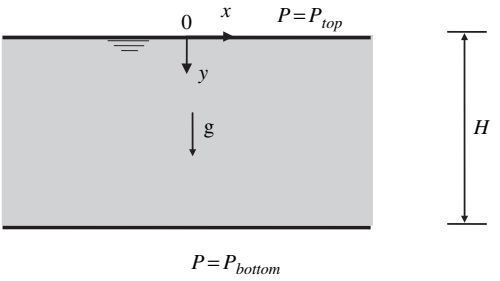

Fig. 2.1 Geometry of the single layer homogeneous crust

$$v = \frac{K}{\mu}\left(-\frac{\partial P}{\partial y} + \rho_f g\right), \tag{2.3}$$

where u and v are the horizontal and vertical velocity components of the pore-fluid in the x and y directions, respectively; P is the pore-fluid pressure; K is the permeability of the porous medium; μ is the dynamic viscosity of the pore-fluid; ρ_f is the density of the pore-fluid and g is the acceleration due to gravity.

Note that (2.1) is the continuity equation that describes the mass conservation of the pore-fluid in every spatial point of the crust. Equations (2.2) and (2.3) are Darcy's equations to describe the relationships between the pore-fluid velocity and pressure gradient within the crust. Solutions to these three equations are dependent on the boundary conditions of the problem to be considered. For this simple system, the horizontal velocity of the pore-fluid is equal to zero. Thus, we only need two boundary conditions to obtain the solutions for the pressure and vertical velocity of the pore-fluid. Clearly, there are three sets of boundary conditions that are of immediate geological significance.

The first set of boundary conditions is that the pore-fluid pressure at the surface of the crust is equal to the atmospheric pressure, P_{top}, while the pore-fluid pressure at the bottom of the crust is equal to the atmospheric pressure plus the hydrostatic pressure, $P_{bottom} = P_{top} + \rho_f g H$, where H is the thickness of the crust. In this particular case, the vertical velocity of the pore-fluid is also equal to zero. Both the pore-fluid pressure and its gradient are hydrostatic:

$$P = P_{top} + \rho_f g y, \tag{2.4}$$

$$\frac{\partial P}{\partial y} = \rho_f g. \tag{2.5}$$

For the second set of boundary conditions, the pore-fluid pressure at the surface of the crust is equal to the atmospheric pressure, P_{top}, while the pore-fluid pressure at the bottom of the crust is equal to the atmospheric pressure plus the lithostatic pressure, $P_{bottom} = P_{top} + \rho_r g H$, where ρ_r is the density of the rock mass in the crust. Unlike the case of the first set of boundary conditions, the vertical velocity of the pore-fluid is constant, but not equal to zero. In this situation, both the pore-fluid pressure and its gradient are lithostatic:

$$P = P_{top} + \rho_r g y, \tag{2.6}$$

$$\frac{\partial P}{\partial y} = \rho_r g, \tag{2.7}$$

$$v = -\frac{K}{\mu}(\rho_r - \rho_f)g. \tag{2.8}$$

Since the density of the rock mass is greater than that of the pore-fluid, the vertical velocity of the pore-fluid has a negative value, indicating that the pore-fluid flow is upward in this particular case. The geological implication of this non-zero vertical velocity is that if the pore-fluid pressure gradient is lithostatic, there must be an upward throughflow in the crust.

For the third set of boundary conditions, the pore-fluid pressure at the surface of the crust is equal to the atmospheric pressure, P_{top}, while the pore-fluid pressure at the bottom of the crust is equal to the atmospheric pressure plus an arbitrary given pressure, $P_{bottom} = P_{top} + \rho_c g H$, where $\rho_c g H$ is the arbitrary given pressure. Just like the case of the second set of boundary conditions, the vertical velocity of the pore-fluid is constant, but not equal to zero. In this situation, both the pore-fluid pressure and its gradient are between hydrostatic and lithostatic under the constraint of $\rho_f < \rho_c < \rho_r$:

$$P = P_{top} + \rho_c g y, \tag{2.9}$$

$$\frac{\partial P}{\partial y} = \rho_c g, \tag{2.10}$$

$$v = -\frac{K}{\mu}(\rho_c - \rho_f)g. \tag{2.11}$$

Under the constraint of $\rho_f < \rho_c < \rho_r$, the vertical velocity of the pore-fluid also has a negative value, indicating that the pore-fluid flow is upward in this particular case. The geological implication of this non-zero vertical velocity is that if the pore-fluid pressure gradient is between hydrostatic and lithostatic, there must be an upward throughflow in the crust.

It is noted that if the pore-fluid pressure gradient in the crust is less than the corresponding hydrostatic pressure gradient (i.e., $\rho_c < \rho_f$), the vertical velocity of the pore-fluid is downward.

The outcome of this simple crustal model is that, in the absence of thermal effects, if the pore-fluid pressure gradient is hydrostatic, then the upward pore-fluid velocity must be identical to zero. The reverse of this statement is also correct. If the upward pore-fluid velocity is identical to zero, the pore-fluid pressure gradient must be hydrostatic. On the other hand, in the absence of thermal effects, the existence of the non-hydrostatic pore-fluid pressure gradient indicates that there must be an upward or a downward throughflow in the crust. For these reasons, it is appropriate

to assign a constant pressure boundary condition at the top surface of the crust and a constant upward throughflow boundary condition at the bottom of the crust, if the crust is comprised of multiple layers.

2.2 The Crust Comprised of Two Homogeneous Layers

For a crust comprised of multiple homogeneous layers, Zhao et al. (1998b) conducted a theoretical analysis to determine both the pore-fluid pressure gradient and the effective stress gradient distribution in the crust. The basic conclusion from that analysis is that the intrinsic effective vertical stress gradient of the solid matrix can be maintained at a value close to the lithostatic pressure gradient, but the pressure gradient of the pore fluid cannot be maintained at a lithostatic pressure gradient in all the layers. In a crust of multiple layers, the layer with the smallest permeability acts as a valve to control the pore-fluid flow in the whole system. Due to the existence of the least impermeable layer, the related geological constraint on the mass conservation of the pore-fluid in the vertical direction indicates that although the pore-fluid pressure gradient can be lithostatic in the least impermeable layer, it must be between the hydrostatic and lithostatic gradient in other relatively permeable layers. In the following, we will consider a crust of multiple homogeneous layers to demonstrate this conclusion.

The problem to be considered in this subsection is a two layer hydrodynamic system shown in Fig. 2.2. It is assumed that the top layer (i.e., layer 1) is more permeable than the bottom layer (i.e., layer 2). Layer 2 is the valve of this two layer hydrodynamic system controlling the overall vertical throughflow. If the pore-fluid pressure gradient in the bottom layer is lithostatic, then the pore-fluid pressure gradient in the top layer must be between hydrostatic and lithostatic, depending on the permeability ratio of the top layer to the bottom layer.

The mathematical model for this problem is exactly the same as that expressed in (2.1), (2.2) and (2.3), except that there are two continuity conditions for the pore-fluid flow velocity and pressure at the interface between the two layers. As mentioned above, a constant pressure boundary condition is applied at the top surface of the model, while a constant upward velocity boundary condition is applied at

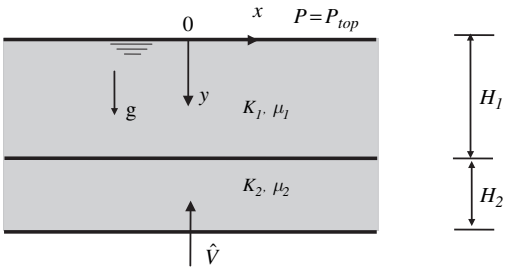

Fig. 2.2 Geometry of the two layer crust model

the bottom of the model. Under these considerations, the analytical solution for the pore-fluid pressure in the system can be derived and expressed as

$$P_{f1} = P_{top} + \rho_f g y - \frac{\mu_1}{K_1}\hat{V} y \quad (0 \le y \le H_1), \tag{2.12}$$

$$P_{f2} = P_{top} + \rho_f g y - \frac{\mu_1}{K_1}\hat{V} H_1 - \frac{\mu_2}{K_2}\hat{V}(y - H_1) \quad (H_1 \le y \le H_1 + H_2), \tag{2.13}$$

where P_{f1} and P_{f2} are the pore-fluid pressures in the top and bottom layers; μ_1 and μ_2 are the corresponding dynamic viscosities of the pore-fluid; K_1 and K_2 are the permeabilities of the top and bottom layers, and H_1 and H_2 are the thicknesses of the top and bottom layers respectively.

Accordingly, the analytical solution for the pore-fluid pressure gradient can be expressed as

$$\frac{\partial P_{f1}}{\partial y} = \rho_f g - \frac{\mu_1}{K_1}\hat{V} \quad (0 \le y \le H_1), \tag{2.14}$$

$$\frac{\partial P_{f2}}{\partial y} = \rho_f g - \frac{\mu_2}{K_2}\hat{V} \quad (H_1 \le y \le H_1 + H_2). \tag{2.15}$$

In the case of upward throughflow in the crust, the upward pore-fluid velocity, $\hat{V}$, has a negative value. Thus, for a non-zero upward throughflow, (2.14) and (2.15) clearly indicate that the corresponding pore-fluid pressure gradient in both the top and the bottom layers must be greater than the hydrostatic pressure gradient.

Since the bottom layer is the valve of this two layer system, the constraint condition for maintaining the pore-fluid pressure gradient at lithostatic in the bottom layer can be derived and expressed as

$$\hat{V}_{control} = -\frac{K_2}{\mu_2}(\rho_r - \rho_f)g, \tag{2.16}$$

where $\hat{V}_{control}$ is the upward throughflow velocity to maintain the pore-fluid pressure gradient at lithostatic in the bottom layer.

It needs to be pointed out that the above solutions are also valid for $K_1 \le K_2$ and $0 \le \left|\hat{V}\right| \le \left|\hat{V}_{control}\right|$, where $\hat{V}_{control}$ is the vertical Darcy velocity to maintain the pore-fluid pressure gradient in the least permeable layer at a lithostatic pressure gradient. In the case of $K_1 < K_2$, the top layer (layer 1) is the controlling valve of the system instead of layer 2.

Clearly, in the case of $0 < \left|\hat{V}\right| < \left|\hat{V}_{control}\right|$, the intrinsic pore-fluid pressure gradient in both layers is greater than hydrostatic, but less than lithostatic. However, in the case of $\hat{V} = \hat{V}_{control}$, the pore-fluid pressure gradient is equal to lithostatic in the less permeable layer, but less than lithostatic in the more permeable layer.

Using the above analytical results, we can investigate the pore-fluid pressure gradient distribution in the following two extreme situations: (1) the bottom layer is the valve of the whole system, and (2) the top layer is the valve of the whole system. Without losing generality, we use the following dimensionless quantities to express the related results:

$$P_f^* = \frac{P_f - P_{top}}{\rho_f g H_{total}}, \qquad y^* = \frac{y}{H_{total}}, \qquad H_{total} = H_1 + H_2. \tag{2.17}$$

In the first case, $K_1 > K_2$ and the results can be expressed as follows:

$$P_{f1}^* = \left(1 - \frac{K_2\mu_1}{K_1\mu_2}\right) y^* + \left(\frac{K_2\mu_1}{K_1\mu_2}\right) \frac{\rho_r}{\rho_f} y^* \qquad \left(0 \le y^* \le \frac{H_1}{H_{total}}\right), \tag{2.18}$$

$$P_{f2}^* = \frac{\rho_r}{\rho_f} y^* - \left(1 - \frac{K_2\mu_1}{K_1\mu_2}\right)\left(\frac{\rho_r}{\rho_f} - 1\right) \frac{H_1}{H_{total}} \qquad \left(\frac{H_1}{H_{total}} \le y^* \le 1\right). \tag{2.19}$$

Similarly, in the second case, $K_1 < K_2$ and the results can be expressed as

$$P_{f1}^* = \frac{\rho_r}{\rho_f} y^* \qquad \left(0 \le y^* \le \frac{H_1}{H_{total}}\right), \tag{2.20}$$

$$\begin{aligned} P_{f2}^* = {} & \left[1 + \frac{K_1\mu_2}{K_2\mu_1}\left(\frac{\rho_r}{\rho_f} - 1\right)\right] y^* \\ & + \left(1 - \frac{K_1\mu_2}{K_2\mu_1}\right)\left(\frac{\rho_r}{\rho_f} - 1\right) \frac{H_1}{H_{total}} \quad \left(\frac{H_1}{H_{total}} \le y^* \le 1\right). \end{aligned} \tag{2.21}$$

If we assume that the density ratio of the rock to the pore-fluid is equal to 2.7, the thickness ratio of the top layer to the whole crust is equal to 0.6, and that $K_2\mu_1/(K_1\mu_2) = 0.2$, in the first case and $K_1\mu_2/(K_2\mu_1) = 0.2$ in the second case, respectively, we can obtain the results shown in Fig. 2.3. It is clear that in case 1, the pore-fluid pressure gradient is lithostatic in the bottom layer, but it is between hydrostatic and lithostatic in the top layer. Since the top layer is the valve of the whole system in case 2, the pore-fluid pressure gradient is lithostatic in the top layer, while it is between hydrostatic and lithostatic in the bottom layer. Nevertheless, the pore-fluid pressure does not exceed lithostatic pressure in both the cases. This indicates that although the pore-fluid pressure gradient can be maintained at lithostatic in a single layer crust model, it cannot be simultaneously maintained at lithostatic in a two layer crustal model.

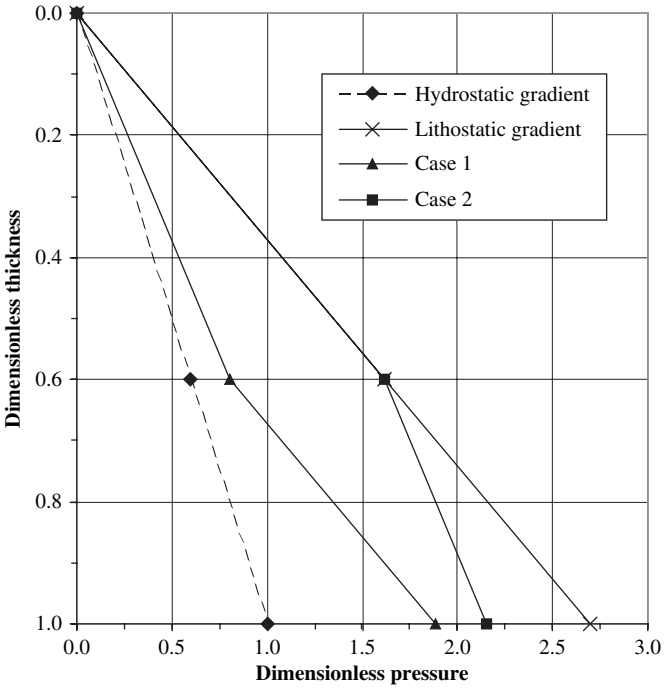

Fig. 2.3 Distribution of dimensionless pressure versus dimensionless thickness

2.3 The Crust Comprised of Three Homogeneous Layers

The same procedure as above is followed to derive the analytical solutions for a three layer hydrodynamic system (Fig. 2.4) in this subsection. To save space, only the final results are given below.

The analytical solution for the pore-fluid pressure in a three layer hydrodynamic system is as follows:

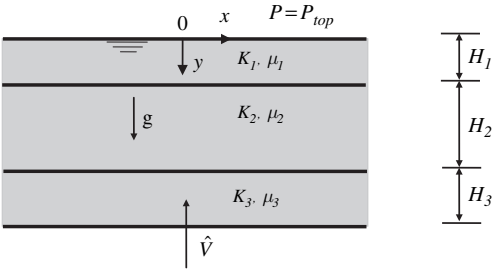

Fig. 2.4 Geometry of the three layer crust model

$$P_{f1} = P_{top} + \rho_f g y - \frac{\mu_1}{K_1}\hat{V} y \qquad (0 \le y \le H_1), \tag{2.22}$$

$$P_{f2} = P_{top} + \rho_f g y - \frac{\mu_1 \hat{V}}{K_1} H_1 - \frac{\mu_2 \hat{V}}{K_2}(y - H_1) \qquad (H_1 \le y \le H_1 + H_2), \tag{2.23}$$

$$P_{f3} = P_{top} + \rho_f g y - \frac{\mu_1 \hat{V}}{K_1} H_1 - \frac{\mu_2 \hat{V}}{K_2} H_2 - \frac{\mu_3 \hat{V}}{K_3}[y - (H_1 + H_2)]$$
$$(H_1 + H_2 \le y \le H_1 + H_2 + H_3), \tag{2.24}$$

where P_{f1}, P_{f2} and P_{f3} are the pore-fluid pressures in the top, middle and bottom layers; μ_1, μ_2 and μ_3 are the corresponding dynamic viscosities of the pore-fluid; K_1, K_2 and K_3 are the permeabilities of the top, middle and bottom layers, and H_1, H_2 and H_3 are the thicknesses of the top, middle and bottom layers, respectively.

From (2.22), (2.23) and (2.24), the corresponding pore-fluid pressure gradient can be expressed as

$$\frac{\partial P_{f1}}{\partial y} = \rho_f g - \frac{\mu_1}{K_1}\hat{V} \qquad (0 \le y \le H_1), \tag{2.25}$$

$$\frac{\partial P_{f2}}{\partial y} = \rho_f g - \frac{\mu_2}{K_2}\hat{V} \qquad (H_1 \le y \le H_1 + H_2), \tag{2.26}$$

$$\frac{\partial P_{f3}}{\partial y} = \rho_f g - \frac{\mu_3}{K_3}\hat{V} \qquad (H_1 + H_2 \le y \le H_1 + H_2 + H_3). \tag{2.27}$$

As expected, the same conclusions as drawn from the previous two layer hydrodynamic system can be drawn from the three layer hydrodynamic system considered here.

In summary, it can be concluded that although the entrapped pore-fluid pressure may reach or even exceed lithostatic pressure in an overpressured system consisting of a permeable layer and two adjacent impermeable layers (Powley 1990; Fisher and Brantley 1992; Yardley 1997), the entrapped pore-fluid pressure gradient cannot reach or exceed lithostatic pressure gradient from the following two points of view:

(1) If the permeable layer is bounded by two relatively impermeable layers, the permeabilities of which are relatively very small, but are not equal to zero, the overpressure (i.e., the pore-fluid pressure minus the hydrostatic pressure) cannot reach steady state since this overpressure must be dissipated at the completion of the consolidation.
(2) On the other hand, if the permeable layer is bounded by two absolutely impermeable layers, the permeabilities of which are exactly identical to zero, the entrapped pore-fluid behaves just like the fluid in a pressure vessel. In this case, the pore-fluid pressure gradient must be exactly equal to zero in the absolutely impermeable layers. Also, the pore-fluid pressure gradient must be exactly equal to the hydrostatic pressure gradient in the permeable layer because the upward

throughflow velocity is exactly identical to zero due to the constraint condition provided by the two absolutely impermeable layers.

2.4 The Critical Crustal Thickness for a Hydrostatic Pore-Fluid Pressure Gradient

The above-mentioned conclusions can be used to determine the critical thickness of a crust that has a hydrostatic pore-fluid pressure gradient. Suppose there is a thin impermeable seal of negligible thickness overlying the top surface of the crust and that the crustal material has a tensile strength, $\bar{\sigma}_{tensile}$, and a compressive strength, $\bar{\sigma}_{compressive}$. In order to maintain the overpressure in the crust, there should be no cracks allowed within the overlying seal. This implies that the limit of the effective stress within the overlying seal is equal to the corresponding tensile strength. According to Terzaghi (1925, 1943, 1960) and Garg and Nur (1973), the total stress is equal to the effective stress plus the pore-fluid pressure so that the pore-fluid pressure within the overlying seal needs to be considered. Since the lower limit of the total vertical stress within the overlying seal of a negligible thickness is equal to zero, the pore-fluid pressure within the overlying seal is of the same value in magnitude as the tensile strength of the overlying seal. On the other hand, in order to avoid the collapse of the pores within the crust, the upper limit of the corresponding effective stress should be less than or equal to the compressive strength of the crustal material. Hence, at the bottom of the crust, the upper limit of the corresponding effective stress is equal to the compressive strength of the crustal material. This is the condition under which a critical thickness of the crust exists that has a hydrostatic pore-fluid pressure gradient. Because the overlying seal is absolutely impermeable, the pore-fluid pressure gradient is hydrostatic within the crust. As a result, the total stress at the bottom of the crust is as follows:

$$\sigma_{total}^{bottom} = \bar{\sigma}_{tensile} + \rho_f g H_{critical} + \bar{\sigma}_{compressive}, \tag{2.28}$$

where $H_{critical}$ is the critical thickness of the crust that has a hydrostatic pore-fluid pressure gradient. As shown in Fig. 2.5, $H_{critical}$ can be determined by considering the vertical force equilibrium condition at the bottom of the crust as follows:

$$\bar{\sigma}_{tensile} + \rho_f g H_{critical} + \bar{\sigma}_{compressive} = \rho_r g H_{critical}. \tag{2.29}$$

Rearranging the terms in (2.29) yields the following equation:

$$H_{critical} = \frac{\bar{\sigma}_{tensile} + \bar{\sigma}_{compressive}}{(\rho_r - \rho_f) g}. \tag{2.30}$$

This equation is easily used to determine the critical thickness of the crust that has a hydrostatic pore-fluid pressure gradient. For instance, the sum of the tensile and compressive strengths of the crustal material is about 170 MPa in magnitude,

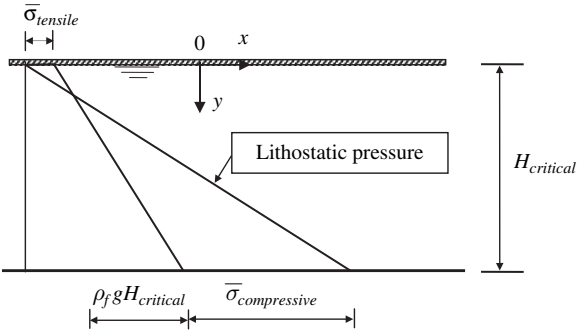

Fig. 2.5 Determination of the critical thickness of the crust

the density difference between the rock and pore-fluid is approximately $1700\,\mathrm{kg/m^3}$ in magnitude, and the acceleration due to gravity is taken as $9.8\,\mathrm{m/s^2}$. Substituting these parameter values into (2.30) yields a critical crustal thickness of approximately 10 km in magnitude.

Equation (2.30) is derived under the assumption that the overlying seal is of negligible thickness so it cannot be subject to bending. In geological reality, the overlying seal may have a considerable thickness and, therefore, it acts as a thin plate overlying the relatively thick crust. In this situation, the overlying impermeable seal can be mechanically treated as an elastic thin plate overlying an elastic foundation (Zhao et al. 2000b; Hetenyi 1980). If the maximum pressure which the elastic overlying seal can sustain without crack failure is $\bar{P}_{additional}$, we need to write this additional pressure into (2.30) instead of the tensile strength of the crustal material as follows:

$$H_{critical}^{new} = \frac{\bar{P}_{additional} + \bar{\sigma}_{compressive}}{(\rho_r - \rho_f)g}. \tag{2.31}$$

Geologically, this additional pressure is the overpressure of the pore-fluid just underneath the impermeable seal. Since the additional pressure $\bar{P}_{additional}$ is mainly dependent on the thickness and mechanical properties of the seal and crust, its value is usually much greater than the value of the tensile strength of the crustal material. This means that the critical crustal thickness obtained from (2.30) is not the maximum thickness of the crust that has a hydrostatic pore-fluid pressure gradient. Thus, the statement that the hydrostatic pore-fluid pressure gradient can only exist in the top a few kilometers (i.e., 10 km) may be too conservative in a situation where the top impermeable seal has a considerable thickness. In this regard, further research is needed to determine the value of the additional pressure, $\bar{P}_{additional}$, due to the bending of the top impermeable seal.

Chapter 3
Pore-Fluid Pressure Gradients in the Crust with Heat Conduction and Advection

Heat transfer in solids through conduction is an important phenomenon associated with a broad range of scientific and engineering problems and, therefore, has been extensively studied for many years (Carslaw and Jaeger 1959; van Genuchten and Alvel 1982; Bear and Bachmat 1990). Heat conduction has also played an important role in transferring heat energy from the mantle into the crust. In a porous medium, heat transfer can take place through the relative movement of pore-fluid to the solid matrix. Such pore-fluid movement can be caused by either advection or convection, depending on the driving force producing pore-fluid flow. As a general rule, if pore-fluid flow is driven by the temperature-dependent buoyancy of the pore-fluid, the pore-fluid flow is called convective flow, or convection for short. Thus, convection is always associated with some kind of thermal process within the whole system. On the other hand, if pore-fluid flow is driven by mechanical processes, the pore-fluid flow is called advective flow, or advection for short. In this section, we investigate the effects of heat conduction and advection on the distribution of pore-fluid pressure gradients in the crust. A detailed discussion of heat convection will be carried out in Chap. 4. To investigate the effects of heat conduction and advection, the conservation of thermal energy needs to be added to the conceptual crustal model used in the previous section. In other words, an energy equation, which describes the conservation of thermal energy within the crust must be added into the mathematical model of the crust.

A conceptual model represents the major characteristics of a real system with some degree of approximation, whereas a mathematical model describes the related conceptual model using scientific principles and mathematical tools. As a result, the mathematical model of a real system is often comprised of a set of simultaneous partial differential equations and, if these equations are solved in a purely mathematical manner, then we obtain analytical (i.e., mathematical) solutions. Otherwise, if this set of simultaneous partial differential equations is solved using numerical methods, such as the finite element method, finite difference method, boundary element method, spectral analysis method, particle simulation method and so forth, then we can only obtain numerical solutions. Since an analytical solution can be used to investigate the behaviors of a system within the whole parameter space of the system, it results in general conclusions for the problem. However, since it is often impossible to use a numerical solution to investigate the behaviors of a system

C. Zhao et al., *Convective and Advective Heat Transfer in Geological Systems*,

© Springer-Verlag Berlin Heidelberg 2008

within the whole parameter space, which is usually of infinite nature, a numerical solution can only produce some kind of specific conclusion for the problem. Therefore, in order to draw general conclusions for a real problem, analytical solutions, if available, are always superior to numerical solutions. In this chapter, we will present analytical solutions that investigate the effect of heat conduction and advection on the distribution of pore-fluid pressure gradients in the crust.

3.1 The Effect of Heat Conduction on the Distribution of Pore-Fluid Pressure Gradients

The first conceptual model of the crust considered in this section is shown in Fig. 3.1. The basic characteristic of this model is that the boundary conditions are applied so that pore-fluid flow does not occur in the model. For this reason, the model can be regarded as a heat transfer through conduction problem. The corresponding mathematical model of the crust in a steady state is expressed as follows:

$$\frac{\partial u}{\partial x}+\frac{\partial v}{\partial y}=0, \tag{3.1}$$

$$u=\frac{K}{\mu}\left(-\frac{\partial P}{\partial x}\right), \tag{3.2}$$

$$v=\frac{K}{\mu}\left(-\frac{\partial P}{\partial y}+\rho_f g\right), \tag{3.3}$$

$$\rho_{f0}c_p\left(u\frac{\partial T}{\partial x}+v\frac{\partial T}{\partial y}\right)=\lambda_e\left(\frac{\partial^2 T}{\partial x^2}+\frac{\partial^2 T}{\partial y^2}\right), \tag{3.4}$$

$$\rho_f=\rho_{f0}[1-\beta_T(T-T_0)],\quad \lambda_e=\phi\lambda_f+(1-\phi)\lambda_s, \tag{3.5}$$

where u and v are the horizontal and vertical velocity components of the pore-fluid in the x and y directions, respectively; P is the pore-fluid pressure; T is the temperature of the crustal material; K is the permeability of the crustal material; μ is the dynamic

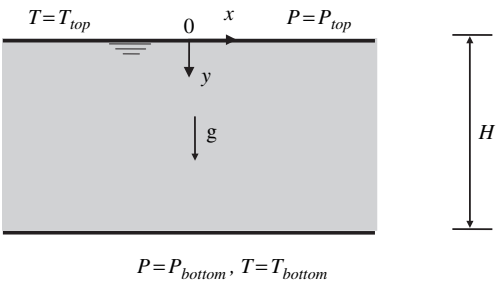

Fig. 3.1 Geometry of the first conceptual model (Conduction model)

viscosity of the pore-fluid; ρ_f is the density of the pore-fluid and g is the acceleration due to gravity; ρ_{f0} and T_0 are the reference density and temperature; λ_f and λ_s are the thermal conductivities of the pore-fluid and rock mass; c_p is the specific heat of the pore-fluid; ϕ and β_T are the porosity of the crustal material and the thermal volume expansion coefficient of the pore-fluid, respectively.

In (3.5), the density variation is assumed to be dependent on temperature only, without a direct consideration of excess pore-fluid pressure. Since the excess pore-fluid pressure due to heat conduction in the crust is much smaller than the hydrostatic pore-fluid pressure, it is analytically acceptable to neglect the effect of excess pore-fluid pressure on the density variation of the pore-fluid. For example, as demonstrated later, the excess pore-fluid pressure due to heat conduction is about 5 percent of the hydrostatic pore-fluid pressure for a crust of more than 30 km thick. This means that the influence of temperature on the pore-fluid density variation is at least one-order magnitude less than that of the excess pore-fluid pressure induced by heat conduction in the crust. Suppose the compressibility of the pore-fluid (i.e., water) is about 0.44 (1/GPa) and that the thermal expansion coefficient of water is about $2 \times 10^{-4}(1/^{\circ}\mathrm{C})$ at an ambient surface temperature of 20 °C, the pore-fluid density variation due to thermal expansion at a depth of 30 km of the crust is:

$$\Delta\rho_T = -30 \times 20 \times 2 \times 10^{-4}\rho_{f0} = -0.12\rho_{f0}, \tag{3.6a}$$

where the temperature gradient of the crust is assumed to be $20\,^{\circ}\mathrm{C}/\mathrm{km}$.

In this case, the pore-fluid density variation due to excess pore-fluid pressure can be estimated as follows:

$$\Delta\rho_{ep} = -0.05 \times (30000 \times 9.8 \times 1000) \times (0.44 \times 10^{-9})\rho_{f0} = -0.0065\rho_{f0}, \tag{3.6b}$$

where the product in the first parentheses is the hydrostatic pore-fluid pressure.

Although the influence of excess pore-fluid pressure due to thermal expansion on the variation of the pore-fluid density is negligible in the theoretical analysis, the influence of hydrostatic pore-fluid pressure on the variation of the pore-fluid density needs to be considered, because it may have the same magnitude as the influence of thermal expansion on the variation of the pore-fluid density. Nevertheless, the thermal expansion of pore-fluid due to a temperature increase causes a decrease in the pore-fluid density, while compression of the pore-fluid due to hydrostatic pore-fluid pressure causes an increase in the pore-fluid density. As a result, the influence of thermal expansion on the variation of pore-fluid density can be largely canceled by that of compression due to hydrostatic pore-fluid pressure. This is one reason why the reference pore-fluid density is commonly used in the heat transfer equation (i.e., (3.4)).

As shown in Fig. 3.1, the boundary conditions of this problem are as follows: constant temperature and pressure boundary conditions are applied at both the top and bottom of the system. The constant value of the bottom pressure is appropriately selected so that the reference pore-fluid pressure gradient is hydrostatic in the system. Once the thermal effect is considered, the density of the pore-fluid is no longer constant, but varies with temperature, as can be seen from (3.5). In this case, the pore-fluid pressure gradient varies linearly with the depth of the crust, while the pore-fluid pressure varies quadratically with the depth of the crust. Under the above

boundary conditions, the pore-fluid velocity in both the horizontal and the vertical directions is identical to zero. Thus, the first conceptual model of the crust shown in Fig. 3.1 can be essentially treated as a one-dimensional problem, for which the analytical solution is already available (Carslaw and Jaeger 1959; van Genuchten and Alvel 1982; Bear and Bachmat 1990). If the top temperature is used as the reference temperature, the related analytical solution can be expressed as follows:

$$u = v = 0, \tag{3.7}$$

$$P = P_{top} + \rho_{f0} g y - \frac{1}{2}\left(\frac{T_{bottom} - T_{top}}{H}\beta_T\right)\rho_{f0} g y^2, \tag{3.8}$$

$$\frac{\partial P}{\partial y} = \rho_{f0} g - \left(\frac{T_{bottom} - T_{top}}{H}\beta_T\right)\rho_{f0} g y, \tag{3.9}$$

$$T = T_{top} + \frac{T_{bottom} - T_{top}}{H} y. \tag{3.10}$$

If the temperature at the top is equal to that at the bottom of the system, the third term on the right hand side of (3.8) vanishes so that the pressure solution is identical to that presented previously (i.e., (2.4)) for the same conceptual model. Equations (3.8) and (3.9) show that the pore-fluid pressure and its gradient vary with the depth quadratically and linearly, respectively. Since the thermal volume expansion coefficient is a small number of the order of $2 \times 10^{-4}/^{\circ}\mathrm{C}$ in magnitude, (3.8) indicates that the thermal effect on the distribution of the pore-fluid pressure is significant in the lower part of the crust, but may not be significant in the upper part of the crust, especially in the case of a thin crust.

To reduce the requirements for parameters, the following dimensionless quantities can be used to express the above analytical solution for the pore-fluid pressure:

$$P^* = \frac{P - P_{top}}{\rho_{f0} g H}, \quad y^* = \frac{y}{H}. \tag{3.11}$$

Using these dimensionless quantities, (3.8) and (3.9) can be rewritten as

$$P^* = y^* - \frac{1}{2}\left(T_{bottom} - T_{top}\right)\beta_T y^{*2}, \tag{3.12}$$

$$\frac{\partial P^*}{\partial y^*} = 1 - \left(T_{bottom} - T_{top}\right)\beta_T y^*. \tag{3.13}$$

Given that the thermal volume expansion coefficient of the pore-fluid is approximately constant, (3.12) and (3.13) indicate that both the dimensionless pore-fluid pressure and its gradient are only dependent on the temperature difference between the top and the bottom of the crust for the conceptual crustal model considered here.

Figure 3.2 shows the thermal effect of this heat conduction model on the distribution of the dimensionless pressure for two different cases. In this figure, the reference hydrostatic pressure is labeled as R. H. Pressure. In case 1, the temperature difference between the top and the bottom of the crust is $600\,^{\circ}\mathrm{C}$, whereas in case 2, this temperature difference is $1000\,^{\circ}\mathrm{C}$. In order to examine the thermal effect

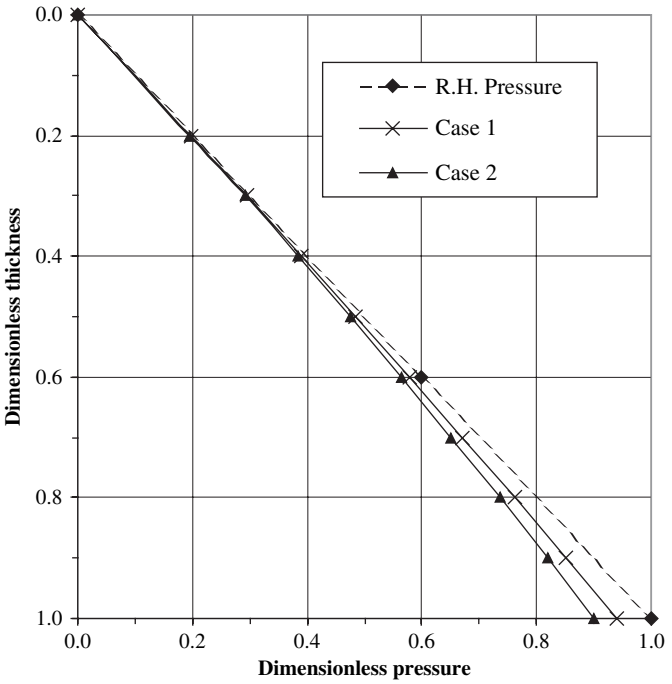

Fig. 3.2 Thermal effect on distribution of dimensionless pressure

on the distribution of the dimensionless pressure, the reference hydrostatic pressure resulting from a constant reference density of the pore-fluid is also shown in this figure for comparison. The related results clearly demonstrate that pure heat conduction may have some influence on the distribution of the dimensionless pressure in the lower part of the crust, but has little influence on the distribution of the dimensionless pressure in the upper part of the crust. Nevertheless, the effect of heat conduction on the distribution of the dimensionless pressure in the lower part of the crust also lies within a limited range. This implies that, for a saturated crust with motionless pore-fluid, the pore-fluid pressure is very close to the reference hydrostatic pressure arising from the constant reference density of the pore-fluid, even though heat conduction takes place in this crust.

3.2 The Effect of Heat Conduction and Advection on the Distribution of Pore-Fluid Pressure Gradients

If the pore-fluid pressure gradient of the crust is lithostatic, there is an upward throughflow in the crust that can cause heat transfer through heat advection within the crust. In this case, heat conduction and advection take place simultaneously. To investigate the combined effect of heat conduction and advection on the distribution of pore-fluid

pressure in the crust, a second conceptual model shown in Fig. 3.3 is considered in this section. Although the mathematical model expressed in (3.1), (3.2), (3.3), (3.4) and (3.5) is equally applicable to both the first and the second conceptual models, the boundary conditions for the second model are different. Since heat conduction and advection take place in the second conceptual model, this model can be regarded as a heat conduction-advection problem. For the second conceptual model, the temperature and pressure are constant at the top boundary of the model. A vertical velocity equal to the upward throughflow resulting from the lithostatic pore-fluid pressure gradient is applied at the bottom of the model. In addition, a constant conductive thermal flux boundary condition with a value of q_0 is applied at the bottom of the model. Since the conductive thermal flux can be expressed as $q_0 = -\lambda_e \partial T / \partial y$ in this instance, an upward constant conductive thermal flux of q_0 means that the temperature gradient, $\partial T / \partial y = -q_0 / \lambda_e$, is a positive constant, because the thermal conductivity of the crustal material is constant here.

The analytical solutions for this heat conduction-advection problem can be derived and expressed as follows:

$$u = 0, \quad v = \hat{V}, \tag{3.14}$$

$$T = T_{top} + \frac{q_0}{c_p \rho_{f0} \hat{V}} e^{-\frac{c_p \rho_{f0} \hat{V} H}{\lambda_e}} \left(1 - e^{\frac{c_p \rho_{f0} \hat{V}}{\lambda_e} y} \right), \tag{3.15}$$

$$P = P_{top} + \rho_{f0} g y - \frac{q_0}{c_p \rho_{f0} \hat{V}} e^{-\frac{c_p \rho_{f0} \hat{V} H}{\lambda_e}} \left[y + \frac{\lambda_e}{c_p \rho_{f0} \hat{V}} \left(1 - e^{\frac{c_p \rho_{f0} \hat{V}}{\lambda_e} y} \right) \right] \beta_T \rho_{f0} g - \frac{\mu}{K} \hat{V} y, \tag{3.16}$$

$$\frac{\partial P}{\partial y} = \rho_{f0} g - \frac{q_0}{c_p \rho_{f0} \hat{V}} e^{-\frac{c_p \rho_{f0} \hat{V} H}{\lambda_e}} \left(1 - e^{\frac{c_p \rho_{f0} \hat{V}}{\lambda_e} y} \right) \beta_T \rho_{f0} g - \frac{\mu}{K} \hat{V}. \tag{3.17}$$

It is obvious that when advection is considered, the temperature, pore-fluid pressure and their gradients vary non-linearly with the depth of the crust. Their distribution patterns, in general, are different from those obtained in the previous section where only heat conduction is considered, depending on the contribution of heat advection to the total heat transfer in the system. In order to minimize the requirements for parameters, the following dimensionless quantities can be used to express the above analytical solution for the pore-fluid pressure and temperature.

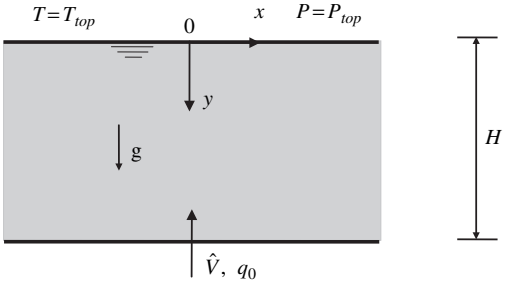

Fig. 3.3 Geometry of the second conceptual model (conduction and advection model)

$$P^* = \frac{P - P_{top}}{\rho_{f0} g H}, \quad y^* = \frac{y}{H}, \tag{3.18}$$

$$P_e = -\frac{H \rho_{f0} c_p}{\lambda_e} \hat{V}, \quad T^* = -\frac{(T - T_{top})\lambda_e}{q_0 H}, \tag{3.19}$$

where P_e is the Peclet number of the hydrothermal system considered here. From the heat transfer point of view, the Peclet number is a dimensionless quantity indicating the relative importance of heat advection to heat conduction in a given hydrothermal system. If heat advection is mainly caused by upward throughflow (as is considered in this section), the Peclet number also indicates the relative importance of the upward throughflow to heat conduction in the hydrothermal system. For this reason, the value of the Peclet number can be used to judge the relative role that heat advection plays in a given hydrothermal system. If the value of the Peclet number is unity, both heat advection and conduction play an equal role in transferring heat energy in the hydrothermal system. If the value of the Peclet number is greater than unity, heat advection plays a predominant role in transferring heat energy. In contrast, if the value of the Peclet number is smaller than unity, heat conduction plays a predominant role in transferring heat energy in the system.

To guarantee the Peclet number and dimensionless temperature expressed in (3.19) will be positive, we must put a minus sign in their definitions because both the upward throughflow velocity and the conductive thermal flux have negative values in the coordinate system used here.

Using these dimensionless quantities, (3.15), (3.16) and (3.17) can be rewritten as

$$T^* = \frac{1}{P_e} e^{P_e} (1 - e^{-P_e y^*}), \tag{3.20}$$

$$P^* = y^* + \frac{q_0 \beta_T H}{\lambda_e P_e} e^{P_e} [y^* - \frac{1}{P_e}(1 - e^{-P_e y^*})] - \frac{\mu \hat{V}}{K \rho_{f0} g} y^*, \tag{3.21}$$

$$\frac{\partial P^*}{\partial y^*} = 1 + \frac{q_0 \beta_T H}{\lambda_e P_e} e^{P_e} (1 - e^{-P_e y^*}) - \frac{\mu \hat{V}}{K \rho_{f0} g}. \tag{3.22}$$

If the pore-fluid pressure gradient is lithostatic in the system, then we have the following formulae to express the upward throughflow velocity:

$$\hat{V} = -\frac{K}{\mu}(\rho_r - \rho_{f0}) g. \tag{3.23}$$

Substituting (3.23) into (3.21) and (3.22) yields the following equations for the case where the pore-fluid pressure gradient is lithostatic:

$$P^* = \frac{\rho_r}{\rho_{f0}} y^* + \frac{q_0 \beta_T H}{\lambda_e P_e} e^{P_e} [y^* - \frac{1}{P_e}(1 - e^{-P_e y^*})], \tag{3.24}$$

$$\frac{\partial P^*}{\partial y^*} = \frac{\rho_r}{\rho_{f0}} + \frac{q_0 \beta_T H}{\lambda_e P_e} e^{P_e} (1 - e^{-P_e y^*}). \tag{3.25}$$

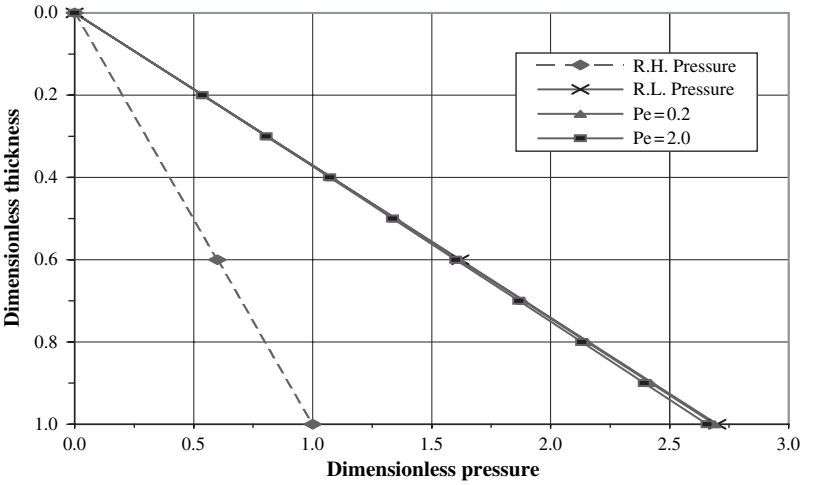

($q_0 = -0.03\ W/m^2$)

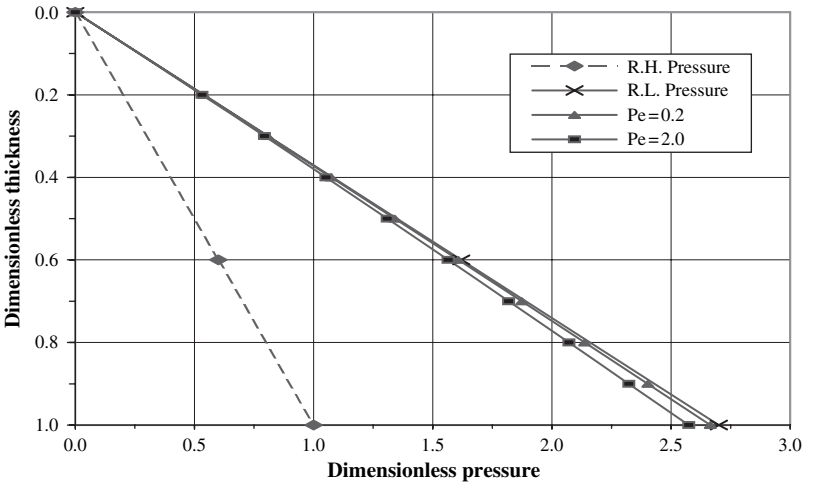

($q_0 = -0.09\ W/m^2$)

Fig. 3.4 Distribution of dimensionless pressure in the thin crustal model ($H = 10\,\text{km}$)

To illustrate the usefulness of the analytical solutions, the following parameters are used to produce numerical results. The reference density of the pore-fluid is $1000\,\text{kg}/\text{m}^3$. The thermal volume expansion coefficient is $2 \times 10^{-4}/^{\circ}\text{C}$. The thermal conductivity coefficient of the porous medium is $3.0W/(m \cdot^{\circ} C)$. The density of the rock mass is $2700\,\text{kg}/\text{m}^3$. Two values of the crustal thickness, namely 10 and 50 km, are used. Also, two different values of the Peclet number (i.e., $P_e = 0.2$ and 2.0) and two different values of conductive thermal flux at the bottom of the

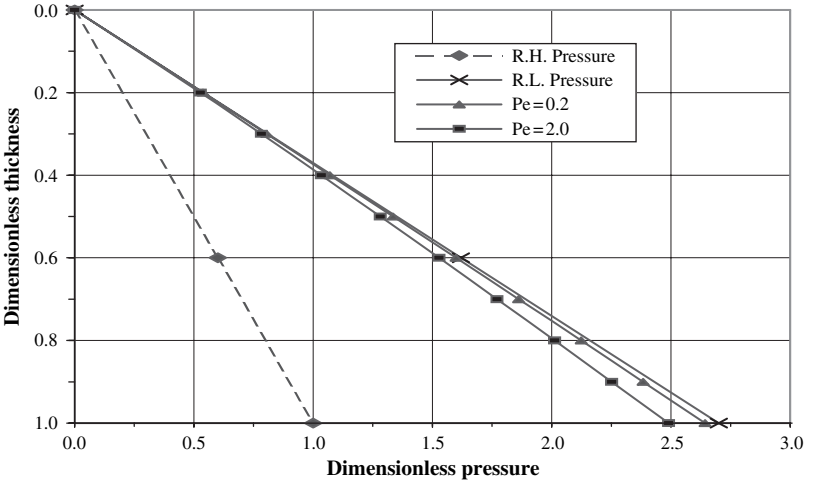

($q_0 = -0.03 W/m^2$)

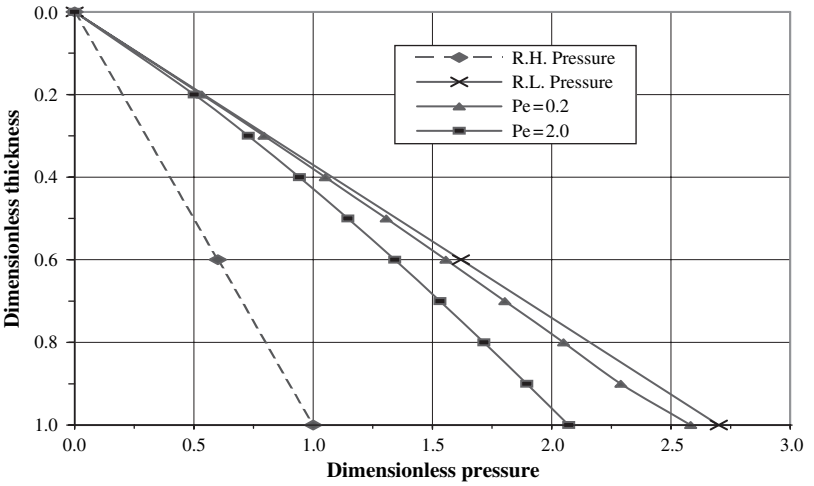

($q_0 = -0.09 W/m^2$)

Fig. 3.5 Distribution of dimensionless pressure in the thick crustal model ($H = 50\,\mathrm{km}$)

crust (i.e., $q_0 = -0.03$ and $-0.09\,\mathrm{W/m^2}$) are used to investigate their effects on the distribution of the pore-fluid pressure.

Figures 3.4 and 3.5 show the distribution of the dimensional pressure in the thin (i.e., $H = 10\,\mathrm{km}$) and thick (i.e., $H = 50\,\mathrm{km}$) crusts, respectively. In these figures, the reference hydrostatic pressure is labeled as R. H. Pressure, while the reference lithostatic pressure is labeled as R. L. Pressure.

It is clear that in the case of the thin crust, the thermal effect of heat advection on the distribution of the pore-fluid pressure is very limited, but in the case of the thick

crust, the effect is significant. Generally, the thermal effect of heat advection on the distribution of the pore-fluid pressure becomes more significant with an increase of the conductive thermal flux at the bottom of the system. For the thin model, the pore-fluid pressure gradient is very close to the reference lithostatic pressure gradient. However, for the thick model, the pore-fluid pressure gradient clearly deviates from the reference lithostatic pressure gradient, especially where the lower boundary has a large conductive thermal flux.

Chapter 4
Convective Heat Transfer in a Homogeneous Crust

If the heat energy transferred from the mantle into the crust is large enough, the hydrothermal systems described in the previous chapter may become unstable. In this case, convective pore-fluid flow takes place and, therefore, may become a predominant mechanism to transfer heat energy from a lower part into the upper part of the crust. Due to the interplay between convective pore-fluid flow and heat transfer, the problem becomes much more complicated so that sophisticated mathematical methods are often needed to obtain analytical solutions. To avoid involving complicated and tedious mathematical deductions, only the final analytical results are presented. In particular, the onset condition for convective pore-fluid flow, which is useful in judging whether or not convection can take place in a given hydrothermal system, will be discussed here. Generally, the onset condition for convective pore-fluid flow is expressed by the critical Rayleigh number of a given hydrothermal system. Hence, both the Rayleigh number and the critical Rayleigh number are addressed in detail in this chapter.

The problem of convective pore-fluid flow in a porous medium with a flat top and bottom was first treated analytically by Horton and Rogers (1945) as well as by Lapwood (1948), and is often called the Horton–Rogers–Lapwood problem. This kind of convection problem is found in many scientific and engineering fields. For example, in geoenvironmental engineering, buried nuclear waste and industrial waste in a fluid-saturated porous medium may generate heat and result in a vertical temperature gradient. If the Rayleigh number, which is directly proportional to the temperature gradient, is equal to or greater than the critical Rayleigh number, natural convection will take place in the porous medium.This may severely contaminate the groundwater due to pore-fluid flow circulation. In geophysics, there exists a vertical temperature gradient in the Earth's crust. If this temperature gradient is large enough, it will cause regional natural convection in the Earth's crust. In this situation, pore-fluid flow circulation can dissolve soluble minerals in some part of a region and carry them to another part of the region. This is the mineralization problem. Since a natural porous medium is often of complicated geometry and composed of many different materials, numerical methods are always needed to solve such problems.

C. Zhao et al., *Convective and Advective Heat Transfer in Geological Systems*,

© Springer-Verlag Berlin Heidelberg 2008

4.1 Convective Heat Transfer in a Homogeneous Crust without Upward Throughflow

The conceptual model to be considered in this section is shown in Fig. 4.1. If convective pore-fluid flow is not allowed to occur, this conceptual model is essentially the same as the conduction model that was discussed in Sect. 3.1. This arises because there is no pore-fluid flowing across the top and bottom of both the models. This means that the top and bottom boundaries are taken as impermeable for these two conceptual models. Since the onset of pore-fluid convective flow is very sensitive to the boundary conditions, a hydrothermal system with different boundary conditions may result in totally different convective patterns. Therefore, the onset condition of pore-fluid convective flow for a particular set of boundary conditions cannot be directly applied to judge the onset of pore-fluid convective flow for similar hydrothermal systems, but with a different set of boundary conditions.

In order to understand why pore-fluid convective flow can take place in the crust of the Earth, it is necessary to introduce the concept of the Rayleigh number of a hydrothermal system. The Rayleigh number is a dimensionless indicator used to represent the overall fundamental physical characteristic of the hydrothermal system. Since the Rayleigh number is independent of the geometry and boundary conditions of the system, the definition of the Rayleigh number is exactly the same for all hydrothermal systems where the same physical processes are taking place. If we only consider the thermal buoyancy of the pore-fluid in a hydrothermal system comprised of homogenous porous materials, the corresponding Rayleigh number of the system is as follows:

$$Ra_T = \frac{(\rho_{f0} c_p)\rho_{f0} g \beta_T \Delta T K H}{\mu \lambda_e}, \tag{4.1}$$

where Ra_T is the Rayleigh number of the hydrothermal system due to thermal buoyancy; K is the permeability of the crustal material; μ is the dynamic viscosity of the pore-fluid; ρ_{f0} is the reference density of the pore-fluid and g is the acceleration due to gravity; β_T is the thermal volume expansion coefficient of the pore-fluid;

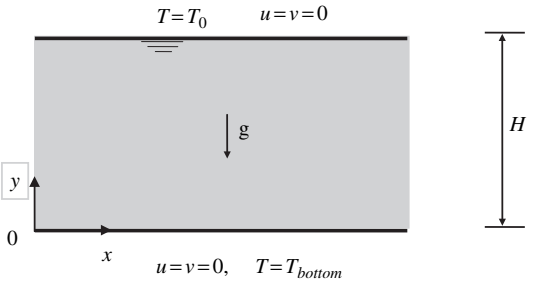

Fig. 4.1 Geometry of the convective model without upward throughflow

ΔT is the temperature difference between the top and the bottom of the hydrothermal system; H is the total thickness of the hydrothermal system; c_p is the specific heat of the pore-fluid; $\lambda_e = \phi\lambda_f + (1-\phi)\lambda_s$, in which λ_f and λ_s are the thermal conductivities of the pore-fluid and rock mass, and ϕ is the porosity of the crustal material.

It is clear from (4.1) that the Rayleigh number of a hydrothermal system is dependent only on the hydrodynamic and thermodynamic properties, but independent of the specific boundary conditions of the system. In addition, the Rayleigh number is also directly proportional to both the thickness and the temperature difference between the top and the bottom of the system. This means that, for a given hydrothermal system of the same hydrodynamic and thermodynamic properties, either a thicker crust or a higher temperature difference between the top and the bottom can result in larger Rayleigh numbers for the hydrothermal system. This is important in understanding why pore-fluid convective flow is facilitated in relatively thick and hot hydrothermal systems.

Now that we have the dimensionless indicator to represent the overall fundamental physical characteristic of a hydrothermal system, we need to determine its corresponding threshold value, below which pore-fluid convective flow cannot take place in the system. We call this threshold value the critical Rayleigh number of the hydrothermal system. In this regard, the critical Rayleigh number represents the onset condition for pore-fluid convective flow in a given hydrothermal system. From extensive studies of convective instability in pore-fluid saturated porous media,[1] it has become apparent that the critical Rayleigh number is dependent on the specific boundary conditions of the hydrothermal system to be considered. Since the critical Rayleigh number is the minimum value of the Rayleigh number to trigger convective flow, it corresponds to the fundamental convective mode of the hydrothermal system. For an idealized hydrothermal system of a square box geometry, if the Rayleigh number is much larger than the critical Rayleigh number defined here, other convective modes and regimes known as stable periodic convection and chaotic convection (Caltagirone 1975; Horne and Caltagirone 1980; Aidun 1987; Kladias and Prasad 1990) are possible. However, whether or not the stable periodic convection and chaotic convection regimes can actually occur in the crust of the Earth remains a very important scientific problem that needs further detailed research.

Owing to the importance of the critical Rayleigh number, it will be derived theoretically as follows. For the conceptual model of a two-dimensional fluid-saturated porous medium shown in Fig. 4.1, if Darcy's Law is used to describe pore-fluid flow and the Oberbeck-Boussinesq approximation is employed to describe a change in

[1] (i.e., Horton and Rogers 1945; Lapwood 1948; Elder 1967; Nield 1968; Palm et al. 1972; Bories and Combarnous 1973; Yen 1974; Caltagirone 1975; Combarnous and Bories 1975; Buretta and Berman 1976; Gasser and Kazimi 1976; Kulacki and Freeman 1979; Kvernvold and Tyvand 1980; Horne and Caltagirone 1980; McKibbin and O'Sullivan 1980; Chan and Banerjee 1981; Bau and Torrance 1982; Beukema and Bruin 1983; Kaviany 1984; Lebon and Cloot 1986; Aidum 1987; Pillatsis et al. 1987; Poulikakos 1987; Prasad and Kulacki 1987; Salt 1988; Chen and Chen 1989; Riley and Winters 1989; Impey et al. 1990; Islam and Nandakumar 1990; Kladias and Prasad 1990; Phillips 1991; Nield and Bejan 1992; Zhao et al. 1997, 1998a, b, 1999a, b, 2000a, 2001a).

pore-fluid density due to a change in pore-fluid temperature, the governing equations of natural convection for an incompressible fluid in a steady state can be expressed as:

$$\frac{\partial u}{\partial x}+\frac{\partial v}{\partial y}=0, \tag{4.2}$$

$$u=\frac{K_x}{\mu}\left(-\frac{\partial P}{\partial x}+\rho_f g_x\right), \tag{4.3}$$

$$v=\frac{K_y}{\mu}\left(-\frac{\partial P}{\partial y}+\rho_f g_y\right), \tag{4.4}$$

$$\rho_{f0}c_p\left(u\frac{\partial T}{\partial x}+v\frac{\partial T}{\partial y}\right)=\lambda_{ex}\frac{\partial^2 T}{\partial x^2}+\lambda_{ey}\frac{\partial^2 T}{\partial y^2}, \tag{4.5}$$

$$\rho_f=\rho_{f0}[1-\beta_T(T-T_0)], \tag{4.6}$$

$$\lambda_{ex}=\phi\lambda_{fx}+(1-\phi)\lambda_{sx}, \qquad \lambda_{ey}=\phi\lambda_{fy}+(1-\phi)\lambda_{sy}, \tag{4.7}$$

where u and v are the horizontal and vertical velocity components of the pore-fluid in the x and y directions, respectively; P is the pore-fluid pressure; T is the temperature of the crustal material; K_x and K_y are the permeabilities of the crustal material in the x and y directions, respectively; μ is the dynamic viscosity of the pore-fluid; ρ_f is the density of the pore-fluid; ρ_{f0} and T_0 are the reference density and temperature; λ_{fx} and λ_{sx} are the thermal conductivities of the pore-fluid and rock mass in the x direction; λ_{fy} and λ_{sy} are the thermal conductivities of the pore-fluid and rock mass in the y direction; c_p is the specific heat of the pore-fluid; g_x and g_y are the gravity acceleration components in the x and y directions; ϕ and β_T are the porosity of the crustal material and the thermal volume expansion coefficient of the pore-fluid.

It is noted that (4.2), (4.3), (4.4) and (4.5) are derived under the assumption that the porous medium considered is orthotropic, in which the y axis is upward in the vertical direction and coincides with the principal direction of medium permeability as well as that of medium thermal conductivity.

In order to simplify (4.2), (4.3), (4.4) and (4.5), the following dimensionless variables are defined:

$$x^*=\frac{x}{H}, \qquad y^*=\frac{y}{H}, \qquad T^*=\frac{T-T_0}{\Delta T}, \tag{4.8}$$

$$u^*=\frac{H\rho_{f0}c_p}{\lambda_{e0}}, \qquad v^*=\frac{H\rho_{f0}c_p}{\lambda_{e0}}v, \qquad P^*=\frac{K_h\rho_{f0}c_p}{\mu\lambda_{e0}}(P-P_0), \tag{4.9}$$

$$K_x^* = \frac{K_x}{K_h}, \qquad K_y^* = \frac{K_y}{K_h}, \qquad \lambda_{ex}^* = \frac{\lambda_{ex}}{\lambda_{e0}}, \qquad \lambda_{ey}^* = \frac{\lambda_0}{\lambda_{e0}}, \tag{4.10}$$

where x^* and y^* are the dimensionless coordinates; u^* and v^* are the dimensionless velocity components in the x and y directions, respectively; P^* and T^* are the dimensionless excess pressure and temperature; K_h is a reference medium permeability coefficient in the horizontal direction; λ_{e0} is a reference thermal conductivity coefficient of the porous medium; $\Delta T = T_{bottom} - T_0$ is the temperature difference between the bottom and top boundaries of the porous medium; H is a reference length and P_0 is the static pore-fluid pressure.

Substituting the above dimensionless variables into (4.2), (4.3), (4.4) and (4.5) yields the following dimensionless equations:

$$\frac{\partial u^*}{\partial x^*} + \frac{\partial v^*}{\partial y^*} = 0, \tag{4.11}$$

$$u^* = K_x^* \left(-\frac{\partial P^*}{\partial x^*} + Ra_T T^* e_1 \right), \tag{4.12}$$

$$v^* = K_y^* \left(-\frac{\partial P^*}{\partial y^*} + Ra_T T^* e_2 \right), \tag{4.13}$$

$$u^* \frac{\partial T^*}{\partial x^*} + v^* \frac{\partial T^*}{\partial y^*} = \lambda_{ex}^* \frac{\partial^2 T^*}{\partial x^{*2}} + \lambda_{ey}^* \frac{\partial^2 T^*}{\partial y^{*2}}, \tag{4.14}$$

where $\boldsymbol{e}$ is a unit vector and $\boldsymbol{e} = e_1 i + e_2 j$ for a two-dimensional problem; Ra_T is the Rayleigh number, defined in this particular case as

$$Ra_T = \frac{(\rho_{f0} c_p) \rho_{f0} g \beta \Delta T K_h H}{\mu \lambda_{e0}}. \tag{4.15}$$

Although analytical solutions for convective instability of pore-fluid in a horizontal layer can be derived using conventional linear stability analysis (Zhao et al. 1997), it is highly desirable to derive the related analytical solutions for a porous medium with a rectangular geometry, at least from the flowing two points of view. First, most geological situations are comprised of complicated geometrical shapes and material distributions so that numerical methods are needed to solve convective flow problems in real geological systems. In order to verify the applicability of a numerical method for solving the Horton–Rogers–Lapwood convection problem, an analytical solution is needed for a benchmark problem, the geometry and boundary conditions of which can be exactly modelled by the numerical method. Second, the analytical solution derived from a problem involving a porous medium of a rectangular shape can be directly or indirectly used to investigate the possibility of convective pore-fluid flow occurring in most sedimentary basins. For these reasons, a benchmark problem of rectangular geometry is constructed and shown in Fig. 4.2. Without losing generality, dimensionless governing equations given in (4.11), (4.12), (4.13) and (4.14) are considered in this Section. The boundary

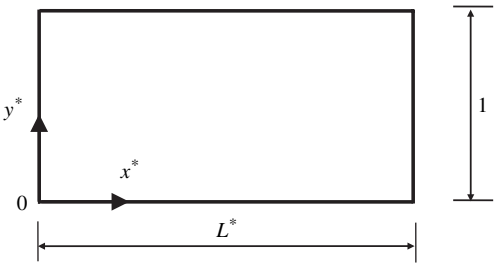

Fig. 4.2 Geometry of a benchmark problem

conditions of the benchmark problem are expressed using these dimensionless variables as follows:

$$u^* = 0, \qquad \frac{\partial T^*}{\partial x^*} = 0 \qquad (\text{at } x^* = 0 \text{ and } x^* = L^*), \tag{4.16}$$

$$v^* = 0, \qquad T^* = 1 \qquad (\text{at } y^* = 0), \tag{4.17}$$

$$v^* = 0, \qquad T^* = 0 \qquad (\text{at } y^* = 1), \tag{4.18}$$

where L^* is a dimensionless length in the horizontal direction and $L^* = L/H$, in which L is the real length of the problem domain in the horizontal direction.

For ease of deriving an analytical solution to the benchmark problem, it is assumed that the porous medium under consideration is fluid-saturated and isotropic. This means that $K_x = K_y = K_h$ and $\lambda_{ex} = \lambda_{ey} = \lambda_{e0}$. As a result, (4.11), (4.12), (4.13) and (4.14) can be further simplified as follows:

$$\frac{\partial u^*}{\partial x^*} + \frac{\partial v^*}{\partial y^*} = 0, \tag{4.19}$$

$$u^* = -\frac{\partial P^*}{\partial x^*} + Ra_T T^* e_1, \tag{4.20}$$

$$v^* = -\frac{\partial P^*}{\partial y^*} + Ra_T T^* e_2, \tag{4.21}$$

$$u^* \frac{\partial T^*}{\partial x^*} + v^* \frac{\partial T^*}{\partial y^*} = \frac{\partial^2 T^*}{\partial x^{*2}} + \frac{\partial^2 T^*}{\partial y^{*2}}. \tag{4.22}$$

Using the linearization procedure for temperature gradient and a dimensionless stream function ψ simultaneously, (4.19), (4.20), (4.21) and (4.22) are reduced into the following two equations:

$$\frac{\partial^2 \psi}{\partial x^{*2}} + \frac{\partial^2 \psi}{\partial y^{*2}} = -Ra_T \frac{\partial T^*}{\partial x^*}, \tag{4.23}$$

$$\frac{\partial \psi}{\partial x^*} = \frac{\partial^2 T^*}{\partial x^{*2}} + \frac{\partial^2 T^*}{\partial y^{*2}}. \tag{4.24}$$

Since (4.23) and (4.24) are linear, solutions to ψ and T^* are of the following forms:

$$\psi = f(y^*)\sin(q\frac{x^*}{L^*}) \qquad (q = m\pi,\ m = 1,\ 2,\ 3,\ \ldots\ldots), \tag{4.25}$$

$$T^* = \theta(y^*)\cos(q\frac{x^*}{L^*}) + (1 - y^*) \qquad (q = m\pi,\ m = 1,\ 2,\ 3,\ldots\ldots). \tag{4.26}$$

Substituting (4.25) and (4.26) into (4.23) and (4.24) yields the following equations:

$$f''(y^*) - \left(\frac{q}{L^*}\right)^2 f(y^*) = \frac{q}{L^*} Ra_T \theta(y^*), \tag{4.27}$$

$$\frac{q}{L^*} f(y^*) = -\left(\frac{q}{L^*}\right)^2 \theta(y^*) + \theta''(y^*). \tag{4.28}$$

Combining (4.27) and (4.28) leads to an equation containing $f(y^*)$ only:

$$f^{IV}(y^*) - 2(\frac{q}{L^*})^2\ f''(y^*) - (\frac{q}{L^*})^2[Ra_T - (\frac{q}{L^*})^2]f(y^*) = 0. \tag{4.29}$$

It is immediately noted that (4.29) is a linear, homogeneous ordinary differentiation equation so that it has a zero trivial solution. For the purpose of finding a non-zero solution, it is noted that the non-zero solution satisfying both (4.29) and the boundary conditions in (4.16), (4.17) and (4.18) can be expressed as

$$f(y^*) = \sin(ry^*) \qquad (r = n\pi,\ n = 1,\ 2,\ 3,\ldots\ldots). \tag{4.30}$$

Using this equation, the condition under which the non-zero solution exists for (4.29) is derived and expressed as

$$Ra_T = (\frac{L^*}{q}r^2 + \frac{q}{L^*})^2 = (\frac{n^2}{m}L^* + \frac{m}{L^*})^2\pi^2 \quad (m = 1,\ 2,\ 3,\ldots\ldots,\ n = 1,\ 2,\ 3,\ldots\ldots). \tag{4.31}$$

It can be observed from (4.31) that in the case of L^* being an integer, the minimum Rayleigh number is $4\pi^2$, which occurs when n = 1 and $m = L^*$. However, if L^* is not an integer, the minimum Rayleigh number is $(L^* + 1/L^*)^2\pi^2$, which occurs when $m = 1$ and $n = 1$. Since the minimum Rayleigh number determines the onset of natural convection in fluid-saturated porous medium for the Horton–Rogers–Lapwood problem, it is often labelled as the critical Rayleigh number, $Ra_{T\,critical}$.

For this benchmark problem, the mode shapes for the stream function and related dimensionless variables corresponding to the critical Rayleigh number can be derived and expressed as follows:

$$\psi = C_1 \sin\left(\frac{m\pi}{L^*}x^*\right)\sin(n\pi y^*), \tag{4.32}$$

$$u^* = n\pi C_1 \sin\left(\frac{m\pi}{L^*}x^*\right)\cos(n\pi y^*), \tag{4.33}$$

$$v^* = -\frac{m\pi}{L^*}C_1 \cos\left(\frac{m\pi}{L^*}x^*\right)\sin(n\pi y^*), \tag{4.34}$$

$$T^* = -\frac{C_1}{\sqrt{Ra_{T\,critical}}}\cos\left(\frac{m\pi}{L^*}x^*\right)\sin(n\pi y^*) + (1-y^*), \tag{4.35}$$

$$P^* = \frac{nL^*}{m}C_1 \cos\left(\frac{m\pi}{L^*}x^*\right)\cos(n\pi y^*) - \frac{Ra_{T\,critical}}{2}(1-y^*)^2 + C_2, \tag{4.36}$$

where the values of *m, n* and $Ra_{T\,critical}$ are dependent on whether L^* is an integer or not; C_1 is a non-zero constant and C_2 is an arbitrary constant. It is interesting to note that since $Ra_{T\,critical}$ is a function of L^*, it can vary with a non-integer L^*. This implies that rectangular porous medium configurations may have different critical Rayleigh numbers for different ratios of length to height.

For the conceptual model shown in Fig. 4.1, the corresponding critical Rayleigh number of the system is as follows:

$$Ra_{T\,critical} = 4\pi^2. \tag{4.37}$$

This critical Rayleigh number is only applicable to a problem with impermeable boundaries and constant temperature at both the top and the bottom boundaries. If the top boundary is permeable, then the corresponding critical Rayleigh number is reduced to 27.1, indicating that pore-fluid convective flow in this instance is much easier, compared with the same system with an impermeable top boundary.

Using the above problem as a benchmark problem, Zhao et al. (1997) developed the progressive asymptotic approach algorithm to simulate pore-fluid convective flow in the crust of the Earth. Since the progressive asymptotic approach algorithm is a numerical algorithm and is based on the finite element method, it must be verified and validated before application. Detailed verification and validation of the progressive asymptotic approach algorithm is available in an open reference (Zhao et al. 1997). The progressive asymptotic approach algorithm was applied to simulate problems with the following parameters. The thickness of the crust is 13 km. For the pore-fluid, dynamic viscosity is $10^{-3}\,\mathrm{N}\times\mathrm{s/m^2}$; the reference density is $1000\,\mathrm{kg/m^3}$; the volumetric thermal expansion coefficient is $2.07\times10^{-4}(1/^\circ C)$; the specific heat is $4185 J/(kg\cdot^\circ C)$; the thermal conductivity coefficient in both the horizontal and the vertical directions is $0.6 W/(m\cdot^\circ C)$. For the porous rock matrix, the porosity is 0.1; the specific heat is $815\,\mathrm{J/(kg\cdot^\circ C)}$; the thermal conductivity coefficient in both the horizontal and the vertical directions is $3.35\,\mathrm{W/(m\cdot^\circ C)}$, and the

permeability of the whole crust in the computational domain is $10^{-14}\,\mathrm{m}^2$. Since the computational model must be finite in size, the length of the crust is assumed to be 110 km. The following boundary conditions are applied to this problem: (1) temperatures at the top and the bottom of the computational domain are 20 °C and 150 °C respectively; (2) both the lateral vertical boundaries are insulated and impermeable in the horizontal direction, and (3) both the top and bottom boundaries are impermeable in the vertical direction. Using these parameters, the Rayleigh number of the system is approximately equal to 46.6, which is greater than the corresponding critical Rayleigh number of $4\pi^2$. Thus, pore-fluid convective flow can take place in this crustal model.

Figure 4.3 shows the distributions of pore-fluid velocity, streamlines and temperature in the crustal model. In the presentation for the streamlines, the core in blue represents clockwise convection cells, while the core in red represents anticlockwise convection cells. It is clear that each of the clockwise convection cells is separated by an anticlockwise convection cell. What we can see from this example is that: (1) multiple convection cells can be reasonably simulated in such a crustal model using the finite element method, and (2) the distribution of temperature is highly localized. This is a direct result of the coupling between the temperature and the pore-fluid velocity within the convective pore-fluid flow.

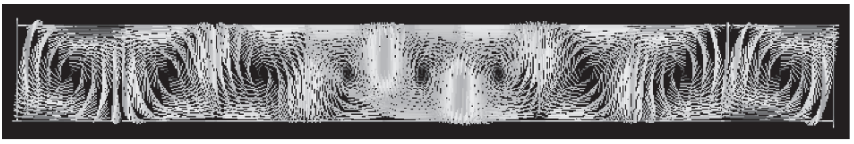

(Pore-fluid velocity)

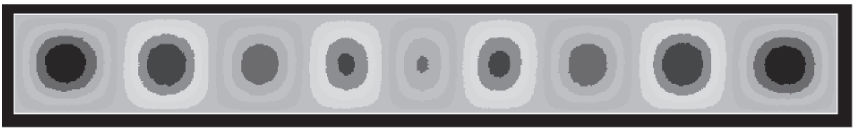

(Streamline)

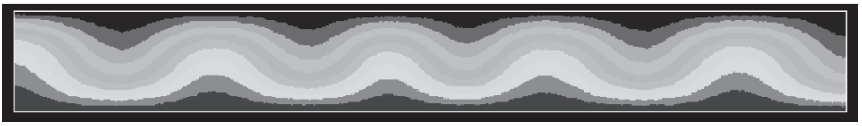

(Temperature)

Fig. 4.3 Distributions of pore-fluid flow, streamlines and temperature in the crustal model

4.2 Convective Heat Transfer in a Homogeneous Crust with Upward Throughflow

In the geological community, there has been an assertion that pore-fluid convective flow can only take place in the top few kilometers of the crust, where the pore-fluid pressure is hydrostatic or, strictly speaking, is close to hydrostatic. Based on this assertion, it was concluded that pore-fluid convective flow cannot take place in the crust where the pore-fluid pressure is lithostatic. This conclusion is correct for a crust which has constant temperature and impermeable boundary conditions at both the top and the bottom of the crust (Jones and Persichetti 1986), just like the conceptual model shown in Fig. 4.1. However, if the crust has a permeable top with a constant pressure and temperature, and a bottom with a constant upward pore-fluid velocity and conductive heat flux, Zhao et al. (1999a) demonstrated in both theoretical and the numerical analyses that the above-mentioned conclusion is incorrect. The conceptual model used in the theoretical and numerical analyses is exactly the same as that shown in Fig. 3.3 of Sect. 3.2.

As shown in Fig. 4.4, the temperature at the bottom of the conceptual crustal model is not specified, but the conductive heat flux at this boundary is. Although the Rayleigh number may have the same definition for hydrothermal systems in which identical physical processes occur, it must be defined and expressed in terms of the known parameters of the system. For this reason, the Rayleigh number defined in (4.1) is inappropriate for the conceptual crustal model considered in this section. If the upward direction is defined as positive for the constant conductive heat flux at the bottom, we have the following general definition for the Rayleigh number for this conceptual crustal model (Zhao et al. 1999a), instead of using (4.1):

$$Ra_T = \frac{(\rho_{f0}c_p)\rho_{f0}g\beta_T q_c K H^2}{\mu\lambda_{e0}^2}. \tag{4.38}$$

Since the Rayleigh number expressed in (4.38) varies quadratically with the thickness of the crust, pore-fluid convective flow is much easier in a relatively thick crust where the pore-fluid pressure gradient is close to the lithostatic value.

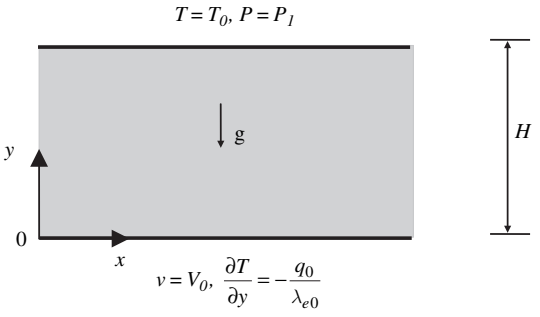

Fig. 4.4 Geometry and boundary conditions of the hydrothermal system

To derive the critical Rayleigh number of this particular system, we need to consider the conceptual model shown in Fig. 4.4. The boundary conditions of this hydrothermal system consist of constant temperature and constant pressure at the top of the layer, and constant vertical Darcy velocity and constant vertical conductive heat flux at the bottom of the layer. This means that the layer is heated from below. The steady state governing equations of this hydrothermal system are exactly the same as those expressed in (4.2), (4.3), (4.4), (4.5), (4.6) and (4.7). However, the boundary conditions of this hydrothermal system are mathematically expressed as follows:

$$T = T_0, \qquad P = P_1 \qquad (\text{at } y = H), \tag{4.39}$$

$$v = V_0, \qquad \frac{\partial T}{\partial y} = -\frac{q_0}{\lambda_{e0}} \qquad (\text{at } y = 0), \tag{4.40}$$

where $T_0,\ P_1,\ V_0,\ \lambda_{e0}$ and q_0 are constants. Physically, q_0 is the (constant) conductive thermal flux and λ_{e0} is a reference conductivity for the porous medium.

Note that if the porous medium of the layer is homogeneous and isotropic, the steady state governing equations of this hydrothermal system can be written in the following dimensionless form:

$$\frac{\partial u^*}{\partial x^*} + \frac{\partial v^*}{\partial y^*} = 0, \tag{4.41}$$

$$u^* = -\frac{\partial P^*}{\partial x^*} + Ra_T T^* e_1, \tag{4.42}$$

$$v^* = -\frac{\partial P^*}{\partial y^*} + Ra_T T^* e_2, \tag{4.43}$$

$$u^* \frac{\partial T^*}{\partial x^*} + v^* \frac{\partial T^*}{\partial y^*} = \frac{\partial^2 T^*}{\partial x^{*2}} + \frac{\partial^2 T^*}{\partial y^{*2}}. \tag{4.44}$$

Equations (4.41), (4.42), (4.43) and (4.44) are exactly the same as (4.19), (4.20), (4.21) and (4.22), except for introducing the following three new dimensionless variables:

$$T^* = \frac{T - T_0}{\Delta T}, \qquad \frac{\partial T^*}{\partial y^*} = \frac{\lambda_{e0}}{q_0}\frac{\partial T}{\partial y}, \tag{4.45}$$

$$Ra_T = \frac{(\rho_{f0} c_p)\rho_{f0} g \beta K_h q_0 H^2}{\mu\ \lambda_{e0}^2}, \tag{4.46}$$

where T^* is the dimensionless temperature; $\partial T^* \big/ \partial y^*$ is the dimensionless vertical temperature gradient, and Ra_T is the modified Rayleigh number expressed in terms of the conductive thermal flux rather than in terms of the conventional temperature difference. Other quantities have the same meanings as defined before.

The boundary conditions of the problem in (4.39) and (4.40) can be written in dimensionless form as follows:

$$T^* = 0, \qquad P^* = P_1^* \qquad (\text{at } y^* = 1), \tag{4.47}$$

$$v^* = P_e = \frac{H\rho_{f0}c_p}{\lambda_{e0}}V_0, \qquad \frac{\partial T^*}{\partial y^*} = -1 \qquad (\text{at } y^* = 0), \tag{4.48}$$

where P_e is the Peclet number of the hydrothermal system.

For the hydrothermal system considered, the trivial solution for the horizontal Darcy pore-fluid velocity is zero:

$$u^* = 0. \tag{4.49}$$

Substituting (4.49) into (4.41) yields the following equation:

$$\frac{\partial v^*}{\partial y^*} = 0. \tag{4.50}$$

It straightforwardly follows from (4.48) and (4.50) that

$$v^* = P_e. \tag{4.51}$$

This indicates that the vertical velocity, which is referred to as the upward throughflow, is constant throughout the whole layer.

Substituting (4.49) and (4.51) into (4.44) yields the following equation:

$$P_e\frac{\partial T^*}{\partial y^*} = \frac{\partial^2 T^*}{\partial y^{*2}}. \tag{4.52}$$

The solution for (4.52) can be expressed as

$$T^* = C_1 e^{P_e y^*} + C_2, \tag{4.53}$$

where C_1 and C_2 are two independent constants.

In order to determine C_1 and C_2 constants uniquely, we must use two thermal boundary conditions, one of which must be a temperature boundary.

Inserting (4.53) into (4.47) and (4.48) yields

$$T^* = \frac{1}{P_e}(e^{P_e} - e^{P_e y^*}). \tag{4.54}$$

It is noted from (4.42) and (4.49) that P^* is a function of y^* only, hence,

$$\frac{\partial P^*}{\partial y^*} = \frac{dP^*}{dy^*} = Ra_T T^* - P_e. \tag{4.55}$$

Integrating (4.55) with respect to y^* yields the following equation:

$$P^* = \frac{Ra_T}{P_e}\left(e^{P_e}y^* - \frac{1}{P_e}e^{P_e y^*}\right) - P_e y^* + C_3, \tag{4.56}$$

where C_3 is a constant which can be determined from (4.47):

$$C_3 = P_1^* + P_e - \frac{Ra_T}{P_e}\left(e^{P_e} - \frac{1}{P_e}e^{P_e}\right). \tag{4.57}$$

It follows that the final solution for the dimensionless pressure can be expressed as

$$p^* = \frac{Ra_T}{P_e}\left(e^{P_e}y^* - \frac{1}{P_e}e^{P_e y^*}\right) - P_e y^* + P_1^* + P_e - \frac{Ra_T}{P_e}\left(e^{P_e} - \frac{1}{P_e}e^{P_e}\right). \tag{4.58}$$

Up to now, we have obtained the exact trivial solutions for the dimensionless Darcy velocities (i.e., (4.49) and (4.51)), dimensionless temperature (i.e., (4.54)) and dimensionless pressure (i.e., (4.58)) of the hydrothermal system.

Next, the stability of the above trivial solution is investigated in a linear stability analysis. Supposing the hydrothermal system is subjected to a small disturbance, the total solutions for the dimensionless velocities, temperature and pressure of the system can be expressed as

$$u_t^* = u^* + \hat{u}^*, \qquad v_t^* = v^* + \hat{v}^*, \tag{4.59}$$

$$T_t^* = T^* + \hat{T}^*, \qquad P_t^* = P^* + \hat{P}^*, \tag{4.60}$$

where $\hat{u}^*$, $\hat{v}^*$, $\hat{T}^*$ and $\hat{P}^*$ are the corresponding perturbation solutions due to the small disturbance. From the linear stability theory point of view, if and only if all these perturbation solutions are zero, then the exact solutions obtained in the previous analysis are stable. This implies that the stability of the exact solutions for the hydrothermal system considered here can be judged by examining the existence of the non-zero solutions for $\hat{u}^*$, $\hat{v}^*$, $\hat{T}^*$ and $\hat{P}^*$.

Note that the small disturbance may be caused by a small tremor of the Earth. From the classical perturbation theory, we can introduce a small parameter, ε, to express the consequence of this small disturbance. For example, using this small parameter, it is possible to express the resulting perturbation velocity, temperature and pressure of a system in the following form:

$$\hat{u}^* = \varepsilon(\hat{u}^{*(0)} + \varepsilon\hat{u}^{*(1)} + \varepsilon^2\hat{u}^{*(2)} + \ldots\ldots), \tag{4.61}$$

$$\hat{v}^* = \varepsilon(\hat{v}^{*(0)} + \varepsilon\hat{v}^{*(1)} + \varepsilon^2\hat{v}^{*(2)} + \ldots\ldots), \tag{4.62}$$

$$\hat{P}^* = \varepsilon(\hat{P}^{*(0)} + \varepsilon\hat{P}^{*(1)} + \varepsilon^2\hat{P}^{*(2)} + \ldots\ldots), \tag{4.63}$$

$$\hat{T}^* = \varepsilon(\hat{T}^{*(0)} + \varepsilon\hat{T}^{*(1)} + \varepsilon^2\hat{T}^{*(2)} + \ldots\ldots). \tag{4.64}$$

Substituting (4.59), (4.60), (4.61), (4.62), (4.63) and (4.64) into (4.41), (4.42), (4.43) and (4.44), considering the linear perturbation terms only (i.e., ε terms only) and then dropping the unnecessary superscripts, we obtain the following eigenvalue problem:

$$\frac{\partial \hat{u}^*}{\partial x^*} + \frac{\partial \hat{v}^*}{\partial y^*} = 0, \tag{4.65}$$

$$\hat{u}^* = -\frac{\partial \hat{P}^*}{\partial x^*} + Ra_T \hat{T}^* e_1, \tag{4.66}$$

$$\hat{v}^* = -\frac{\partial \hat{P}^*}{\partial y^*} + Ra_T \hat{T}^* e_2, \tag{4.67}$$

$$\hat{u}^* \frac{\partial T^*}{\partial x^*} + \hat{v}^* \frac{\partial T^*}{\partial y^*} + P_e \frac{\partial \hat{T}^*}{\partial y^*} = \frac{\partial^2 \hat{T}^*}{\partial x^{*2}} + \frac{\partial^2 \hat{T}^*}{\partial y^{*2}}, \tag{4.68}$$

where

$$\frac{\partial T^*}{\partial x^*} = 0 \qquad \text{and} \qquad \frac{\partial T}{\partial y^*} = -e^{P_e y^*}. \tag{4.69}$$

The corresponding boundary conditions for the perturbation solutions are:

$$\hat{T}^* = 0, \qquad \hat{P}^* = 0 \qquad (\text{at } y^* = 1), \tag{4.70}$$

$$\hat{v}^* = 0, \qquad \frac{\partial \hat{T}}{\partial y^*} = 0 \qquad (\text{at } y^* = 0). \tag{4.71}$$

It is noted that $\hat{P}^* = 0$ in (4.70) implies that $\dfrac{\partial \hat{v}^*}{\partial y^*} = 0$ at $y^* = 1$ (Nield 1968).

Using the standard linear stability analysis, we have the following expressions:

$$\hat{v}^* = V(y^*) e^{-ik_1^* x^*}, \qquad \hat{T}^* = \theta(y^*) e^{-ik_1^* x^*}. \tag{4.72}$$

Inserting (4.72) into (4.65), (4.66), (4.67) and (4.68) yields:

$$V''(y^*) - (k_1^*)^2 V(y^*) = -(k_1^*)^2 Ra_T \theta(y^*), \tag{4.73}$$

$$\theta''(y^*) - P_e \theta'(y^*) - (k_1^*)^2 \theta(y^*) = -V(y^*) e^{P_e y^*}, \tag{4.74}$$

where k_1^* is the dimensionless wave number in the x^* direction:

$$k_1^* = k_1 H, \tag{4.75}$$

with k_1 being the wave number in the x direction.

Using (4.72), (4.70) and (4.71) can also be rewritten as

$$\theta = 0, \qquad V' = 0 \qquad (\text{at } y^* = 1), \tag{4.76}$$

$$V = 0, \qquad \theta' = 0 \qquad (\text{at } y^* = 0). \tag{4.77}$$

Substituting (4.73) into (4.74) yields the following equation:

$$V^{(IV)}(y^*) - P_e V'''(y^*) - 2(k_1^*)^2 V''(y^*) + P_e (k_1^*)^2 V'(y^*) + (k_1^*)^2 [(k_1^*)^2 - Ra_T e^{P_e y^*}] V(y^*) = 0. \tag{4.78}$$

The analytical solution of (4.78) is troublesome because it contains all order derivatives. Instead we solve (4.73) and (4.74) approximately through a single member Galerkin *ansatze*. The quality of approximation is excellent for Peclet number less than one, as will be shown subsequently by comparison with numerical solutions.

With $V(y^*) = A\overline{V}(y^*)$ and $\theta(y^*) = B\bar{\theta}(y^*)$, (4.73) and (4.74) can be rewritten in the Galerkin form as follows:

$$\int_0^1 [A\bar{V}''(y^*) - (k_1^*)^2 A\bar{V}(y^*) + (k_1^*)^2 Ra_T B\bar{\theta}(y^*)]\bar{V}(y^*)dy^* = 0, \tag{4.79}$$

$$\int_0^1 [B\bar{\theta}''(y^*) - P_e B\bar{\theta}'(y^*) - (k_1^*)^2 B\bar{\theta}(y^*) + A\bar{V}(y^*)e^{P_e y^*}]\bar{\theta}(y^*)dy^* = 0, \tag{4.80}$$

where A and B are independent constants; $\overline{V}(y^*)$ and $\bar{\theta}(y^*)$ are trial functions for $V(y^*)$ and $\theta(y^*)$. They must be chosen so that all boundary conditions of the problem are satisfied identically.

From (4.79) and (4.80), it follows that

$$\begin{bmatrix} C_{11} & C_{12} \\ C_{21} & C_{22} \end{bmatrix} \begin{Bmatrix} A \\ B \end{Bmatrix} = \begin{Bmatrix} 0 \\ 0 \end{Bmatrix}, \tag{4.81}$$

where

$$C_{11} = \int_0^1 [\bar{V}''(y^*) - (k_1^*)^2 \bar{V}(y^*)]\bar{V}(y^*)dy^*, \tag{4.82}$$

$$C_{12} = Ra_T (k_1^*)^2 \int_0^1 \bar{\theta}(y^*)\bar{V}(y^*)dy^*, \tag{4.83}$$

$$C_{21} = \int_0^1 e^{P_e y^*} \bar{V}(y^*)\bar{\theta}(y^*)dy^*, \tag{4.84}$$

$$C_{22} = \int_0^1 [\bar{\theta}''(y^*) - P_e\bar{\theta}'(y^*) - (k_1^*)^2 \bar{\theta}(y^*)]\bar{\theta}(y^*)dy^*. \tag{4.85}$$

Clearly, the condition, under which (4.81) has a non-zero solution, is:

$$C_{11}C_{22} - C_{12}C_{21} = 0. \tag{4.86}$$

In theory, any function, which satisfies the boundary conditions of the problem considered, can be chosen as the candidate for the trial function. However, in practice, for the purpose of avoiding any unnecessary difficulty in the mathematics, it is advantageous to use a polynomial function as the trial function because many preliminary functions can be expressed as the combination of polynomial functions using a Taylor expansion. For the hydrothermal system considered, we have tested various candidate trial functions (Zhao et al. 1999a). The best result (minimum error in horizontal wave number at $P_e = 0$) was obtained with:

$$\bar{V}(y^*) = \frac{1}{2}(y^*)^2 - y^*, \tag{4.87}$$

$$\bar{\theta}(y^*) = \frac{1}{5}[(y^*)^5 - 1]. \tag{4.88}$$

Substituting (4.87) and (4.88) into (4.82), (4.83), (4.84) and (4.85) yields the following equations:

$$C_{11} = -\left[\frac{1}{3} + \frac{2}{15}(k_1^*)^2\right], \tag{4.89}$$

$$C_{12} = \frac{17}{336} Ra_T (k_1^*)^2, \tag{4.90}$$

$$\begin{aligned} C_{21} = &\frac{1}{P_e^8}[e^{P_e}(\frac{1}{2}P_e^6 - 2P_e^5 + 3P_e^4 + 12P_e^3 - 108P_e^2 + 306P_e - 504) \\ &+ (504 + 144P_e + \frac{1}{5}P_e^5 + \frac{1}{5}P_e^6)], \end{aligned} \tag{4.91}$$

$$C_{22} = -\left[\frac{1}{9} + \frac{1}{33}(k_1^*)^2 - \frac{1}{50}P_e\right]. \tag{4.92}$$

From (4.86), (4.89), (4.90), (4.91) and (4.92), the critical Rayleigh number, for which temperature driven convective flow may occur, can be expressed as

$$Ra_{critical} = \frac{366 C_{11} C_{22}}{17 (k_1^*)^2 C_{21}}. \tag{4.93}$$

Since $Ra_{critical}$ is a function of $(k_1^*)^2$, its minimum value is obtained from:

$$\frac{\partial Ra_{critical}}{\partial[(k_1^*)^2]} = 0. \tag{4.94}$$

Substituting the related equations (i.e., (4.89), (4.90), (4.91), (4.92) and (4.93)) into (4.94) leads to the following condition, under which $Ra_{critical}$ has a minimum value for a given Peclet number:

$$k_1^* = \left(\frac{55}{6}\right)^{\frac{1}{4}} \left(1 - \frac{9}{50}P_e\right)^{\frac{1}{4}}. \tag{4.95}$$

Obviously, our approximate solution is only valid for

$$P_e < \frac{50}{9}. \tag{4.96}$$

The above restriction is a consequence of the specific trial function we have used in our linear stability analysis and convective solutions may exist (and indeed exist, as demonstrated later in this chapter) for $P_e \geq 50/9$.

Unlike the conceptual crustal model that has constant temperature and impermeable boundary conditions at both the top and the bottom, the critical Rayleigh number for the upward throughflow model is no longer a constant, but varies with the value of the upward throughflow. As has been mentioned previously, the importance of the upward throughflow can be represented by the dimensionless Peclet number as defined in (4.48). Thus, it is logical to use the dimensionless Peclet number to express the critical Rayleigh number for the upward throughflow model (Zhao et al. 1999a).

Figure 4.5 shows the variation of the critical Rayleigh number $(Ra_{critical})$ with the velocity of the upward throughflow, which is represented by the dimensionless Peclet number P_e. Within the range of the Peclet number considered $(P_e < 50/9)$, $Ra_{critical}$ decreases as P_e increases, that is, pore-fluid convective flow becomes easier when the velocity of the upward throughflow is increased. Conversely, a decrease in the velocity of the upward throughflow makes the pore-fluid convective flow difficult.

Based on the above recognition, Zhao et al. (1999a) also numerically simulated pore-fluid convective flow in the crust with upward throughflow. However, from the computational point of view, the problem domain must be finite in size. This contradicts the conceptual crustal model that comprises horizontal layer of infinite length. However, considering the periodic nature of the solutions for the critical Rayleigh number makes it possible to overcome this difficulty. Theoretically, it is appropriate to place two vertical boundaries of the finite element computational domain at the convective cell boundaries, where both the horizontal velocity and the normal thermal flux are identical to zero. Since there are two convective cells (a clockwise cell and an anticlockwise cell) in one horizontal wavelength of the solution, the length of a convective cell in the horizontal direction is equal to half the horizontal wavelength of the system. This indicates that the minimum length of the

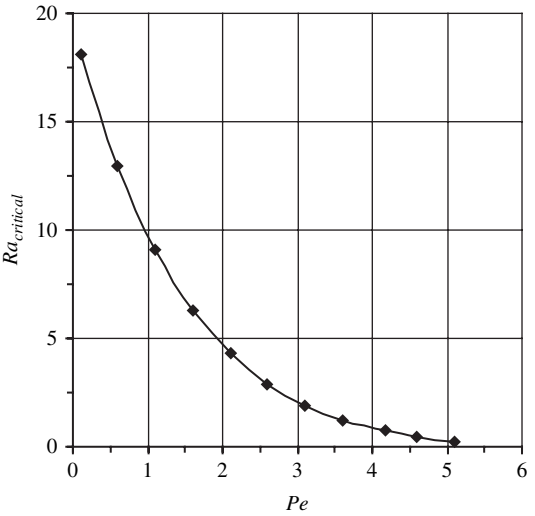

Fig. 4.5 Variation of the critical Rayleigh number with the Peclet number of a conceptual model with upward throughflow

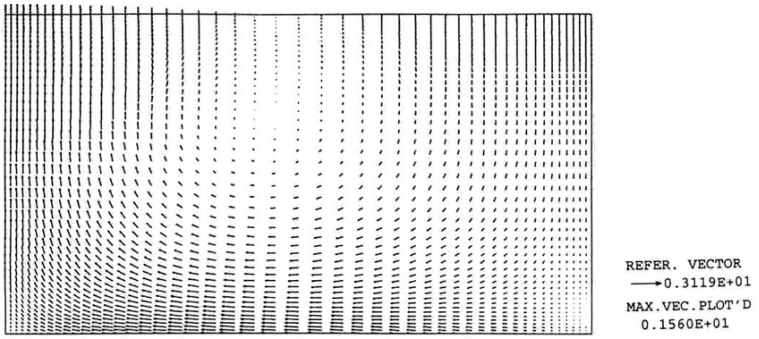

(Pe=0.1, Ra=17.5)

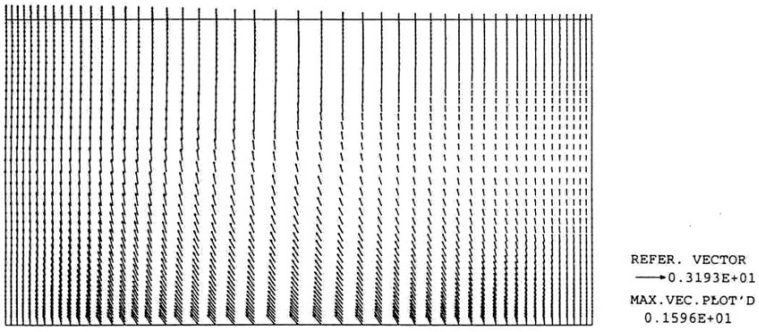

(Pe=1.0, Ra=9.8)

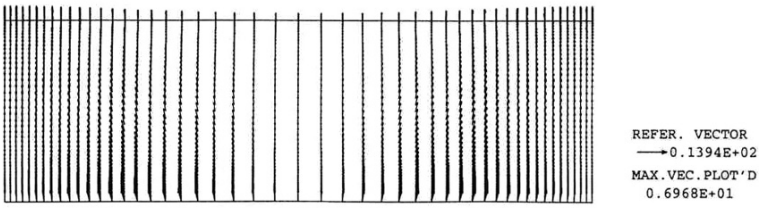

(Pe=5.0, Ra=1.5)

Fig. 4.6 Dimensionless total velocity distribution due to different upward throughflow

finite element computational domain should equal half the horizontal wavelength of the system. For a conceptual crustal model with upward throughflow, the ratio of the length to thickness of a computational model can be expressed as (Zhao et al. 1999a)

$$\frac{L}{H} = \pi \left(\frac{55}{6}\right)^{-\frac{1}{4}} \left(1 - \frac{9}{50} P_e\right)^{-\frac{1}{4}}, \tag{4.97}$$

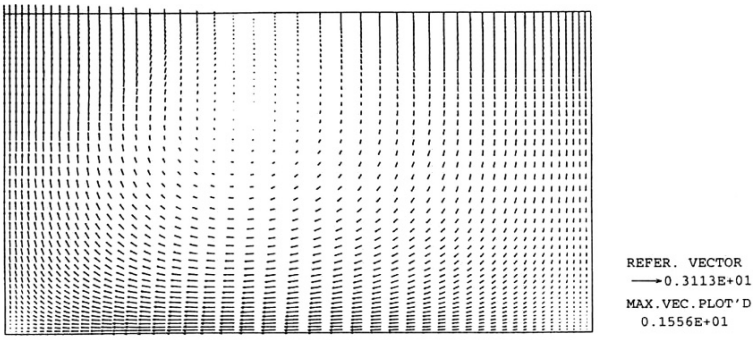

(Pe=0.1, Ra=17.5)

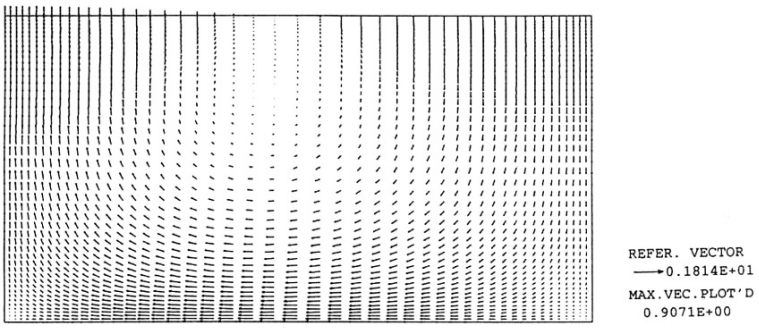

(Pe=1.0, Ra=9.8)

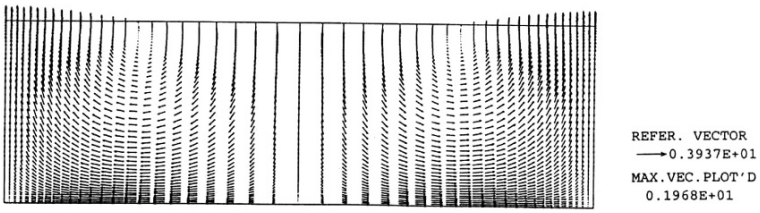

(Pe=5.0, Ra=1.5)

Fig. 4.7 Dimensionless perturbation velocity distribution due to different upward throughflow

where L and H are the length and thickness of the computational domain. The thickness of the computational domain is also equal to the thickness of the conceptual crustal model.

Figures 4.6 and 4.7 show the distributions of both the total and the perturbation pore-fluid velocity under different conditions of upward throughflow. The perturbation pore-fluid velocity is calculated by taking the upward throughflow velocity

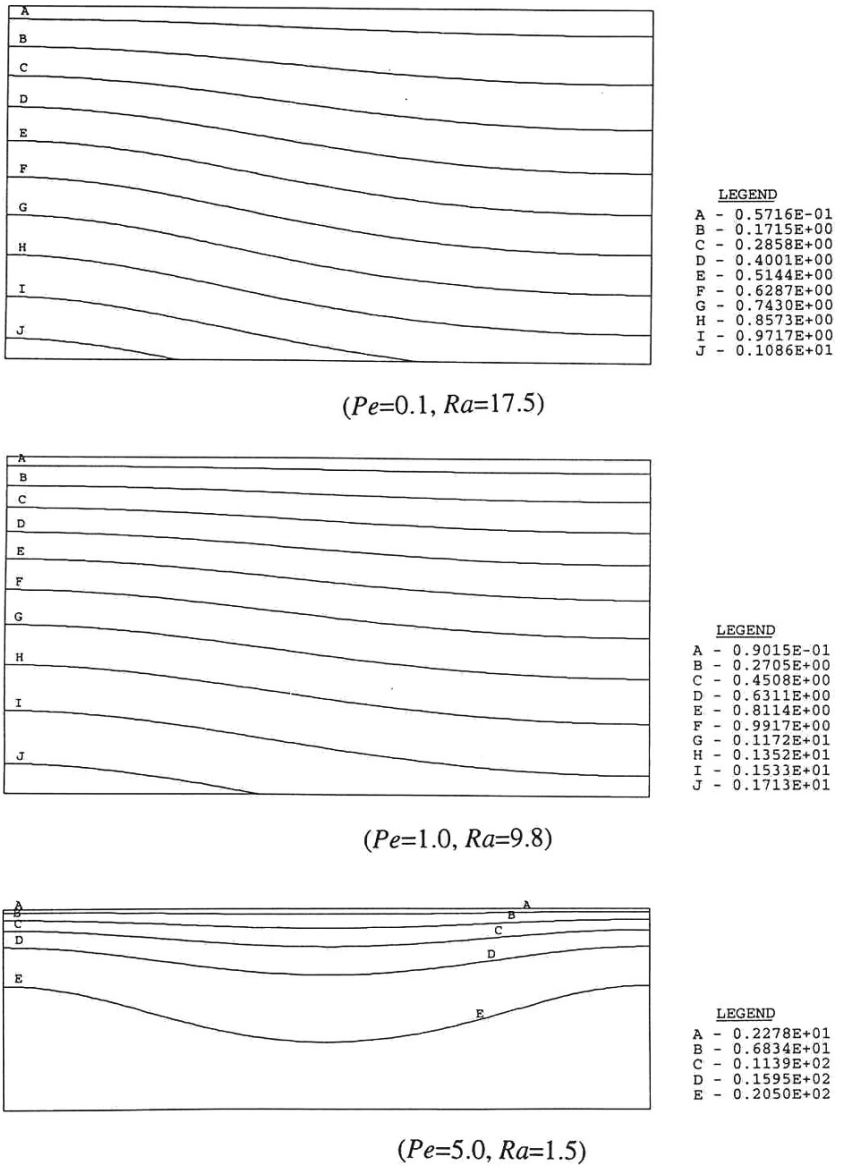

Fig. 4.8 Dimensionless temperature distribution due to different upward throughflow

from the total pore-fluid velocity. Therefore, the perturbation pore-fluid velocity is essentially the convective pore-fluid velocity, while the total pore-fluid velocity is the sum of the convective pore-fluid velocity plus the advective pore-fluid velocity. In this situation, the upward throughflow velocity is essentially identical to the advective pore-fluid velocity. Since the size of the convection cell is dependent on the Peclet number of the system with upward throughflow, the ratios of the length to

thickness of the computational models are 1.8, 1.9 and 3.2 when the Peclet number is 0.1, 1.0 and 5.0, respectively. It is obvious from Fig. 4.6 that the Peclet number P_e has a significant effect on the pattern of total convective pore-fluid flow in the hydrothermal system. Since the perturbation pore-fluid velocity is induced by the thermal buoyancy only, the corresponding convection cells can be clearly exhibited in Fig. 4.7.

Figure 4.8 shows the dimensionless temperature distribution in conceptual crustal models with different values of the upward throughflow velocity. If temperature gradient driven convective flow does not occur, the isotherms are horizontal lines. However, once temperature gradient driven convective flow takes place, the isotherms become curved lines. Since the distance between two neighboring isotherms represents the magnitude of the temperature gradient, Fig. 4.8 shows that the temperature gradient at the top of the layer becomes much larger than that at the bottom of the layer. Generally, the temperature gradient at the top of the layer increases as the Peclet number P_e increases.

In summary, a conceptual model with upward throughflow differs from a conceptual model without upward throughflow in the following aspects. First, the critical Rayleigh number is a constant for a conceptual model without upward throughflow, while it depends on the vertical input velocity value at the bottom for a conceptual model with upward throughflow. Second, the ratio of the length to thickness of the convective cell is a constant for a conceptual model without upward throughflow, whereas it varies with the Peclet number for a conceptual model with upward throughflow. Third, the convective pore-fluid flow pattern for a conceptual model without upward throughflow is clearly different from that of a conceptual model with upward throughflow.

Chapter 5
Convective Heat Transfer in a Heterogeneous Crust

The heterogeneity of crustal material may have many different manifestations: comprising, for instance, sedimentary layering, large folds, large faults and shear zones. Also there may be nonuniform variations in material properties if a geothermal gradient is present in the crust. Depending on the nature and scale of the heterogeneities, the convective flow patterns may be modified compared to those that take place in a homogeneous model of the crust of the Earth. Nevertheless, the discussions on convective heat transfer in a homogenous crust provide the theoretical basis for a fundamental understanding of possible heat transfer mechanisms at the crustal scale. In this chapter, we will investigate how the heterogeneity of crustal material may affect convective heat transfer in the crust. In particular, the following three aspects, namely the effects of layering, of an uneven porosity distribution due to thermoelasticity of crustal material and of temperature-dependent viscosity of the pore-fluids, are considered either numerically or analytically to demonstrate the corresponding effects on heat transfer in a heterogeneous crust.

5.1 The Influence of Layered Material Heterogeneity on Convective Heat Transfer in a Heterogeneous Crust

In order to investigate both material heterogeneity and geometrical irregularity of the crust, the finite element method has become a very useful tool in recent years. In the finite element analysis of high Rayleigh number convective heat transfer problems, the full nonlinear term in the energy equation must be considered in the analysis because it usually dominates both the magnitude and the pattern of temperature distribution within the system. In this kind of problem, the conventional finite element method often suffers difficulties in discovering the nontrivial solution beyond the bifurcation point, which corresponds with the critical Rayleigh number of the problem. For this reason, the progressive asymptotic approach procedure associated with the finite element method is used to investigate how geological heterogeneity affects steady-state heat transfer in the crust.

The following dimensionless equations as described by (4.11) and (4.12) are used to investigate the influence of both material heterogeneity and geometrical irregularity on convective heat transfer within a heterogeneous crust.

C. Zhao et al., *Convective and Advective Heat Transfer in Geological Systems*,

© Springer-Verlag Berlin Heidelberg 2008

$$\frac{\partial u^*}{\partial x^*} + \frac{\partial v^*}{\partial y^*} = 0, \tag{5.1}$$

$$u^* = K_x^* \left(-\frac{\partial P^*}{\partial x^*} + Ra_T T^* e_1 \right), \tag{5.2}$$

$$v^* = K_y^* \left(-\frac{\partial P^*}{\partial y^*} + Ra_T T^* e_2 \right), \tag{5.3}$$

$$u^* \frac{\partial T^*}{\partial x^*} + v^* \frac{\partial T^*}{\partial y^*} = \lambda_{ex}^* \frac{\partial^2 T^*}{\partial x^{*2}} + \lambda_{ey}^* \frac{\partial^2 T^*}{\partial y^{*2}}, \tag{5.4}$$

where x^* and y^* are the dimensionless coordinates; u^* and v^* are the dimensionless velocity components in the x and y directions, respectively; P^* and T^* are the dimensionless excess pressure and temperature; λ_{ex}^* and λ_{ey}^* are the dimensionless thermal conductivities of the porous medium in the x and y directions; K_x^* and K_y^* are the dimensionless permeabilities of the crustal material in the x and y directions, respectively; $\boldsymbol{e}$ is a unit vector and $\boldsymbol{e} = e_1 \boldsymbol{i} + e_2 \boldsymbol{j}$ for a two-dimensional problem, and Ra_T is the Rayleigh number. These dimensionless quantities have the same definitions as those defined in (4.8), (4.9) and (4.10).

By considering the dimensionless velocity, pressure and temperature as basic variables, (5.1), (5.2), (5.3) and (5.4) can be discretized using the conventional finite element method (Zienkiewicz 1977). For a typical 4-node quadrilateral element, the velocity, pressure, temperature and species concentration fields at the elemental level can be expressed as

$$u^*(x^*, y^*) = \boldsymbol{\varphi}^T \, \mathbf{U^e}, \tag{5.5}$$

$$v^*(x^*, y^*) = \boldsymbol{\varphi}^T \, \mathbf{V^e}, \tag{5.6}$$

$$p^*(x^*, y^*) = \psi^T \, \mathbf{P^e}, \tag{5.7}$$

$$T^*(x^*, y^*) = \boldsymbol{\varphi}^T \, \mathbf{T^e}, \tag{5.8}$$

where $\mathbf{U^e}$, $\mathbf{V^e}$, $\mathbf{P^e}$ and $\mathbf{T^e}$ are the column vectors of the nodal velocity, excessive pressure and temperature of the element; $\boldsymbol{\varphi}$ is the column vector of the interpolation functions for the dimensionless velocity and temperature fields within the element, and $\boldsymbol{\psi}$ is the column vector of the interpolation functions for the excessive pressure within the element. For the 4-node quadrilateral element, it is assumed that $\boldsymbol{\varphi}$ is identical to $\boldsymbol{\psi}$ in the following numerical analysis.

The global coordinate components within the element can be defined as

$$x^* = \mathbf{N}^T \, \mathbf{X}, \quad y^* = \mathbf{N}^T \, \mathbf{Y}, \tag{5.9}$$

where $\mathbf{X}$ and $\mathbf{Y}$ are the column vectors of nodal coordinate components in the x and y directions of the global coordinate system, respectively; $\mathbf{N}$ is the column vector of the coordinate mapping function of the element. Based on the isoparametric element concept, the following relationships exist:

$$\mathbf{N}\,(\xi, \eta) = \boldsymbol{\varphi}\,(\xi, \eta) = \boldsymbol{\psi}\,(\xi, \eta), \tag{5.10}$$

where ξ and η are the local coordinate components of the element.

Using the Galerkin weighted residual method, (5.1), (5.2), (5.3) and (5.4) can be expressed, with consideration of (5.5), (5.6), (5.7) and (5.8), as follows:

$$\int_A \boldsymbol{\psi} \frac{\partial \boldsymbol{\varphi}^T}{\partial x^*} \mathbf{U^e}\, dA + \int_A \boldsymbol{\psi} \frac{\partial \boldsymbol{\varphi}^T}{\partial y^*} \mathbf{V^e}\, dA = 0, \tag{5.11}$$

$$\int_A \boldsymbol{\varphi}\boldsymbol{\varphi}^T\, \mathbf{U^e}\, dA + \int_A \boldsymbol{\varphi}\, K_x^* \frac{\partial \psi^T}{\partial x^*} \mathbf{P^e}\, dA + \int_A \boldsymbol{\varphi} K_x^* Ra_T \boldsymbol{\varphi}^T\, \mathbf{T^e}\, e_1 dA = 0, \tag{5.12}$$

$$\int_A \boldsymbol{\varphi}\boldsymbol{\varphi}^T\, \mathbf{V^e}\, dA + \int_A \boldsymbol{\varphi}\, K_y^* \frac{\partial \psi^T}{\partial y^*} \mathbf{P^e}\, dA + \int_A \boldsymbol{\varphi} K_y^* Ra_T \boldsymbol{\varphi}^T\, \mathbf{T^e}\, e_2 dA = 0, \tag{5.13}$$

$$\int_A \boldsymbol{\varphi} u^* \frac{\partial \boldsymbol{\varphi}^T}{\partial x^*} \mathbf{T^e}\, dA + \int_A \boldsymbol{\varphi} v^* \frac{\partial \boldsymbol{\varphi}^T}{\partial y^*} \mathbf{T^e}\, dA - \int_A \boldsymbol{\varphi}\, \lambda_{ex}^* \frac{\partial^2 \boldsymbol{\varphi}^T}{\partial x^{*2}} \mathbf{T^e}\, dA - \int_A \boldsymbol{\varphi}\, \lambda_{ey}^* \frac{\partial^2 \boldsymbol{\varphi}^T}{\partial y^{*2}} \mathbf{T^e}\, dA = 0. \tag{5.14}$$

Using the Green theorem and the technique of integration by parts, the terms involving the second derivatives in (5.14) can be rewritten as

$$\int_A \boldsymbol{\varphi}\, \lambda_{ex}^* \frac{\partial^2 \boldsymbol{\varphi}^T}{\partial x^{*2}} \mathbf{T^e}\, dA = -\int_A \frac{\partial \boldsymbol{\varphi}}{\partial x^*} \lambda_{ex}^* \frac{\partial \boldsymbol{\varphi}^T}{\partial x^*} \mathbf{T^e}\, dA + \int_S \boldsymbol{\varphi} q_y^* dS = 0, \tag{5.15}$$

$$\int_A \boldsymbol{\varphi}\, \lambda_{ey}^* \frac{\partial^2 \boldsymbol{\varphi}^T}{\partial y^{*2}} \mathbf{T^e}\, dA = -\int_A \frac{\partial \boldsymbol{\varphi}}{\partial y^*} \lambda_{ey}^* \frac{\partial \boldsymbol{\varphi}^T}{\partial y^*} \mathbf{T^e}\, dA + \int_S \boldsymbol{\varphi} q_x^* dS = 0, \tag{5.16}$$

where q_x^* and q_y^* are the dimensionless heat fluxes on the boundary of the element, and A and S are the area and boundary length of the element.

Note that (5.11), (5.12), (5.13) and (5.14) can be expressed in a matrix form as follows:

$$\begin{bmatrix} \mathbf{M^e} & \mathbf{0} & -\mathbf{B_x^e} & -\mathbf{A_x^e} \\ 0 & \mathbf{M^e} & -\mathbf{B_y^e} & -\mathbf{A_y^e} \\ 0 & 0 & \mathbf{E^e} & 0 \\ \mathbf{C_x^e} & \mathbf{C_y^e} & 0 & 0 \end{bmatrix} \begin{Bmatrix} \mathbf{U^e} \\ \mathbf{V^e} \\ \mathbf{T^e} \\ \mathbf{P^e} \end{Bmatrix} = \begin{Bmatrix} \mathbf{F_x^e} \\ \mathbf{F_y^e} \\ \mathbf{G^e} \\ \mathbf{0} \end{Bmatrix}, \tag{5.17}$$

where $\mathbf{U^e}$ and $\mathbf{V^e}$ are the nodal dimensionless velocity vectors of the element in the x and y directions, respectively; $\mathbf{T^e}$ and $\mathbf{P^e}$ are the nodal dimensionless temperature and pressure vectors of the element; $\mathbf{A_x^e}$, $\mathbf{A_y^e}$, $\mathbf{B_x^e}$, $\mathbf{B_y^e}$ $\mathbf{C_x^e}$, $\mathbf{C_y^e}$, $\mathbf{E^e}$ and $\mathbf{M^e}$ are the property matrices of the element, and $\mathbf{F_x^e}$, $\mathbf{F_y^e}$ and $\mathbf{G^e}$ are the dimensionless nodal load vectors due to the dimensionless stress and heat flux on the boundary of the element. These matrices and vectors can be derived and expressed as follows:

$$\mathbf{A_x^e} = \int_A \frac{\partial \boldsymbol{\varphi}}{\partial x^*} K_x^* \psi^T\, dA, \quad \mathbf{B_x^e} = \int_A \boldsymbol{\varphi} K_x^* Ra_T \boldsymbol{\varphi}^T\, e_1 dA, \quad \mathbf{C_x^e} = \int_A \psi \frac{\partial \boldsymbol{\varphi}^T}{\partial x^*} dA, \tag{5.18}$$

$$\mathbf{A_y^e} = \int_A \frac{\partial \boldsymbol{\varphi}}{\partial y^*} K_y^* \psi^T dA, \quad \mathbf{B_y^e} = \int_A \boldsymbol{\varphi} K_y^* Ra_T \boldsymbol{\varphi}^T e_2 dA, \quad \mathbf{C_y^e} = \int_A \psi \frac{\partial \boldsymbol{\varphi}^T}{\partial y^*} dA, \tag{5.19}$$

$$\mathbf{D}_x^{\mathbf{e}}(u^*) = \int_A \boldsymbol{\varphi} u^* \frac{\partial \boldsymbol{\varphi}^T}{\partial x^*} dA, \quad \mathbf{L}_x^{\mathbf{e}} = \int_A \frac{\partial \boldsymbol{\varphi}}{\partial x^*} \lambda_{ex}^* \frac{\partial \boldsymbol{\varphi}^T}{\partial x^*} dA, \quad \mathbf{F}_x^{\mathbf{e}} = \int_S \sigma_x^* \boldsymbol{\varphi}\, dS, \tag{5.20}$$

$$\mathbf{D}_y^{\mathbf{e}}(v^*) = \int_A \boldsymbol{\varphi} v^* \frac{\partial \boldsymbol{\varphi}^T}{\partial x^*} dA, \quad \mathbf{L}_y^{\mathbf{e}} = \int_A \frac{\partial \boldsymbol{\varphi}}{\partial y^*} \lambda_{ey}^* \frac{\partial \boldsymbol{\varphi}^T}{\partial y^*} dA, \quad \mathbf{F}_y^{\mathbf{e}} = \int_S \sigma_y^* \boldsymbol{\varphi}\, dS, \tag{5.21}$$

$$\mathbf{E}^{\mathbf{e}} = \mathbf{D}_x^{\mathbf{e}}(u^*) + \mathbf{D}_y^{\mathbf{e}}(v^*) + \mathbf{L}_x^{\mathbf{e}} + \mathbf{L}_y^{\mathbf{e}}, \quad \mathbf{G}^{\mathbf{e}} = -\int_S q^* \boldsymbol{\varphi} dS, \tag{5.22}$$

$$\mathbf{M}^{\mathbf{e}} = \int_A \boldsymbol{\varphi}\boldsymbol{\varphi}^T dA, \quad q^* = \frac{H}{\Delta T \lambda_{e0}} q, \quad \sigma_i^* = \frac{K_h \rho_{f0} c_p}{\mu \lambda_{e0}} \sigma_i, \quad (i = x, y) \tag{5.23}$$

where $\boldsymbol{\varphi}$ is the shape function vector for the temperature and velocity components of the element; ψ is the shape function vector for the pressure of the element; σ_i and q are the stresses and heat flux on the boundary of the element, and A and S are the area and boundary length of the element.

It is noted that since the full nonlinear term of the energy equation in the Horton–Rogers–Lapwood problem is considered in the finite element analysis, matrix $\mathbf{E}^{\mathbf{e}}$ is dependent on the velocity components of the element. Thus, a prediction for the initial velocities of an element is needed to have this matrix evaluated. Based on the progressive asymptotic approach procedure (Zhao et al. 1997), the modified Horton–Rogers–Lapwood problem needs to be solved to offer a good prediction for the initial velocities of all elements in the system.

From the penalty finite element approach (Zienkiewicz 1977), the following equation exists:

$$\mathbf{C}_{\mathbf{x}}^{\mathbf{e}}\mathbf{U}^{\mathbf{e}} + \mathbf{C}_{\mathbf{y}}^{\mathbf{e}}\mathbf{V}^{\mathbf{e}} = -\varepsilon \mathbf{M}_{\mathbf{p}}\mathbf{P}^{\mathbf{e}}. \tag{5.24}$$

Equation (5.24) can be rewritten as

$$\mathbf{P}^{\mathbf{e}} = -\frac{1}{\varepsilon}\mathbf{M}_{\mathbf{p}}^{-1}(\mathbf{C}_{\mathbf{x}}^{\mathbf{e}}\mathbf{U}^{\mathbf{e}} + \mathbf{C}_{\mathbf{y}}^{\mathbf{e}}\mathbf{V}^{\mathbf{e}}) \tag{5.25}$$

Substituting (5.25) into (5.17) yields the following equation in the elemental level:

$$\begin{bmatrix} \mathbf{Q}^{\mathbf{e}} & -\mathbf{B}^{\mathbf{e}} \\ \mathbf{0} & \mathbf{E}^{\mathbf{e}} \end{bmatrix} \begin{Bmatrix} \mathbf{U_F}^{\mathbf{e}} \\ \mathbf{T}^{\mathbf{e}} \end{Bmatrix} = \begin{Bmatrix} \mathbf{F}^{\mathbf{e}} \\ \mathbf{G}^{\mathbf{e}} \end{Bmatrix}, \tag{5.26}$$

where

$$\mathbf{Q}^{\mathbf{e}} = \bar{\mathbf{M}}^{\mathbf{e}} + \frac{1}{\varepsilon}\mathbf{A}^{\mathbf{e}}(\mathbf{M}_{\mathbf{p}}^{\mathbf{e}})^{-1}(\mathbf{C}^{\mathbf{e}})^T, \tag{5.27}$$

$$\bar{\mathbf{M}}^{\mathbf{e}} = \begin{bmatrix} \mathbf{M}^{\mathbf{e}} & \mathbf{0} \\ \mathbf{0} & \mathbf{M}^{\mathbf{e}} \end{bmatrix}, \quad \mathbf{U}_{\mathbf{F}}^{\mathbf{e}} = \begin{Bmatrix} \mathbf{U}^{\mathbf{e}} \\ \mathbf{V}^{\mathbf{e}} \end{Bmatrix}, \quad \mathbf{F}^{\mathbf{e}} = \begin{Bmatrix} \mathbf{F}_x^{\mathbf{e}} \\ \mathbf{F}_y^{\mathbf{e}} \end{Bmatrix}, \tag{5.28}$$

$$\mathbf{B}^{\mathbf{e}} = \begin{Bmatrix} \mathbf{B}_x^{\mathbf{e}} \\ \mathbf{B}_y^{\mathbf{e}} \end{Bmatrix}, \quad \mathbf{A}^{\mathbf{e}} = \begin{Bmatrix} \mathbf{A}_x^{\mathbf{e}} \\ \mathbf{A}_y^{\mathbf{e}} \end{Bmatrix}, \quad \mathbf{C}^{\mathbf{e}} = \begin{Bmatrix} \mathbf{C}_x^{\mathbf{e}} \\ \mathbf{C}_y^{\mathbf{e}} \end{Bmatrix}, \tag{5.29}$$

$$\mathbf{M}_{\mathbf{p}}^{\mathbf{e}} = \int_A \boldsymbol{\psi}\boldsymbol{\psi}^T dA. \tag{5.30}$$

It needs to be pointed out that ε is a penalty parameter in (5.27). To obtain an accurate solution, this parameter must be chosen small enough to approximate fluid incompressibility well, but large enough to prevent the resulting matrix problem from becoming too ill-conditioned to solve.

By assembling all elements in a system, the finite element equation of the system can be expressed in a matrix form as

$$\begin{bmatrix} \mathbf{Q} & -\mathbf{B} \\ \mathbf{0} & \mathbf{E} \end{bmatrix} \begin{Bmatrix} \mathbf{U_F} \\ \mathbf{T} \end{Bmatrix} = \begin{Bmatrix} \mathbf{F} \\ \mathbf{G} \end{Bmatrix}, \tag{5.31}$$

where **Q, B** and **E** are global property matrices of the system; $\mathbf{U_F}$ and **T** are global nodal velocity and temperature vectors of the system, and **F** and **G** are global nodal load vectors of the system. Since (5.31) is nonlinear, either the successive substitution method or the Newton-Raphson method can be used to solve this equation.

The problem considered in this section is a vertical compartment with a top folded layer. Without lose of generality, dimensionless quantities are used to present the problem and related results (Zhao et al. 1998c). The dimensionless width of the compartment is one. The total dimensionless height of the column is 1.2, in which the dimensionless height of the top layer is 0.2. The finite element mesh for the problem is shown in Fig. 5.1, where the top folded layer and its underlying medium are discretized into 120 and 576 nine-node quadrilateral elements, respectively. The mesh gradation technique is employed to satisfy the mesh size requirement for high velocity regions. In order to introduce the heterogeneous nature of the porous medium, the medium permeability in the horizontal direction is assumed to

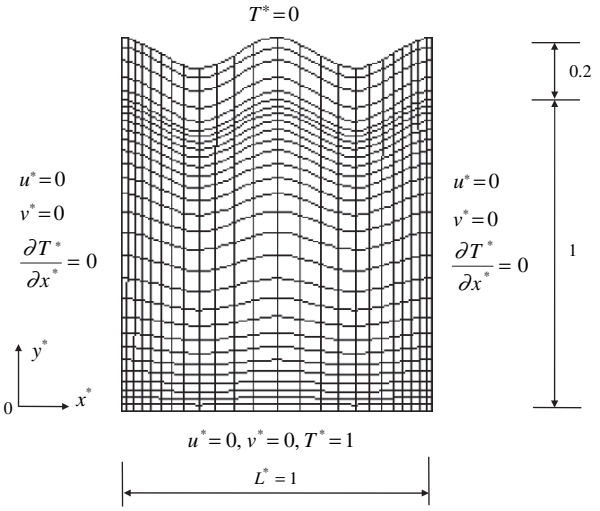

Fig. 5.1 Problem definition and finite element mesh for convective heat transfer in a heterogeneous crust

be three times that in the vertical direction for all calculations in this section. The boundary conditions of the problem are shown in Fig. 5.1.

First, the thermal conductivity ratio of the underlying medium to its top folded layer is fixed as a constant at unity. This focuses the investigation on the effect of permeability ratios of the underlying medium to the top folded layer on heat and mass transfer in the porous medium. For this purpose, three different permeability ratios, namely $\eta = 1$, 10 and 100, are used in the corresponding calculations.

Figures 5.2 and 5.3 show the dimensionless pore-fluid velocity distribution and dimensionless temperature contours within the whole column arising from different permeability ratios between the underlying medium and the top folded layer. With the continuous increase of the permeability ratio, the top folded layer becomes relatively more and more impermeable so that the pore-fluid flow within the layer becomes weaker and weaker. In the case of $\eta = 100$, the pore-fluid flow within the top folded layer nearly vanishes for both Rayleigh numbers considered. Thus, the heterogeneity of medium permeability has a significant effect on convective pore-fluid flow within the system. Figure 5.3 shows that although the permeability ratio has little effect on the temperature distribution in the case of $Ra = 100$, it has a considerable effect in the case of $Ra = 400$, especially in the range between $\eta = 1$ and $\eta = 10$. This is due to the fact that with an increase in the Rayleigh number, heat convection plays a more important role than heat conduction in the whole process of heat transfer in the system. As expected, the Rayleigh number does significantly affect the velocity distribution and temperature contours within the medium.

The effect of thermal conductivity heterogeneity on heat transfer in the fluid-saturated porous medium is investigated next. For this purpose, three different thermal conductivity ratios, ζ, of the underlying medium to the top folded layer are considered as $\zeta = 1$, 3 and 5, respectively. The permeability ratio of the underlying medium to the top folded layer is set to a constant of 10 in all the related calculations.

The dimensionless pore-fluid velocity distribution and dimensionless temperature contours are shown in Figs. 5.4 and 5.5 for three different thermal conductivity ratios. Figure 5.4 shows that, although the thermal conductivity ratio has a negligible effect on the pattern of the dimensionless velocity distribution, it has a significant effect on the maximum amplitude of the dimensionless velocity within the system. For example, in the case of $Ra = 100$, the maximum amplitudes of the dimensionless velocity are 8.624 and 4.940 for $\zeta = 1$ and $\zeta = 3$, respectively. More importantly, when the thermal conductivity ratio is increased to 5, $Ra = 100$ cannot trigger the convective flow of pore-fluid so that $Ra = 110$ is used in this situation. Hence, when the thermal conductivity ratio increases, the critical Rayleigh number increases for the onset of the pore-fluid convective flow in the system because, with the continuous increase in the thermal conductivity ratio, more and more isotherms reside in the top folded layer. As a consequence, the vertical temperature gradient increases in the top folded layer, but decreases in the underlying medium because the temperature is kept constant on both the top surface and the bottom of the whole system in the calculation. This phenomenon can be clearly seen from Fig. 5.5, in which the isotherms become denser and denser in the top folded layer when the thermal

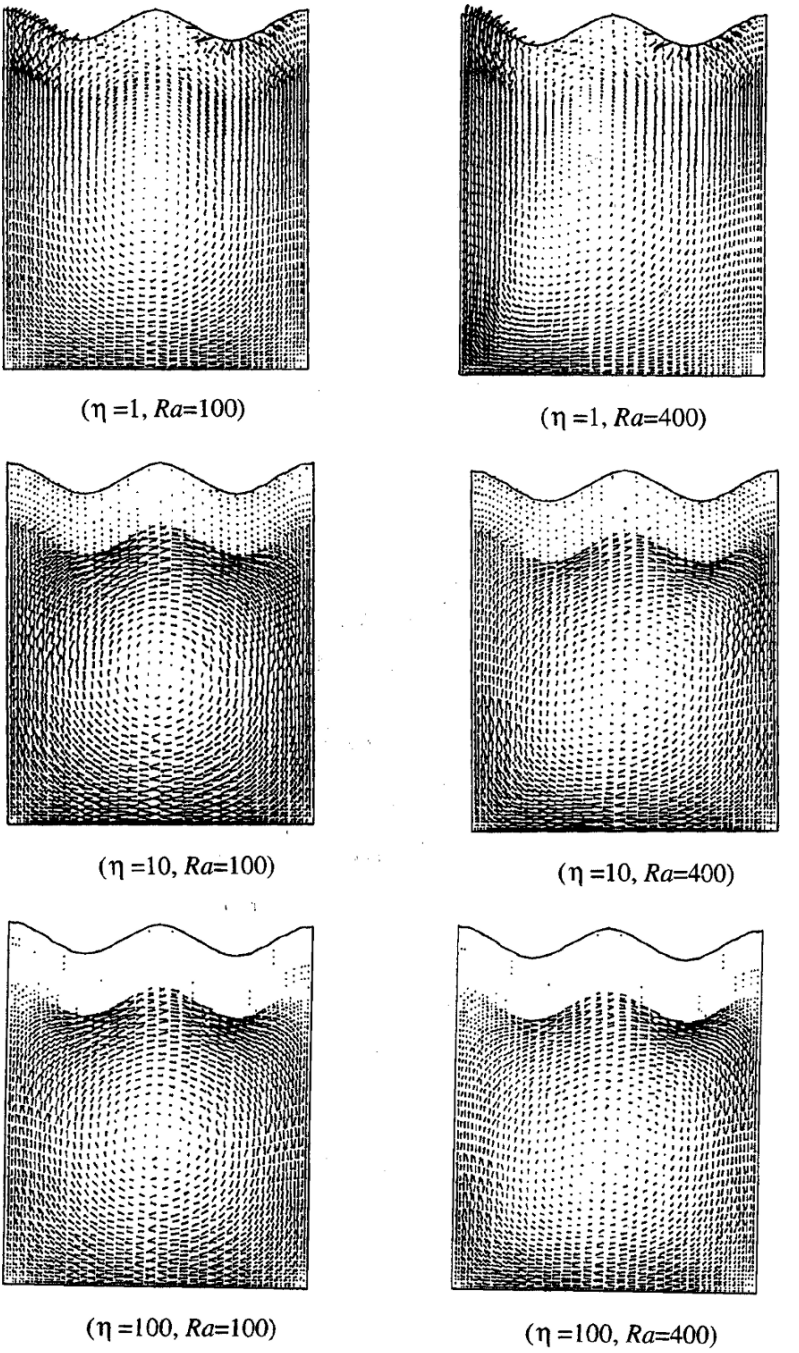

Fig. 5.2 Effect of permeability ratio on convective pore-fluid velocity distribution

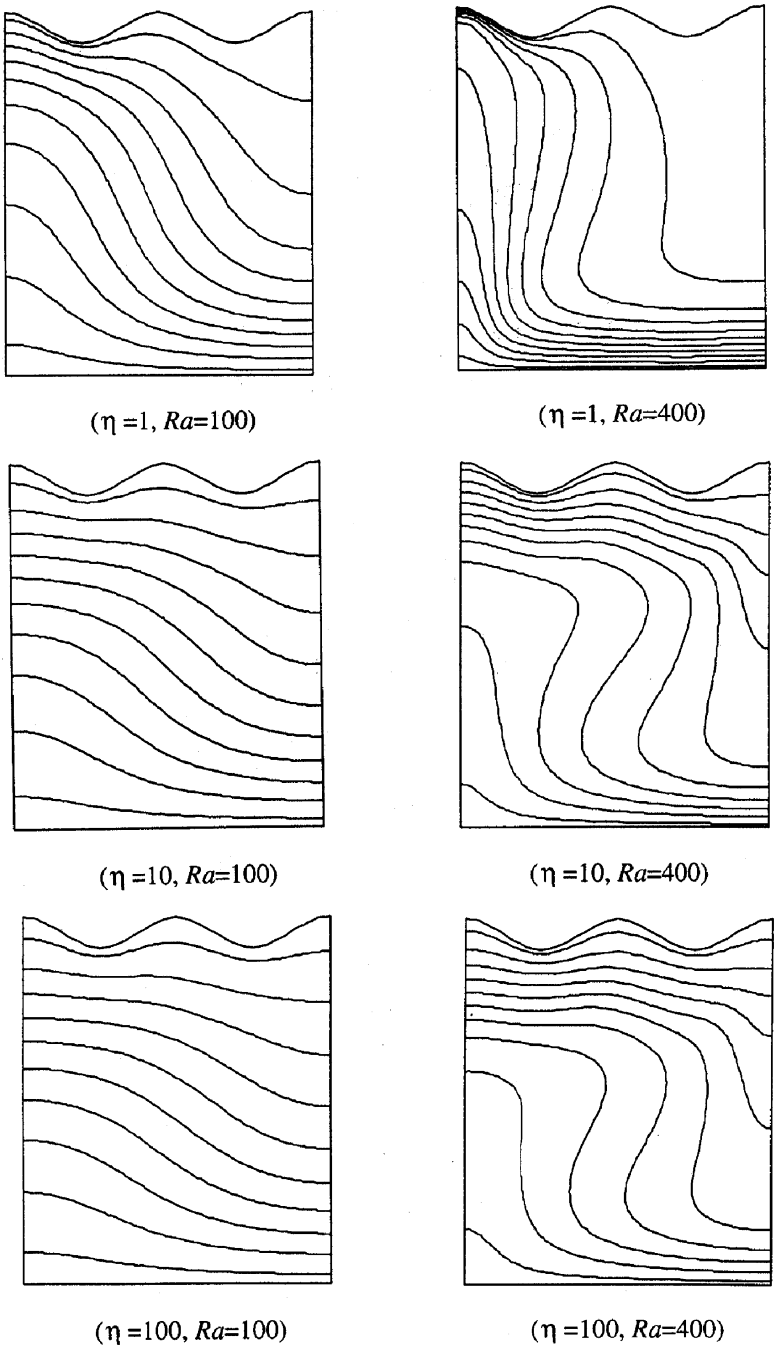

Fig. 5.3 Effect of permeability ratio on the dimensionless temperature contour distribution. The dimensionless temperature at the top and bottom are zero and unity, respectively, meaning that the bottom is hotter than the top

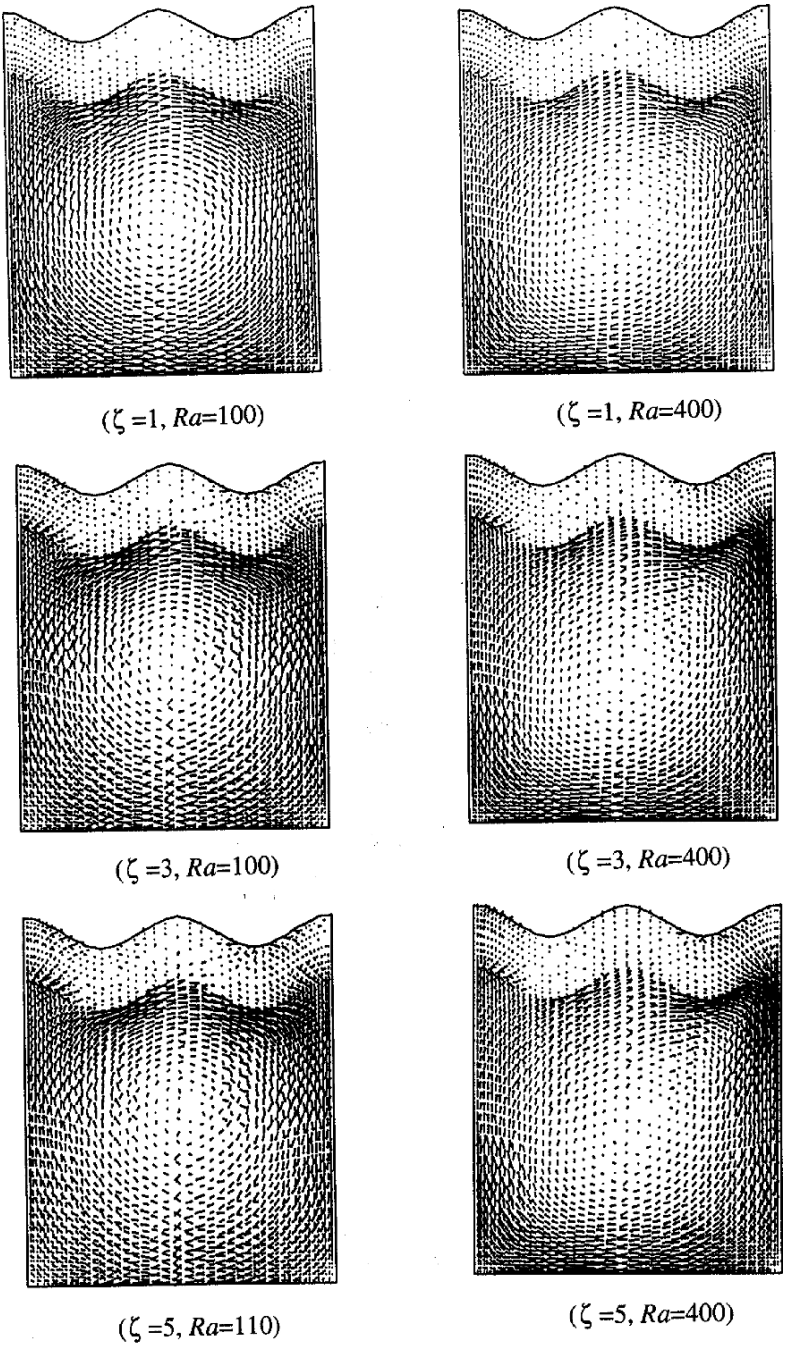

Fig. 5.4 Effect of thermal conductivity ratio on the convective pore-fluid velocity distribution

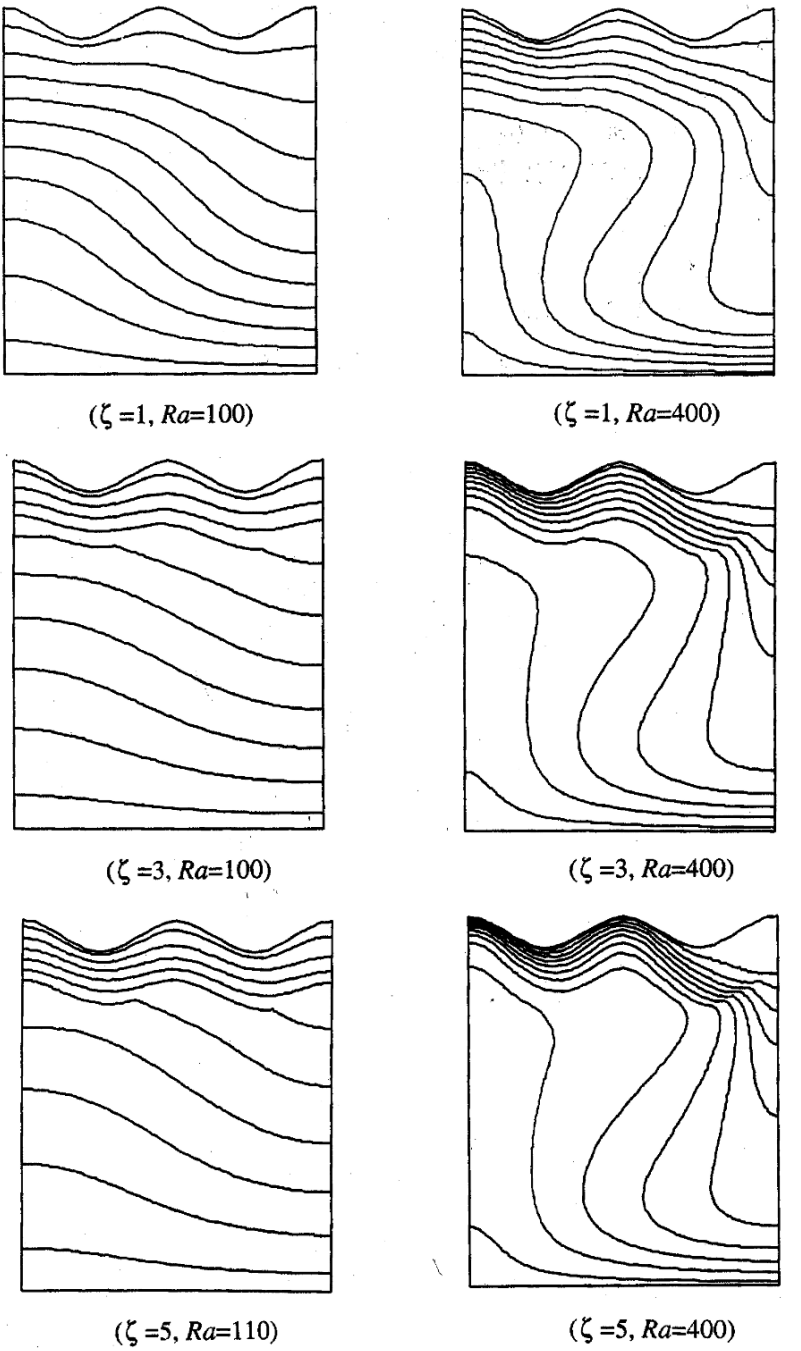

Fig. 5.5 Effect of thermal conductivity ratio on the dimensionless temperature contour distribution. The dimensionless temperature at the top and bottom are zero and unity, respectively, meaning that the bottom is hotter than the top

conductivity ratio increases from 1 to 5. Since the top folded layer is relatively impermeable with respect to the underlying medium, it is difficult to initiate convective flow cells in this layer, even if the thermal conductivity ratio is increased to 5.

5.2 The Influence of Material Thermoelasticity on Convective Heat Transfer in a Heterogeneous Crust

This section investigates the effects of material thermoelasticity on high Rayleigh number convective heat transfer in a fluid-saturated porous medium when it is heated from below. From the geoscience point of view, we are interested in a horizontal layer of a porous medium. However, from the computational point of view, we need to model a domain of finite size. This leads to a contradiction. Nevertheless, considering the periodic nature of convective solutions (Zhao et al. 1997) for high Rayleigh numbers makes it possible to overcome this difficulty. Theoretically, as was mentioned previously, it is appropriate to place two vertical boundaries of a computational domain at the cell boundaries, where the horizontal velocity, the horizontal displacement and the normal thermal flux are identical to zero. Since there are two cells (a clockwise cell and an anticlockwise cell) in a periodic cycle of the solutions, the length of a cell in the horizontal direction is just equal to half the wavelength of the layer. This means that the minimum computing length of a computational domain should equal half the wavelength of the layer. It turns out that half the wavelength of a horizontal layer is equal to the thickness of the layer if the layer deformation is neglected.

We consider a horizontal layer of a fluid-saturated porous medium in a two-dimensional domain. The temperature at the top of the layer is assumed to be lower than that at the bottom of the layer. This means that the layer is heated from below. The porous medium to be considered is a homogeneous, isotropic and elastic medium. We use Darcy's Law for describing pore-fluid flow and Fourier's Law for describing heat transfer, respectively. In addition, the Oberbeck-Boussinesq approximation is employed to describe the change in pore-fluid density due to a change in pore-fluid temperature. Under the above conditions, the corresponding governing equations for the steady state pore-fluid flow and heat transfer (which we label the first subproblem) in the porous medium can be expressed as follows:

$$\frac{\partial u}{\partial x} + \frac{\partial v}{\partial y} = 0, \tag{5.32}$$

$$u = \frac{K_x}{\mu}\left(-\frac{\partial P}{\partial x}\right), \tag{5.33}$$

$$v = \frac{K_y}{\mu}\left(-\frac{\partial P}{\partial y} + \rho_f g\right), \tag{5.34}$$

$$\rho_{f0}c_p\left(u\frac{\partial T}{\partial x}+v\frac{\partial T}{\partial y}\right)=\lambda_{ex}\frac{\partial^2 T}{\partial x^2}+\lambda_{ey}\frac{\partial^2 T}{\partial y^2}, \tag{5.35}$$

$$\rho_f=\rho_{f0}[1-\beta_T(T-T_0)], \tag{5.36}$$

$$\lambda_{ex}=\phi\lambda_{fx}+(1-\phi)\lambda_{sx},\quad \lambda_{ey}=\phi\lambda_{fy}+(1-\phi)\lambda_{sy}, \tag{5.37}$$

where u and v are the horizontal and vertical velocity components of the pore-fluid in the x and y directions, respectively; P is the pore-fluid pressure; T is the temperature of the crustal material; K_x and K_y are the permeabilities of the crustal material in the x and y directions, respectively; μ is the dynamic viscosity of the pore-fluid; ρ_f is the density of the pore-fluid and g is the acceleration due to gravity; ρ_{f0} and T_0 are the reference density and temperature; λ_{fx} and λ_{sx} are the thermal conductivities of the pore-fluid and rock mass in the x direction; λ_{fy} and λ_{sy} are the thermal conductivities of the pore-fluid and rock mass in the y direction; c_p is the specific heat of the pore-fluid, ϕ and β_T are the porosity of the crustal material and the thermal volume expansion coefficient of the pore-fluid.

If a coupling problem involving pore-fluid flow and material thermoelasticity is treated as a transient state problem, then a term involving strain dissipation that is associated with the solid material needs to be added to the energy equation (i.e., (5.35)). In this case, the strain dissipation caused by the thermoelasticity of the solid is directly proportional to the product of the stress and thermoelastically induced strain rate of the solid material. For a steady state problem, since the thermoelastically induced strain rate of the solid material is identical to zero, the corresponding strain energy dissipation caused by the thermoelasticity of the solid must be equal to zero. As a result, a term involving strain dissipation that is associated with the solid material can be safely neglected in the energy equation (i.e., (5.35)).

As expected, the governing equations (i.e., (5.32), (5.33), (5.34), (5.35), (5.36) and (5.37)) of the first subproblem are exactly the same as those expressed in (4.2), (4.3), (4.4), (4.5), (4.6) and (4.7). For the purpose of coupling with the medium elastic deformation, these equations are considered, rather than their dimensionless counterparts from the previous analysis.

Since this study is focused on the medium deformation caused by thermal effects, body forces are neglected in the equilibrium equations. Thus, the governing equations for static deformation (which is labeled as the second subproblem) in the porous medium under plane strain conditions are:

$$\frac{\partial\sigma_x}{\partial x}+\frac{\partial\tau_{yx}}{\partial y}=0, \tag{5.38}$$

$$\frac{\partial\tau_{xy}}{\partial x}+\frac{\partial\sigma_y}{\partial y}=0, \tag{5.39}$$

$$\sigma_x=\frac{E(1-\nu)}{(1-2\nu)(1+\nu)}\left(\varepsilon_x+\frac{\nu}{1-\nu}\varepsilon_y\right)-\frac{E\alpha T}{1-2\nu}, \tag{5.40}$$

$$\sigma_y = \frac{E(1-\nu)}{(1-2\nu)(1+\nu)}\left(\frac{\nu}{1-\nu}\varepsilon_x + \varepsilon_y\right) - \frac{E\alpha T}{1-2\nu}, \tag{5.41}$$

$$\tau_{xy} = \tau_{yx} = 2G\gamma_{xy}, \tag{5.42}$$

$$\varepsilon_x = \frac{\partial u_s}{\partial x}, \quad \varepsilon_y = \frac{\partial v_s}{\partial y}, \quad \gamma_{xy} = \frac{1}{2}\left(\frac{\partial u_s}{\partial y} + \frac{\partial v_s}{\partial x}\right), \tag{5.43}$$

where σ_x and σ_y are normal stresses of the solid matrix in the x and y directions; ε_x and ε_y are the normal strains of the solid matrix in relation to σ_x and σ_y; τ_{xy} and γ_{xy} are shear stress and shear strain of the solid matrix; u_s and v_s are the horizontal and vertical displacements of the solid matrix; E and G are the elastic and shear modulus, respectively; ν is the Poisson's ratio of the solid matrix and α is the linear thermal expansion coefficient of the solid matrix.

Note that (5.38) and (5.39) represent the equilibrium equations, whereas (5.40), (5.41), (5.42) and (5.43) are the constitutive equations and strain displacement relationship equations, respectively.

To couple the first subproblem with the second subproblem, we need to establish a relationship between the volumetric strain and the porosity of the porous medium. For small strain problems, such a relationship can be expressed as (Itasca Consulting Group 1995):

$$\phi = 1 - \frac{1-\phi_0}{1+\varepsilon_v}, \quad \varepsilon_v = \varepsilon_x + \varepsilon_y, \tag{5.44}$$

where ϕ and ϕ_0 are the porosity and initial porosity of the porous medium (i.e., the crustal material), and ε_v is the volumetric strain of the solid matrix.

Using the Carman–Kozeny formula (Nield and Bejan 1992), the permeability of an isotropic porous medium is expressed as a function of porosity as follows:

$$K_x = K_y = \frac{K_0(1-\phi_0)^2\phi^3}{\phi_0^3(1-\phi)^2}, \tag{5.45}$$

where K_0 is the initial permeability corresponding to the initial porosity, ϕ_0.

Clearly, the first subproblem is coupled with the second subproblem through the medium temperature, T, and permeabilities, K_x and K_y. Within the first subproblem, the pore-fluid flow is coupled with the thermal flow through the medium temperature and pore-fluid velocity components, u and v. However, within the second subproblem, the medium deformation (displacement) is coupled with the medium temperature and permeability through the volumetric strain, ε_v, and the medium porosity, ϕ.

When the Rayleigh number of a fluid-saturated porous medium is equal to or greater than its corresponding critical value, it is difficult to derive an analytical nontrivial solution to the coupled problem described by the above-mentioned equations. Thus, we will use a numerical method to solve the problem. Although a computer program can be developed to solve this problem, it is desirable to make best use of existing computer codes for the following reasons: (1) built-in preprocessing and post-processing tools make it easy and attractive to prepare, input and output data which are essential in a numerical analysis; (2) provision of movie/animation

functions enables numerical results, the treatment of which is often a cumbersome and tedious task, to be visualised via clear and colourful pictures, and (3) detailed benchmark solutions and documentations as well as many embedded robust solution algorithms allow the codes to be used more easily, correctly, effectively and efficiently for solving a wide range of practical problems. Therefore, two commercial computer codes, FIDAP (Fluid Dynamics International 1997) and FLAC (Itasca Consulting Group 1995), are used as two super subroutines in the solution method of the coupled problem. Basically, FIDAP is used to solve the first subproblem, while FLAC is used to solve the second subproblem. A simple interface program has been developed to link FIDAP and FLAC (Zhao et al. 1999c). However, when a fluid-saturated porous medium involves a geometry comprising a horizontal layer, and is heated uniformly from the bottom of the layer, directly solving the first subproblem using the conventional finite element method (as in FIDAP) always leads to a trivial solution of zero values for the velocity field of pore-fluid flow, even if the Rayleigh number is high enough to trigger pore-fluid flow in the fluid-saturated porous medium. To overcome this difficulty, the progressive asymptotic approach procedure was developed (Zhao et al. 1997). The basic idea behind the procedure is that, through solving a sequence of the modified problems in which gravity is assumed to tilt a small angle away from vertical, an accurate nontrivial solution to the first subproblem, with the tilted angle being zero, can be obtained. Although FIDAP, FLAC and the progressive asymptotic approach procedure (Zhao et al. 1997) have been validated separately and extensively by many benchmark problems, it is highly desirable to validate the proposed solution method because it links the above three together. For this purpose, a benchmark problem will be constructed and an analytical solution for this benchmark problem will be derived below.

Although, as we have indicated, it is very difficult to derive analytical nontrivial solutions to (5.32), (5.33), (5.34), (5.35), (5.36), (5.37), (5.38), (5.39), (5.40), (5.41), (5.42) and (5.43) when the Rayleigh number of a pore-fluid saturated medium is supercritical, it is possible to derive analytical solutions for some special situations. For example, when the porous medium is dry or when the Rayleigh number of a fluid-saturated porous medium is subcritical, it is possible to derive analytical solutions to (5.32), (5.33), (5.34), (5.35), (5.36), (5.37), (5.38), (5.39), (5.40), (5.41), (5.42) and (5.43) with some simple geometric and boundary conditions.

Keeping the above in mind, a horizontal layer shown in Fig. 5.6 is considered as the benchmark problem, the boundary conditions of which are free stresses and

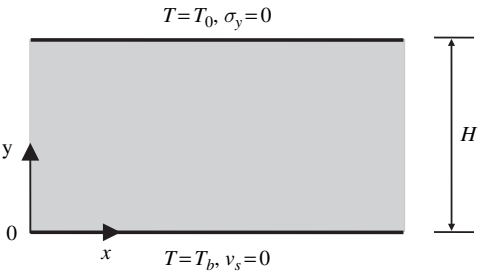

Fig. 5.6 Geometry and boundary conditions of a benchmark system

constant temperature at the top of the layer, and zero displacements and constant temperature at the bottom of the layer. The temperature at the bottom of the layer is assumed to be higher than that at the top of the layer. The layer is comprised of a fluid-saturated porous medium and the Rayleigh number of the medium is below its critical value. This implies that the pore-fluid velocities in the layer are zero.

$$u = 0, \quad v = 0. \tag{5.46}$$

Substituting (5.46) into (5.35) and considering the nature of temperature distribution in the horizontal layer yields the following equation:

$$\frac{\partial^2 T}{\partial y^2} = 0. \tag{5.47}$$

The solution to (5.47) with the boundary conditions shown in Fig. 5.6 can be expressed as follows:

$$T = T_b - \frac{y}{H}(T_b - T_0). \tag{5.48}$$

For the benchmark problem shown in Fig. 5.6, the displacement and strain of the solid matrix in the horizontal direction, the normal stress of the solid matrix in the vertical direction and the shear stress of the solid matrix should vanish:

$$u_s = 0, \quad \varepsilon_x = 0, \quad \sigma_y = 0, \quad \tau_{xy} = \tau_{yx} = 0. \tag{5.49}$$

Substituting (5.49) into (5.40), (5.41) and (5.42) yields the following equation:

$$\frac{\partial v_s}{\partial y} - \frac{1+\nu}{1-\nu}\alpha T = 0. \tag{5.50}$$

The solution to (5.50) with the corresponding boundary conditions in Fig. 5.6 can be expressed as

$$v_s = \frac{1+\nu}{1-\nu}\alpha \left[T_b - \frac{y}{2H}(T_b - T_0)\right] y. \tag{5.51}$$

The volumetric strain for the benchmark problem is

$$\varepsilon_v = \frac{1+\nu}{1-\nu}\alpha \left[T_b - \frac{y}{H}(T_b - T_0)\right]. \tag{5.52}$$

Thus, the solution to the medium porosity and permeability can be straightforwardly expressed as

$$\phi = \frac{\phi_0(1-\nu) + \alpha(1+\nu)[T_b - \frac{y}{H}(T_b - T_0)]}{1-\nu+\alpha(1+\nu)[T_b - \frac{y}{H}(T_b - T_0)]}, \tag{5.53}$$

$$K_x = K_y = \frac{K_0(1-\phi_0)^2\{\phi_0(1-\nu) + \alpha(1+\nu)[T_b - \frac{y}{H}(T_b - T_0)]\}^3}{\phi_0^3[(1-\phi_0)(1-\nu)]^2\{1-\nu+\alpha(1+\nu)[T_b - \frac{y}{H}(T_b - T_0)]\}}. \tag{5.54}$$

Using the analytical solutions derived for the benchmark problem, the proposed numerical method consisting of a combination of two separate commercial computer codes, FIDAP and FLAC, can be verified. For this purpose, the benchmark problem addressed above is solved numerically. Table 5.1 shows the parameters used in the calculation. In addition, the thickness of the horizontal layer is 50 m; temperatures at the top and the bottom of the layer are 0 °C and 10 °C, respectively. For the parameters selected here, the Rayleigh number of the porous medium is about 0.014, which is far below the corresponding critical value of $4\pi^2$ when the deformation of the porous medium is neglected. This indicates that the benchmark analytical solution derived above is valid for this particular problem.

Figure 5.7 compares the numerical solutions with analytical solutions for the benchmark problem considered. In this figure, v_s/v_s^{top}, where v_s^{top} is the vertical displacement at the top of the layer, is the dimensionless vertical displacement of the layer. $\Delta K/K_0$ is the ratio of a variation in permeability to its initial value, while $\Delta\phi/\phi_0$ is the ratio of a variation in porosity to its initial value. Clearly, all the numerical solutions shown in Fig. 5.7 agree with the corresponding analytical solutions. This demonstrates that the proposed solution method, especially the link between FIDAP, FLAC and the progressive asymptotic approach procedure, works well in obtaining a numerical solution.

It is interesting to note that the maximum volumetric strain takes place at the bottom of the layer, where the relative temperature is the highest within the whole layer. Generally, the higher the relative temperature, the larger the volumetric strain in a porous medium. Since the volumetric expansion of a porous medium causes a porosity redistribution, the maximum variation in porosity occurs at the region of the highest relative temperature, i.e., at the bottom of the layer for this particular problem. Although the maximum variation in porosity is about 0.45 percent, the

Table 5.1 Parameters used for the benchmark problem

Material type	Parameter	Value
	dynamic viscosity	$10^{-3}\,\mathrm{N}\times\mathrm{s/m^2}$
	reference density	$1000\,\mathrm{kg/m^3}$
pore-fluid	volumetric thermal expansion coefficient	$2.07\times10^{-4}(1/^\circ\mathrm{C})$
	specific heat	$4185\,\mathrm{J/(kg\cdot^\circ C)}$
	thermal conductivity coefficient	$0.6\,\mathrm{W/(m\times^\circ C)}$
	initial porosity	0.1
	initial permeability	$10^{-14}\,\mathrm{m^2}$
porous matrix	elastic modulus	$10^{10}\,\mathrm{Pa}$
	Poisson's ratio	0.25
	linear thermal expansion coefficient	$3\times10^{-5}(1/^\circ\mathrm{C})$
	thermal conductivity coefficient	$3.35\,\mathrm{W/(m\cdot^\circ C)}$

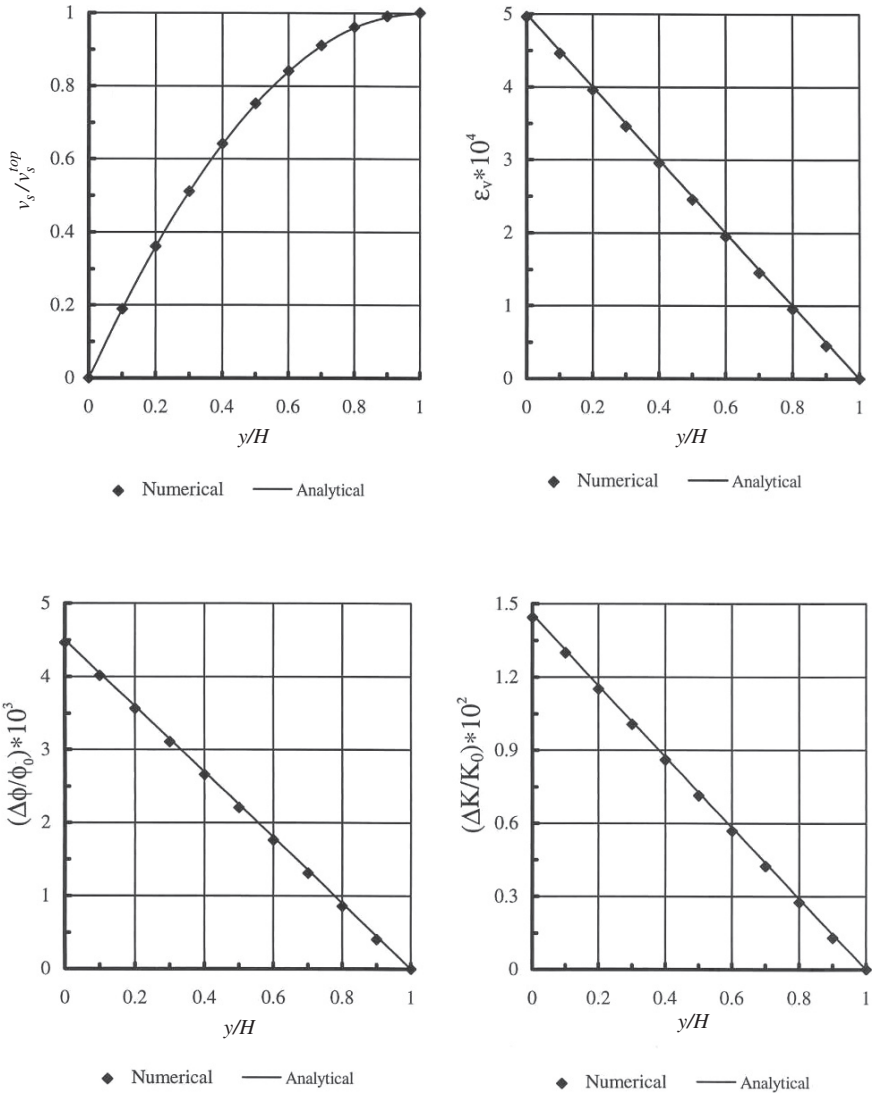

Fig. 5.7 Comparison of numerical solutions with analytical solutions

maximum variation in permeability can reach about 1.45 percent. Thus, the porosity and permeability of a porous medium may vary with the same relative temperature, but at different rates. This finding implies that, for an elastic porous medium, a region of relatively high temperature favors the formation of flow channels due to increased porosity in the region arising from the medium thermoelasticity effect.

After the proposed numerical solution method is verified, it is used to investigate the effect of medium thermoelasticity on convective pore-fluid flow when the hydrothermal system becomes supercritical. To this end, a square box of side

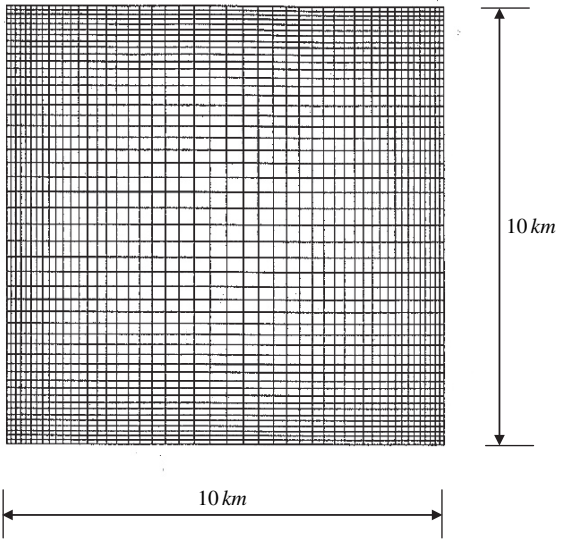

Fig. 5.8 Finite element computational model for the convective heat transfer problem with thermoelasticity

length $H = 10\,\text{km}$ is considered as the computing domain in the forthcoming computations. As shown in Fig. 5.8, this square box is discretized into 2,304 four-node quadrilateral elements. Table 5.2 shows the parameters used for this problem. In addition, temperature at the top and the bottom of the layer is 20 °C and 220 °C, respectively. From these parameters, the Rayleigh number of the porous medium is about 55.2, which is above the corresponding critical value of 39.48 when the medium deformation is neglected. This indicates that temperature buoyancy driven convective pore-fluid flow definitely takes place in the porous medium considered here.

Figure 5.9 shows the effects of material thermoelasticity on the distributions of temperature contours for three different models. In the rigid medium model, the medium deformation is excluded and, consequently, the material thermoelasticity effect is eliminated. Thus, the numerical results from the rigid model can be compared with those from the deformable medium models to identify the material thermoelasticity effect on the solutions. The overall distribution patterns of the temperature contours are very similar for these three models. This indicates that if one is only interested in the overall pattern of temperature distribution in the Earth's crust, then material thermoelasticity effects are minimal and, therefore, can be excluded in the analysis, especially for a porous medium consisting of elastically hard rock masses. Even though the effect of material thermoelasticity on the overall pattern of temperature distribution is minimal, the material thermoelasticity has a considerable influence on the local distribution of the solutions. For example, the maximum

Table 5.2 Parameters used for the material thermoelasticity effect problem

Material type	Parameter	Value
	dynamic viscosity	$10^{-3}\,\mathrm{N}\times\mathrm{s}/\mathrm{m}^2$
	reference density	$1000\,\mathrm{kg}/\mathrm{m}^3$
pore-fluid	volumetric thermal expansion coefficient	$2.07\times10^{-4}(1/^\circ\mathrm{C})$
	specific heat	$4185\,\mathrm{J}/(\mathrm{kg}\cdot^\circ\mathrm{C})$
	thermal conductivity coefficient	$0.6\,\mathrm{W}/(\mathrm{m}\cdot^\circ\mathrm{C})$
	initial porosity	0.1
	initial permeability	$10^{-14}\,\mathrm{m}^2$
porous matrix	elastic modulus for soft rock	$1.78\times10^{9}\,\mathrm{Pa}$
	elastic modulus for hard rock	$1.78\times10^{10}\,\mathrm{Pa}$
	Poisson's ratio	0.23
	linear thermal expansion coefficient for soft rock	$7\times10^{-5}(1/^\circ\mathrm{C})$
	linear thermal expansion coefficient for hard rock	$7\times10^{-6}(1/^\circ\mathrm{C})$
	thermal conductivity coefficient	$3.35\,\mathrm{W}/(\mathrm{m}\cdot^\circ\mathrm{C})$

values of convective pore-fluid velocities are $7.11\times10^{-10}\,\mathrm{m}/\mathrm{s}$, $7.38\times10^{-10}\,\mathrm{m}/\mathrm{s}$ and $1.24\times10^{-9}\,\mathrm{m}/\mathrm{s}$ for the rigid medium model, the deformable medium (hard rock) model and the deformable medium (soft rock) model, respectively. This indicates that if one is interested in the formation of minerals in the Earth's crust, then material thermoelasticity effects should be included in the analysis, because it is the localizing effect of fluid flow that often influences mineralization in the Earth's crust.

Figures 5.10 and 5.11 display the distributions of porosity and permeability due to different rock types in the deformable models. Clearly, the material thermoelasticity affects both the porosity and the permeability distributions and, therefore, significantly affects the local distribution of flow channels in the porous medium. Thus, material thermoelasticity effects should be considered in the analysis of convective heat transfer problems in a hydrothermal system.

Figures 5.12 and 5.13 show the effects of convective pore-fluid flow on the distributions of deformation, porosity and permeability in the deformable medium (hard rock) model. It is clear that the solutions corresponding to the post-convection situation are different from those corresponding to the pre-convection situation. This means that convective pore-fluid flow plays an important role in the localization of deformation, porosity and permeability in a deformable porous medium. Thus, an error in finding a nontrivial solution to a hydrothermal system having supercritical Rayleigh numbers will definitely result in some misunderstanding and misinterpretation of convective heat transfer phenomena in the system.

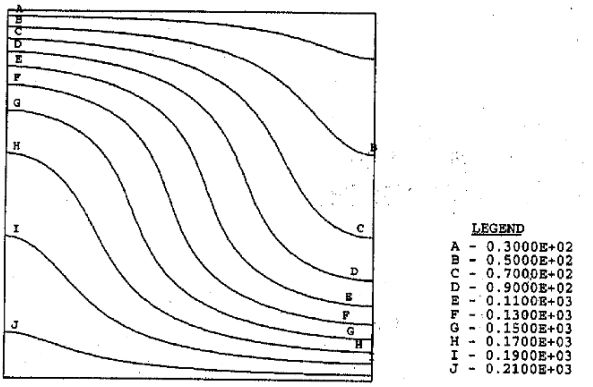

(Rigid medium)

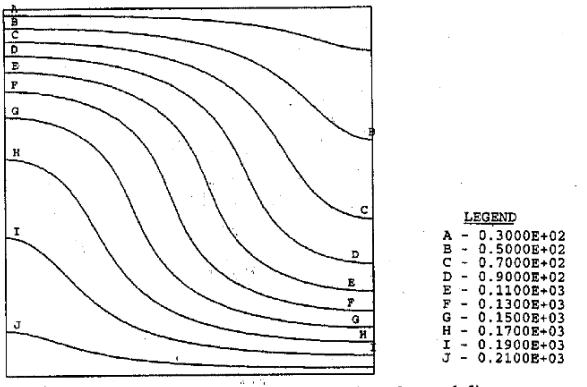

(Deformable medium, Hard rock model)

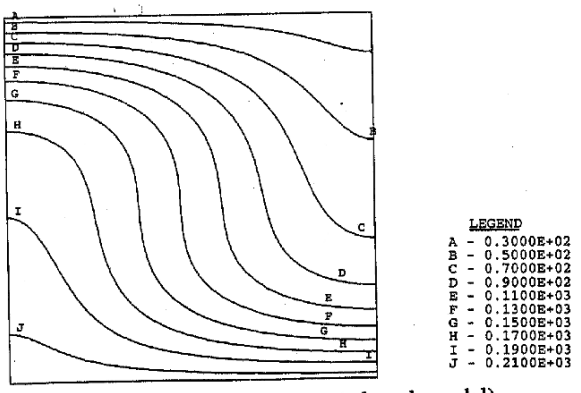

(Deformable medium, Soft rock model)

Fig. 5.9 Effect of material thermoelasticity on temperature distributions

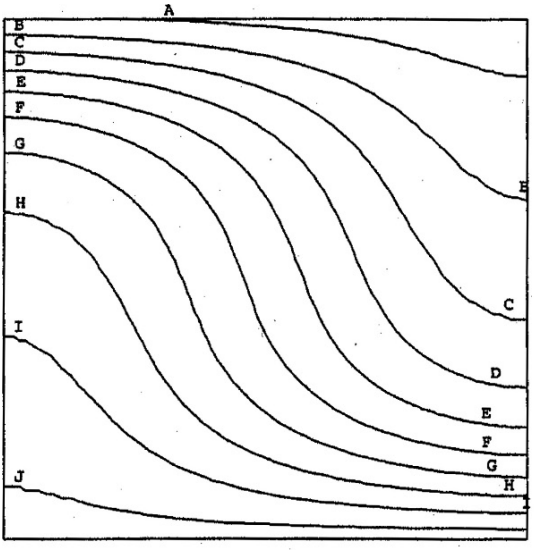

LEGEND
A - 0.1001E+00
B - 0.1004E+00
C - 0.1008E+00
D - 0.1011E+00
E - 0.1015E+00
F - 0.1018E+00
G - 0.1022E+00
H - 0.1025E+00
I - 0.1029E+00
J - 0.1032E+00

(Hard rock model)

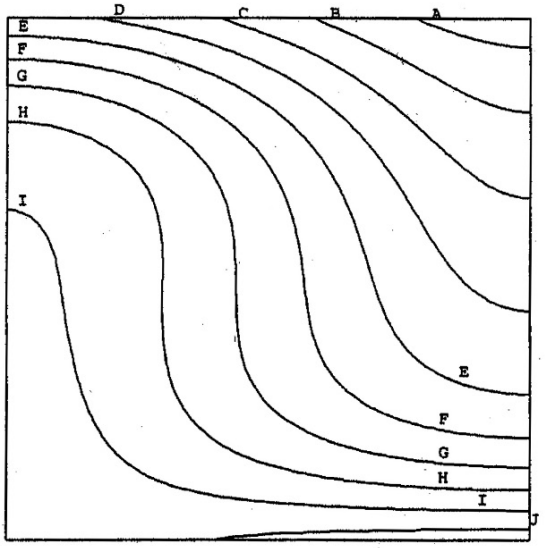

LEGEND
A - 0.9651E-01
B - 0.9900E-01
C - 0.1015E+00
D - 0.1040E+00
E - 0.1065E+00
F - 0.1090E+00
G - 0.1115E+00
H - 0.1140E+00
I - 0.1165E+00
J - 0.1190E+00

(Soft rock model)

Fig. 5.10 Effect of material thermoelasticity on porosity distributions

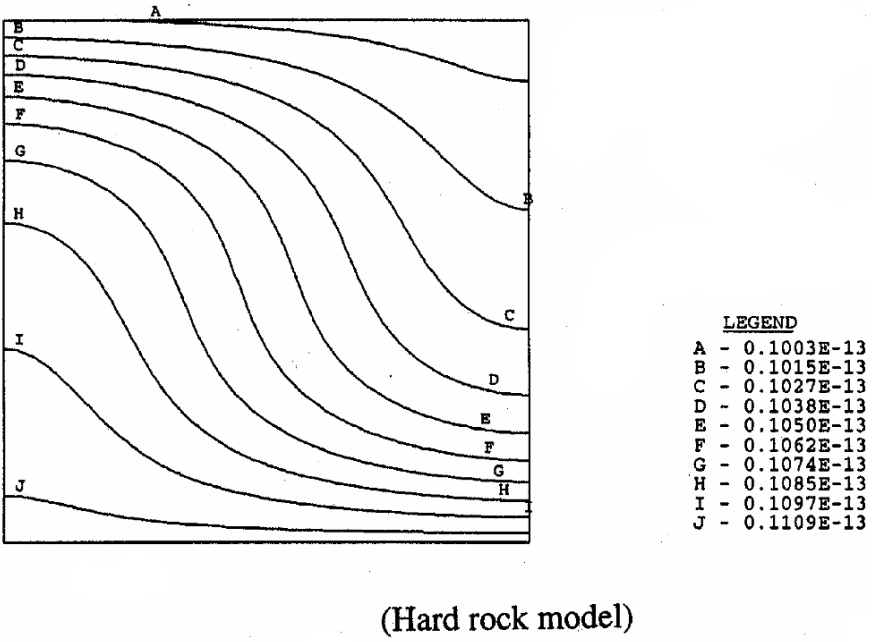

(Hard rock model)

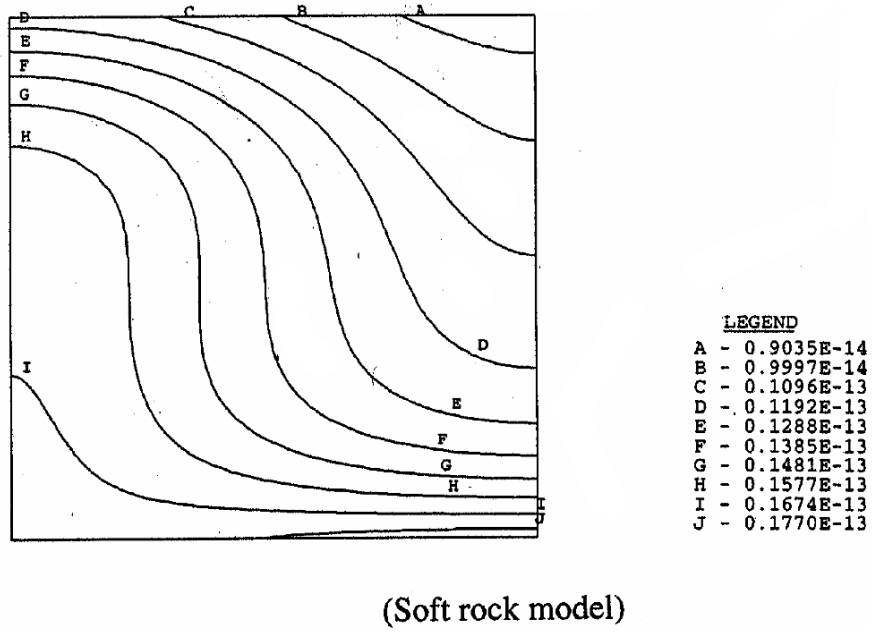

(Soft rock model)

Fig. 5.11 Effect of material thermoelasticity on permeability distributions

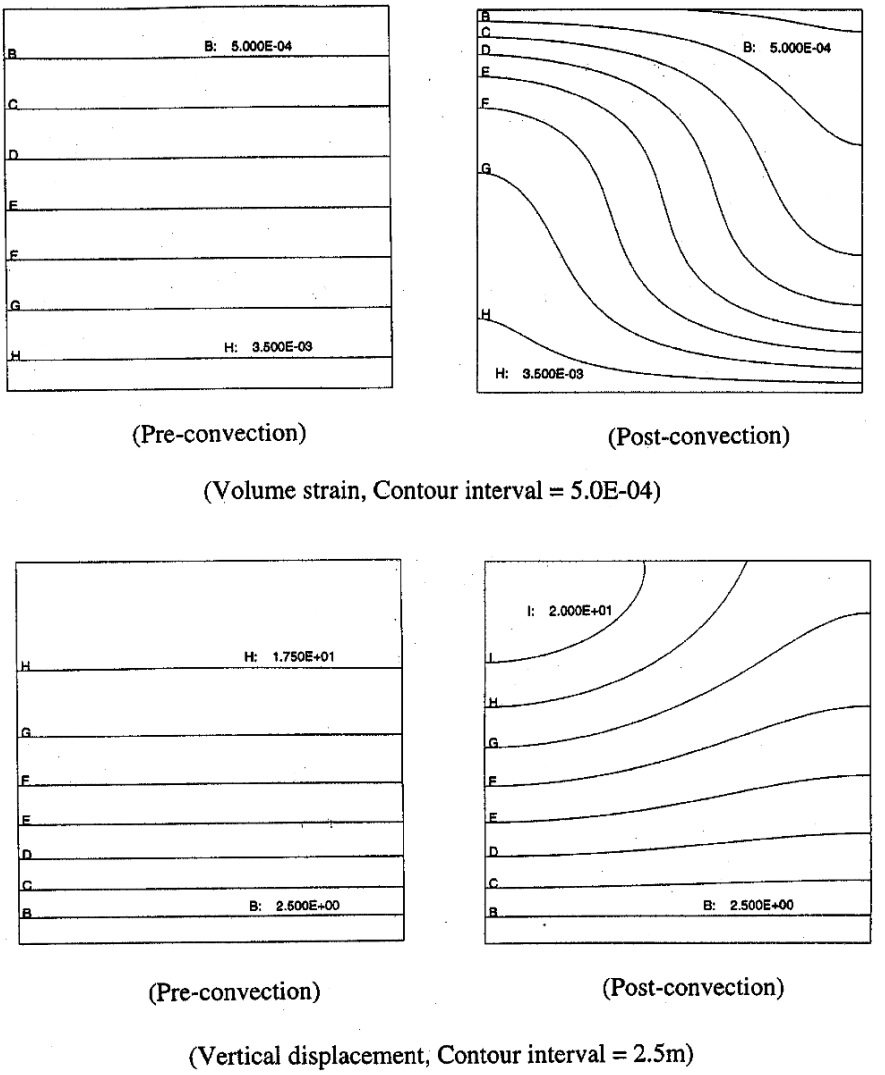

Fig. 5.12 Effect of material thermoelasticity on distributions of volume strain and vertical displacement

5.3 The Influence of Pore-Fluid Viscosity on Convective Heat Transfer in a Heterogeneous Crust

If the pore-fluid viscosity is dependent on temperature only, it can vary with depth in the crust because of the depth-dependent temperature distribution. In this situation, heterogeneity within the crust is due to the variation of the pore-fluid viscosity with depth. Since convective heat transfer within the crust is caused by convective

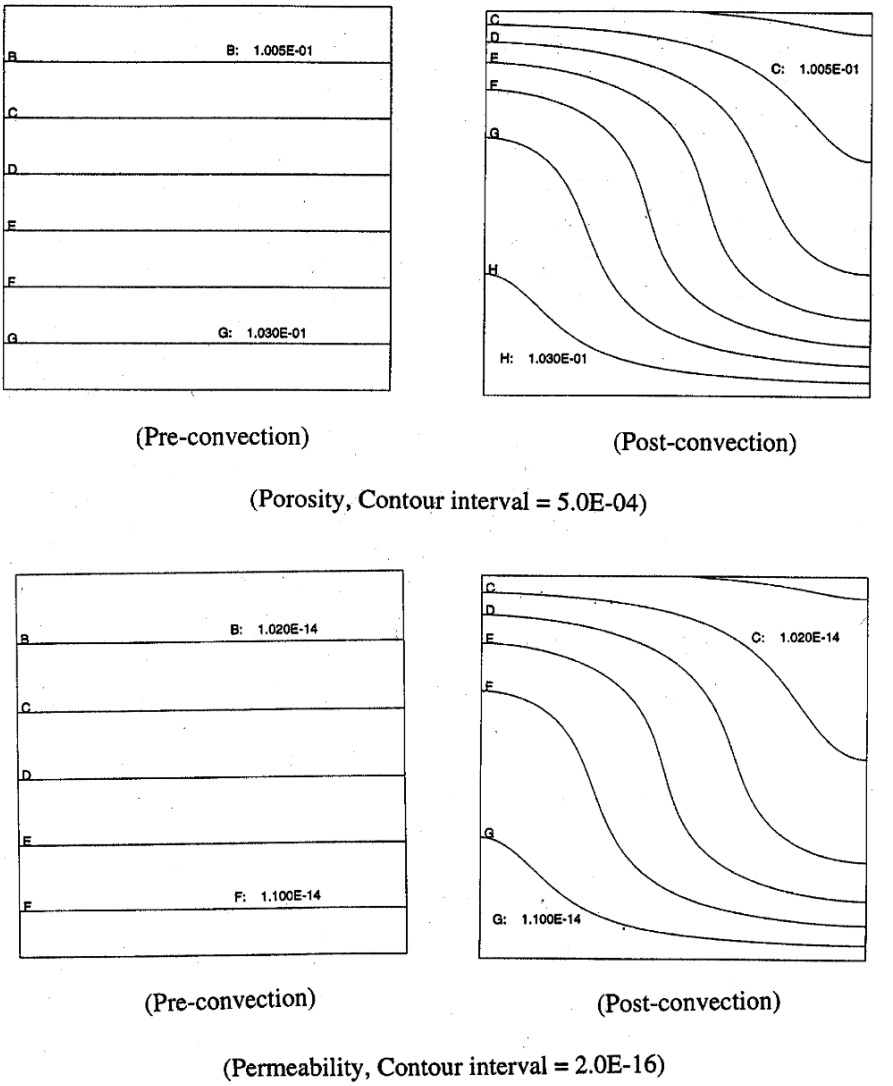

Fig. 5.13 Effect of material thermoelasticity on distributions of porosity and permeability

instability of the pore-fluid, it is useful to investigate the effect of temperature-dependent viscosity on convective instability (Lin et al. 2003).

5.3.1 Statement of the Problem

The hydrothermal system considered is a horizontal layer of infinite length and thickness, H, with temperature-dependent viscosity in a fluid-saturated porous medium. The boundary conditions are constant temperature and zero Darcy velocity

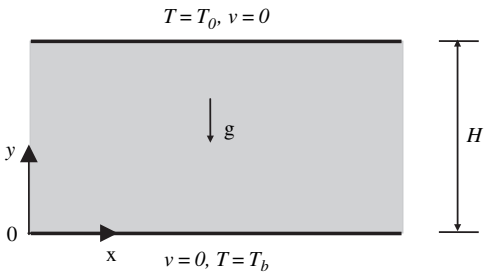

Fig. 5.14 Geometry and boundary conditions for a hydrothermal system

at both the top and bottom of the layer (see Fig. 5.14). The steady state governing equations for this hydrothermal system are expressed as (Phillips 1991; Nield and Bejan 1992):

$$\frac{\partial u}{\partial x}+\frac{\partial v}{\partial y}=0, \tag{5.55}$$

$$u=\frac{K_x}{\mu}\left(-\frac{\partial P}{\partial x}\right), \tag{5.56}$$

$$v=\frac{K_y}{\mu}\left(-\frac{\partial P}{\partial y}+\rho_f g\right), \tag{5.57}$$

$$\rho_{f0}c_p\left(u\frac{\partial T}{\partial x}+v\frac{\partial T}{\partial y}\right)=\lambda_{ex}\frac{\partial^2 T}{\partial x^2}+\lambda_{ey}\frac{\partial^2 T}{\partial y^2}, \tag{5.58}$$

$$\rho_f=\rho_{f0}[1-\beta_T(T-T_0)], \tag{5.59}$$

$$\lambda_{ex}=\phi\lambda_{fx}+(1-\phi)\lambda_{sx},\quad \lambda_{ey}=\phi\lambda_{fy}+(1-\phi)\lambda_{sy}, \tag{5.60}$$

$$\mu=\mu_0 e^{-\alpha(T-T_0)}, \tag{5.61}$$

where u and v are the horizontal and vertical velocity components of the pore-fluid in the x and y directions respectively; P is the pore-fluid pressure; T is the temperature of the crustal material; K_x and K_y are the permeabilities of the crustal material in the x and y directions, respectively; μ is the dynamic viscosity of the pore-fluid; μ_0 is the reference dynamic viscosity of the pore-fluid; ρ_f is the density of the pore-fluid and g is the acceleration due to gravity; ρ_{f0} and T_0 are the reference density and temperature; λ_{fx} and λ_{sx} are the thermal conductivities of the pore-fluid and rock mass in the x direction; λ_{fy} and λ_{sy} are the thermal conductivities of the pore-fluid and rock mass in the y direction; c_p is the specific heat of the pore-fluid; ϕ and β_T are the porosity of the crustal material and the thermal volume expansion coefficient of the pore-fluid, and α is a material constant.

The boundary conditions of the problem can be expressed as

$$T=T_0,\quad v=0\quad (\text{at } y=H), \tag{5.62}$$

$$T = T_b, \quad v = 0 \quad (\text{at } y = 0), \tag{5.63}$$

where T_0 and T_b are temperatures at the top and bottom of the hydrothermal system.

Note that if the porous medium comprising the layer is homogeneous and isotropic, (5.55), (5.56), (5.57) and (5.58) can be written in the following dimensionless form:

$$\frac{\partial u^*}{\partial x^*} + \frac{\partial v^*}{\partial y^*} = 0, \tag{5.64}$$

$$e^{-(\alpha\Delta T)(1-y^*)}u^* = -\frac{\partial P^*}{\partial x^*} + Ra_T T^* e_1, \tag{5.65}$$

$$e^{-(\alpha\Delta T)(1-y^*)}v^* = -\frac{\partial P^*}{\partial y^*} + Ra_T T^* e_2, \tag{5.66}$$

$$u^*\frac{\partial T^*}{\partial x^*} + v^*\frac{\partial T^*}{\partial y^*} = \frac{\partial^2 T^*}{\partial x^{*2}} + \frac{\partial^2 T^*}{\partial y^{*2}}, \tag{5.67}$$

where $\boldsymbol{e}$ is a unit vector and $\boldsymbol{e} = e_1\boldsymbol{i} + e_2\boldsymbol{j}$ for a two-dimensional problem; Ra_T is the Rayleigh number, defined in this particular case as

$$Ra_T = \frac{(\rho_{f0}c_p)\rho_{f0}g\beta\Delta T K_h H}{\mu\lambda_{e0}}. \tag{5.68}$$

Other dimensionless variables are defined as

$$x^* = \frac{x}{H}, \quad y^* = \frac{y}{H}, \quad T^* = \frac{T - T_0}{\Delta T}, \tag{5.69}$$

$$u^* = \frac{H\rho_{f0}c_p}{\lambda_{e0}}u, \quad v^* = \frac{H\rho_{f0}c_p}{\lambda_{e0}}v, \quad P^* = \frac{K_h\rho_{f0}c_p}{\mu\lambda_{e0}}(P - P_0), \tag{5.70}$$

$$\Delta T = T_b - T_0, \tag{5.71}$$

where x^* and y^* are the dimensionless coordinates; u^* and v^* are the dimensionless velocity components in the x and y directions, respectively; P^* and T^* are the dimensionless excess pressure and temperature; K_h is a reference medium permeability coefficient in the horizontal direction; λ_{e0} is a reference thermal conductivity coefficient of the porous medium; ΔT is the temperature difference between the bottom and top boundaries of the porous medium; H is a reference length, and P_0 is the static pore-fluid pressure.

It is noted that in (5.67), the conductive dimensionless temperature in the hydrothermal system was expressed as

$$T^* = 1 - y^*. \tag{5.72}$$

The boundary conditions of the problem in (5.62) and (5.63) can also be written in the dimensionless form as

$$T^* = 0, \qquad v^* = 0 \qquad (\text{at } y^* = 1), \tag{5.73}$$

$$T^* = 1, \qquad v^* = 0 \qquad (\text{at } y^* = 0). \tag{5.74}$$

5.3.2 Derivation of Analytical Solutions

Using the dimensionless streamline function, (5.64) can be automatically satisfied. Note that (5.65) and (5.66) can be further expressed as follows:

$$e^{-(\alpha\Delta T)(1-y^*)}\frac{\partial u^*}{\partial y^*} + (\alpha\Delta T)u^* e^{-(\alpha\Delta T)(1-y^*)} + \frac{\partial^2 P^*}{\partial x^* \partial y^*} = 0, \tag{5.75}$$

$$e^{-(\alpha\Delta T)(1-y^*)}\frac{\partial v^*}{\partial x^*} + \frac{\partial^2 P^*}{\partial y^* \partial x^*} = Ra_T \frac{\partial T^*}{\partial x^*}. \tag{5.76}$$

Subtracting (5.76) from (5.75) yields the following equation:

$$e^{-(\alpha\Delta T)(1-y^*)}\left[\left(\frac{\partial u^*}{\partial y^*} - \frac{\partial v^*}{\partial x^*}\right) + (\alpha\Delta T)\,u^*\right] = -Ra_T \frac{\partial T^*}{\partial x^*}. \tag{5.77}$$

Equation (5.77) can be also expressed as follows:

$$e^{-(\alpha\Delta T)(1-y^*)}\left[\left(\frac{\partial^2 \psi^*}{\partial y^{*2}} + \frac{\partial^2 \psi^*}{\partial x^{*2}}\right) + (\alpha\Delta T)\frac{\partial \psi^*}{\partial y^*}\right] = -Ra_T \frac{\partial T^*}{\partial x^*}, \tag{5.78}$$

where

$$\psi^* = \frac{\rho_0 c_p}{\lambda_{e0}}\psi, \quad u^* = \frac{\partial \psi^*}{\partial y^*}, \quad v^* = -\frac{\partial \psi^*}{\partial x^*}. \tag{5.79}$$

It is noted that if the streamline function is used to replace the related governing equations (i.e., (5.55), (5.56), (5.57) and (5.58)) in the beginning of this chapter, the analytical procedure may be slightly simplified. However, since (5.55), (5.56), (5.57) and (5.58) are the basic governing equations of the problem, the streamline function concept is only employed at this stage.

Using the dimensionless streamline function, (5.67) can be expressed as

$$\frac{\partial \psi^*}{\partial x^*} = \frac{\partial^2 T^*}{\partial x^{*2}} + \frac{\partial^2 T^*}{\partial y^{*2}}. \tag{5.80}$$

Solutions to ψ^* and T^* in (5.78) and (5.80) are of the following forms:

$$\psi^* = f(y^*)\sin\left(q\frac{x^*}{L^*}\right) \qquad (q = m\pi, m = 1,2,3,\ldots\ldots), \tag{5.81}$$

$$T^* = \theta(y^*)\cos\left(q\frac{x^*}{L^*}\right) + (1-y^*) \qquad (q = m\pi, m = 1,2,3,\ldots\ldots), \tag{5.82}$$

where $f(y^*)$ and $\theta(y^*)$ are two functions to be determined; $L^* = L/H$ is the dimensionless half wavelength in the horizontal direction, while L is the physical half wavelength in the horizontal direction. Substituting (5.81) and (5.82) into (5.78) and (5.80) yields the following equations:

$$e^{-(\alpha\Delta T)(1-y^*)}\left[f''(y^*) - \left(\frac{q}{L^*}\right)^2 f(y^*) + (\alpha\Delta T) f'(y^*)\right] = \frac{q}{L^*} Ra_T \theta(y^*), \quad (5.83)$$

$$\frac{q}{L^*} f(y^*) = -\left(\frac{q}{L^*}\right)^2 \theta(y^*) + \theta''(y^*). \quad (5.84)$$

Combining (5.83) and (5.84) leads to an equation containing $\theta(x_2^*)$ only:

$$\theta^{IV}(y^*) + \alpha\Delta T\theta'''(y^*) - 2\left(\frac{q}{L^*}\right)^2 \theta''(y^*) - \alpha\Delta T\left(\frac{q}{L^*}\right)^2 \theta'(y^*) + \left(\frac{q}{L^*}\right)^4 \theta(y^*) = Ra_T\left(\frac{q}{L^*}\right)^2 e^{\alpha\Delta T(1-y^*)}\theta(y^*). \quad (5.85)$$

To solve (5.85) analytically, the following equations are needed:

$$\theta = \theta_0 + \alpha\theta_1 + O(\alpha^2), \quad Ra_T = Ra_{T0} + \alpha Ra_{T1} + O(\alpha^2), \quad (5.86)$$

$$e^{\alpha\Delta T(1-y^*)} = 1 + \alpha\Delta T(1-y^*) + O\{[\alpha\Delta T(1-y^*)]^2\}. \quad (5.87)$$

Substituting (5.86) and (5.87) into (5.85) yields the following two equations for α^0 and α^1 terms, respectively.

$$\theta_0^{IV}(y^*) - 2\left(\frac{q}{L^*}\right)^2 \theta_0''(y^*) + \left(\frac{q}{L^*}\right)^4 \theta_0(y^*) = Ra_{T0}\left(\frac{q}{L^*}\right)^2 \theta_0(y^*), \quad (5.88)$$

$$\theta_1^{IV}(y^*) - 2\left(\frac{q}{L^*}\right)^2 \theta_1''(y^*) + \left(\frac{q}{L^*}\right)^4 \theta_1(y^*) - Ra_{T0}\left(\frac{q}{L^*}\right)^2 \theta_1(y^*) = -\Delta T\theta_0'''(y^*) + \Delta T\left(\frac{q}{L^*}\right)^2 \theta_0'(y^*) + [Ra_{T0}\Delta T(1-y^*) + Ra_{T1}]\left(\frac{q}{L^*}\right)^2 \theta_0(y^*). \quad (5.89)$$

It is clear that (5.88) and (5.89) can be solved sequentially. Once a non-zero solution for $\theta_0(y^*)$ is obtained, it can be substituted into (5.89) to find a non-zero solution for $\theta_1(y^*)$. For this purpose, it is noted that the non-zero solution satisfying both (5.88) and the related boundary conditions in (5.73) and (5.74) can be expressed as

$$\theta_0(y^*) = \sin(ry^*) \qquad (r = n\pi, n = 1, 2, 3, \ldots\ldots). \quad (5.90)$$

Using this equation, the condition under which the non-zero solution exists for (5.88) is derived and expressed as

$$Ra_{T0}|_{critical} = \left(\frac{L^*}{q}r^2 + \frac{q}{L^*}\right)^2 = \left(\frac{n^2}{m}L^* + \frac{m}{L^*}\right)^2 \pi^2 \quad (m = 1,2,3,\ldots\ldots, n = 1,2,3,\ldots\ldots). \tag{5.91}$$

Note that the zero-order critical Rayleigh number expressed in (5.91) is exactly the same as that of a hydrothermal system with constant viscosity (Zhao et al. 1997). Therefore, the effect of temperature-dependent viscosity on temperature gradient driven convective flow can be determined by the first-order critical Rayleigh number of the hydrothermal system with temperature-dependent viscosity.

Next, we will deduce the first-order critical Rayleigh number of the hydrothermal system with temperature-dependent viscosity. Substituting (5.90) into (5.89) yields the following equation:

$$\begin{aligned}
&\theta_1{}^{IV}(y^*) - 2\left(\frac{q}{L^*}\right)^2 \theta_1{}''(y^*) + \left(\frac{q}{L^*}\right)^4 \theta_1(y^*) - Ra_{T0}\left(\frac{q}{L^*}\right)^2 \theta_1(y^*) \\
&= \left[r^3 + \left(\frac{q}{L^*}\right)^2 r\right] \Delta T \cos(ry^*) + [Ra_{T0}\Delta T(1-y^*)]\left(\frac{q}{L^*}\right)^2 \sin(ry^*) \\
&\quad + Ra_{T1}\left(\frac{q}{L^*}\right)^2 \sin(ry^*).
\end{aligned} \tag{5.92}$$

In order to determine the first-order critical Rayleigh number, we need to find a non-zero solution for $\theta_1(y^*)$. For this purpose, it is noted that the non-zero solution satisfying both (5.92) and the related boundary conditions in (5.73) and (5.74) can be expressed as

$$\theta_1(y^*) = a_1 y^* \sin(ry^*) + a_2 y^*(1-y^*)\cos(ry^*). \tag{5.93}$$

Substituting (5.93) into (5.92) yields the following equations:

$$8a_2\left[r^3 + \left(\frac{q}{L^*}\right)^2 r\right] = Ra_{T0}\left(\frac{q}{L^*}\right)^2 \Delta T, \tag{5.94}$$

$$4\left[3r^2 + \left(\frac{q}{L^*}\right)^2\right] a_2 - 4a_1\left[r^3 + r\left(\frac{q}{L^*}\right)^2\right] = \left[r^3 + \left(\frac{q}{L^*}\right)^2 r\right] \Delta T, \tag{5.95}$$

$$4a_2 r\left[r^2 + \left(\frac{q}{L^*}\right)^2\right] = (Ra_{T0}\Delta T + Ra_{T1})\left(\frac{q}{L^*}\right)^2. \tag{5.96}$$

It is noted that (5.94), (5.95) and (5.96) are obtained by considering the coefficients in front of $y^* \sin(ry^*)$ term, $\cos(ry^*)$ term and $\sin(ry^*)$ term, respectively.

From (5.94), (5.95) and (5.96), a_1, a_2 and R_{aT1}; can be straightforwardly expressed as follows:

$$a_2 = \frac{\left[r^2 + \left(\frac{q}{L^*}\right)^2\right] \Delta T}{8r}, \tag{5.97}$$

$$a_1 = \frac{4\left[3r^2 + \left(\frac{q}{L^*}\right)^2\right] a_2 - \left[r^3 + \left(\frac{q}{L^*}\right)^2 r\right] \Delta T}{4r\left[r^2 + \left(\frac{q}{L^*}\right)^2\right]}, \tag{5.98}$$

$$Ra_{T1}|_{critical} = -\frac{1}{2} Ra_{T0} \Delta T. \tag{5.99}$$

Finally, the total critical Rayleigh number of the hydrothermal system with temperature-dependent viscosity is expressed as

$$Ra_T|_{critical} = Ra_{T0}|_{critical} + \alpha\, Ra_{T1}|_{critical} + O(\alpha^2). \tag{5.100}$$

If the viscosity of pore-fluid is constant, namely $\alpha = 0$, (5.100) degenerates to the previous solution for a hydrothermal system with constant viscosity (Zhao et al. 1997). Since $Ra_{T1}|_{critical}$ is less than zero, it is immediately recognized that the effect of temperature-dependent viscosity is to destabilize temperature gradient driven convective flow in a hydrothermal system. In other words, temperature gradient driven convective flow is easier when temperature-dependent viscosity is considered in a hydrothermal system.

It is also noted that if the coefficient, α, is large enough, the effect of the second term on the right-hand side of (5.100) may become very important, indicating that some new physical phenomenon may occur in the corresponding case. However, for real geological systems in the upper crust of the Earth, the coefficient, α, is usually a very small number, so that the first term on the right-hand side of (5.100) always plays a dominant role in real geological systems.

From the previous analytical solutions (Zhao et al. 1997), the hydrothermal system with constant viscosity has a minimum critical Rayleigh number of $4\pi^2$. This will happen when $L^* = 1$ and $q = r = \pi$. However, for the same hydrothermal system but with temperature-dependent viscosity, the minimum critical Rayleigh number is reduced to about 36 if the product of α and ΔT is 0.2 in the system. This recognition can be used to test the progressive asymptotic approach procedure (Zhao et al. 1997) associated with the finite element method (Zienkiewicz 1977; Lewis and Schrefler 1998) when it is used to solve this kind of convective instability problem. For this purpose, a square domain of unit length is discretized by finite elements (see Fig. 5.15). This means that symmetrical boundary conditions are considered between two fundamental convective cells. If periodic boundary conditions are used to consider the general aspect of multiple fundamental convective cells, the horizontal length of the model should be extended, but this is beyond the range of this study. The Rayleigh number used in the computation is 36. Two cases are considered: one is with constant viscosity and another is with temperature-dependent viscosity, in which the product of α and ΔT is 0.2. As expected, in the case of the hydrothermal system with constant viscosity, convective pore-fluid flow does not take place, but in the case of the same system with temperature-dependent viscosity, convective pore-fluid flow does take place. This indicated that the previously developed progressive asymptotic approach is also applicable to the solution of convective pore-fluid flow problems in hydrothermal systems with temperature-dependent viscosity.

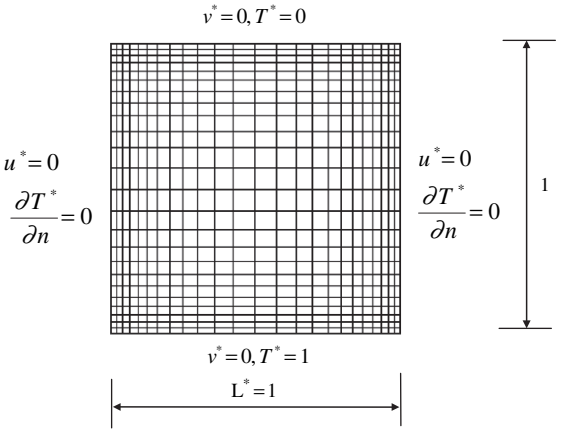

Fig. 5.15 Finite element mesh for the problem

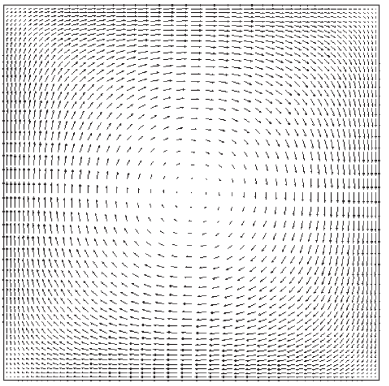

(Constant viscosity)

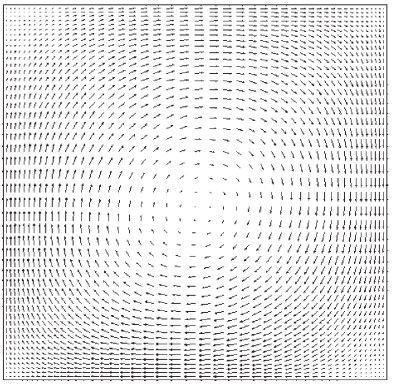

(Temperature-dependent viscosity)

Fig. 5.16 Distributions of the dimensionless pore-fluid velocities

Next, the progressive asymptotic approach procedure (Zhao et al. 1997) associated with the finite element method (Zienkiewicz 1977; Lewis and Schrefler 1998) is used to examine the effect of temperature-dependent viscosity on the distribution patterns of pore-fluid flow, streamlines and temperature in a hydrothermal system. The same computational model as in Fig. 5.15 is used, but the Rayleigh number is 40 for the forthcoming computations. Two cases, one with constant viscosity and another with temperature-dependent viscosity, are also considered in the numerical analysis. The product of α and ΔT is 0.5 for the case of temperature-dependent viscosity.

Figures 5.16, 5.17 and 5.18 show the distributions of the dimensionless pore-fluid velocity, streamlines and temperature for the hydrothermal systems with constant viscosity and temperature-dependent viscosity, respectively. Although convective pore-fluid flow takes place in both cases, convective pore-fluid flow in the case of

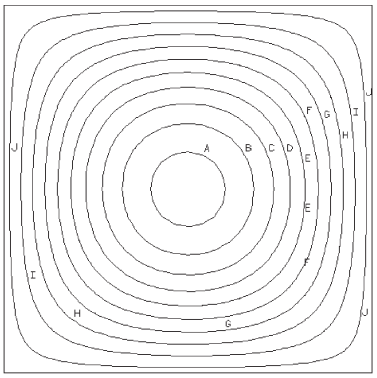

LEGEND
A - -.6711E+00
B - -.6005E+00
C - -.5298E+00
D - -.4592E+00
E - -.3885E+00
F - -.3179E+00
G - -.2472E+00
H - -.1766E+00
I - -.1060E+00
J - -.3532E-01

(Constant viscosity)

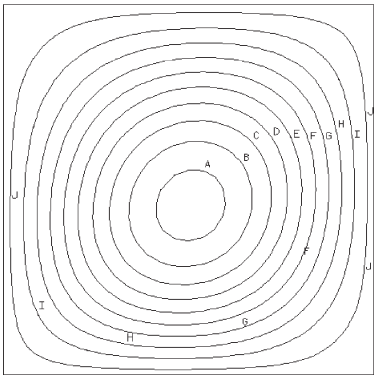

LEGEND
A - -.1370E+01
B - -.1225E+01
C - -.1081E+01
D - -.9367E+00
E - -.7924E+00
F - -.6480E+00
G - -.5037E+00
H - -.3594E+00
I - -.2150E+00
J - -.7071E-01

(Temperature-dependent viscosity)

Fig. 5.17 Distributions of dimensionless streamlines

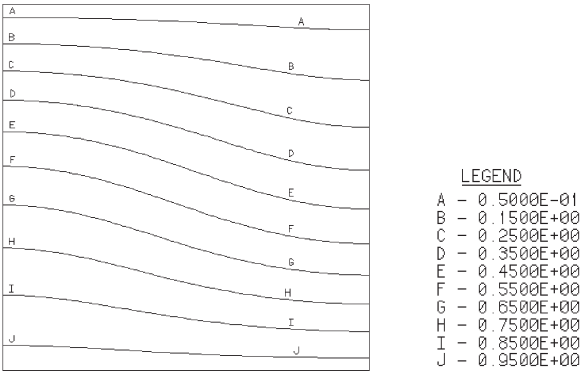

(Constant viscosity)

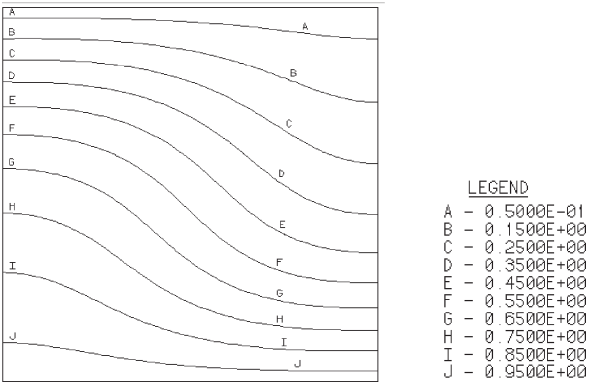

(Temperature-dependent viscosity)

Fig. 5.18 Distributions of dimensionless temperature

temperature-dependent viscosity is stronger than that in the case of constant viscosity. For instance, in the case of temperature-dependent viscosity, the maximum dimensionless velocity which occurs only at the bottom part of the system is 4.909, while in the case of constant viscosity, the equivalent maximum dimensionless velocity is 2.301. This further indicates that temperature-dependent viscosity destabilizes convective pore-fluid flow in hydrothermal systems. In other words, since the viscosity of the pore-fluid decreases with an increase in the temperature, the viscosity of the pore-fluid in the bottom part of a hydrothermal system becomes smaller than that in the top part of the system. As a result, convective pore-fluid flow becomes much stronger in the bottom part of the hydrothermal system.

Chapter 6
Pore-Fluid Focusing within Two-Dimensional Faults and Cracks of Crustal Scales with No Temperature Effects: Solutions Expressed in a Local Coordinate System

Large cracks and faults play an important and diverse role in controlling pore-fluid flow patterns in pore-fluid saturated porous rocks (Toth 1962; Person and Baumgartner 1995; Wieck et al. 1995; Zhao and Valliappan 1994a, b; Person et al. 1996; Roberts et al. 1996; Connolly 1997; Jamtveit and Yardley 1997; Zhao et al. 1999b, 2001b, 2002a; Hoaglund and Pollard 2003; Matthai 2003). Examples of fault-related fluid flow include (1) geological structural controls on groundwater flow and contaminant transport, (2) formation and localization of some valuable mineral deposits around and within fault zones, (3) impacts of heterogeneous fault zone hydraulic properties on the formation and location of petroleum reservoirs through fault sealing, compartmentalization and variability in pore-fluid flow pathways and (4) induced rupture and failure processes by the interaction between material deformation and pore-fluid flow around and within faults through cycles of brittle deformation and seismicity. For these reasons, a better understanding of the pore-fluid flow pattern around and within large cracks and faults in pore-fluid saturated porous rocks has become an important research topic in numerous Earth science disciplines.

To understand pore-fluid flow patterns around and within large cracks and faults, it is fundamentally important to understand and recognize the underlying physical processes that influence pore-fluid flow patterns around and within these structures. Toward this end, fundamental scientific principles can be used to describe the pore-fluid flow process in pore-fluid saturated porous rocks. Since analytical solutions can be used to investigate the general behavior of pore-fluid flow patterns around large cracks and faults within the whole parameter space of the system, general conclusions can be drawn about the problems associated with pore-fluid flow patterns around and within these structures. However, since it is often impossible to use numerical solutions to investigate the behaviors of pore-fluid flow patterns around large cracks and faults within the whole parameter space, which is usually of infinite nature, numerical solutions can only produce specific conclusions for the problem. Therefore, in order to draw general conclusions for the problem associated with pore-fluid flow patterns around and within large cracks and faults, analytical solutions, if available, are always superior to numerical solutions. On the other hand, analytical solutions to benchmark problems provide an important and often unique tool for validating and verifying numerical methods and algorithms, which are used to solve problems with complicated geometries. However, it is always difficult, if not

C. Zhao et al., *Convective and Advective Heat Transfer in Geological Systems*,

© Springer-Verlag Berlin Heidelberg 2008

impossible, to mathematically derive analytical solutions to a set of simultaneous partial differential equations, even with simple geometry and boundary conditions. For this reason, numerical methods have been widely used to investigate pore-fluid flow patterns around and within large cracks and faults in pore-fluid saturated porous rocks (Ohnishi et al. 1985; Jiao and Hudson 1995; Person and Baumgartner 1995; Wieck et al. 1995; Person et al. 1996; Roberts et al. 1996; Bower and Zyvoloski 1997; Thomas et al. 1998; Zhao et al. 1997, 1998c; Hoaglund and Pollard 2003; Matthai 2003).

For a prolate spheroid embedded in a full space, an analytical potential function solution is available for the three-dimensional Laplace's equation (Webster 1897; Morse and Feshbach 1953). This analytical solution was applied to the steady state heat conduction problem (Carslaw and Jaeger 1959) and steady state pore-fluid flow problem (Toth 1962) around such a spheroid. Although the embedded prolate spheroid and the surrounding rocks can have different permeabilities, the analytical solution to such a prolate spheroid may only be suitable for describing the pore-fluid pattern around a geological lens, both the short axes of which can be assumed to be approximately the same length. Since the length of a geological fault in the strike direction is significantly different from that in its thickness direction, it is reasonable to treat the fault as an elliptical inclusion in a two-dimensional full plane, at least from the mathematical point of view. Toward this end, Lamb (1975) and Phillips (1991) presented the analytical solutions for the steady state pore-fluid flow problem around both a perfectly permeable elliptical fault and a perfectly impermeable elliptical fault embedded in a two-dimensional full plane. Because the fundamental solution (i.e., the Green's function) of a three-dimensional Laplace's equation is significantly different from that of a two-dimensional one, a full set of analytical solutions is not available for pore-fluid flow around and within an elliptical fault, which has any finite, but non-zero value of permeability and is embedded in a two-dimensional full plane. Therefore, the major purpose of this chapter is to derive a full set of analytical solutions for pore-fluid flow patterns around and within an *inclined* elliptical fault with *any value of the permeability* in a two-dimensional full plane (Zhao et al. 2006a, b).

6.1 Description of the Problem

To derive analytical solutions, large cracks and faults are assumed to be of elliptical shape so that they can be treated as embedded elliptical inclusions in pore-fluid saturated porous rocks. Both the pore-fluid flow channeling and sealing effects of an elliptical inclusion can be considered by allowing the material properties of the inclusion to be different from those of the surrounding rocks. For instance, if the permeability of an elliptical inclusion is greater than that of the surrounding rock, the inclusion will function as an enhanced pore-fluid flow channel. On the contrary, if the permeability of an inclusion is smaller than that of its surrounding rock, the inclusion will function as an isolated pore-fluid flow seal. Since the size of an elliptical

inclusion is a free parameter, the derived analytical solution to pore-fluid flow patterns around and within the elliptical inclusion is valid for dealing with pore-fluid flow patterns around and within large cracks and faults. This is one of the main advantages of an analytical solution over a numerical one in dealing with pore-fluid flow problems in pore-fluid saturated porous rocks.

As shown in Fig. 6.1A, we consider an isolated elliptical inclusion in pore-fluid saturated porous rocks to derive the analytical solution. We assume that the problem domain is comprised of pore-fluid saturated porous rocks, although the permeability of the inclusion is different from that of the surrounding rock. We also assume that the pore-fluid flow in the far field away from the inclusion is uniform and is parallel to the long axis of the elliptical inclusion in the first case (i.e., Fig. 6.1A). This implies that pore-fluid pressure gradients are constant and zero in the x and y directions, if the system is not disturbed by the elliptical inclusion. If the pore-fluid is incompressible, the steady state governing equations for such a problem can be expressed in the Cartesian coordinate system as

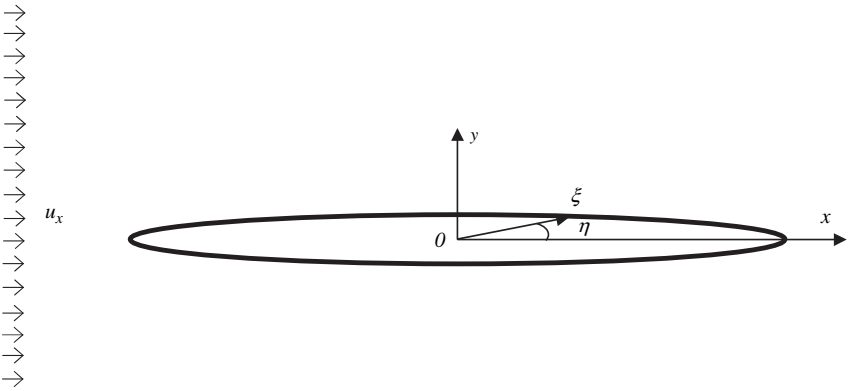

A (The long axis of the inclusion is parallel to the inflow in the far field)

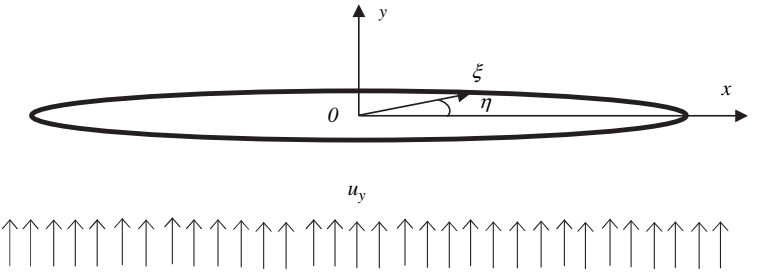

B (The short axis of the inclusion is parallel to the inflow in the far field)

Fig. 6.1 Description of an elliptical inclusion in two coordinate systems

$$\frac{\partial u_x}{\partial x} + \frac{\partial u_y}{\partial y} = 0, \tag{6.1}$$

$$u_x = -\frac{K}{\mu}\frac{\partial p}{\partial x}, \tag{6.2}$$

$$u_y = -\frac{K}{\mu}\frac{\partial p}{\partial y}, \tag{6.3}$$

where u_x and u_y are the velocity components in the x and y directions; p is the excess pore-fluid pressure (i. e., the total pore-fluid pressure minus the hydrostatic pressure); μ is the dynamic viscosity of pore-fluid, and K is the permeability of the porous rock mass. Note that $K = K_{in}$ for the elliptical inclusion and $K = K_{out}$ for the surrounding rock, where K_{in} and K_{out} are the permeabilities of the inclusion and the surrounding rock, respectively.

Equation (6.1) is the continuity equation of the pore-fluid, while (6.2) and (6.3) are Darcy's equations to describe the pore-fluid flow in porous media. Since excess pore-fluid pressure is used, gravity is not included in (6.3). If the xy plane is a horizontal one, there is no need to consider gravity in (6.3), because gravity is perpendicular to this xy plane. If the xy plane is a vertical one, it is not necessary to consider gravity in (6.3), as long as the inflow in the far field is driven by non-buoyancy mechanisms such as topography, metamorphic reaction, devolatilization and so forth (Person et al. 1996). However, if the xy plane is vertical and the inflow is driven by the buoyancy of the pore-fluid, it is necessary to consider gravity in (6.3). This may be one deficiency of this theoretical investigation.

Substituting (6.2) and (6.3) into (6.1) leads to

$$\frac{\partial^2 p}{\partial x^2} + \frac{\partial^2 p}{\partial y^2} = 0. \tag{6.4}$$

6.2 Derivation of Governing Equations of the Problem in a Local Elliptical $\xi\eta$ Coordinate System

To facilitate the derivation of analytical solutions for the problem considered, we rewrite (6.4) in a local elliptical $\xi\eta$ coordinate system using the following coordinate mappings:

$$x = c\cosh\xi\cos\eta, \qquad y = c\sinh\xi\sin\eta, \tag{6.5}$$

where c is an arbitrary non-zero positive constant, the physical meaning of which, as can be demonstrated, is half the focal distance of an ellipse. This means that different sizes of similar ellipses can be represented by choosing different values of c.

Since c is an arbitrary non-zero positive constant, instead of a constant of unity, the analytical solutions derived in this section are suitable for investigating pore-fluid flow focusing within elliptical faults and cracks of any length scales. This is the

main difference between the present analytical solutions and previous ones (Zhao et al. 2006a), because the previous solutions were derived under the assumption that the focal distance of the ellipse is a constant of 2.

Because the coordinate mapping expressed by (6.5) is a conformal one, the form of the governing equation expressed in (6.4) remains the same when it is transformed into the local elliptical $\xi\eta$ coordinate system. For the sake of completeness, the transformation of (6.4) from the Cartesian coordinate system into the local elliptical $\xi\eta$ coordinate one is given below. However, if one is familiar with conformal mapping, the rest of this section may be skipped.

Using the coordinate mapping relationship expressed in (6.5), the following equation can be obtained in a matrix form:

$$\begin{Bmatrix} \dfrac{\partial p}{\partial \xi} \\ \dfrac{\partial p}{\partial \eta} \end{Bmatrix} = \begin{bmatrix} \dfrac{\partial x}{\partial \xi} & \dfrac{\partial y}{\partial \xi} \\ \dfrac{\partial x}{\partial \eta} & \dfrac{\partial y}{\partial \eta} \end{bmatrix} \begin{Bmatrix} \dfrac{\partial p}{\partial x} \\ \dfrac{\partial p}{\partial y} \end{Bmatrix} = [A] \begin{Bmatrix} \dfrac{\partial p}{\partial x} \\ \dfrac{\partial p}{\partial y} \end{Bmatrix}, \tag{6.6}$$

where

$$\begin{aligned} \frac{\partial x}{\partial \xi} &= c \sinh \xi \cos \eta, \qquad & \frac{\partial x}{\partial \eta} &= -c \cosh \xi \sin \eta, \\ \frac{\partial y}{\partial \xi} &= c \cosh \xi \sin \eta, \qquad & \frac{\partial y}{\partial \eta} &= c \sinh \xi \cos \eta. \end{aligned} \tag{6.7}$$

Using (6.7), the determinant value of matrix A in (6.6) can be expressed as

$$|A| = \frac{\partial x}{\partial \xi}\frac{\partial y}{\partial \eta} - \frac{\partial x}{\partial \eta}\frac{\partial y}{\partial \xi} = c^2 \left(\sinh^2 \xi \cos^2 \eta + \cosh^2 \xi \sin^2 \eta\right) \neq 0. \tag{6.8}$$

This indicates that matrix A is invertible so that

$$\begin{Bmatrix} \dfrac{\partial p}{\partial x} \\ \dfrac{\partial p}{\partial y} \end{Bmatrix} = \frac{\begin{bmatrix} \sinh \xi \cos \eta & -\cosh \xi \sin \eta \\ \cosh \xi \sin \eta & \sinh \xi \cos \eta \end{bmatrix}}{\sinh^2 \xi \cos^2 \eta + \cosh^2 \xi \sin^2 \eta} \begin{Bmatrix} \dfrac{\partial p}{\partial \xi} \\ \dfrac{\partial p}{\partial \eta} \end{Bmatrix}. \tag{6.9}$$

Mathematically, we have the following relationship:

$$\frac{\partial^2 p}{\partial x^2} = \frac{\partial}{\partial \xi}\left(\frac{\partial p}{\partial x}\right)\frac{\partial \xi}{\partial x} + \frac{\partial}{\partial \eta}\left(\frac{\partial p}{\partial x}\right)\frac{\partial \eta}{\partial x}, \tag{6.10}$$

$$\frac{\partial^2 p}{\partial^2 y} = \frac{\partial}{\partial \xi}\left(\frac{\partial p}{\partial y}\right)\frac{\partial \xi}{\partial y} + \frac{\partial}{\partial \eta}\left(\frac{\partial p}{\partial y}\right)\frac{\partial \eta}{\partial y}. \tag{6.11}$$

If we could determine the first derivative terms such as $\partial\xi/\partial x$, $\partial\xi/\partial y$, $\partial\eta/\partial x$ and $\partial\eta/\partial y$ in the full xy plane, then we would determine the second derivative terms, $\partial^2 p/(\partial x^2)$ and $\partial^2 p/(\partial y^2)$, in (6.10) and (6.11). Due to the singularity of $\partial\xi/\partial x$, $\partial\xi/\partial y$, $\partial\eta/\partial x$ and $\partial\eta/\partial y$ in the full xy plane, the second derivative terms,

$\partial^2 p/(\partial x^2)$ and $\partial^2 p/(\partial y^2)$, in (6.10) and (6.11) need to be determined in the following manner.

Using the chain rule in mathematics, we have

$$\frac{\partial^2 p}{\partial \xi^2} = \frac{\partial^2 p}{\partial x^2}\left(\frac{\partial x}{\partial \xi}\right)^2 + 2\frac{\partial^2 p}{\partial x \partial y}\frac{\partial x}{\partial \xi}\frac{\partial y}{\partial \xi} + \frac{\partial^2 p}{\partial y^2}\left(\frac{\partial y}{\partial \xi}\right)^2 + \frac{\partial p}{\partial x}\frac{\partial^2 x}{\partial \xi^2} + \frac{\partial p}{\partial y}\frac{\partial^2 y}{\partial \xi^2}, \quad (6.12)$$

$$\frac{\partial^2 p}{\partial \eta^2} = \frac{\partial^2 p}{\partial x^2}\left(\frac{\partial x}{\partial \eta}\right)^2 + 2\frac{\partial^2 p}{\partial x \partial y}\frac{\partial x}{\partial \eta}\frac{\partial y}{\partial \eta} + \frac{\partial^2 p}{\partial y^2}\left(\frac{\partial y}{\partial \eta}\right)^2 + \frac{\partial p}{\partial x}\frac{\partial^2 x}{\partial \eta^2} + \frac{\partial p}{\partial y}\frac{\partial^2 y}{\partial \eta^2}, \quad (6.13)$$

$$\begin{aligned}\frac{\partial^2 p}{\partial \xi \partial \eta} = {} & \frac{\partial^2 p}{\partial x^2}\left(\frac{\partial x}{\partial \xi}\frac{\partial x}{\partial \eta}\right) + \frac{\partial^2 p}{\partial x \partial y}\left(\frac{\partial x}{\partial \xi}\frac{\partial y}{\partial \eta} + \frac{\partial x}{\partial \eta}\frac{\partial y}{\partial \xi}\right) + \frac{\partial^2 p}{\partial y^2}\left(\frac{\partial y}{\partial \xi}\frac{\partial y}{\partial \eta}\right) \\ & + \frac{\partial p}{\partial x}\frac{\partial^2 x}{\partial \xi \partial \eta} + \frac{\partial p}{\partial y}\frac{\partial^2 y}{\partial \xi \partial \eta}. \end{aligned} \quad (6.14)$$

The product of (6.12) and $(\partial x/\partial \eta)(\partial y/\partial \eta)$ minus that of (6.13) and $(\partial x/\partial \xi)$ $(\partial y/\partial \xi)$ yields the following equation:

$$\begin{aligned}\frac{\partial^2 p}{\partial \xi^2}\frac{\partial x}{\partial \eta}\frac{\partial y}{\partial \eta} - \frac{\partial^2 p}{\partial \eta^2}\frac{\partial x}{\partial \xi}\frac{\partial y}{\partial \xi} = {} & \frac{\partial^2 p}{\partial x^2}\frac{\partial x}{\partial \xi}\frac{\partial x}{\partial \eta}\left(\frac{\partial x}{\partial \xi}\frac{\partial y}{\partial \eta} - \frac{\partial x}{\partial \eta}\frac{\partial y}{\partial \xi}\right) \\ & + \frac{\partial^2 p}{\partial y^2}\frac{\partial y}{\partial \xi}\frac{\partial y}{\partial \eta}\left(\frac{\partial x}{\partial \eta}\frac{\partial y}{\partial \xi} - \frac{\partial x}{\partial \xi}\frac{\partial y}{\partial \eta}\right) + \frac{\partial p}{\partial x}\left(\frac{\partial^2 x}{\partial \xi^2}\frac{\partial x}{\partial \eta}\frac{\partial y}{\partial \eta} - \frac{\partial^2 x}{\partial \eta^2}\frac{\partial x}{\partial \xi}\frac{\partial y}{\partial \xi}\right) \\ & + \frac{\partial p}{\partial y}\left(\frac{\partial^2 y}{\partial \xi^2}\frac{\partial x}{\partial \eta}\frac{\partial y}{\partial \eta} - \frac{\partial^2 y}{\partial \eta^2}\frac{\partial x}{\partial \xi}\frac{\partial y}{\partial \xi}\right). \end{aligned} \quad (6.15)$$

From (6.7), we have

$$\frac{\partial x}{\partial \xi}\frac{\partial y}{\partial \xi} = \frac{\partial y}{\partial \xi}\frac{\partial y}{\partial \eta} = -\frac{\partial x}{\partial \eta}\frac{\partial y}{\partial \eta} = -\frac{\partial x}{\partial \xi}\frac{\partial x}{\partial \eta} = c^2 \sinh\xi \cosh\xi \sin\eta \cos\eta, \quad (6.16)$$

$$\frac{\partial^2 x}{\partial \xi^2} = c\cosh\xi\cos\eta, \qquad \frac{\partial^2 x}{\partial \eta^2} = -c\cosh\xi\cos\eta, \quad (6.17)$$

$$\frac{\partial^2 y}{\partial \xi^2} = -c\sinh\xi\sin\eta, \qquad \frac{\partial^2 y}{\partial \eta^2} = -c\sinh\xi\sin\eta, \quad (6.18)$$

Substituting (6.16), (6.17) and (6.18) into the last two terms in the right hand side of (6.15) yields the following equations:

$$\frac{\partial^2 x}{\partial \xi^2}\frac{\partial x}{\partial \eta}\frac{\partial y}{\partial \eta} - \frac{\partial^2 x}{\partial \eta^2}\frac{\partial x}{\partial \xi}\frac{\partial y}{\partial \xi} = 0, \qquad \frac{\partial^2 y}{\partial \xi^2}\frac{\partial x}{\partial \eta}\frac{\partial y}{\partial \eta} - \frac{\partial^2 y}{\partial \eta^2}\frac{\partial x}{\partial \xi}\frac{\partial y}{\partial \xi} = 0. \quad (6.19)$$

Therefore, (6.15) can be written into the following form:

$$\frac{\partial^2 p}{\partial \xi^2}+\frac{\partial^2 p}{\partial \eta^2}=\left(\frac{\partial^2 p}{\partial x^2}+\frac{\partial^2 p}{\partial y^2}\right)\left(\frac{\partial x}{\partial \xi}\frac{\partial y}{\partial \eta}-\frac{\partial x}{\partial \eta}\frac{\partial y}{\partial \xi}\right). \tag{6.20}$$

Considering (6.4), (6.8) and (6.20) simultaneously yields the following equation:

$$\frac{\partial^2 p}{\partial \xi^2}+\frac{\partial^2 p}{\partial \eta^2}=0. \tag{6.21}$$

Equation (6.21) is the governing equation of the excess pore-fluid pressure in the $\xi\eta$ coordinate system.

6.3 Derivation of Analytical Solutions when the Long Axis of an Elliptical Inclusion Is Parallel to the Inflow in the Far Field

In this case, it is assumed that the pore-fluid flow in the far field away from the elliptical inclusion is uniform and parallel to the long axis of the elliptical inclusion in the first case (i.e., Fig. 6.1A). This implies that pore-fluid pressure gradients are constant in the x direction and zero in the y direction, respectively, if the system is not disturbed by the inclusion.

The boundary condition of the pore-fluid flow problem can be expressed in the following form:

$$p_{in}=p_{out} \qquad (\text{at } \xi=\xi_0), \tag{6.22}$$

$$K_{in}\frac{\partial p_{in}}{\partial \xi}=K_{out}\frac{\partial p_{out}}{\partial \xi} \qquad (\text{at } \xi=\xi_0), \tag{6.23}$$

$$\lim_{\xi\to\infty} p_{out}=-\omega_x c\cosh\xi\cos\eta, \tag{6.24}$$

where p_{in} and p_{out} are the excess pore-fluid pressures inside and outside the elliptical inclusion, respectively; ξ_0 is the boundary of the elliptical inclusion; K_{in} and K_{out} are the permeabilities of the porous media inside and outside of the inclusion, and ω_x is the amplitude (i.e., $\left|\partial p/\partial x\right|$ in this particular case) of the excess pore-fluid pressure gradient in the far field of the inclusion.

The general solution to the excess pore-fluid pressure inside and outside the elliptical inclusion can be expressed as

$$p_{in}=-\omega_x c C_1\cosh\xi\cos\eta, \tag{6.25}$$

$$p_{out}=-\omega_x c\cosh\xi\cos\eta+\omega_x C_2 e^{-(\xi-\xi_0)}\cos\eta, \tag{6.26}$$

where C_1 and C_2 are two constants to be determined by the boundary conditions of the problem.

Substituting (6.25) and (6.26) into (6.22) and (6.23) yields:

$$c(1-C_1)\cosh\xi_0 - C_2 = 0, \tag{6.27}$$

$$c\left(\frac{K_{in}}{K_{out}}C_1 - 1\right)\sinh\xi_0 - C_2 = 0. \tag{6.28}$$

Solving (6.27) and (6.28) simultaneously, C_1 and C_2 are determined as

$$C_1 = \frac{\beta+1}{\beta+\alpha}, \qquad C_2 = \frac{(\alpha-1)a}{\beta+\alpha}, \tag{6.29}$$

where β is the aspect ratio of the elliptical inclusion; α is the permeability ratio of the inclusion to the surrounding rock; a is the half-length of the long axis of the elliptical inclusion. These quantities can be defined as

$$\alpha = \frac{K_{in}}{K_{out}}, \qquad \beta = \frac{a}{b} = \frac{c\cosh\xi_0}{c\sinh\xi_0} = \frac{\cosh\xi_0}{\sinh\xi_0}, \qquad a = c\cosh\xi_0 = \frac{c\beta}{\sqrt{\beta^2-1}}, \tag{6.30}$$

where a and b are the half-lengths of the long and short axes of the elliptical inclusion.

Note that the half-lengths of the long and short axes of the elliptical fault are represented by $a = c\cosh\xi_0$ and $b = c\sinh\xi_0$ in the $\xi\eta$ coordinate system, respectively. Since $a^2 - b^2 = c^2$, the physical meaning of c is half the focal distance of the elliptical fault. This means that the aspect ratio of the fault can be represented by the ratio of $c\cosh\xi_0$ to $c\sinh\xi_0$. For the convenience of expression, we define this ratio as $\beta = a/b = (c\cosh\xi_0)/(c\sinh\xi_0) = (\cosh\xi_0)/(\sinh\xi_0)$ hereafter.

Consideration of (6.2), (6.3), (6.9), (6.25) and (6.26) results in the corresponding analytical solution for the pore-fluid velocity:

$$u_x^{in} = \frac{\omega_x C_1 K_{in}}{\mu} \qquad (\xi \le \xi_0), \tag{6.31}$$

$$u_y^{in} = 0 \qquad (\xi \le \xi_0), \tag{6.32}$$

$$u_x^{out} = \frac{\omega_x K_{out}}{\mu}\left[1 + \frac{C_2(\sinh\xi\cos^2\eta - \cosh\xi\sin^2\eta)e^{-(\xi-\xi_0)}}{c(\sinh^2\xi\cos^2\eta + \cosh^2\xi\sin^2\eta)}\right] \qquad (\xi \ge \xi_0), \tag{6.33}$$

$$u_y^{out} = \frac{\omega_x K_{out}}{\mu}\left[\frac{C_2(\cosh\xi\sin\eta\cos\eta + \sinh\xi\sin\eta\cos\eta)e^{-(\xi-\xi_0)}}{c(\sinh^2\xi\cos^2\eta + \cosh^2\xi\sin^2\eta)}\right] \qquad (\xi \ge \xi_0), \tag{6.34}$$

where the superscripts, *in* and *out*, represent the inside and outside domains of the inclusion, respectively.

To quantitatively describe the flow focusing effect, a pore-fluid flow focusing factor due to this elliptical inclusion is defined as

$$\lambda_x = \frac{u_x^{in}}{\lim\limits_{\xi\to\infty} u_x^{out}} = \frac{\alpha(\beta+1)}{\beta+\alpha}, \tag{6.35}$$

where λ_x is the pore-fluid flow focusing factor due to the inflow being parallel to the long axis of the elliptical inclusion.

The pore-fluid flow focusing factor of an elliptical inclusion is dependent only upon the aspect ratio representing its specific geometry and the permeability ratio representing the hydrodynamic system, but is independent of the specific length scale of the inclusion used in the theoretical analysis. If the aspect ratio of an elliptical inclusion is equal to unity, then the inclusion becomes circular so that the corresponding pore-fluid flow focusing factor degenerates into that of a circular one, as obtained in a previous study (Zhao et al. 1999b).

From potential flow theory (Gerhart et al. 1993), the following relationship between the stream function ψ and the pore-fluid velocity exists:

$$\frac{\partial\psi}{\partial y} = u_x, \qquad \frac{\partial\psi}{\partial x} = -u_y. \tag{6.36}$$

Similar to (6.9), we have:

$$\begin{Bmatrix} \dfrac{\partial\psi}{\partial x} \\ \dfrac{\partial\psi}{\partial y} \end{Bmatrix} = \frac{\begin{bmatrix} \sinh\xi\cos\eta & -\cosh\xi\sin\eta \\ \cosh\xi\sin\eta & \sinh\xi\cos\eta \end{bmatrix}}{\sinh^2\xi\cos^2\eta + \cosh^2\xi\sin^2\eta} \begin{Bmatrix} \dfrac{\partial\psi}{\partial\xi} \\ \dfrac{\partial\psi}{\partial\eta} \end{Bmatrix}. \tag{6.37}$$

Consideration of (6.2), (6.3), (6.9), (6.36) and (6.37) yields the analytical solution for the stream function as

$$\psi_{in} = \frac{\omega_x K_{in} C_1}{\mu} c\sinh\xi\sin\eta + C, \tag{6.38}$$

$$\psi_{out} = \frac{\omega_x K_{out}}{\mu}\left[c\sinh\xi\sin\eta + C_2 e^{-(\xi-\xi_0)}\sin\eta\right] + C, \tag{6.39}$$

where ψ_{in} and ψ_{out} are the stream functions inside and outside the elliptical inclusion, respectively; C is an arbitrary constant.

Substituting the expressions for C_1 and C_2 yields the analytical solution to the stream functions inside and outside the elliptical inclusion, the long axis of which is parallel to the inflow direction in the undisturbed far field:

$$\psi_{in} = \frac{\omega_x K_{in}}{\mu}\left(\frac{\beta+1}{\beta+\alpha}\right) c\sinh\xi\sin\eta + C, \tag{6.40}$$

$$\psi_{out} = \frac{\omega_x K_{out}}{\mu}\left[c\sinh\xi\sin\eta + \frac{(\alpha-1)a}{\beta+\alpha} e^{-(\xi-\xi_0)}\sin\eta\right] + C. \tag{6.41}$$

In summary, in the case of the long axis of an elliptical inclusion being parallel to the inflow direction in the undisturbed far field, the analytical solutions for

the excess pore-fluid pressure and velocity around and within the inclusion can be expressed as

$$p_{in} = -\omega_x \left(\frac{\beta+1}{\beta+\alpha}\right) c\cosh\xi\cos\eta \qquad (\xi \le \xi_0), \tag{6.42}$$

$$p_{out} = -\omega_x c\cosh\xi\cos\eta + \omega_x \frac{(\alpha-1)a}{\beta+\alpha} e^{-(\xi-\xi_0)}\cos\eta \qquad (\xi \ge \xi_0), \tag{6.43}$$

$$u_x^{in} = \frac{\omega_x K_{out}\alpha}{\mu}\left(\frac{\beta+1}{\beta+\alpha}\right) \qquad (\xi \le \xi_0), \tag{6.44}$$

$$u_y^{in} = 0 \qquad (\xi \le \xi_0), \tag{6.45}$$

$$u_x^{out} = \frac{\omega_x K_{out}}{\mu}\left[1 + \left(\frac{(\alpha-1)a}{(\beta+\alpha)c}\right)\frac{(\sinh\xi\cos^2\eta - \cosh\xi\sin^2\eta)e^{-(\xi-\xi_0)}}{\sinh^2\xi\cos^2\eta + \cosh^2\xi\sin^2\eta}\right] \quad (\xi \ge \xi_0), \tag{6.46}$$

$$u_y^{out} = \frac{\omega_x K_{out}}{\mu}\left[\left(\frac{(\alpha-1)a}{(\beta+\alpha)c}\right)\frac{(\cosh\xi\sin\eta\cos\eta + \sinh\xi\sin\eta\cos\eta)e^{-(\xi-\xi_0)}}{\sinh^2\xi\cos^2\eta + \cosh^2\xi\sin^2\eta}\right] \quad (\xi \ge \xi_0). \tag{6.47}$$

Note that since the intrinsic permeability must have a value between zero (in the case of perfectly impermeable) and one (in the case of perfectly permeable), $\alpha \to 0$ results in $K_{in} \to 0$. In such a case, (6.44) indicates that as the inclusion becomes perfectly impermeable, the pore-fluid velocity within the elliptical inclusion approaches zero.

In order to compare the present analytical solution with a previous one (Phillips 1991), it is necessary to examine the behavior of (6.41) in the limiting case. If an elliptical inclusion is perfectly permeable relative to the surrounding rock, the permeability ratio of the inclusion approaches infinite (i.e., $\alpha \to \infty$). If this perfectly permeable inclusion is also very thin but very long, then the aspect ratio of the inclusion approaches infinite (i.e., $\beta \to \infty$). In this particular case, (6.41) can be rewritten as follows:

$$\begin{aligned}
\lim_{\alpha\to\infty,\beta\to\infty} \psi_{out} &= \frac{\omega_x K_{out}}{\mu} \lim_{\alpha\to\infty,\beta\to\infty}\left[c\sinh\xi + \left(\frac{(\alpha-1)a}{\alpha+\beta}\right)e^{-(\xi-\xi_0)}\right]\sin\eta \\
&= \frac{\omega_x K_{out}}{\mu}\sin\eta \lim_{\beta\to\infty}\left[c\sinh\xi + c\left(\frac{\beta}{\beta-1}\right)e^{-\xi}\right] \\
&= \frac{\omega_x K_{out}}{\mu} c\cosh\xi\sin\eta = U_x c\cosh\xi\sin\eta.
\end{aligned} \tag{6.48}$$

Since Phillips (1991) used a conformal mapping of the form $x = d\cosh\xi\cos\eta$ and $y = d\sinh\xi\sin\eta$ (note that d, instead of a, is used here to avoid unnecessary confusion) in deriving the previous solutions, the value of d needs to be set to c so

that the present solution can be compared with the previous solution (Phillips 1991) in the limiting case. Clearly, (6.48) is identical to the previous solution derived for the limiting case of a perfectly permeable and very thin, but very long, inclusion (Phillips 1991).

6.4 Derivation of Analytical Solutions when the Short Axis of an Elliptical Inclusion Is Parallel to the Inflow in the Far Field

To understand the effect of cross-formational flow along large cracks and faults, the inflow in the far field is assumed to be parallel to the short axis of an elliptical inclusion (see Fig. 6.1B). In this case, the boundary condition of the pore-fluid flow problem can be mathematically expressed in the following form:

$$p_{in} = p_{out} \qquad (\text{at } \xi = \xi_0), \tag{6.49}$$

$$K_{in}\frac{\partial p_{in}}{\partial \xi} = K_{out}\frac{\partial p_{out}}{\partial \xi} \qquad (\text{at } \xi = \xi_0), \tag{6.50}$$

$$\lim_{\xi \to \infty} p_{out} = -\omega_y c \sinh\xi \sin\eta, \tag{6.51}$$

where p_{in} and p_{out} are the excess pore-fluid pressures inside and outside the elliptical inclusion, respectively; ξ_0 is the boundary of the inclusion; K_{in} and K_{out} are the intrinsic permeabilities of the porous medium inside and outside the inclusion, and $\omega_y = \left|\partial p/\partial y\right|$ is the amplitude of the excess pore-fluid pressure gradient in the y direction of the far field.

Equation (6.49) expresses the excess pore-fluid pressure continuity at the boundary between the inclusion and the surrounding rock, while (6.50) expresses the pore-fluid flux continuity in the normal direction of this boundary. Equation (6.51) is used to express the distribution of the excess pore-fluid pressure in the far field, namely the boundary condition of the excess pore-fluid pressure at infinity.

The general solution to the excess pore-fluid pressure inside and outside the elliptical inclusion due to an inflow in the y direction of the far field can be expressed as

$$p_{in} = -\omega_y C_1 c \sinh\xi \sin\eta, \tag{6.52}$$

$$p_{out} = -\omega_y c \sinh\xi \sin\eta + \omega_y C_2 e^{-(\xi-\xi_0)} \sin\eta, \tag{6.53}$$

where C_1 and C_2 are two constants to be determined by the boundary conditions of the problem.

Substituting (6.52) and (6.53) into (6.49) and (6.50) yields the following equations:

$$(1 - C_1)c \sinh\xi_0 - C_2 = 0, \tag{6.54}$$

$$\left(\frac{K_{in}}{K_{out}}C_1 - 1\right) c \cosh\xi_0 - C_2 = 0. \tag{6.55}$$

Solving (6.54) and (6.55) simultaneously yields the following expressions for C_1 and C_2:

$$C_1 = \frac{1+\beta}{1+\alpha\beta}, \qquad C_2 = \frac{(\alpha-1)a}{1+\alpha\beta}, \tag{6.56}$$

where

$$\beta = \frac{a}{b} = \frac{c\cosh\xi_0}{c\sinh\xi_0} = \frac{\cosh\xi_0}{\sinh\xi_0}, \qquad \alpha = \frac{K_{in}}{K_{out}}, \tag{6.57}$$

where α is the permeability ratio of the elliptical inclusion to the surrounding rock; β is the aspect ratio of the elliptical inclusion, and $a = \cosh\xi_0$ and $b = \sinh\xi_0$ are half the length of the long and short axes of the elliptical inclusion.

Note that the following mathematical equalities exist for the elliptical inclusion:

$$e^{\xi_0} = \cosh\xi_0 + \sinh\xi_0 = \frac{a+b}{c}, \quad e^{\xi_0} = \frac{1}{e^{-\xi_0}} = \frac{1}{\cosh\xi_0 - \sinh\xi_0} = \frac{c}{a-b}. \tag{6.58}$$

Using these two equalities yields the following equations:

$$a^2 - b^2 = c^2, \qquad a = \frac{c\beta}{\sqrt{\beta^2-1}}, \qquad b = \frac{c}{\sqrt{\beta^2-1}}. \tag{6.59}$$

Considering (6.2), (6.3), (6.9), (6.52), (6.53), (6.56) and (6.57) yields the corresponding analytical solution to the pore-fluid velocity as follows:

$$u_x^{in} = 0 \qquad (\xi \le \xi_0), \tag{6.60}$$

$$u_y^{in} = \frac{\omega_y K_{in}}{\mu}\left(\frac{1+\beta}{1+\alpha\beta}\right) \qquad (\xi \le \xi_0), \tag{6.61}$$

$$u_x^{out} = \frac{\omega_y K_{out}}{\mu}\left[\left(\frac{(\alpha-1)a}{1+\alpha\beta}\right)\frac{(\sinh\xi+\cosh\xi)\sin\eta\cos\eta\, e^{-(\xi-\xi_0)}}{c(\sinh^2\xi\cos^2\eta+\cosh^2\xi\sin^2\eta)}\right] \quad (\xi \ge \xi_0), \tag{6.62}$$

$$u_y^{out} = \frac{\omega_y K_{out}}{\mu}\left[1+\left(\frac{(\alpha-1)a}{1+\alpha\beta}\right)\frac{(\cosh\xi\sin^2\eta-\sinh\xi\cos^2\eta)e^{-(\xi-\xi_0)}}{c(\sinh^2\xi\cos^2\eta+\cosh^2\xi\sin^2\eta)}\right] (\xi \ge \xi_0), \tag{6.63}$$

where the superscripts, *in* and *out*, represent the inside and outside domains of the inclusion, respectively.

Equation (6.61) indicates that, as the inclusion becomes perfectly impermeable, the intrinsic permeability of the inclusion goes to zero so that the pore-fluid velocity within the inclusion approaches zero. Since the intrinsic permeability must have a value between zero (in the case of perfectly impermeable) and one (in the case of perfectly permeable), $\alpha \to 0$ as $K_{in} \to 0$. This implies that if $\alpha \to \infty$, then the surrounding rock must be perfectly impermeable so that $K_{out} \to 0$. In this case, (6.61) can be rewritten as $u_y^{in} = (\omega_y \alpha K_{out})(1+\beta)/[\mu(1+\alpha\beta)]$, which tends to a value of $\omega_y K_{out}(1+\beta)/(\mu\beta)$ as $\alpha \to \infty$. Clearly, $u_y^{in} \to 0$ as $K_{out} \to 0$. This indicates

that if the surrounding rock is perfectly impermeable, the pore-fluid velocity within the inclusion expressed by (6.61) approaches the far field velocity, which has a limiting value of zero. If the surrounding rock is not perfectly impermeable (i.e., the inclusion is not perfectly permeable), the pore-fluid velocity within the inclusion is, strictly speaking, not equal to the far field velocity unless the aspect ratio of the elliptical inclusion approaches infinite (i.e., $\beta \to \infty$). This is consistent with the previous solutions for perfectly permeable and very thin, but very long inclusions (Phillips 1991).

In order to quantitatively describe the flow focusing effect, a flow focusing factor due to this elliptical inclusion is defined as

$$\lambda_y = \frac{u_y^{in}}{\lim\limits_{\xi\to\infty} u_y^{out}} = \frac{\alpha(1+\beta)}{1+\alpha\beta}, \tag{6.64}$$

where λ_y is the pore-fluid flow focusing factor of the inclusion in the case of the inflow being in the y direction in the far field of the local xy coordinate system.

The pore-fluid flow focusing factor of an elliptical inclusion is dependent on the aspect ratio representing the specific geometry of the inclusion and the permeability ratio representing the hydrodynamic system associated with the inclusion. If the aspect ratio of an elliptical inclusion is equal to unity, then the inclusion becomes a circular one so that the pore-fluid flow focusing factor of the inclusion degenerates into that of a circular inclusion, as obtained in a previous study (Zhao et al. 1999b).

Considering (6.2), (6.3), (6.9), (6.36) and (6.37) yields the analytical solution for the stream function due to the elliptical inclusion as follows:

$$\psi_{in} = -\frac{\omega_y K_{in}}{\mu}\left(\frac{1+\beta}{1+\alpha\beta}\right) c\cosh\xi\cos\eta + C \qquad (\xi \le \xi_0), \tag{6.65}$$

$$\psi_{out} = -\frac{\omega_y K_{out}}{\mu}\left[c\cosh\xi\cos\eta + \left(\frac{(\alpha-1)a}{1+\alpha\beta}\right) e^{-(\xi-\xi_0)}\cos\eta\right] + C \quad (\xi \ge \xi_0), \tag{6.66}$$

where ψ_{in} and ψ_{out} are the stream functions inside and outside the elliptical inclusion, respectively; C is an arbitrary constant.

For a perfectly permeable inclusion relative to the surrounding rock, the permeability ratio of the inclusion approaches infinite (i.e., $\alpha \to \infty$). If this perfectly permeable inclusion is very thin, but very long, then the aspect ratio of the inclusion approaches infinite (i.e., $\beta \to \infty$). In this particular case, (6.66) can be rewritten as follows:

$$\begin{aligned}
\lim_{\alpha\to\infty,\beta\to\infty} \psi_{out} &= -\frac{\omega_y K_{out}}{\mu} \lim_{\alpha\to\infty,\beta\to\infty}\left[c\cosh\xi\cos\eta + \left(\frac{(\alpha-1)a}{1+\alpha\beta}\right) e^{-(\xi-\xi_0)}\cos\eta\right] \\
&= -\frac{\omega_y K_{out}}{\mu}\cos\eta \lim_{\beta\to\infty}\left[c\cosh\xi + c\left(\frac{1}{\beta-1}\right) e^{-\xi}\right] \\
&= -\frac{\omega_y K_{out}}{\mu} c\cosh\xi\cos\eta = U_y x.
\end{aligned} \tag{6.67}$$

Note that (6.67) is exactly the same as the previous solution derived for the limiting case of a perfectly permeable and very thin, but very long inclusion (Phillips 1991).

6.5 Derivation of Analytical Solutions when the Inflow of the Far Field Is Parallel to the *X* Direction of the Global *XY* Coordinate System

In this case, the inflow of the far field is not parallel to either the long or the short axes of the elliptical inclusion. Due to mathematical complexities in describing the problem of pore-fluid flow around an inclined elliptical inclusion of any inclined angle, three different coordinate systems are used to mathematically derive the analytical solution for the problem. As shown in Fig. 6.2, these three different coordinate systems are a global Cartesian (*XY)* coordinate system, a local Cartesian (*xy)* coordination system and a local elliptical $\xi\eta$ coordinate system, respectively. Both the pore-fluid flow in the unperturbed far field and the dip angle of an inclined elliptical inclusion are described in the global *XY* coordinate system. The perturbed pore-fluid flow around the inclined elliptical inclusion is described in the local *xy* and $\xi\eta$ coordinate systems. As previously demonstrated, using a local $\xi\eta$ coordinate system enables boundary conditions between the inclined inclusion and the surrounding rock to be easily described. If the pore-fluid flow in the unperturbed far field is horizontal, its corresponding components in the local *xy* coordinate system can be expressed as follows:

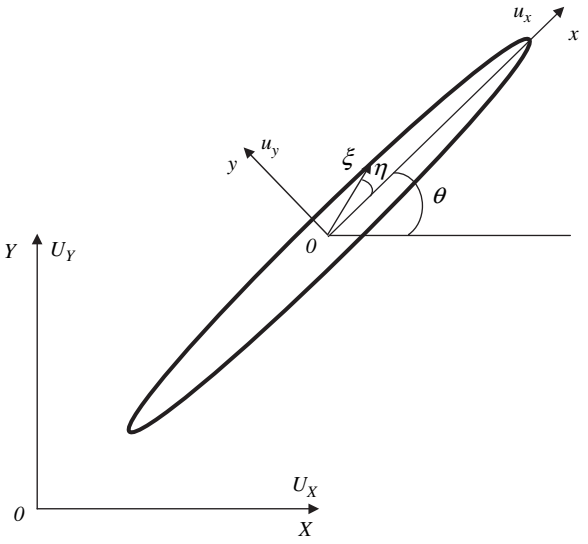

Fig. 6.2 Description of an inclined elliptical inclusion in three coordinate systems

$$U_x = U_X \cos\theta, \qquad U_y = -U_X \sin\theta, \tag{6.68}$$

where U_x and U_y are the pore-fluid velocity components of the far field in the x and y directions of the local xy coordinate system; U_X is the horizontal pore-fluid velocity component of the far field in the X direction of the global XY coordinate system, and θ is the dip angle of the inclined elliptical inclusion relative to the global coordinate system.

Since the governing equation of excess pore-fluid pressure in a pore-fluid saturated porous medium is described using (6.4), which is a linear second-order partial differential equation, the superposition principle is valid in deriving analytical solutions for pore-fluid flow around an inclined elliptical inclusion when the inflow of the far field is parallel to the X direction of the global XY coordinate system.

Substituting Darcy's Law into (6.68) yields the following equations:

$$-\frac{K_{out}}{\mu}\omega_x = -\frac{K_{out}}{\mu}\omega_X \cos\theta, \qquad -\frac{K_{out}}{\mu}\omega_y = \frac{K_{out}}{\mu}\omega_X \sin\theta, \tag{6.69}$$

where ω_x and ω_y are the amplitudes of the excess pore-fluid pressure gradient in the x and y directions of the local xy coordinate system in the far field, and ω_X is the amplitude of the excess pore-fluid pressure gradient in the X direction of the global XY coordinate system in the far field.

Equation (6.69) can be straightforwardly written as follows:

$$\omega_x = \omega_X \cos\theta, \qquad \omega_y = -\omega_X \sin\theta. \tag{6.70}$$

Superposing the analytical solutions derived in the previous two sections yields the analytical solutions for pore-fluid flow around an inclined elliptical inclusion when the inflow of the far field is parallel to the X direction of the global XY coordinate system.

$$\psi_{in} = \frac{\omega_X K_{in}}{\mu}\left[\left(\frac{\beta+1}{\beta+\alpha}\right)c\sinh\xi\sin\eta\cos\theta + \left(\frac{1+\beta}{1+\alpha\beta}\right)c\cosh\xi\cos\eta\sin\theta\right]+C \qquad (\xi \le \xi_0), \tag{6.71}$$

$$\psi_{out} = \frac{\omega_X K_{out}}{\mu}\left[c\sinh\xi + \left(\frac{(\alpha-1)a}{\beta+\alpha}\right)e^{-(\xi-\xi_0)}\right]\sin\eta\cos\theta + \frac{\omega_X K_{out}}{\mu}\left[c\cosh\xi + \left(\frac{(\alpha-1)a}{1+\alpha\beta}\right)e^{-(\xi-\xi_0)}\right]\cos\eta\sin\theta + C \qquad (\xi \ge \xi_0), \tag{6.72}$$

$$p_{in} = -\omega_X\left(\frac{\beta+1}{\beta+\alpha}\right)c\cosh\xi\cos\eta\cos\theta + \omega_X\left(\frac{1+\beta}{1+\alpha\beta}\right)c\sinh\xi\sin\eta\sin\theta \quad (\xi \le \xi_0), \tag{6.73}$$

$$p_{out} = -\omega_X \left[c\cosh\xi - \left(\frac{(\alpha-1)a}{\beta+\alpha} \right) e^{-(\xi-\xi_0)} \right] \cos\eta\cos + \omega_X \left[c\sinh\xi - \omega_X \left(\frac{(\alpha-1)a}{1+\alpha\beta} \right) e^{-(\xi-\xi_0)} \right] \sin\eta\sin\theta \quad (\xi \geq \xi_0), \tag{6.74}$$

$$u_x^{in} = \frac{\omega_X K_{in}}{\mu} \left(\frac{\beta+1}{\beta+\alpha} \right) \cos\theta \qquad (\xi \leq \xi_0), \tag{6.75}$$

$$u_y^{in} = -\frac{\omega_X K_{in}}{\mu} \left(\frac{1+\beta}{1+\alpha\beta} \right) \sin\theta \qquad (\xi \leq \xi_0), \tag{6.76}$$

$$u_x^{out} = \frac{\omega_X K_{out}}{\mu} \left[1 + \left(\frac{(\alpha-1)a}{\beta+\alpha} \right) \frac{(\sinh\xi\cos^2\eta - \cosh\xi\sin^2\eta)e^{-(\xi-\xi_0)}}{c(\sinh^2\xi\cos^2\eta + \cosh^2\xi\sin^2\eta)} \right] \cos\theta - \frac{\omega_X K_{out}}{\mu} \left[\left(\frac{(\alpha-1)a}{1+\alpha\beta} \right) \frac{(\sinh\xi + \cosh\xi)\sin\eta\cos\eta e^{-(\xi-\xi_0)}}{c(\sinh^2\xi\cos^2\eta + \cosh^2\xi\sin^2\eta)} \right] \sin\theta \quad (\xi \geq \xi_0), \tag{6.77}$$

$$u_y^{out} = \frac{\omega_X K_{out}}{\mu} \left[\left(\frac{(\alpha-1)a}{\beta+\alpha} \right) \frac{(\cosh\xi\sin\eta\cos\eta + \sinh\xi\sin\eta\cos\eta)e^{-(\xi-\xi_0)}}{c(\sinh^2\xi\cos^2\eta + \cosh^2\xi\sin^2\eta)} \right] \cos\theta - \frac{\omega_X K_{out}}{\mu} \left[1 + \left(\frac{(\alpha-1)a}{1+\alpha\beta} \right) \frac{(\cosh\xi\sin^2\eta - \sinh\xi\cos^2\eta)e^{-(\xi-\xi_0)}}{c(\sinh^2\xi\cos^2\eta + \cosh^2\xi\sin^2\eta)} \right] \sin\theta \quad (\xi \geq \xi_0). \tag{6.78}$$

In order to derive the pore-fluid flow focusing factor of the inclined elliptical inclusion in the case of the inflow being parallel to the X direction in the far field of the global XY coordinate system, the following equality needs to be considered:

$$\lambda_X = \frac{u_x^{in}\cos\theta - u_y^{in}\sin\theta}{U_X} = \frac{u_x^{in}\cos^2\theta}{U_X\cos\theta} - \frac{u_y^{in}\sin^2\theta}{U_X\sin\theta} = \frac{u_x^{in}\cos^2\theta}{\lim\limits_{\xi\to\infty} u_x^{out}} + \frac{u_y^{in}\sin^2\theta}{\lim\limits_{\xi\to\infty} u_y^{out}}. \tag{6.79}$$

Inserting (6.35) and (6.64) into (6.79) yields the following equation:

$$\lambda_X = \lambda_x\cos^2\theta + \lambda_y\sin^2\theta, \tag{6.80}$$

where λ_x and λ_y are the pore-fluid flow focusing factors of the inclined elliptical inclusion in the case of the inflow being parallel to the x and y directions in the far field of the local xy coordinate system, and λ_X is the pore-fluid flow focusing factor of the inclined elliptical inclusion in the case of the inflow being parallel to the X direction in the far field of the global XY coordinate system.

Clearly, (6.80) indicates that if the inflow of the far field is not parallel to either the long axis or the short axis of an inclined elliptical inclusion, the pore-fluid flow focusing factor is also dependent on the dip angle of the inclined inclusion.

6.6 Derivation of Analytical Solutions when the Inflow of the Far Field Is Parallel to the *Y* Direction of the Global *XY* Coordinate System

In this case, the pore-fluid flow in the unperturbed far field is vertical, so that its corresponding components in the local *xy* coordinate system can be expressed as follows:

$$U_x = U_Y \sin\theta, \qquad U_y = U_Y \cos\theta, \tag{6.81}$$

where U_x and U_y are the pore-fluid velocity components of the far field in the x and y directions of the local xy coordinate system; U_Y is the vertical pore-fluid velocity component of the far field in the Y direction of the global XY coordinate system, and θ is the dip angle of the inclined elliptical inclusion.

Similarly, the superposition principle is valid in deriving analytical solutions for pore-fluid flow around an inclined elliptical inclusion when the inflow of the far field is parallel to the Y direction of the global XY coordinate system.

Substituting Darcy's Law into (6.81) yields the following equations:

$$-\frac{K_{out}}{\mu}\omega_x = -\frac{K_{out}}{\mu}\omega_Y \sin\theta, \qquad -\frac{K_{out}}{\mu}\omega_y = -\frac{K_{out}}{\mu}\omega_Y \cos\theta, \tag{6.82}$$

where ω_x and ω_y are the amplitudes of the excess pore-fluid pressure gradient in the x and y directions of the local xy coordinate system in the far field, and ω_Y is the amplitude of the excess pore-fluid pressure gradient in the Y direction of the global XY coordinate system in the far field.

Equation (6.82) can be straightforwardly written as follows:

$$\omega_x = \omega_Y \sin\theta, \qquad \omega_y = \omega_Y \cos\theta. \tag{6.83}$$

Superposing the analytical solutions derived in the previous two sections yields the analytical solutions for pore-fluid flow around an inclined elliptical inclusion when the inflow of the far field is parallel to the Y direction of the global XY coordinate system.

$$\begin{aligned}\psi_{in} = \frac{\omega_Y K_{in}}{\mu}\Bigg[&\left(\frac{\beta+1}{\beta+\alpha}\right) c\sinh\xi\sin\eta\sin\theta \\ &-\left(\frac{1+\beta}{1+\alpha\beta}\right) c\cosh\xi\cos\eta\cos\theta\Bigg] + C \qquad (\xi \le \xi_0),\end{aligned} \tag{6.84}$$

$$\psi_{out} = \frac{\omega_Y K_{out}}{\mu}\left[c\sinh\xi + \left(\frac{(\alpha-1)a}{\beta+\alpha}\right)e^{-(\xi-\xi_0)}\right]\sin\eta\sin\theta$$
$$-\frac{\omega_Y K_{out}}{\mu}\left[c\cosh\xi + \left(\frac{(\alpha-1)a}{1+\alpha\beta}\right)e^{-(\xi-\xi_0)}\right]\cos\eta\cos\theta + C \qquad (\xi \geq \xi_0), \tag{6.85}$$

$$p_{in} = -\omega_Y\left(\frac{\beta+1}{\beta+\alpha}\right)c\cosh\xi\cos\eta\sin\theta$$
$$-\omega_Y\left(\frac{1+\beta}{1+\alpha\beta}\right)c\sinh\xi\sin\eta\cos\theta \qquad (\xi \leq \xi_0), \tag{6.86}$$

$$p_{out} = -\omega_Y\left[c\cosh\xi - \left(\frac{(\alpha-1)a}{\beta+\alpha}\right)e^{-(\xi-\xi_0)}\right]\cos\eta\sin\theta$$
$$-\omega_Y\left[c\sinh\xi - \omega_X\left(\frac{(\alpha-1)a}{1+\alpha\beta}\right)e^{-(\xi-\xi_0)}\right]\sin\eta\cos\theta \quad (\xi \geq \xi_0), \tag{6.87}$$

$$u_x^{in} = \frac{\omega_Y K_{in}}{\mu}\left(\frac{\beta+1}{\beta+\alpha}\right)\sin\theta \qquad (\xi \leq \xi_0), \tag{6.88}$$

$$u_y^{in} = \frac{\omega_Y K_{in}}{\mu}\left(\frac{1+\beta}{1+\alpha\beta}\right)\cos\theta \qquad (\xi \leq \xi_0), \tag{6.89}$$

$$u_x^{out} = \frac{\omega_Y K_{out}}{\mu}\left[1 + \left(\frac{(\alpha-1)a}{\beta+\alpha}\right)\frac{(\sinh\xi\cos^2\eta - \cosh\xi\sin^2\eta)e^{-(\xi-\xi_0)}}{c(\sinh^2\xi\cos^2\eta + \cosh^2\xi\sin^2\eta)}\right]\sin\theta$$
$$+\frac{\omega_Y K_{out}}{\mu}\left[\left(\frac{(\alpha-1)a}{1+\alpha\beta}\right)\frac{(\sinh\xi + \cosh\xi)\sin\eta\cos\eta e^{-(\xi-\xi_0)}}{c(\sinh^2\xi\cos^2\eta + \cosh^2\xi\sin^2\eta)}\right]\cos\theta \quad (\xi \geq \xi_0), \tag{6.90}$$

$$u_y^{out} = \frac{\omega_Y K_{out}}{\mu}\left[\left(\frac{(\alpha-1)a}{\beta+\alpha}\right)\frac{(\cosh\xi\sin\eta\cos\eta + \sinh\xi\sin\eta\cos\eta)e^{-(\xi-\xi_0)}}{c(\sinh^2\xi\cos^2\eta + \cosh^2\xi\sin^2\eta)}\right]\sin\theta$$
$$+\frac{\omega_Y K_{out}}{\mu}\left[1 + \left(\frac{(\alpha-1)a}{1+\alpha\beta}\right)\frac{(\cosh\xi\sin^2\eta - \sinh\xi\cos^2\eta)e^{-(\xi-\xi_0)}}{c(\sinh^2\xi\cos^2\eta + \cosh^2\xi\sin^2\eta)}\right]\cos\theta \quad (\xi \geq \xi_0), \tag{6.91}$$

In order to derive the pore-fluid flow focusing factor of the inclined elliptical inclusion in the case of the inflow being parallel to the Y direction in the far field of the global XY coordinate system, the following equality needs to be considered:

$$\lambda_Y = \frac{u_x^{in}\sin\theta + u_y^{in}\cos\theta}{U_Y} = \frac{u_x^{in}\sin^2\theta}{U_Y\sin\theta} + \frac{u_y^{in}\cos^2\theta}{U_Y\cos\theta} = \frac{u_x^{in}\sin^2\theta}{\lim\limits_{\xi\to\infty} u_x^{out}} + \frac{u_y^{in}\cos^2\theta}{\lim\limits_{\xi\to\infty} u_y^{out}}. \tag{6.92}$$

Inserting (6.35) and (6.64) into (6.92) yields the following equation:

$$\lambda_Y = \lambda_x\sin^2\theta + \lambda_y\cos^2\theta, \tag{6.93}$$

where λ_x and λ_y are the pore-fluid flow focusing factors of the inclined elliptical inclusion in the case of the inflow being parallel to the x and y directions in the far field of the local xy coordinate system, and λ_Y is the pore-fluid flow focusing factor of the inclined elliptical inclusion in the case of the inflow being parallel to the Y direction in the far field of the global XY coordinate system.

6.7 Application Examples of the Present Analytical Solutions for Pore-Fluid Focusing Factors within Inclined Elliptical Inclusions

The present analytical solutions provide a useful tool for fundamentally understanding the general behavior of pore-fluid flow around a buried inclined fault or crack within the crust of the Earth. For instance, the simple and elegant analytical solution for the flow focusing factor within a buried inclined fault can be used to understand how the pore-fluid flow is focused into buried inclined faults with any dip angles. Since the pore-fluid flow focusing factor is dependent on the angle between the long axis of the inclusion and the inflow direction in the unperturbed far field, we can consider all possible flow focusing situations by setting the inflow parallel to the X direction in the far field of the global XY coordinate system and varying the dip angle of the inclusion.

In the case of the dip angle being zero, Fig. 6.3 shows the variation of analytical flow focusing factors with the aspect ratio of the inclusion for several different permeability ratios (i.e., PR in this figure) of the inclusion to the surrounding rock, while Fig. 6.4 shows the variation of analytical flow focusing factors with the permeability ratio of the inclusion to the surrounding rock for several different aspect ratios (i.e., AR in this figure). Clearly, for a given aspect ratio of the inclusion in the case of the dip angle being zero, the flow focusing factor increases as the permeability ratio of the inclusion to the surrounding rock increases until it reaches the corresponding limiting value. Similarly, for a given permeability ratio of the fault to the surrounding rock, the flow focusing factor increases as the aspect ratio of the inclusion increases until it reaches its corresponding limiting value. At this point, it is interesting to compare the present results with previous ones in the limiting case (Phillips 1991). For a perfectly permeable inclusion, the previous result indicated that the flow focusing factor (λ) is equal to the aspect ratio (β), namely $\lambda = \beta$. In the case of the aspect ratio (AR) being 10, 100, 1,000 and 10,000, the asymptotes

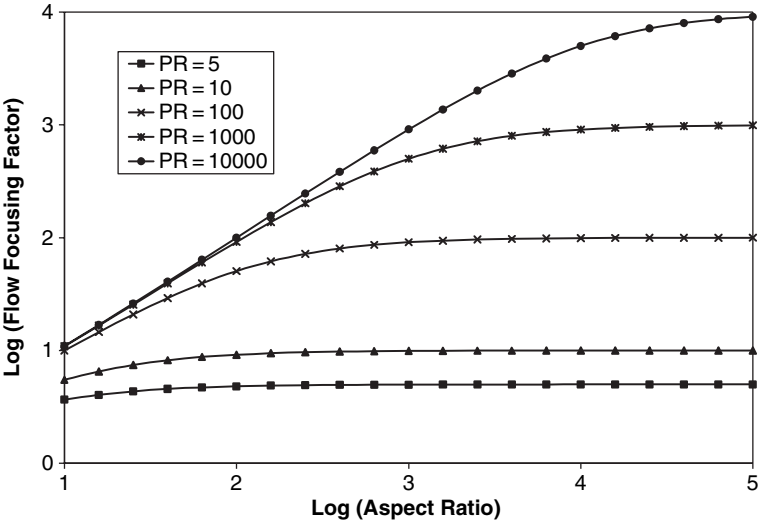

Fig. 6.3 Variation of flow focusing factor with aspect ratio due to different permeability ratios (inflow parallel to the long axis of the inclusion)

of the corresponding logarithmic values of the flow focusing factor are 1, 2, 3 and 4, respectively. Since the present results of the flow focusing factor approach the previous ones, it has been demonstrated that when the inflow is parallel to the long axis of the inclusion, the present results are consistent with the previous results for perfectly permeable inclusions.

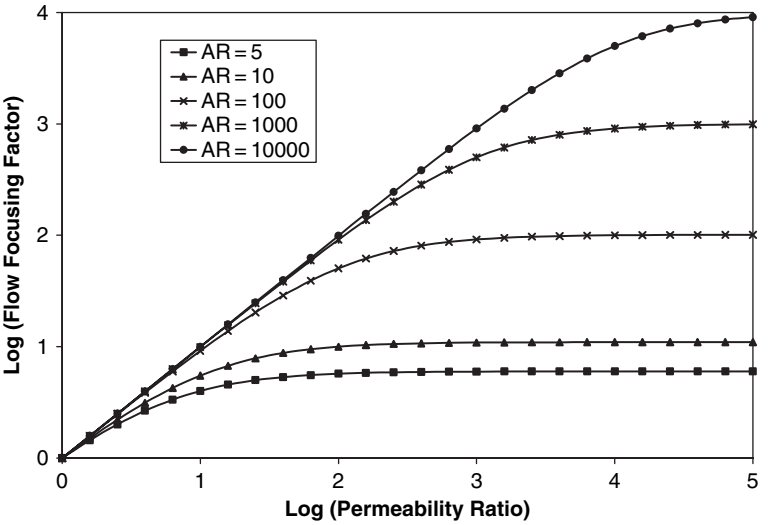

Fig. 6.4 Variation of flow focusing factor with permeability ratio due to different aspect ratios (inflow parallel to the long axis of the inclusion)

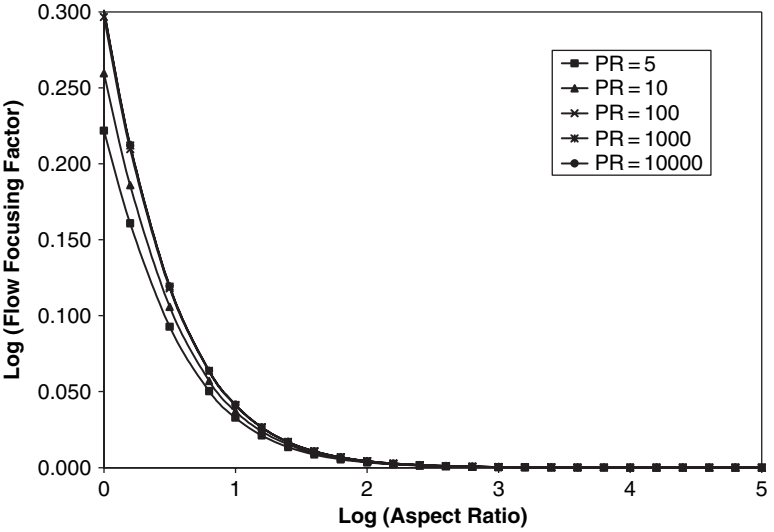

Fig. 6.5 Variation of flow focusing factor with aspect ratio due to different permeability ratios (inflow parallel to the short axis of the inclusion)

If the dip angle of the inclusion is 90°, the horizontal inflow in the unperturbed far field is parallel to the short axis of the inclusion. Figure 6.5 shows the variation of analytical flow focusing factors with the aspect ratio of the inclusion for several different permeability ratios (i.e., PR in this figure) of the inclusion to the surrounding rock, while Fig. 6.6 shows the variation of analytical flow focusing factors with

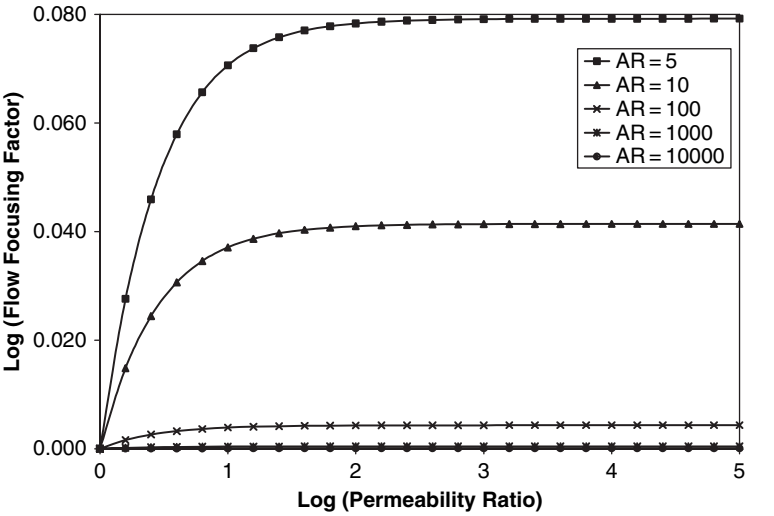

Fig. 6.6 Variation of flow focusing factor with permeability ratio due to different aspect ratios (inflow parallel to the short axis of the inclusion)

the permeability ratio of the inclusion to the surrounding rock for several different aspect ratios (i.e., AR in this figure) of the inclusion. Since the logarithm of the flow focusing factor is shown in the direction of the vertical axis (in Figs. 6.5 and 6.6), a logarithmic value of zero corresponds with the flow focusing factor of one. It is obvious that, for a given permeability ratio, the pore-fluid flow focusing factor approaches unity as the aspect ratio of the inclusion increases. This is because, when the aspect ratio of an elliptical inclusion is infinite or very large, the inclusion behaves as an interface between surrounding rocks, so that the pore-fluid flow focusing factor must be unity, as required by the pore-fluid mass conservation in the pore-fluid flow direction. For a given aspect ratio of the inclusion, the pore-fluid flow focusing factor can also approach a limit value. Although this limit value may vary with different aspect ratios of the inclusion, it goes to unity as the aspect ratio approaches infinite. Thus, for a perfectly permeable and very thin but very long inclusion, the flow focusing factor approaches one, implying that when the inflow is parallel to the short axis of the inclusion, the perfectly permeable inclusion does not perturb the flow field. This conclusion is consistent with that obtained from a previous study in the limiting case (Phillips 1991). Comparing the analytical results in Figs. 6.3 and 6.4 with those in Figs. 6.5 and 6.6, clearly, the pore-fluid flow focusing factors in the case of the inflow parallel to the short axis of the inclusion are much smaller than those in the case of the inflow parallel to the long axis of the inclusion. This indicates that the relative direction of the inflow in the far field to the long axis of an elliptical inclusion has a significant influence on the pore-fluid flow focusing factor of the inclusion.

In order to further examine the effect of the relative direction of the inflow in the far field to the long axis of an elliptical inclusion on the pore-fluid flow focusing factor, three different intermediate dip angles, namely 30°, 45° and 60°, are considered to produce the related analytical solutions. Figures 6.7, 6.9 and 6.11 show the variation of analytical flow focusing factors with the aspect ratio of the inclusion for several different permeability ratios (i.e., PR in these figures) due to the three different dip angles. Figures 6.8, 6.10 and 6.12 show the variation of analytical flow focusing factors with the permeability ratio of the inclusion to the surrounding rock for several different aspect ratios (i.e., AR in these figures) due to the three different dip angles. Clearly the maximum value of the pore-fluid flow focusing factor decreases as the dip angle of the inclusion increases. For example, if the permeability ratio is 10,000, the maximum logarithm value of the pore-fluid flow focusing factor can reach 2.969 in the case of $\theta = 30°$, while it decreases to 1.979 and 0.99 in the case of $\theta = 45°$ and $\theta = 60°$, respectively. The previous findings, such as the variation trend of pore-fluid flow focusing factors with either different permeability ratios or different aspect ratios of the inclusion, can be also observed from the analytical solutions shown in Figs. 6.7, 6.8, 6.9, 6.10, 6.11 and 6.12.

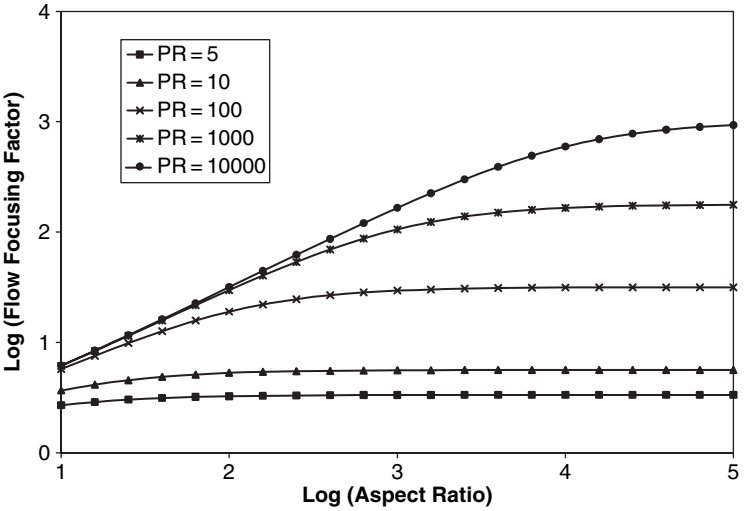

Fig. 6.7 Variation of flow focusing factor with aspect ratio due to different permeability ratios (inflow parallel to the X axis, $\theta = 30^\circ$)

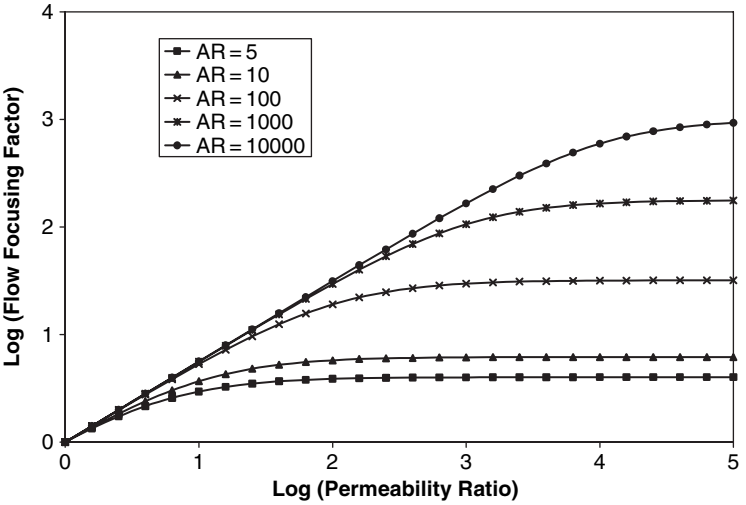

Fig. 6.8 Variation of flow focusing factor with permeability ratio due to different aspect ratios (inflow parallel to the X axis, $\theta = 30^\circ$)

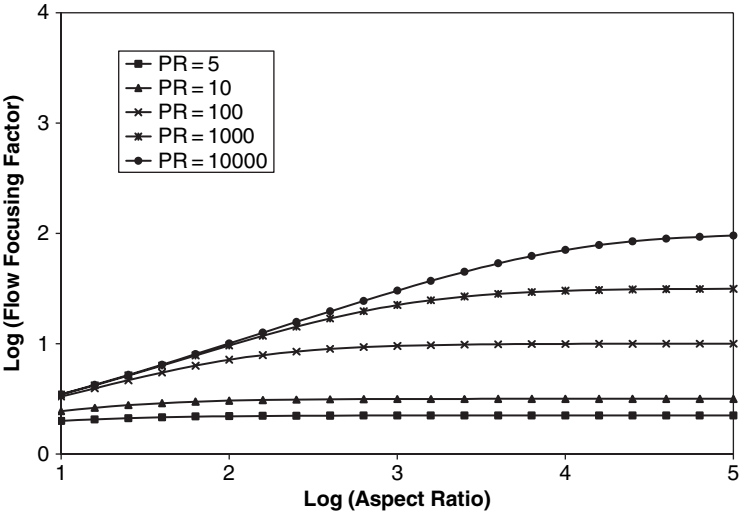

Fig. 6.9 Variation of flow focusing factor with aspect ratio due to different permeability ratios (inflow parallel to the X axis, $\theta = 45°$)

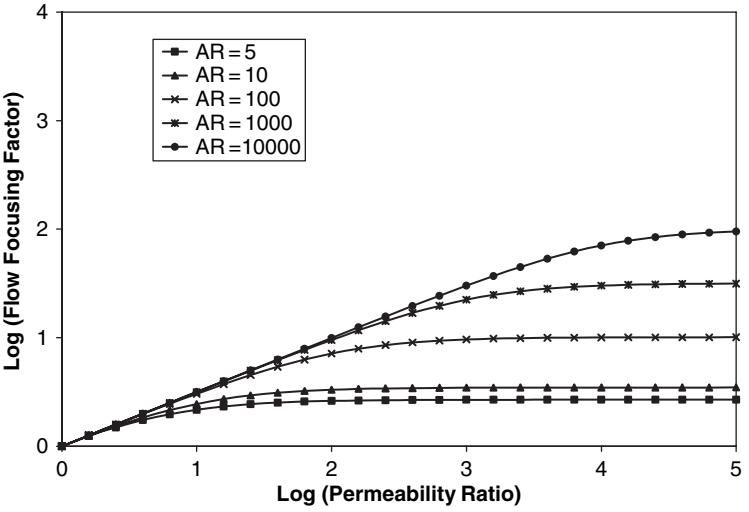

Fig. 6.10 Variation of flow focusing factor with permeability ratio due to different aspect ratios (inflow parallel to the X axis, $\theta = 45°$)

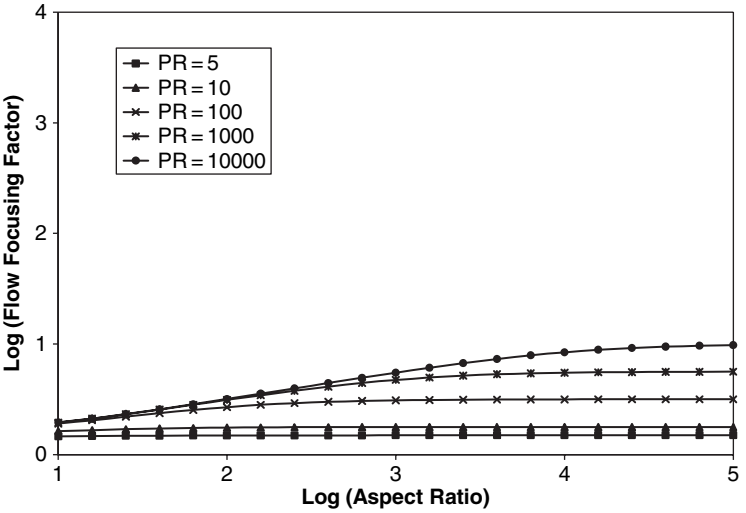

Fig. 6.11 Variation of flow focusing factor with aspect ratio due to different permeability ratios (inflow parallel to the X axis, $\theta = 60^\circ$)

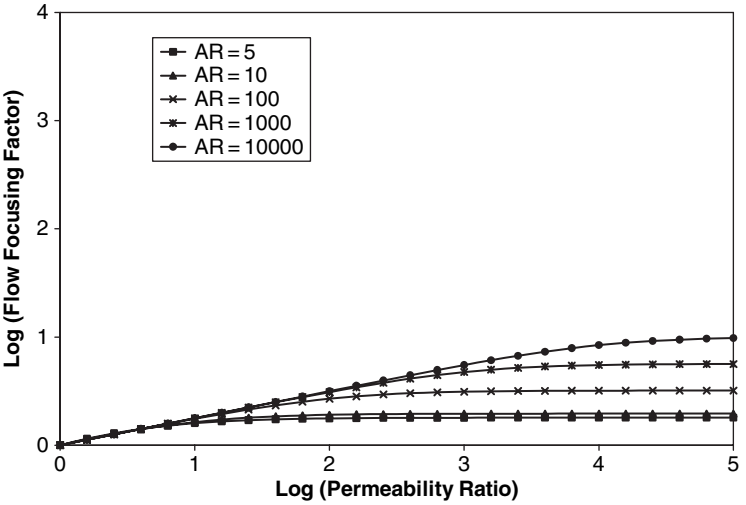

Fig. 6.12 Variation of flow focusing factor with permeability ratio due to different aspect ratios (inflow parallel to the X axis, $\theta = 60^\circ$)

Chapter 7
Pore-Fluid Focusing within Two-Dimensional Faults and Cracks of Crustal Scales with No Temperature Effects: Solutions Expressed in a Global Coordinate System

The analytical solutions derived in the local elliptical coordinate system as derived in Chap. 6 are not convenient to investigate pore-fluid flow patterns around and within an elliptical inclusion. It is necessary to convert the analytical solutions expressed in the local elliptical coordinate system into those expressed in a conventional Cartesian one. Toward this goal, we need to deal with an inverse problem between the local elliptical coordinate system and the conventional Cartesian coordinate system. Specifically, we need to solve ξ and η from (6.5) in Chap. 6 through inverse mappings so that ξ and η can be expressed using x and y coordinates.

7.1 Derivation of Inverse Mappings between the Elliptical and the Cartesian Coordinate Systems

From (6.5) in Chap. 6, the following relationships exist mathematically:

$$\frac{x^2}{c^2\cos^2\eta} - \frac{y^2}{c^2\sin^2\eta} = 1, \tag{7.1}$$

$$\frac{x^2}{c^2\cosh^2\xi} + \frac{y^2}{c^2\sinh^2\xi} = 1. \tag{7.2}$$

Equation (7.1) can be written into the following form:

$$\sin^4\eta + \left(\frac{x^2}{c^2} + \frac{y^2}{c^2} - 1\right)\sin^2\eta - \frac{y^2}{c^2} = 0. \tag{7.3}$$

The algebraic solution to (7.3) can be expressed as follows:

$$\sin\eta = \mathrm{sgn}(\frac{y}{c})\sqrt{\frac{\left(1-\frac{x^2}{c^2}-\frac{y^2}{c^2}\right)+\sqrt{\left(\frac{x^2}{c^2}+\frac{y^2}{c^2}-1\right)^2+4\frac{y^2}{c^2}}}{2}}, \tag{7.4}$$

where $\mathrm{sgn}(y/c)$ is the sign function, with a value of $\mathrm{sgn}(y/c) = -1$ if $y/c < 0$ and $\mathrm{sgn}(y/c) = 1$ otherwise.

C. Zhao et al., *Convective and Advective Heat Transfer in Geological Systems*,
© Springer-Verlag Berlin Heidelberg 2008

Thus, (7.4) results in the following inverse mapping of η:

$$\eta = \sin^{-1}\left[\operatorname{sgn}\left(\frac{y}{c}\right)\sqrt{\frac{\left(1-\frac{x^2}{c^2}-\frac{y^2}{c^2}\right)+\sqrt{\left(\frac{x^2}{c^2}+\frac{y^2}{c^2}-1\right)^2+4\frac{y^2}{c^2}}}{2}}\right], \tag{7.5}$$

where $\sin^{-1}$ is the inverse of the sine function.

From (7.4) and the identity $\sin^2\eta+\cos^2\eta=1$, the following expression exists:

$$\cos\eta = \operatorname{sgn}\left(\frac{x}{c}\right)\sqrt{\frac{\left(\frac{x^2}{c^2}+\frac{y^2}{c^2}+1\right)-\sqrt{\left(\frac{x^2}{c^2}+\frac{y^2}{c^2}-1\right)^2+4\frac{y^2}{c^2}}}{2}}, \tag{7.6}$$

where $\operatorname{sgn}(x/c)$ is the sign function, with a value of $\operatorname{sgn}(x/c)=-1$ if $x/c<0$ and $\operatorname{sgn}(x/c)=1$ otherwise.

Similarly, (7.2) yields the inverse mapping of ξ as follows:

$$\xi = ar\sinh\left[\sqrt{\frac{\left(\frac{x^2}{c^2}+\frac{y^2}{c^2}-1\right)+\sqrt{\left(\frac{x^2}{c^2}+\frac{y^2}{c^2}-1\right)^2+4\frac{y^2}{c^2}}}{2}}\right], \tag{7.7}$$

where $ar\sinh$ is the inverse of the hyperbolic sine function.

Using (7.7), the following equation can be straightforwardly obtained:

$$\sinh\xi = \sqrt{\frac{\left(\frac{x^2}{c^2}+\frac{y^2}{c^2}-1\right)+\sqrt{\left(\frac{x^2}{c^2}+\frac{y^2}{c^2}-1\right)^2+4\frac{y^2}{c^2}}}{2}}. \tag{7.8}$$

From (7.8) and the identity $\cosh^2\xi-\sinh^2\xi=1$, the following equation holds:

$$\cosh\xi = \sqrt{\frac{\left(\frac{x^2}{c^2}+\frac{y^2}{c^2}+1\right)+\sqrt{\left(\frac{x^2}{c^2}+\frac{y^2}{c^2}-1\right)^2+4\frac{y^2}{c^2}}}{2}}. \tag{7.9}$$

Another expression for $\cosh\xi$ can be also derived by considering (7.2) and the identity $\cosh^2\xi-\sinh^2\xi=1$ directly as follows:

$$\cosh^4\xi-\left(\frac{x^2}{c^2}+\frac{x^2}{c^2}+1\right)\cosh^2\xi+\frac{x^2}{c^2}=0. \tag{7.10}$$

Solving (7.10) yields the following alternative expression for $\cosh\xi$:

$$\cosh\xi = \sqrt{\frac{\left(\frac{x^2}{c^2}+\frac{y^2}{c^2}+1\right)+\sqrt{\left(\frac{x^2}{c^2}+\frac{y^2}{c^2}+1\right)^2-4\frac{x^2}{c^2}}}{2}}. \tag{7.11}$$

As expected, it can be demonstrated that (7.9) and (7.11) are mathematically identical, even though they are expressed in different forms. For this reason, (7.9) is used hereafter.

Using the above inverse mappings, the following expression exists:

$$\begin{aligned} e^{-(\xi-\xi_0)} = &\frac{a+b}{c}\left(\sqrt{\frac{\left(\frac{x^2}{c^2}+\frac{y^2}{c^2}+1\right)+\sqrt{\left(\frac{x^2}{c^2}+\frac{y^2}{c^2}-1\right)^2+4\frac{y^2}{c^2}}}{2}}\right), \\ &-\frac{a+b}{c}\left(\sqrt{\frac{\left(\frac{x^2}{c^2}+\frac{y^2}{c^2}-1\right)+\sqrt{\left(\frac{x^2}{c^2}+\frac{y^2}{c^2}-1\right)^2+4\frac{y^2}{c^2}}}{2}}\right) \end{aligned} \tag{7.12}$$

where a and b are the half-lengths of the long and short axes of the elliptical fault, respectively.

7.2 The Long Axis of an Elliptical Inclusion Is Parallel to the Inflow in the Far Field

Substituting the inverse mappings into (6.40), (6.41), (6.42), (6.43), (6.44), (6.45), (6.46) and (6.47) in Chap. 6, the following analytical solutions, which are expressed in a conventional Cartesian coordinate system for the excessive pore-fluid pressure, pore-fluid velocity and stream function around an elliptical fault, can be obtained when the long axis of the fault is parallel to the inflow direction in the undisturbed far field.

$$p_{in}(x,y) = -\omega_x\left(\frac{\beta+1}{\beta+\alpha}\right)x, \tag{7.13}$$

$$\begin{aligned} p_{out}(x,y) = &-\omega_x x \\ &+\omega_x \mathrm{sgn}\left(\frac{x}{c}\right)\frac{(\alpha-1)(a+b)a}{(\beta+\alpha)c}\left(\frac{x}{c}\mathrm{sgn}\left(\frac{x}{c}\right)-\sqrt{\frac{\left(\frac{x^2}{c^2}-\frac{y^2}{c^2}-1\right)+\sqrt{\left(\frac{x^2}{c^2}+\frac{y^2}{c^2}-1\right)^2+4\frac{y^2}{c^2}}}{2}}\right), \end{aligned} \tag{7.14}$$

$$u_x^{in}(x,y) = \frac{\omega_x K_{in}}{\mu}\left(\frac{\beta+1}{\beta+\alpha}\right), \tag{7.15}$$

$$u_y^{in}(x,y) = 0, \tag{7.16}$$

$$u_x^{out}(x,y) = \frac{\omega_x K_{out}}{\mu}\left\{1+\frac{(\alpha-1)(a+b)a}{(\beta+\alpha)c^2}\left(\frac{x}{c}\operatorname{sgn}\left(\frac{x}{c}\right)\right)\sqrt{\frac{\left(\frac{x^2}{c^2}-\frac{y^2}{c^2}-1\right)+\sqrt{\left(\frac{x^2}{c^2}+\frac{y^2}{c^2}-1\right)^2+4\frac{y^2}{c^2}}}{2\left(\frac{x^2}{c^2}+\frac{y^2}{c^2}-1\right)^2+8\frac{y^2}{c^2}}}\right\},$$
$$+\frac{\omega_x K_{out}}{\mu}\left\{\frac{(\alpha-1)(a+b)a}{(\beta+\alpha)c^2}\left(\frac{y}{c}\operatorname{sgn}\left(\frac{y}{c}\right)\sqrt{\frac{\left(-\frac{x^2}{c^2}+\frac{y^2}{c^2}+1\right)+\sqrt{\left(\frac{x^2}{c^2}+\frac{y^2}{c^2}-1\right)^2+4\frac{y^2}{c^2}}}{2\left(\frac{x^2}{c^2}+\frac{y^2}{c^2}-1\right)^2+8\frac{y^2}{c^2}}}-1\right)\right\} \tag{7.17}$$

$$u_y^{out}(x,y) = \frac{\omega_x K_{out}}{\mu}\left(\frac{(\alpha-1)(a+b)a}{(\beta+\alpha)c^2}\left(\frac{x}{c}\operatorname{sgn}\left(\frac{y}{c}\right)\right)\sqrt{\frac{\left(-\frac{x^2}{c^2}+\frac{y^2}{c^2}+1\right)+\sqrt{\left(\frac{x^2}{c^2}+\frac{y^2}{c^2}-1\right)^2+4\frac{y^2}{c^2}}}{2\left(\frac{x^2}{c^2}+\frac{y^2}{c^2}-1\right)^2+8\frac{y^2}{c^2}}}\right),$$
$$-\frac{\omega_x K_{out}}{\mu}\left(\frac{(\alpha-1)(a+b)a}{(\beta+\alpha)c^2}\left(\frac{y}{c}\operatorname{sgn}\left(\frac{x}{c}\right)\right)\sqrt{\frac{\left(\frac{x^2}{c^2}-\frac{y^2}{c^2}-1\right)+\sqrt{\left(\frac{x^2}{c^2}+\frac{y^2}{c^2}-1\right)^2+4\frac{y^2}{c^2}}}{2\left(\frac{x^2}{c^2}+\frac{y^2}{c^2}-1\right)^2+8\frac{y^2}{c^2}}}\right) \tag{7.18}$$

$$\psi_{in}(x,y) = \frac{\omega_x K_{in}}{\mu}\left(\frac{\beta+1}{\beta+\alpha}\right)y + C, \tag{7.19}$$

$$\psi_{out}(x,y) = \frac{\omega_x K_{out}}{\mu}\left(y+\operatorname{sgn}\left(\frac{y}{c}\right)\frac{(\alpha-1)(a+b)a}{(\beta+\alpha)c}\sqrt{\frac{\left(-\frac{x^2}{c^2}+\frac{y^2}{c^2}+1\right)+\sqrt{\left(\frac{x^2}{c^2}+\frac{y^2}{c^2}-1\right)^2+4\frac{y^2}{c^2}}}{2}}\right)$$
$$-\frac{\omega_x K_{out}}{\mu}\left(\operatorname{sgn}\left(\frac{y}{c}\right)\frac{(\alpha-1)(a+b)a}{(\beta+\alpha)c}\left(\operatorname{sgn}\left(\frac{y}{c}\right)\frac{y}{c}\right)\right)+C \tag{7.20}$$

If two elliptical faults have the same aspect ratio β, then these two faults are referred to as similar faults geometrically. For these faults, the following relationships exist:

$$\frac{a}{c} = \sqrt{\frac{\beta^2}{\beta^2 - 1}}, \quad \frac{b}{c} = \sqrt{\frac{1}{\beta^2 - 1}}. \tag{7.21}$$

In the case where the inflow is parallel to the long axis of an elliptical crack, Fig. 7.1 shows the effect of the permeability ratio on streamlines and excess pore-fluid pressure distributions around and within the crack. In this figure, except

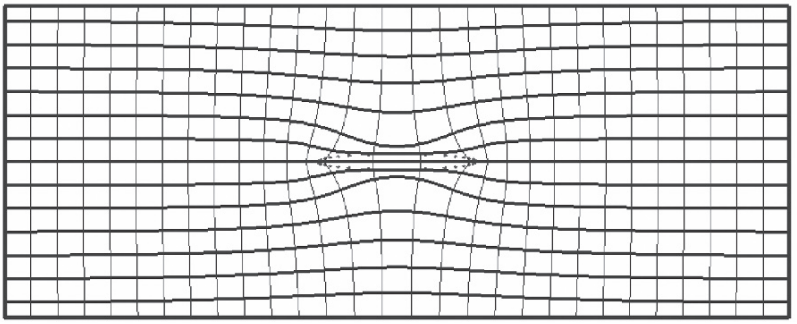

$(K_{in} / K_{out} = 10)$

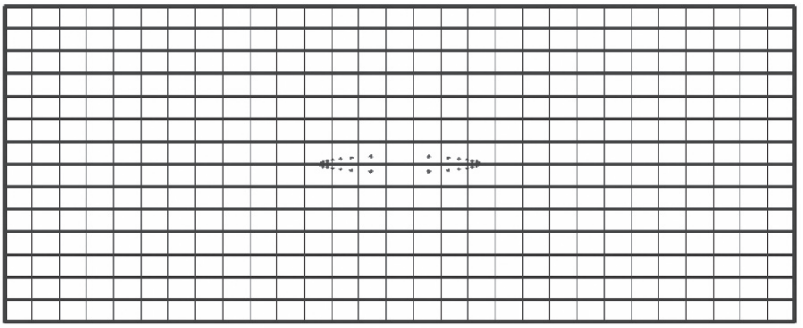

$(K_{in} / K_{out} = 1)$

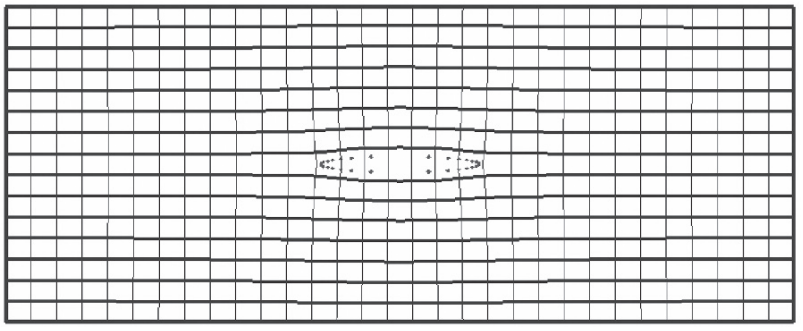

$(K_{in} / K_{out} = 0.1)$

Fig. 7.1 Effect of permeability ratio on streamline and pressure patterns around and within an elliptical inclusion (inflow is parallel to the long axis)

for the domain boundaries, thick lines are used to show streamlines, while thin lines are used to show the equal value lines of the excess pore-fluid pressure (i.e., isopotential lines). Dot points are used to show the outline of the elliptical crack. The aspect ratio of the crack is assumed to be 10 and three different permeability ratios, namely $\alpha = 10$, $\alpha = 1$ and $\alpha = 0.1$, are used to produce the numerical results. The present analytical solution clearly indicates that although the amplitude of the excess pore-fluid pressure gradient of the inflow may affect the absolute values of the excess pore-fluid pressure and stream function, it does not affect their distribution patterns around and within large cracks and faults. For this reason, the amplitude of the excess pore-fluid pressure gradient of the inflow is assumed to be unity to produce the numerical results shown in Fig. 7.1. It is obvious that in the case of the crack being permeable, the inflow is focused into the crack, while in the case of the crack being impermeable, the pore-fluid flow within the crack becomes weaker than the inflow from the far field. As expected, if the permeability of the crack is exactly the same as that of its surrounding rock, the crack has no influence on the inflow field within the whole problem domain.

It can be recognized, from the present analytical solutions that, within an elliptical crack, both the excess pore-fluid pressure distribution and the pore-fluid flow pattern, which are expressed by either excess pore-fluid pressure distributions or streamlines, are only dependent on the aspect and permeability ratios of the crack, and are independent of the specific size of the crack (see (7.13) and (7.19)). This is because a and b, which are used to define the aspect ratio of an elliptical crack, are specified as a fraction of L, where L is the length of the crack. Thus, if we define cracks of the same aspect and permeability ratios as similar cracks, then excess pore-fluid pressure distributions and pore-fluid flow patterns are exactly the same within similar cracks. We call this conclusion the similarity theory for a crack. This theory lays an important theoretical foundation of extending the present analytical solutions to deal with pore-fluid flow patterns within large cracks and faults in pore-fluid saturated porous rocks.

7.3 The Short Axis of an Elliptical Inclusion Is Parallel to the Inflow in the Far Field

Following the same procedures as those used in the previous sections, analytical solutions for the stream function, excess pore-fluid pressure and velocity around and within an elliptical inclusion can be obtained in a conventional Cartesian coordinate system.

$$u_x^{in}(x,y) = 0, \tag{7.22}$$

$$u_y^{in}(x,y) = \frac{\omega_y K_{in}}{\mu}\left(\frac{\beta+1}{1+\alpha\beta}\right), \tag{7.23}$$

$$u_x^{out}(x,y) = \frac{\omega_y K_{out}}{\mu}\left[\frac{(\alpha-1)(a+b)a}{(1+\alpha\beta)c^2}\left(\frac{x}{c}\operatorname{sgn}\left(\frac{y}{c}\right)\sqrt{\frac{\left(-\frac{x^2}{c^2}+\frac{y^2}{c^2}+1\right)+\sqrt{\left(\frac{x^2}{c^2}+\frac{y^2}{c^2}-1\right)^2+4\frac{y^2}{c^2}}}{2\left(\frac{x^2}{c^2}+\frac{y^2}{c^2}-1\right)^2+8\frac{y^2}{c^2}}}\right)\right],$$
$$-\frac{\omega_y K_{out}}{\mu}\left[\frac{(\alpha-1)(a+b)a}{(1+\alpha\beta)c^2}\left(\frac{y}{c}\operatorname{sgn}\left(\frac{x}{c}\right)\sqrt{\frac{\left(\frac{x^2}{c^2}-\frac{y^2}{c^2}-1\right)+\sqrt{\left(\frac{x^2}{c^2}+\frac{y^2}{c^2}-1\right)^2+4\frac{y^2}{c^2}}}{2\left(\frac{x^2}{c^2}+\frac{y^2}{c^2}-1\right)^2+8\frac{y^2}{c^2}}}\right)\right] \tag{7.24}$$

$$u_y^{out}(x,y) = \frac{\omega_y K_{out}}{\mu}\left[1-\frac{(\alpha-1)(a+b)a}{(1+\alpha\beta)c^2}\left(\frac{x}{c}\operatorname{sgn}\left(\frac{x}{c}\right)\sqrt{\frac{\left(\frac{x^2}{c^2}-\frac{y^2}{c^2}-1\right)+\sqrt{\left(\frac{x^2}{c^2}+\frac{y^2}{c^2}-1\right)^2+4\frac{y^2}{c^2}}}{2\left(\frac{x^2}{c^2}+\frac{y^2}{c^2}-1\right)^2+8\frac{y^2}{c^2}}}\right)\right],$$
$$+\frac{\omega_y K_{out}}{\mu}\left[\frac{(\alpha-1)(a+b)a}{(1+\alpha\beta)c^2}\left(\frac{y}{c}\operatorname{sgn}\left(\frac{y}{c}\right)\sqrt{\frac{\left(-\frac{x^2}{c^2}+\frac{y^2}{c^2}+1\right)+\sqrt{\left(\frac{x^2}{c^2}+\frac{y^2}{c^2}-1\right)^2+4\frac{y^2}{c^2}}}{2\left(\frac{x^2}{c^2}+\frac{y^2}{c^2}-1\right)^2+8\frac{y^2}{c^2}}}-1\right)\right] \tag{7.25}$$

$$\psi_{in}(x,y) = -\frac{\omega_y K_{in}}{\mu}\left(\frac{\beta+1}{1+\alpha\beta}\right)x + C, \tag{7.26}$$

$$\psi_{out}(x,y) = -\frac{\omega_y K_{out}}{\mu}x$$
$$+\frac{\omega_y K_{out}}{\mu}\operatorname{sgn}\left(\frac{x}{c}\right)\frac{(\alpha-1)(a+b)a}{(1+\alpha\beta)c}\left[\sqrt{\frac{\left(\frac{x^2}{c^2}-\frac{y^2}{c^2}-1\right)+\sqrt{\left(\frac{x^2}{c^2}+\frac{y^2}{c^2}-1\right)^2+4\frac{y^2}{c^2}}}{2}}-\operatorname{sgn}\left(\frac{x}{c}\right)\frac{x}{c}\right]+C, \tag{7.27}$$

$$p_{in}(x,y) = -\omega_y\left(\frac{\beta+1}{1+\alpha\beta}\right)y, \tag{7.28}$$

$$p_{out}(x,y) = -\omega_y y$$
$$+\omega_y\operatorname{sgn}\left(\frac{y}{c}\right)\frac{(\alpha-1)(a+b)a}{(1+\alpha\beta)c}\left[\sqrt{\frac{\left(-\frac{x^2}{c^2}+\frac{y^2}{c^2}+1\right)+\sqrt{\left(\frac{x^2}{c^2}+\frac{y^2}{c^2}-1\right)^2+4\frac{y^2}{c^2}}}{2}}-\operatorname{sgn}\left(\frac{y}{c}\right)\frac{y}{c}\right] \tag{7.29}$$

where ω_y is the amplitude (i.e., $\left|\partial p / \partial y\right|$ in this particular case) of the excess pore-fluid pressure gradient in the far field of the elliptical inclusion. Other quantities have the same meanings as defined before.

To compare the analytical results in the case of the inflow being parallel to the short axis with those in the case of the inflow being parallel to the long axis, the aspect ratio of the elliptical crack remains equal to 10. The same three permeability

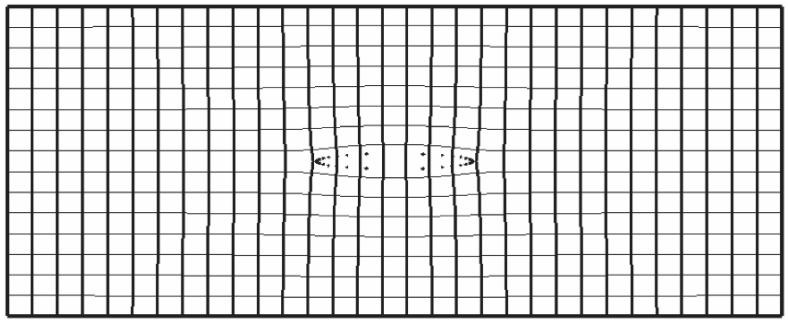

($K_{in} / K_{out} = 10$)

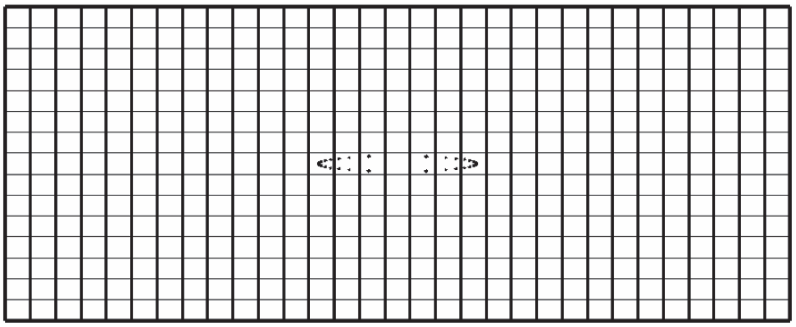

($K_{in} / K_{out} = 1$)

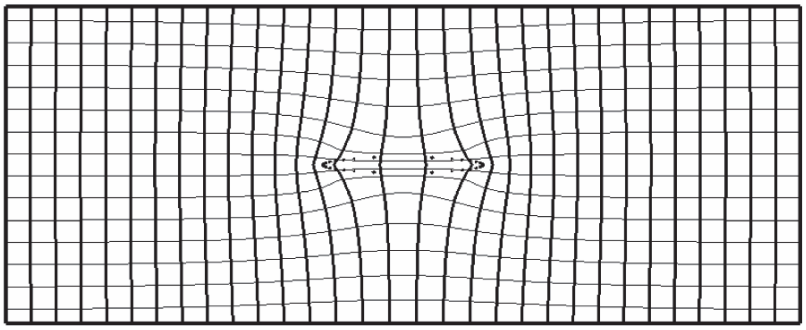

($K_{in} / K_{out} = 0.1$)

Fig. 7.2 Effect of permeability ratio on streamline and pressure patterns around and within an elliptical inclusion (inflow is parallel to the short axis)

ratios, namely $\alpha = 10,\ \alpha = 1$ and $\alpha = 0.1$, are used to produce the numerical results in this section. Figure 7.2 shows the effect of the permeability ratio on streamlines and excess pore-fluid pressure distributions around and within the crack. It is observed that in the case of the crack being either permeable or impermeable, the crack only has a small local effect on the inflow that is parallel to the short axis of the crack. The influence of the crack on the inflow parallel to the short axis is much weaker than that on the inflow parallel to the long axis of the crack. This is illustrated by comparing the results of Fig. 7.1 with those in Fig. 7.2.

In addition, the analytical solutions expressed in (7.26) and (7.28) also indicate that both the pore-fluid flow pattern and the excess pore-fluid pressure distribution within a large crack are only dependent on the aspect and permeability ratios of the crack, but independent of the specific size of the crack. This demonstrates that the similarity theory of a crack is valid when the inflow (in the far field) is parallel to the short axis of the crack in pore-fluid saturated porous rocks.

7.4 The Inflow of the Far Field Is Parallel to the X Direction of the Global XY Coordinate System

Superposing the analytical solutions derived in the previous two sections yields the analytical solutions for pore-fluid flow around and within an inclined elliptical inclusion when the inflow of the far field is parallel to the X direction of the global XY coordinate system.

$$\psi_{in} = \frac{\omega_X K_{in}}{\mu}\left[\left(\frac{\beta+1}{\beta+\alpha}\right) y\cos\theta + \left(\frac{\beta+1}{1+\alpha\beta}\right) x\sin\theta\right] + C \qquad \left(\frac{x^2}{a^2}+\frac{y^2}{b^2} < 1\right), \tag{7.30}$$

$$\begin{aligned}\psi_{out} = {} & \frac{\omega_X K_{out}}{\mu} y\cos\theta + \frac{\omega_X K_{out}}{\mu} x\sin\theta \\ & + \frac{\omega_X K_{out}}{\mu}\frac{(\alpha-1)(a+b)a}{(\beta+\alpha)c}\operatorname{sgn}\left(\frac{y}{c}\right)\left(\sqrt{\frac{\left(-\frac{x^2}{c^2}+\frac{y^2}{c^2}+1\right)+\sqrt{\left(\frac{x^2}{c^2}+\frac{y^2}{c^2}-1\right)^2+4\frac{y^2}{c^2}}}{2}} - \operatorname{sgn}\left(\frac{y}{c}\right)\frac{y}{c}\right)\cos\theta \\ & - \frac{\omega_X K_{out}}{\mu}\operatorname{sgn}\left(\frac{x}{c}\right)\frac{(\alpha-1)(a+b)a}{(1+\alpha\beta)c}\left(\sqrt{\frac{\left(\frac{x^2}{c^2}-\frac{y^2}{c^2}-1\right)+\sqrt{\left(\frac{x^2}{c^2}+\frac{y^2}{c^2}-1\right)^2+4\frac{y^2}{c^2}}}{2}} - \operatorname{sgn}\left(\frac{x}{c}\right)\frac{x}{c}\right)\sin\theta + C \\ & \qquad \left(\frac{x^2}{a^2}+\frac{y^2}{b^2} \geq 1\right),\end{aligned} \tag{7.31}$$

$$p_{in} = -\omega_X\left(\frac{\beta+1}{\beta+\alpha}\right) x\cos\theta + \omega_X\left(\frac{1+\beta}{1+\alpha\beta}\right) y\sin\theta \qquad \left(\frac{x^2}{a^2}+\frac{y^2}{b^2} < 1\right), \tag{7.32}$$

$$
\begin{aligned}
p_{out} = & -\omega_X x\cos\theta + \omega_X y\sin\theta \\
& + \omega_X \operatorname{sgn}\left(\frac{x}{c}\right)\frac{(\alpha-1)(a+b)a}{(\beta+\alpha)c}\left(\frac{x}{c}\operatorname{sgn}\left(\frac{x}{c}\right) - \sqrt{\frac{\left(\frac{x^2}{c^2}-\frac{y^2}{c^2}-1\right)+\sqrt{\left(\frac{x^2}{c^2}+\frac{y^2}{c^2}-1\right)^2+4\frac{y^2}{c^2}}}{2}}\right)\cos\theta \\
& - \omega_X \operatorname{sgn}\left(\frac{y}{c}\right)\frac{(\alpha-1)(a+b)a}{(1+\alpha\beta)c}\left(\sqrt{\frac{\left(-\frac{x^2}{c^2}+\frac{y^2}{c^2}+1\right)+\sqrt{\left(\frac{x^2}{c^2}+\frac{y^2}{c^2}-1\right)^2+4\frac{y^2}{c^2}}}{2}} - \operatorname{sgn}\left(\frac{y}{c}\right)\frac{y}{c}\right)\sin\theta \\
& \left(\frac{x^2}{a^2}+\frac{y^2}{b^2}\geq 1\right), \qquad (7.33)
\end{aligned}
$$

$$
u_x^{in} = \frac{\omega_X K_{in}}{\mu}\left(\frac{\beta+1}{\beta+\alpha}\right)\cos\theta \qquad \left(\frac{x^2}{a^2}+\frac{y^2}{b^2}<1\right), \qquad (7.34)
$$

$$
u_y^{in} = -\frac{\omega_X K_{in}}{\mu}\left(\frac{1+\beta}{1+\alpha\beta}\right)\sin\theta \qquad \left(\frac{x^2}{a^2}+\frac{y^2}{b^2}<1\right), \qquad (7.35)
$$

$$
\begin{aligned}
u_x^{out} = & \frac{\omega_X K_{out}}{\mu}\left\{1+\frac{(\alpha-1)(a+b)a}{(\beta+\alpha)c^2}\left(\frac{x}{c}\operatorname{sgn}(\frac{x}{c})\sqrt{\frac{\left(\frac{x^2}{c^2}-\frac{y^2}{c^2}-1\right)+\sqrt{\left(\frac{x^2}{c^2}+\frac{y^2}{c^2}-1\right)^2+4\frac{y^2}{c^2}}}{2\left(\frac{x^2}{c^2}+\frac{y^2}{c^2}-1\right)^2+8\frac{y^2}{c^2}}}\right)\right\}\cos\theta \\
& + \frac{\omega_X K_{out}}{\mu}\left\{\frac{(\alpha-1)(a+b)a}{(\beta+\alpha)c^2}\left(\frac{y}{c}\operatorname{sgn}(\frac{y}{c})\sqrt{\frac{\left(-\frac{x^2}{c^2}+\frac{y^2}{c^2}+1\right)+\sqrt{\left(\frac{x^2}{c^2}+\frac{y^2}{c^2}-1\right)^2+4\frac{y^2}{c^2}}}{2\left(\frac{x^2}{c^2}+\frac{y^2}{c^2}-1\right)^2+8\frac{y^2}{c^2}}}-1\right)\right\}\cos\theta \\
& - \frac{\omega_X K_{out}}{\mu}\left\{\frac{(\alpha-1)(a+b)a}{(1+\alpha\beta)c^2}\left(\frac{x}{c}\operatorname{sgn}(\frac{y}{c})\sqrt{\frac{\left(-\frac{x^2}{c^2}+\frac{y^2}{c^2}+1\right)+\sqrt{\left(\frac{x^2}{c^2}+\frac{y^2}{c^2}-1\right)^2+4\frac{y^2}{c^2}}}{2\left(\frac{x^2}{c^2}+\frac{y^2}{c^2}-1\right)^2+8\frac{y^2}{c^2}}}\right)\right\}\sin\theta \\
& + \frac{\omega_X K_{out}}{\mu}\left\{\frac{(\alpha-1)(a+b)a}{(1+\alpha\beta)c^2}\left(\frac{y}{c}\operatorname{sgn}(\frac{x}{c})\sqrt{\frac{\left(\frac{x^2}{c^2}-\frac{y^2}{c^2}-1\right)+\sqrt{\left(\frac{x^2}{c^2}+\frac{y^2}{c^2}-1\right)^2+4\frac{y^2}{c^2}}}{2\left(\frac{x^2}{c^2}+\frac{y^2}{c^2}-1\right)^2+8\frac{y^2}{c^2}}}\right)\right\}\sin\theta \\
& (\frac{x^2}{a^2}+\frac{y^2}{b^2}\geq 1), \qquad (7.36)
\end{aligned}
$$

$$u_y^{out} = \frac{\omega_X K_{out}}{\mu}\left\{\frac{(\alpha-1)(a+b)a}{(\beta+\alpha)c^2}\left(\frac{x}{c}\mathrm{sgn}(\frac{y}{c})\sqrt{\frac{\left(-\frac{x^2}{c^2}+\frac{y^2}{c^2}+1\right)+\sqrt{\left(\frac{x^2}{c^2}+\frac{y^2}{c^2}-1\right)^2+4\frac{y^2}{c^2}}}{2\left(\frac{x^2}{c^2}+\frac{y^2}{c^2}-1\right)^2+8\frac{y^2}{c^2}}}\right)\right\}\cos\theta$$
$$-\frac{\omega_X K_{out}}{\mu}\left\{\frac{(\alpha-1)(a+b)a}{(\beta+\alpha)c^2}\left(\frac{y}{c}\mathrm{sgn}(\frac{x}{c})\sqrt{\frac{\left(\frac{x^2}{c^2}-\frac{y^2}{c^2}-1\right)+\sqrt{\left(\frac{x^2}{c^2}+\frac{y^2}{c^2}-1\right)^2+4\frac{y^2}{c^2}}}{2\left(\frac{x^2}{c^2}+\frac{y^2}{c^2}-1\right)^2+8\frac{y^2}{c^2}}}\right)\right\}\cos\theta$$
$$-\frac{\omega_X K_{out}}{\mu}\left\{1-\frac{(\alpha-1)(a+b)a}{(1+\alpha\beta)c^2}\left(\frac{x}{c}\mathrm{sgn}(\frac{x}{c})\sqrt{\frac{\left(\frac{x^2}{c^2}-\frac{y^2}{c^2}-1\right)+\sqrt{\left(\frac{x^2}{c^2}+\frac{y^2}{c^2}-1\right)^2+4\frac{y^2}{c^2}}}{2\left(\frac{x^2}{c^2}+\frac{y^2}{c^2}-1\right)^2+8\frac{y^2}{c^2}}}\right)\right\}\sin\theta$$
$$+\frac{\omega_X K_{out}}{\mu}\left\{\frac{(\alpha-1)(a+b)a}{(1+\alpha\beta)c^2}\left(\frac{y}{c}\mathrm{sgn}(\frac{y}{c})\sqrt{\frac{\left(-\frac{x^2}{c^2}+\frac{y^2}{c^2}+1\right)+\sqrt{\left(\frac{x^2}{c^2}+\frac{y^2}{c^2}-1\right)^2+4\frac{y^2}{c^2}}}{2\left(\frac{x^2}{c^2}+\frac{y^2}{c^2}-1\right)^2+8\frac{y^2}{c^2}}}-1\right)\right\}\sin\theta$$
$$(\frac{x^2}{a^2}+\frac{y^2}{b^2}\geq 1). \tag{7.37}$$

7.5 The Inflow of the Far Field Is Parallel to the Y Direction of the Global XY Coordinate System

Similarly, superposing the analytical solutions derived in the previous two sections (i.e. Sections 7.2 and 7.3) yields the analytical solutions for pore-fluid flow around and within an inclined elliptical inclusion when the inflow of the far field is parallel to the Y direction of the global XY coordinate system.

$$\psi_{in} = \frac{\omega_Y K_{in}}{\mu}\left[\left(\frac{\beta+1}{\beta+\alpha}\right)y\sin\theta-\left(\frac{\beta+1}{1+\alpha\beta}\right)x\cos\theta\right]+C \qquad (\frac{x^2}{a^2}+\frac{y^2}{b^2}<1), \tag{7.38}$$

$$\psi_{out} = \frac{\omega_Y K_{out}}{\mu}y\sin\theta-\frac{\omega_Y K_{out}}{\mu}x\cos\theta$$
$$+\frac{\omega_Y K_{out}}{\mu}\frac{(\alpha-1)(a+b)a}{(\beta+\alpha)c}\mathrm{sgn}(\frac{y}{c})\left(\sqrt{\frac{\left(-\frac{x^2}{c^2}+\frac{y^2}{c^2}+1\right)+\sqrt{\left(\frac{x^2}{c^2}+\frac{y^2}{c^2}-1\right)^2+4\frac{y^2}{c^2}}}{2}}-\mathrm{sgn}(\frac{y}{c})\frac{y}{c}\right)\sin\theta$$
$$+\frac{\omega_Y K_{out}}{\mu}\frac{(\alpha-1)(a+b)a}{(1+\alpha\beta)c}\mathrm{sgn}(\frac{x}{c})\left(\sqrt{\frac{\left(\frac{x^2}{c^2}-\frac{y^2}{c^2}-1\right)+\sqrt{\left(\frac{x^2}{c^2}+\frac{y^2}{c^2}-1\right)^2+4\frac{y^2}{c^2}}}{2}}-\mathrm{sgn}(\frac{x}{c})\frac{x}{c}\right)\cos\theta+C$$
$$(\frac{x^2}{a^2}+\frac{y^2}{b^2}\geq 1), \tag{7.39}$$

$$p_{in} = -\omega_Y \left(\frac{\beta+1}{\beta+\alpha}\right) x\sin\theta - \omega_Y \left(\frac{1+\beta}{1+\alpha\beta}\right) y\cos\theta \qquad (\frac{x^2}{a^2}+\frac{y^2}{b^2}<1), \tag{7.40}$$

$$\begin{aligned} p_{out} &= -\omega_Y x\sin\theta - \omega_Y y\cos\theta \\ &+ \omega_Y \mathrm{sgn}(\tfrac{x}{c})\frac{(\alpha-1)(a+b)a}{(\beta+\alpha)c}\left(\frac{x}{c}\mathrm{sgn}(\frac{x}{c}) - \sqrt{\frac{\left(\frac{x^2}{c^2}-\frac{y^2}{c^2}-1\right)+\sqrt{\left(\frac{x^2}{c^2}+\frac{y^2}{c^2}-1\right)^2+4\frac{y^2}{c^2}}}{2}}\right)\sin\theta \\ &+ \omega_Y \mathrm{sgn}(\tfrac{y}{c})\frac{(\alpha-1)(a+b)a}{(1+\alpha\beta)c}\left(\sqrt{\frac{\left(-\frac{x^2}{c_2}+\frac{y^2}{c^2}+1\right)+\sqrt{\left(\frac{x^2}{c^2}+\frac{y^2}{c^2}-1\right)^2+4\frac{y^2}{c^2}}}{2}} - \mathrm{sgn}(\tfrac{y}{c})\frac{y}{c}\right)\cos\theta \\ &\qquad (\frac{x^2}{a^2}+\frac{y^2}{b^2}\geq 1), \end{aligned} \tag{7.41}$$

$$u_x^{in} = \frac{\omega_Y K_{in}}{\mu}\left(\frac{\beta+1}{\beta+\alpha}\right)\sin\theta \qquad (\frac{x^2}{a^2}+\frac{y^2}{b^2}<1), \tag{7.42}$$

$$u_y^{in} = \frac{\omega_Y K_{in}}{\mu}\left(\frac{1+\beta}{1+\alpha\beta}\right)\cos\theta \qquad (\frac{x^2}{a^2}+\frac{y^2}{b^2}<1), \tag{7.43}$$

$$\begin{aligned} u_x^{out} &= \frac{\omega_Y K_{out}}{\mu}\left\{1+\frac{(\alpha-1)(a+b)a}{(\beta+\alpha)c^2}\left(\frac{x}{c}\mathrm{sgn}(\frac{x}{c})\sqrt{\frac{\left(\frac{x^2}{c^2}-\frac{y^2}{c^2}-1\right)+\sqrt{\left(\frac{x^2}{c^2}+\frac{y^2}{c^2}-1\right)^2+4\frac{y^2}{c^2}}}{2\left(\frac{x^2}{c^2}+\frac{y^2}{c^2}-1\right)^2+8\frac{y^2}{c^2}}}\right)\right\}\sin\theta \\ &+ \frac{\omega_Y K_{out}}{\mu}\left\{\frac{(\alpha-1)(a+b)a}{(\beta+\alpha)c^2}\left(\frac{y}{c}\mathrm{sgn}(\frac{y}{c})\sqrt{\frac{\left(-\frac{x^2}{c^2}+\frac{y^2}{c^2}+1\right)+\sqrt{\left(\frac{x^2}{c^2}+\frac{y^2}{c^2}-1\right)^2+4\frac{y^2}{c^2}}}{2\left(\frac{x^2}{c^2}+\frac{y^2}{c^2}-1\right)^2+8\frac{y^2}{c^2}}}-1\right)\right\}\sin\theta \\ &+ \frac{\omega_Y K_{out}}{\mu}\left\{\frac{(\alpha-1)(a+b)a}{(1+\alpha\beta)c^2}\left(\frac{x}{c}\mathrm{sgn}(\frac{y}{c})\sqrt{\frac{\left(-\frac{x^2}{c^2}+\frac{y^2}{c^2}+1\right)+\sqrt{\left(\frac{x^2}{c^2}+\frac{y^2}{c^2}-1\right)^2+4\frac{y^2}{c^2}}}{2\left(\frac{x^2}{c^2}+\frac{y^2}{c^2}-1\right)^2+8\frac{y^2}{c^2}}}\right)\right\}\cos\theta \\ &- \frac{\omega_Y K_{out}}{\mu}\left\{\frac{(\alpha-1)(a+b)a}{(1+\alpha\beta)c^2}\left(\frac{y}{c}\mathrm{sgn}(\frac{x}{c})\sqrt{\frac{\left(\frac{x^2}{c^2}-\frac{y^2}{c^2}-1\right)+\sqrt{\left(\frac{x^2}{c^2}+\frac{y^2}{c^2}-1\right)^2+4\frac{y^2}{c^2}}}{2\left(\frac{x^2}{c^2}+\frac{y^2}{c^2}-1\right)^2+8\frac{y^2}{c^2}}}\right)\right\}\cos\theta \\ &\qquad (\frac{x^2}{a^2}+\frac{y^2}{b^2}\geq 1), \end{aligned} \tag{7.44}$$

$$u_y^{out} = \frac{\omega_\gamma K_{out}}{\mu}\left\{\frac{(\alpha-1)(a+b)a}{(\beta+\alpha)c^2}\left(\frac{x}{c}\mathrm{sgn}(\frac{y}{c})\sqrt{\frac{\left(-\frac{x^2}{c^2}+\frac{y^2}{c^2}+1\right)+\sqrt{\left(\frac{x^2}{c^2}+\frac{y^2}{c^2}-1\right)^2+4\frac{y^2}{c^2}}}{2\left(\frac{x^2}{c^2}+\frac{y^2}{c^2}-1\right)^2+8\frac{y^2}{c^2}}}\right)\right\}\sin\theta$$

$$-\frac{\omega_\gamma K_{out}}{\mu}\left\{\frac{(\alpha-1)(a+b)a}{(\beta+\alpha)c^2}\left(\frac{y}{c}\mathrm{sgn}(\frac{x}{c})\sqrt{\frac{\left(\frac{x^2}{c^2}-\frac{y^2}{c^2}-1\right)+\sqrt{\left(\frac{x^2}{c^2}+\frac{y^2}{c^2}-1\right)^2+4\frac{y^2}{c^2}}}{2\left(\frac{x^2}{c^2}+\frac{y^2}{c^2}-1\right)^2+8\frac{y^2}{c^2}}}\right)\right\}\sin\theta$$

$$+\frac{\omega_\gamma K_{out}}{\mu}\left\{1-\frac{(\alpha-1)(a+b)a}{(1+\alpha\beta)c^2}\left(\frac{x}{c}\mathrm{sgn}(\frac{x}{c})\sqrt{\frac{\left(\frac{x^2}{c^2}-\frac{y^2}{c^2}-1\right)+\sqrt{\left(\frac{x^2}{c^2}+\frac{y^2}{c^2}-1\right)^2+4\frac{y^2}{c^2}}}{2\left(\frac{x^2}{c^2}+\frac{y^2}{c^2}-1\right)^2+8\frac{y^2}{c^2}}}\right)\right\}\cos\theta$$

$$-\frac{\omega_\gamma K_{out}}{\mu}\left\{\frac{(\alpha-1)(a+b)a}{(1+\alpha\beta)c^2}\left(\frac{y}{c}\mathrm{sgn}(\frac{y}{c})\sqrt{\frac{\left(-\frac{x^2}{c^2}+\frac{y^2}{c^2}+1\right)+\sqrt{\left(\frac{x^2}{c^2}+\frac{y^2}{c^2}-1\right)^2+4\frac{y^2}{c^2}}}{2\left(\frac{x^2}{c^2}+\frac{y^2}{c^2}-1\right)^2+8\frac{y^2}{c^2}}}-1\right)\right\}\cos\theta$$

$$(\frac{x^2}{a^2}+\frac{y^2}{b^2}\geq 1). \tag{7.45}$$

The pore-fluid pressure gradient can be close to a hydrostatic pressure gradient within a permeable fault (Zhao et al. 1998b; Flemings et al. 2002). For the first time, the present analytical solution has shown that the pore-fluid pressure gradient is exactly equal to the hydrostatic pressure gradient within a fault if the fault is perfectly permeable, implying that the permeability ratio of the fault is infinite. This can be clearly demonstrated from (7.40), where the excess pore-fluid pressure gradient is identical to zero when the permeability ratio (i.e., α in this equation) of a fault of finite size is approaching infinity. However, if a fault is not perfectly permeable, the value of the excess pore-fluid pressure gradient within the fault is non-zero and dependent on the permeability ratio, aspect ratio and dip angle of the inclined fault. This finding demonstrates that the pore-fluid pressure gradient is close to the hydrostatic pressure gradient within a permeable fault of finite size. In this case, the specific value of the pore-fluid pressure within a permeable fault is dependent on the permeability ratio, aspect ratio and dip angle of the inclined fault.

7.6 Application Examples of the Present Analytical Solutions

Since the present analytical solutions are expressed in a conventional Cartesian coordinate system, they provide a useful tool for fundamentally understanding the general distribution pattern of pore-fluid flow and excess pore-fluid pressure around and within a buried inclined fault or crack within the crust of the Earth. From this point of view, the present analytical solutions are used to show the distribution patterns of the excess pore-fluid pressure and stream function around and within an

elliptical inclusion in fluid-saturated porous rocks. Since both the excess pore-fluid pressure and the stream function are dependent on the dip angle, permeability and aspect ratios, several examples are used to show the distribution patterns of the excess pore-fluid pressure and stream function around and within the inclusion. As shown in Fig. 6.2 in Chap. 6, the different dip angles of the elliptical inclusion can be considered by setting the inflow parallel to the X direction in the far field of the global XY coordinate system and varying the dip angle of the inclusion. This means that the analytical solutions expressed in (7.30) and (7.31) can be used to show the distribution pattern of the stream function, while (7.32) and (7.33) can be used to show that of the excess pore-fluid pressure.

In order to investigate the effect of the dip angle on the distribution pattern of both the excess pore-fluid pressure and the stream function, three different dip angles, namely $\theta = 30^\circ,\ \theta = 45^\circ$ and $\theta = 60^\circ$, are considered in the first example, in which the aspect ratio of the inclusion has a constant value of 5 and the permeability ratio of the inclusion to the surrounding rock has a fixed value of 10,000. Figure 7.3 shows the effect of the dip angle on the distribution pattern of the streamlines and excess pore-fluid pressure around and within the elliptical inclusion. In this figure, except for the domain outline expressed using thick lines, the streamlines are shown using thick lines, while the equal value lines of the excess pore-fluid pressure are shown using thin lines. Apart from the near field of the elliptical inclusion, the streamlines are horizontal parallel lines, while the equal value lines of the excess pore-fluid pressure are vertical parallel lines. Dot points are used to show the outline of the elliptical inclusion. This indicates that the inclusion has only a local effect on the overall pore-fluid flow in the fluid-saturated porous rock. Within the elliptical inclusion, the streamlines are parallel to each other. The slope of the streamline is a little smaller than the dip angle of the elliptical inclusion in the case of the inclusion being more permeable (i.e., $\alpha = 10,000$). Clearly, the dip angle of the inclusion can significantly affect the distribution patterns of both the streamlines and the excess pore-fluid pressure around and within the inclusion.

Five different permeability ratios, namely $\alpha = 10,000,\ \alpha = 10,\ \alpha = 1,\ \alpha = 0.1$ and $\alpha = 0$, are considered to examine the effect of the permeability ratio on the distribution patterns of both the streamlines and the excess pore-fluid pressure around and within the elliptical inclusion. In this exercise, the aspect ratio of the elliptical inclusion is kept as a constant of 5, while the dip angle of the inclusion is taken to have three different values (i.e., $\theta = 30^\circ,\ \theta = 45^\circ$ and $\theta = 60^\circ$). In the case of $\alpha = 10,000$, the inclusion is almost perfectly permeable, while in the case of $\alpha = 0$, the inclusion is perfectly impermeable. Compared with the case of $\alpha = 1$, which indicates that the permeability of the inclusion is exactly the same as that of its surrounding rock, $\alpha = 10$ and $\alpha = 0.1$ represent moderately permeable and impermeable inclusions, respectively.

Figures 7.4, 7.5, 7.6 and 7.7 show the effect of permeability ratios on the distribution patterns of both the streamlines and the excess pore-fluid pressure around and within the elliptical inclusion due to three different dip angles. In these figures, thick lines are used to show the streamlines, while thin lines are used to show the equal value lines of the excess pore-fluid pressure. Dot points are used to show the outline

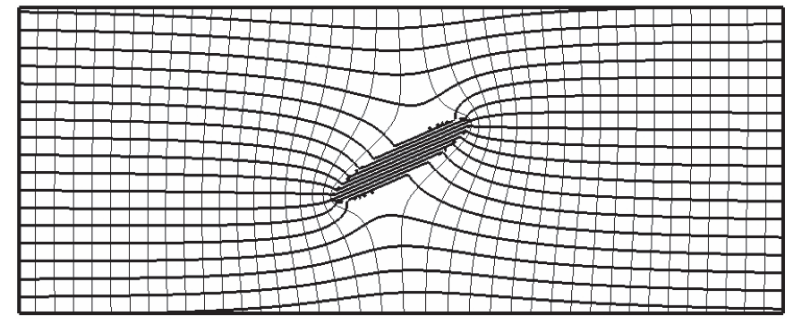

($\theta = 30°$)

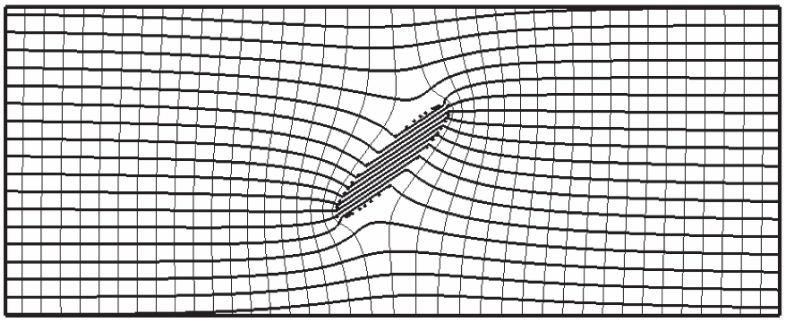

($\theta = 45°$)

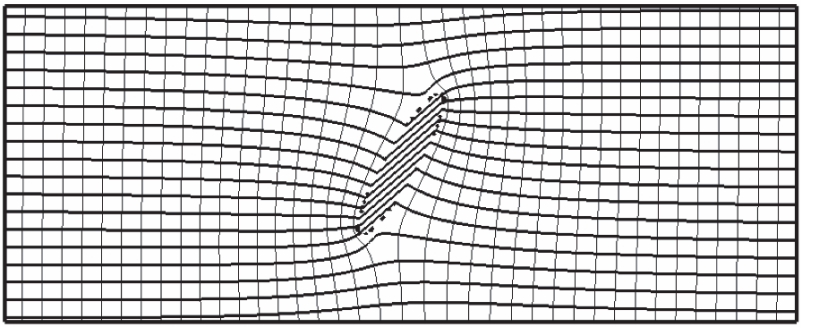

($\theta = 60°$)

Fig. 7.3 Effect of dip angle on streamline and excess pressure patterns around and within an elliptical inclusion ($\alpha = 10000$)

of the inclusion. The permeability ratio of the inclusion to the surrounding rock has a significant influence on the distribution patterns of both the streamlines and the excess pore-fluid pressure around and within the inclusion. Generally, the slope of the streamlines within the elliptical inclusion gradually decreases to zero when the permeability ratio decreases from 10,000 into 1. This slope becomes negative when the inclusion is moderately impermeable (i.e., $\alpha = 0.1$). If the inclusion is perfectly

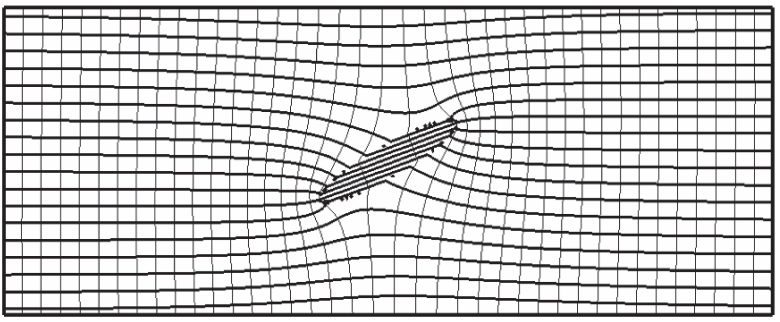

($\theta = 30°$)

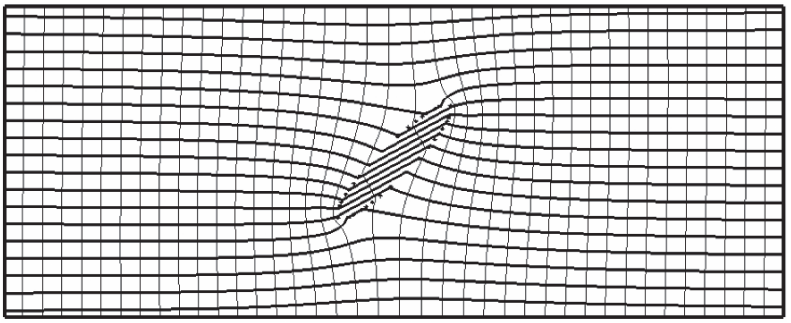

($\theta = 45°$)

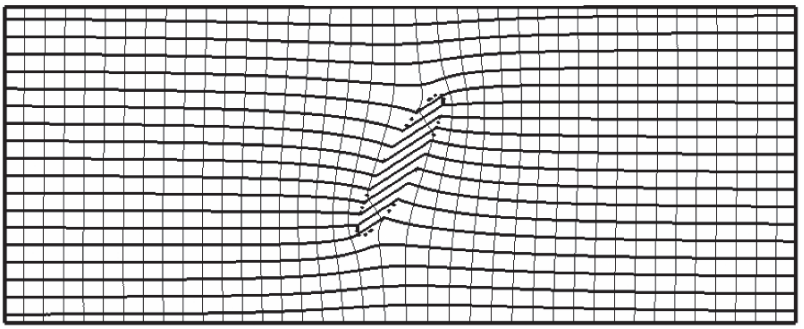

($\theta = 60°$)

Fig. 7.4 Effect of dip angle on streamline and excess pressure patterns around and within an elliptical inclusion ($\alpha = 10$)

impermeable (i.e., $\alpha = 0$), no streamlines exist within the inclusion, as can be seen from the results shown in Fig. 7.7. The slope of the equal value line of the excess pore-fluid pressure is a little greater than the dip angle of the elliptical inclusion in the case of the inclusion being perfectly impermeable (i.e., $\alpha = 0$). In addition, the results shown in Fig. 7.5 indicate that if the permeability of the inclusion is exactly the same as that of the surrounding rock, the inclusion has no influence on the overall pore-fluid flow field.

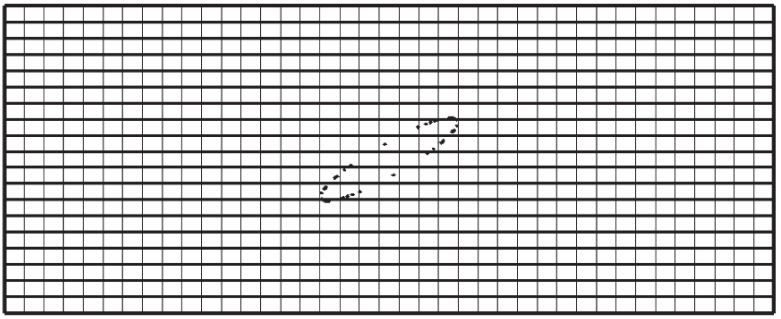

($\theta = 30°$)

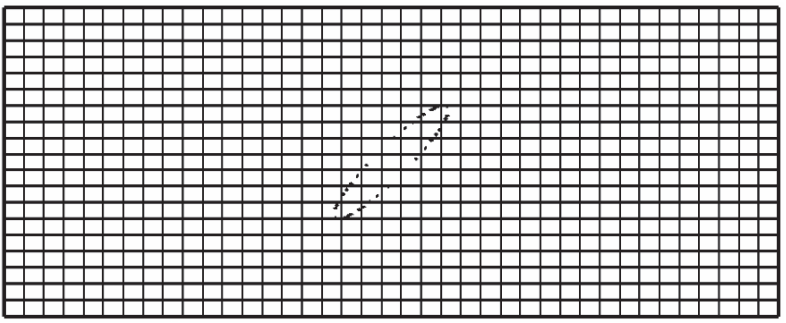

($\theta = 45°$)

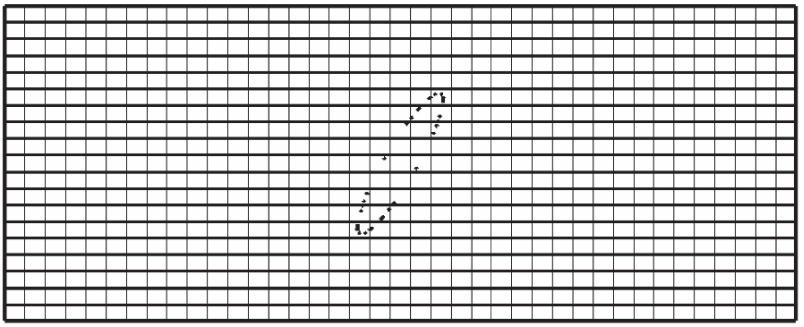

($\theta = 60°$)

Fig. 7.5 Effect of dip angle on streamline and excess pressure patterns around and within an elliptical inclusion ($\alpha = 1$)

To examine the effect of the aspect ratio of an elliptical inclusion on the distribution patterns of both the streamlines and the excess pore-fluid pressure around and within the inclusion, the dip angle of the inclusion is kept as a constant value of 30 degrees, while the permeability ratio is set to be a constant value of 10. Three different aspect ratios, namely $\beta = 2.5$, $\beta = 5.0$ and $\beta = 7.5$, are considered to produce the numerical results. Figure 7.8 shows the effect of the aspect

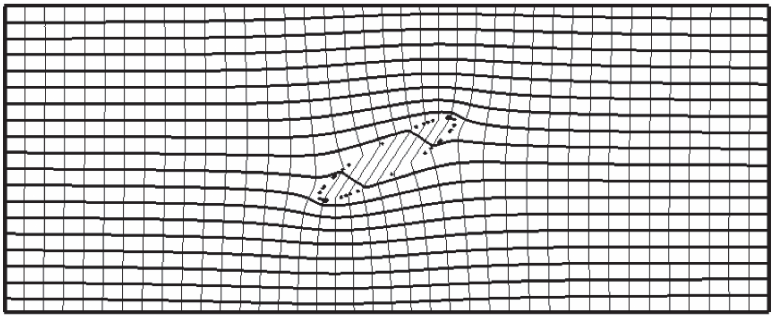

($\theta = 30°$)

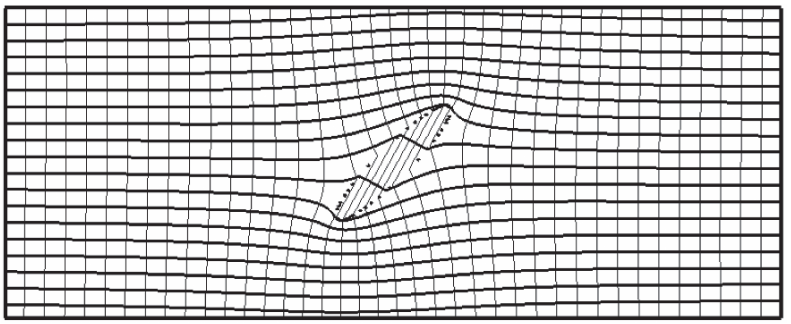

($\theta = 45°$)

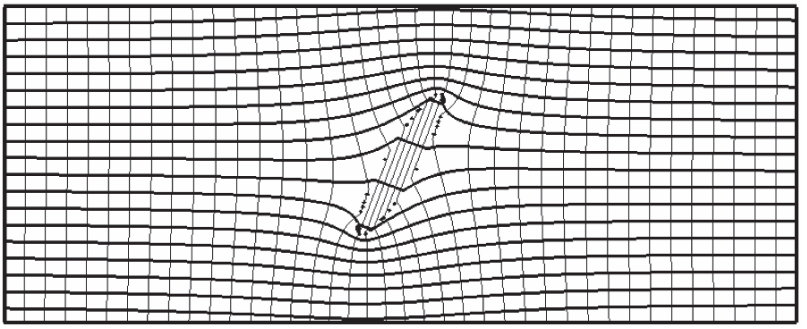

($\theta = 60°$)

Fig. 7.6 Effect of dip angle on streamline and excess pressure patterns around and within an elliptical inclusion ($\alpha = 0.1$)

ratio of an elliptical inclusion on the streamlines and excess pore-fluid pressure patterns around and within the inclusion. The aspect ratio of an elliptical inclusion can significantly affect both of these distribution patterns. Since the density of the streamlines reflects the magnitude of the pore-fluid flow, when the aspect ratio increases, the pore-fluid flow velocity increases within the inclusion. The maximum values of the pore-fluid flow focusing factor, which is defined as the ratio of the

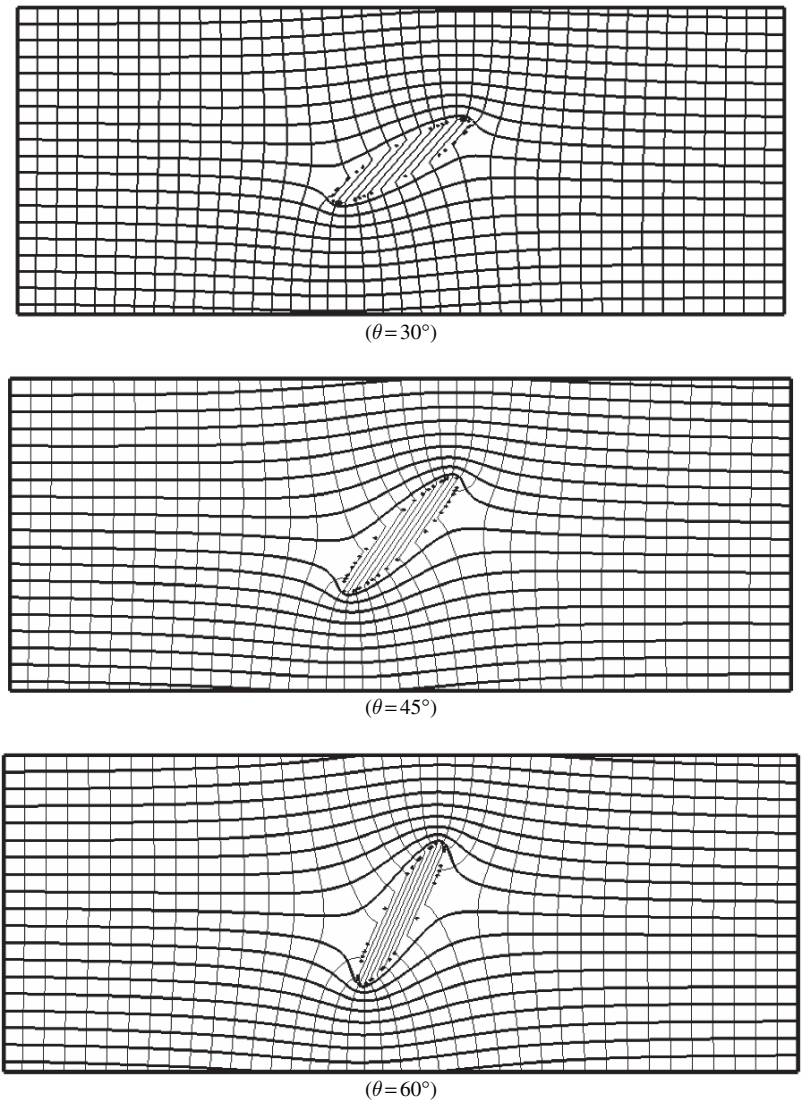

Fig. 7.7 Effect of dip angle on streamline and excess pressure patterns around and within an elliptical inclusion ($\alpha = 0$)

pore-fluid velocity within the inclusion to that of the inflow in the far field, are approximately 2.44, 3.29 and 3.92 for aspect ratios of 2.5, 5.0 and 7.5, respectively. The total flux of the pore-fluid across the elliptical inclusion is also dependent on the aspect ratio of the inclusion. For example, the pore-fluid enclosed by about 11 streamlines passes across the inclusion of an aspect ratio of 2.5, while the pore-fluid enclosed by about eight streamlines flows across the inclusion of an aspect ratio

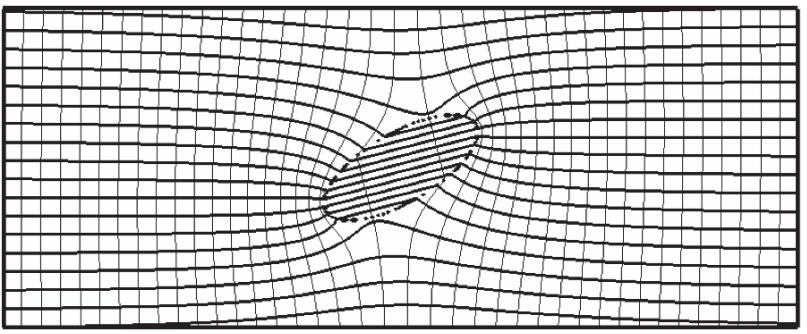

(β=2.5)

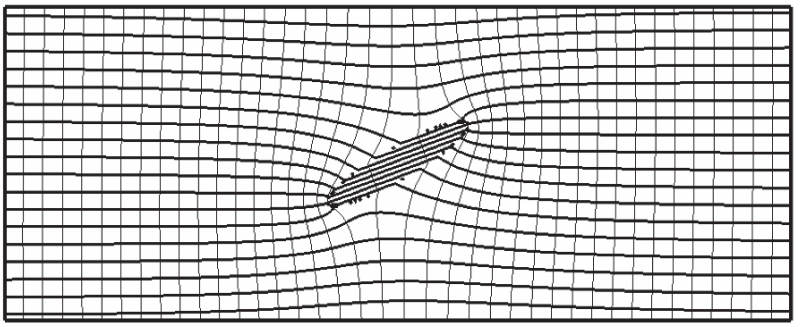

(β=5)

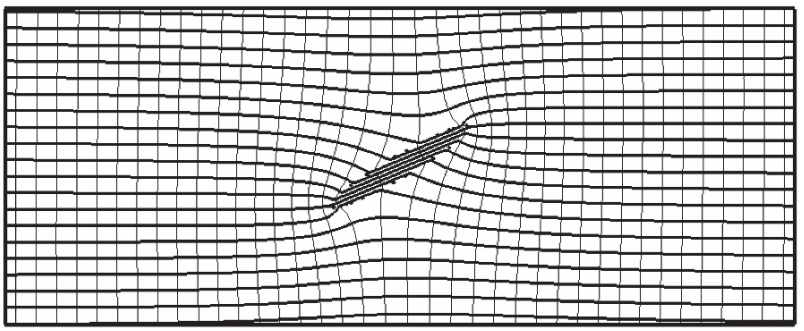

(β=7.5)

Fig. 7.8 Effect of aspect ratio on streamline and excess pressure patterns around and within an elliptical inclusion ($\alpha = 10$ and $\theta = 30°$)

of 7.5. This indicates that the smaller the aspect ratio of an elliptical inclusion, the larger the total flux across the inclusion. Moreover, since the quality of ore body formation and mineralization is controlled by the pore-fluid velocity within faults and large cracks (Zhao et al. 1998a), an elliptical inclusion with a large aspect ratio is more favorable for high-grade ore formation and mineralization within the inclusion.

The present analytical solutions provide important and often unique tools for validating and verifying numerical methods and algorithms used to solve problems characterized by complicated geometries. To demonstrate this point, the finite element method (Zienkiewicz 1977) is used to simulate pore-fluid flow around and within a vertical crack embedded in a pore-fluid saturated porous rock. Figure 7.9 shows the geometry of the problem to be modeled using the finite element method. The height and length of the computational model are 4 m and 10 m, respectively. The inflow of the excess pore-fluid pressure gradient being unity in the far field is assumed to be vertical, while the aspect ratio of the crack is 10. The permeability values of the crack and its surrounding rock are $10^{-12}\,\mathrm{m}^2$ and $10^{-13}\,\mathrm{m}^2$, so that the permeability ratio of the crack to the surrounding rock is 10. The dynamic viscosity of the pore-fluid is $10^{-3}\,\mathrm{N}\cdot\mathrm{s}/\mathrm{m}^2$. To appropriately simulate the pore-fluid flow around and within the vertical crack, a fine mesh of small element sizes is used to simulate the crack, while a mesh gradation scheme is used to simulate the surrounding rock by gradually changing the mesh size from the outline of the crack within the computational model. As a result, the whole computational domain is simulated by 233,214 three-node triangle elements.

Figure 7.10 shows the numerical and analytical solutions for the streamline distribution around and within the vertical crack. Since the inflow is uniformly and vertically injected into the system at the lower boundary, the pore-fluid flow converges into the crack at the inlet (i.e., the lower end) of the crack, but diverges out of the crack at the outlet (i.e., the upper end) of the crack. This phenomenon can be clearly observed from Fig. 7.10. The numerical solution obtained from the computational model is in good agreement with the analytical one (i.e., (7.38) and (7.39) with $\theta = 90^\circ$). The numerical solution for pore-fluid flow can be quantitatively validated through the theoretical flow focusing factor within the crack. Since the flow focusing factor of the crack is equal to the ratio of the maximum velocity within the crack to that of the injected fluid at the bottom of the computational model, it can be straightforwardly calculated from the related numerical results. The computed

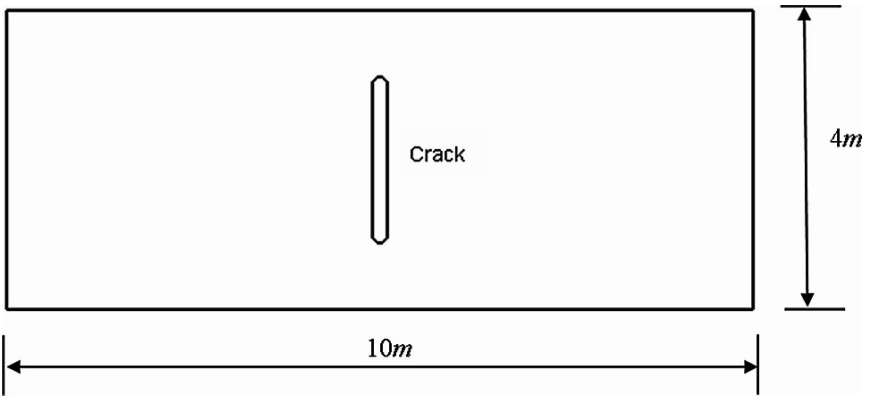

Fig. 7.9 Geometry of a vertical crack

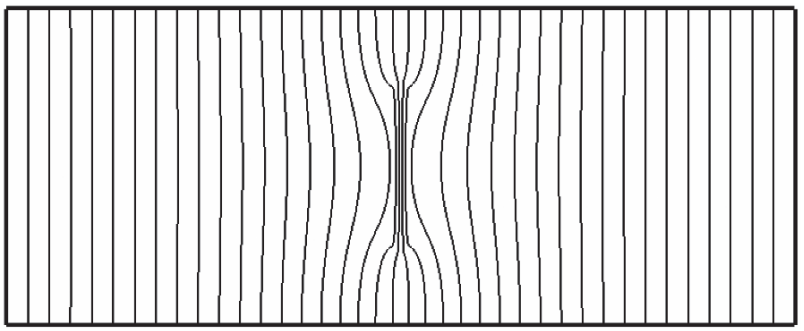

(Numerical solution)

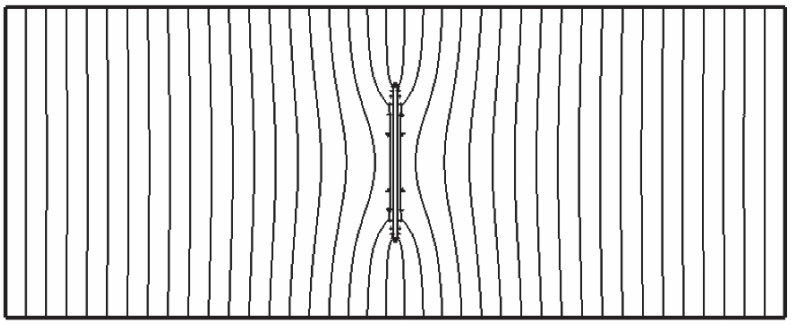

(Analytical solution)

Fig. 7.10 Comparison of the numerical solution with the analytical solution for the stream function

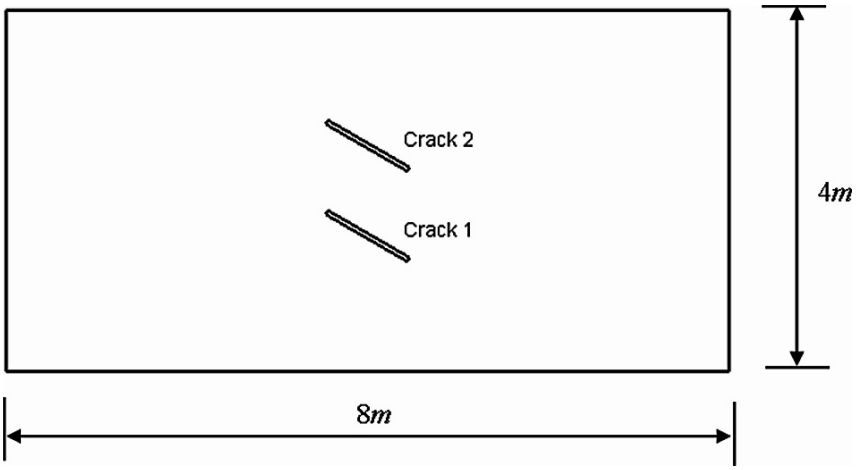

Fig. 7.11 Geometry of two parallel inclined cracks

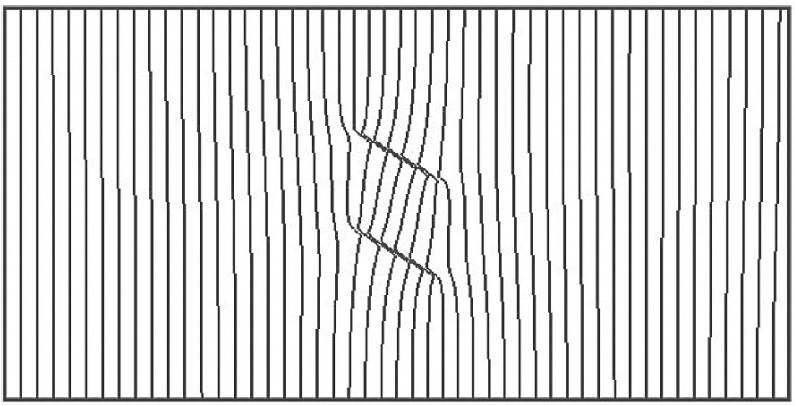

($\theta = 30°$)

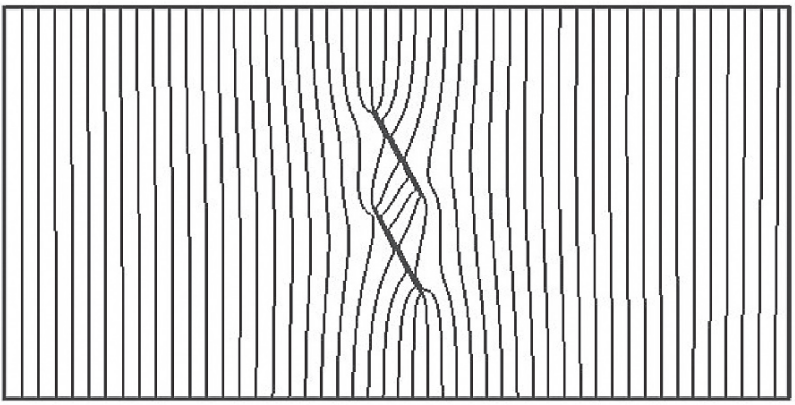

($\theta = 60°$)

Fig. 7.12 Effect of dip angle on streamline patterns around and within two parallel inclined cracks ($K_{in}/K_{out} = 10$)

flow focusing factor of the crack from the computational model is 5.25, while the analytical value of the flow focusing factor of the crack is 5.5, which is obtained from (6.35) in Chap. 6. Since the relative error of the flow focusing factor from the numerical simulation is within 4.5 percent, it quantitatively demonstrates that the finite element mesh used in the computational model can produce accurate numerical solutions for pore-fluid flow around and within the crack. In this regard, the present analytical solutions have provided a useful tool to validate numerical models so that the overall accuracy of the corresponding numerical solutions can be quantitatively evaluated by the relative error.

Having validated the finite element method by the present analytical solution, it is now used to investigate the effect of two parallel inclined cracks on the pore-fluid flow pattern around and within these two cracks. Figure 7.11 shows the geometry of

the problem. Two different dip angles, namely $\theta = 30^\circ$ and $\theta = 60^\circ$, are considered in the resulting computational models. The height and length of the computational model are 4 m and 8 m, respectively. The inflow of the excess pore-fluid pressure gradient being unity in the far field is assumed to be vertical, while the aspect ratio of the crack is 20. The permeability values of the crack and its surrounding rock are $10^{-12}\,m^2$ and $10^{-13}\,m^2$, implying that a permeability ratio of the crack to the surrounding rock is 10. The dynamic viscosity of the pore-fluid is $10^{-3}\,\mathrm{N}\cdot\mathrm{s/m}^2$. The whole computational domain is simulated using 194,208 and 206,200 three-node triangle elements in the case of $\theta = 30^\circ$ and $\theta = 60^\circ$, respectively.

Figure 7.12 shows the effect of the dip angle on the streamline distribution around and within two parallel inclined cracks in the pore-fluid saturated porous rock. The dip angle has a significant influence on the streamline distribution around and within these two parallel inclined cracks. Since the cracks are more permeable than the surrounding rock and the inflow is vertically injected at the lower boundary of the computational model, more pore-fluid is focused into the cracks as the dip angle of the crack increases from 30° to 60°. Note that the injected inflow arises from the application of an excess pore-fluid pressure gradient, the amplitude of which is unity, to the lower boundary of the computational model. In terms of the streamline distribution between the two parallel inclined cracks, there exists an interaction between these two parallel cracks, especially when they are close to each other. This indicates that the distance between two parallel inclined cracks may significantly affect the pore-fluid flow pattern.

Chapter 8
Pore-Fluid Flow Focused Transient Heat Transfer within and around Two-Dimensional Faults and Cracks of Crustal Scales

Geological faults and large cracks play an important and diverse role in pore-fluid flow focused heat transfer within fluid-saturated porous media (Toth 1962; Person and Baumgartner 1995; Wieck et al. 1995; Zhao and Valliappan 1994a, b; Roberts et al. 1996; Person et al. 1996; Jamtveit and Yardley 1997; Connolly 1997; Zhao et al. 1999b, 2001b, 2002a; Hoaglund and Pollard 2003). A typical example of pore-fluid flow focused heat transfer is the formation of hot spots around and within geological fault zones in the upper crust of the Earth. In terms of clean energy development and utilization, these hot spots are favorable locations for the storage and utilization of geothermal energy. On the other hand, the formation of such hot spots may be closely associated with the formation of high-grade ore deposits within the upper crust of the Earth. As modern mineralization theory indicates, the mineralization rate for a particular mineral is dependent on the scalar product of the pore-fluid flow velocity and temperature gradient at the location of the mineral (Phillips 1991; Zhao et al. 1998a). Since geological fault zones and large cracks are favorable locations for pore-fluid flow focusing and temperature localization to take place simultaneously, they become favorable locations for hot spots to form in the upper crust of the Earth. For this reason, a better understanding of the transient process associated with pore-fluid flow focused heat transfer around geological faults and large cracks has become an important research topic in the field of geoscience. Compared with steady state solutions that describe the extreme state of a system, transient solutions are useful for describing the specific process in which the system reaches a steady state.

As has been mentioned previously, analytical solutions to benchmark problems provide an important and often unique tool for validating and verifying numerical methods and algorithms, which can be used to solve problems of complicated geometries, such as pore-fluid flow focused heat transfer problems within the upper crust of the Earth (i.e., Ohnishi et al. 1985; Jiao and Hudson 1995; Person and Baumgartner 1995; Wieck et al. 1995; Roberts et al. 1996; Person et al. 1996; Bower and Zyvoloski 1997; Thomas et al. 1998; Zhao et al. 1997, 1998c; Hoaglund and Pollard 2003). On the engineering length scale, Booker and Savvidou (1985) developed an analytical solution for a simplified consolidation problem around a heat source in thermoelastic soils. It is assumed that the heat source considered in their study is caused by a canister of radioactive waste, which is buried

C. Zhao et al., *Convective and Advective Heat Transfer in Geological Systems*,

© Springer-Verlag Berlin Heidelberg 2008

in a saturated soil. If the temperature field is uncoupled from the determination of displacements and pressure by neglecting mechanical contributions to both the energy balance and the convective terms, then an analytical solution can be derived for the fundamental problem of a point heat source buried deep in a saturated soil (Booker and Savvidou 1985). Based on this analytical solution, Lewis and Schrefler (1998) have verified that the finite element method can be used to solve thermoelastic consolidation problems in more complicated engineering situations.

Since the length of a geological fault in the strike direction is significantly different from that in its thickness and height directions, it is reasonable, from the mathematical point of view, to treat the fault as an elliptical inclusion in a two-dimensional full plane, which is perpendicular to the strike direction of the geological fault. Thus, the elliptical inclusion to be considered in this study is a cross section perpendicular to the strike direction of the geological fault, hereafter referred to as the elliptical fault. To this end, Lamb (1975) and Phillips (1991) presented the analytical solutions for the steady state pore-fluid flow problem around either a perfectly permeable elliptical fault or a perfectly impermeable elliptical fault, which is embedded in a two-dimensional full plane. Obdam and Veling (1987) derived the analytical solutions for the pore-fluid flow around and within elliptical inhomogeneities using the complex variable function approach. Zimmerman (1996) also extended Obdam and Veling's solutions to the solution of pore-fluid flow in a more complicated situation. Wallstrom et al. (2002) extended the two-dimensional potential solution from an electrostatic problem (Stratton 1941) into a steady state pore-fluid flow problem around an ellipse using a special elliptical coordinate system. Using elementary algebraic functions only, Zhao et al. (2006a) derived a complete set of analytical solutions for pore-fluid flow around an elliptical fault of specific size, which has any finite, but non-zero value of the permeability and is embedded in a two-dimensional full plane. To remove the size limitation of the previous analytical solutions (Zhao et al. 2006a), it is necessary to derive the analytical solutions for an elliptical fault of any size, so that the solutions are suitable for investigating pore-fluid flow focused heat transfer problems of any length scales within fluid-saturated porous media.

8.1 Statement of the Problem

To investigate the influence of a geological fault on pore-fluid flow focused transient heat transfer around the fault, a fully coupled problem comprising pore-fluid flow and transient heat transfer needs to be solved for the fluid-saturated porous medium. Since it is very difficult, if not impossible, to derive analytical solutions for this fully coupled problem, the finite element method (Zienkiewicz 1977) is used to obtain numerical solutions for the fully coupled problem. One of the main purposes of this chapter is to validate the computational model before it is used to investigate the effect of the dip angle of a geological fault on pore-fluid flow focused

transient temperature distribution around a geological fault. By adding a time-dependent term reflecting transient heat transfer into the energy equation presented in previous chapters, the mathematical model for the fully coupled problem can be described below.

$$\frac{\partial u}{\partial x} + \frac{\partial v}{\partial y} = 0, \tag{8.1}$$

$$u = -\frac{K}{\mu}\frac{\partial P}{\partial x}, \tag{8.2}$$

$$v = -\frac{K}{\mu}\left(\frac{\partial P}{\partial y} + \rho_f g\right), \tag{8.3}$$

$$\left[\phi\rho_f c_{pf} + (1-\phi)\rho_s c_{ps}\right]\frac{\partial T}{\partial t} + \rho_f c_p\left(u\frac{\partial T}{\partial x} + v\frac{\partial T}{\partial y}\right) = \lambda_0^e\left(\frac{\partial^2 T}{\partial x^2} + \frac{\partial^2 T}{\partial y^2}\right), \tag{8.4}$$

$$\rho_f = \rho_0[1-\beta_T(T-T_0)], \quad \lambda_0^e = \phi\lambda_0^f + (1-\phi)\lambda_0^s, \tag{8.5}$$

where u and v are the velocity components of pore-fluid in the x and y directions; P and T are the pore-fluid pressure and temperature; μ is the dynamic viscosity of pore-fluid; ρ_0 and T_0 are the reference density of pore-fluid and the reference temperature of the medium; c_{pf} and c_{ps} are the specific heats of the pore-fluid and solid matrix, respectively; λ_0^f and λ_0^s are the thermal conductivity coefficients for the pore-fluid and solid matrix in the porous medium; ϕ and β_T are the porosity of the medium and the thermal volume expansion coefficient of the pore-fluid; ρ_f and ρ_s are the densities of the pore-fluid and solid matrix in the porous medium; K is the permeability of the isotropic porous medium and g is the gravity acceleration component in the vertical direction, which is assumed to be opposite to the positive direction of the y axis.

In the above-mentioned mathematical model, the pore-fluid is also assumed to be incompressible and that the Oberbeck-Boussinesq approximation (Phillips 1991; Zhao et al. 1997, 2005a) is employed to describe the change in pore-fluid density due to a change in the pore-fluid temperature. Since a transient heat transfer problem is considered to investigate the detailed warming up process within the upper crust of the Earth, the time variable is clearly involved in the energy equation (i.e., (8.4)).

Consider the pore-fluid pressure within the crust of the Earth as background to the numerical model considered in this section. Many authors consider this pressure to be lithostatic. It is then the lithostatic pore-fluid pressure gradient that drives the pore-fluid flow and the corresponding focused heat transfer. This is a fundamental issue associated with understanding high-grade ore deposits within the upper crust

of the Earth. For instance, it has been postulated that the pore-fluid pressure gradient was lithostatic in the Yilgarn craton, Western Australia (Korsch et al. 1998; Sorjonen-Ward et al. 2002). Extensive studies (Connolly and Ko 1995; Etheridge et al. 1983; Fyfe et al. 1978; Walther and Orville 1982; Peacock 1989; Yardley and Bottrell 1992; Hanson 1992; Yardley and Lloyd 1995; Norton and Knapp 1970) have shown that lithostatic pore-fluid pressure can be built up by metamorphic fluids due to devolatilization and dehydration reactions, if the permeability is low enough to control the fluid flow in the lower crust. Since the Yilgarn craton has undergone several heating and cooling cycles during ore body formation and mineralization (Korsch et al. 1998; Sorjonen-Ward et al. 2002), it is of interest to investigate how the dip angle of a geological fault affects the transient thermal structure around a geological fault within the upper crust during a heating process through some generic models. With this in mind, we will use a generic model to examine the effects of a geological fault of different dip angles on pore-fluid flow focused transient heat transfer around the fault within the upper crust, where the pore-fluid pressure gradient is lithostatic, during a heating cycle.

8.2 Validation of the Numerical Models

Figure 8.1 shows the geometry of the generic problem for simulating pore-fluid flow focused transient heat transfer around geological faults of different dip angles. For this generic problem, the pore-fluid pressure is assumed to be lithostatic, implying that there is an upward throughflow in the computational model. The height and width of the computational model are 10 km and 20 km, respectively. The length of the fault is 5 km, with an aspect ratio of 20. The permeability of the fault is about 43 times that of the surrounding rock, which is assumed to have a perme-

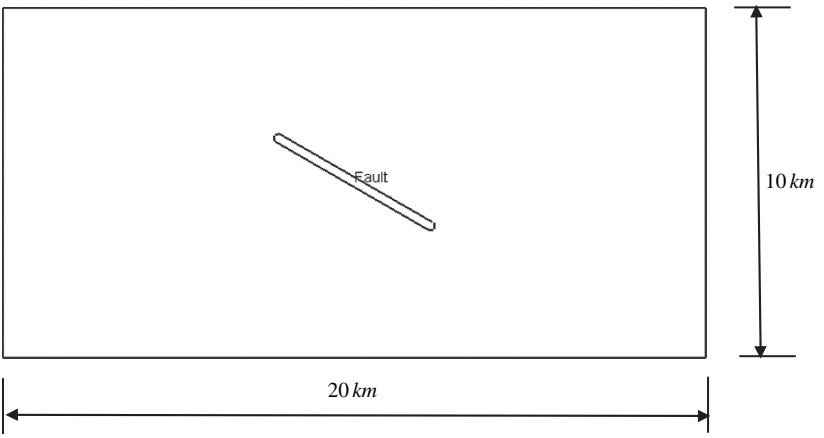

Fig. 8.1 Geometry of a fault with an arbitrary dip angle

ability of $10^{-16}\,m^2$. The top temperature is 25 °C, while the initial temperature at the bottom is 125 °C, implying that the initial geothermal gradient is 10 °C/km. In order to simulate the warming up process within the crust, the bottom temperature is first increased to 325 °C at the start of the computational model and then kept at a constant temperature boundary of 325 °C. A flow boundary condition consisting of a vertical flux of injected fluid due to the lithostatic pore-fluid pressure gradient equal to $1.6 \times 10^{-9}\,m/s$ is applied at the bottom, while a pressure boundary condition, which has a prescribed constant pressure of zero, is applied at the top of the computational model. The following parameters are used in the numerical simulation. For the pore-fluid, dynamic viscosity is $10^{-3}\,N \cdot s/m^2$; reference density is $1000\,kg/m^3$; volumetric thermal expansion coefficient is $2.1 \times 10^{-4}(1/°C)$; specific heat is $4184\,J/(kg \cdot °C)$, and thermal conductivity coefficient is $0.59\,W/(m \cdot °C)$. For the porous matrix, porosity is 0.35 and 0.1 for the fault and the surrounding rock, respectively; thermal conductivity coefficient is $2.9\,W/(m \cdot °C)$; specific heat is $878\,J/(kg \cdot °C)$, and reference rock density is $2600\,kg/m^3$. In order to examine the effect of the dip angle on the pore-fluid flow focused temperature distribution around the geological fault, three different dip angles, namely 90° (i.e., a vertical fault), 60° and 30°, of the fault are considered in the finite element computation. In the case of the dip angle being 90°, the computational model is simulated by 306,818 three-node triangle elements, while in the case of the dip angles being 60° and 30°, the computational model is simulated using 212,918 and 234,598 three-node triangular elements, respectively.

Figure 8.2 compares the numerical solution with the analytical one for the streamline distribution for a hydrothermal system with a vertical fault. Since the pore-fluid flow is uniformly and vertically injected into the system at the lower boundary of the computational model, the pore-fluid flow converges into the fault at the inlet (i.e., the lower end) of the fault, but diverges out of the fault at the outlet (i.e., the upper end) of the fault (see Fig. 8.2). Note that the numerical result obtained from the computational model is in good agreement with the analytical result predicted from the theoretical analysis in the previous chapter, indicating that the finite element mesh used in the computational model is qualitatively suitable for simulating pore-fluid flow focusing in the larger length scale geological fault. The numerical solution for pore-fluid flow can be quantitatively validated through the theoretical flow focusing factor within the fault. The vertical velocity of the injected fluid due to the lithostatic pore-fluid pressure gradient is equal to $1.6 \times 10^{-9}\,m/s$ and the numerical solution for the maximum vertical velocity within the equivalent elliptical fault is equal to $2.37 \times 10^{-8}\,m/s$. The corresponding flow focusing factor for the fault is equal to the ratio of the maximum velocity within the fault to that of the injected fluid at the bottom of the computational model. This results in a flow focusing factor of 14.16. The analytical value of the flow focusing factor for the elliptical fault is 14.33, which is calculated from the related equation in Chap. 6. Since the relative error of the flow focusing factor from the numerical simulation is within 1.2 percent, it is quantitatively demonstrated that the finite element mesh used in the computational model can produce accurate numerical solutions for the pore-fluid focusing around the geological fault, because we have used a large number

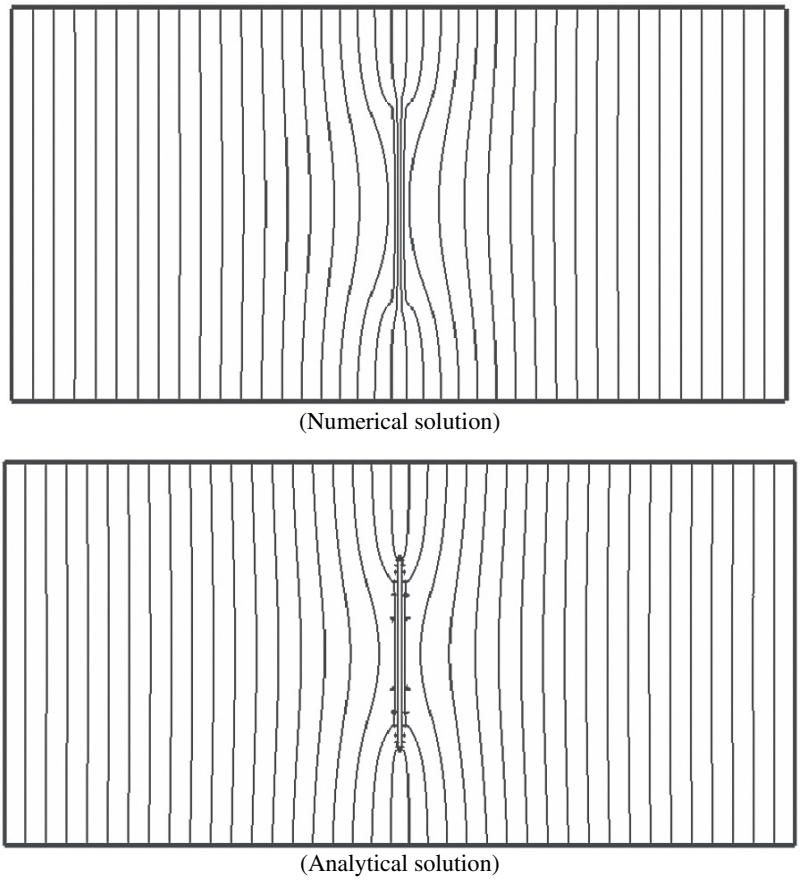

Fig. 8.2 Comparison of the numerical solution with the analytical result for the stream function

of fine finite elements to simulate the geological fault and its surrounding rocks in the near field around the fault. In this regard, the present analytical solutions have provided a useful tool to verify numerical models so that the overall accuracy of the corresponding numerical solutions can be quantitatively evaluated by the relative error.

8.3 Numerical Simulation Results

In order to investigate the influence of focused pore-fluid flow on the transient temperature distribution around the vertical fault, the temperature evolution within the computational model has been simulated and the related numerical results are shown in Fig. 8.3. Since the simulated heat transfer is a transient process, the thermal

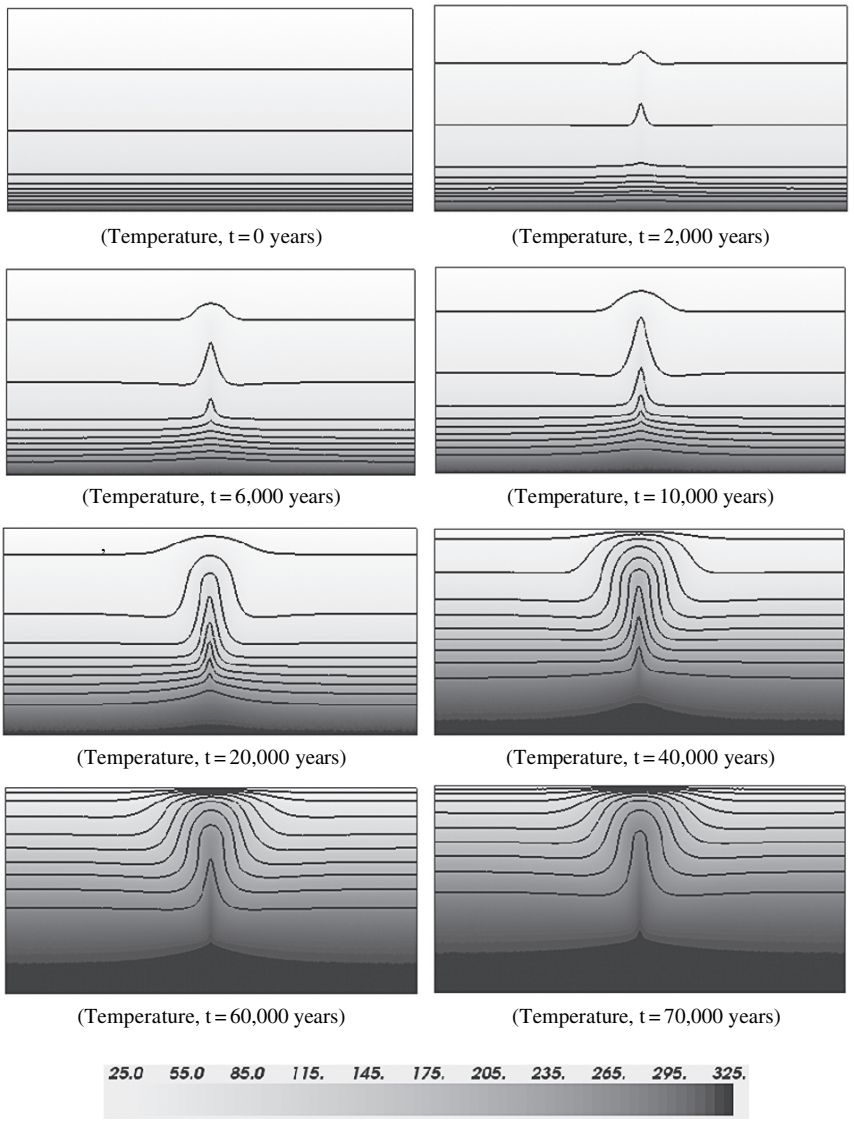

Fig. 8.3 Temperature evolution due to flow through a vertical fault

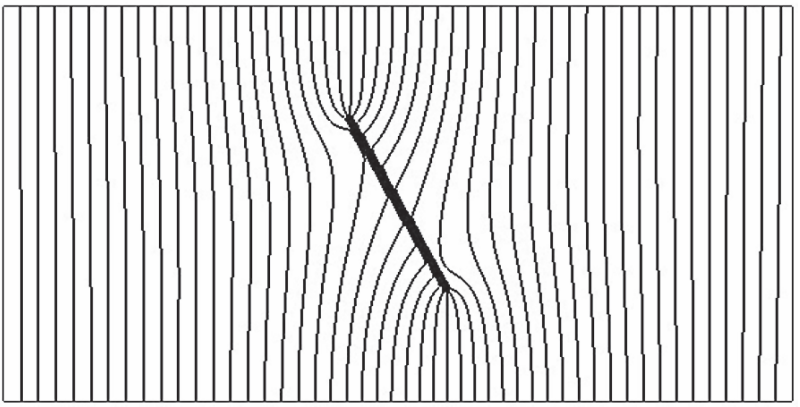

(Whole system view)

Fig. 8.4 Streamline distributions due to pore-fluid flow in an inclined fault of 60 degrees dip

structure around the fault is clearly dependent on the computational time. For example, it takes about 40,000 years to warm up the lower quarter of the computational model, while it takes about 70,000 years to warm up the lower half of the computational model. Thus, the thermal structure around the fault is strongly dependent on the heating history of the crust under the influence of the lithostatic pore-fluid pressure gradient. Due to the heat advection of the focused pore-fluid flow, the upper crust just above the vertical fault becomes much hotter (up to 100 °C) than the surrounding rock after 40,000 years.

In the following text, the influence of the fault dip angle on the pore-fluid flow pattern and temperature distribution is examined. Figure 8.4 shows the streamline distribution of the hydrothermal system with an inclined fault of 60 degrees dip. Similarly, the pore-fluid flow is uniformly and vertically injected into the system at the lower bottom of the computational model so that the pore-fluid flow converges into the fault at the inlet (i.e., the lower end) of the fault, but diverges out of the fault at the outlet (i.e., the upper end) of the fault (see Fig. 8.4). To investigate the influence of focused pore-fluid flow on the temperature distribution around the inclined fault of 60 degrees dip, the temperature evolution process has been simulated and the related numerical results are shown in Fig. 8.5. The focused pore-fluid flow causes the upper crust just above the inclined fault to become much hotter than the surrounding rock after 40,000 years. Compared with the numerical results shown in Figs. 8.2 and 8.3, the numerical solutions shown in Figs. 8.4 and 8.5 demonstrate that the dip angle of the fault can have a remarkable influence on the pore-fluid flow pattern and temperature distribution. At a time of 40,000 years, the temperature differences relative to the ambient temperature vary from about 100 °C above a vertical fault with a lithostatic pore-fluid pressure gradient, to a maximum of about 60 °C above a fault dipping at 60 degrees.

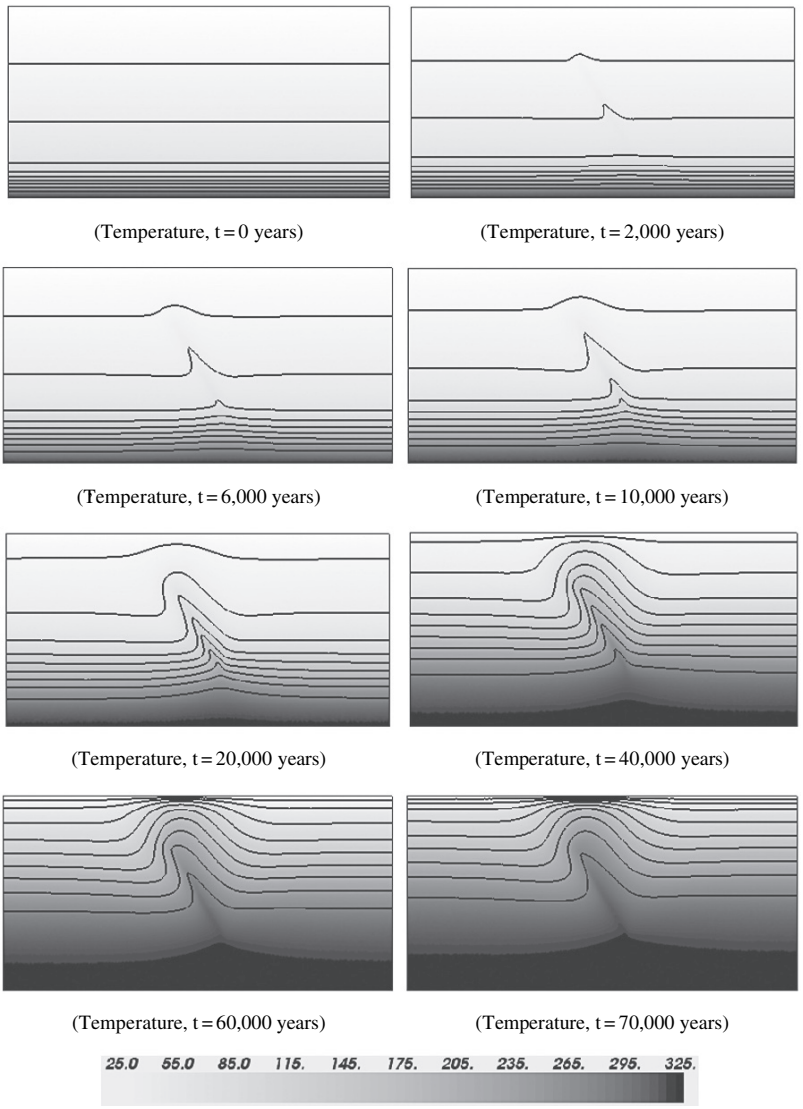

Fig. 8.5 Temperature evolution due to pore-fluid flow in an inclined fault of 60 degrees dip

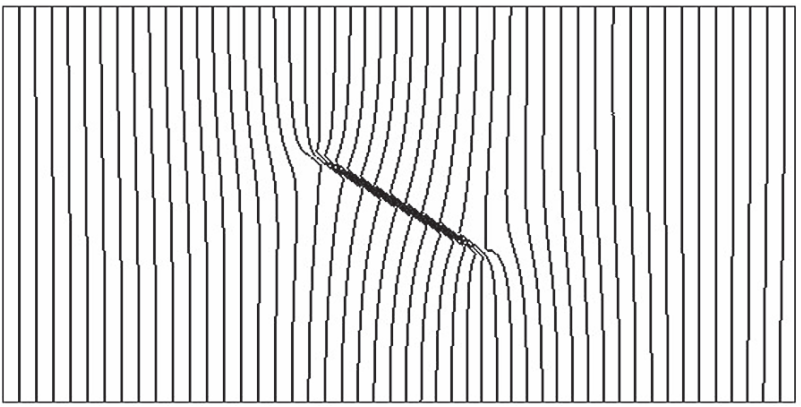

(Whole system view)

Fig. 8.6 Streamline distributions due to pore-fluid flow in an inclined fault of 30 degrees dip

An inclined fault of 30 degrees dip is considered next. Figure 8.6 shows the streamline distribution of the hydrothermal system, while Fig. 8.7 shows the velocity distributions at both the inlet and outlet of this fault. The maximum amplitude of the velocity vector shown in Fig. 8.7 is equal to 1.46×10^{-8} m/s. The arrow size is used to reflect the amplitude of the velocity vector. The temperature evolution is shown in Fig. 8.8. Compared with the previous numerical solutions for both a vertical fault and an inclined fault of 60 degrees dip, it can be clearly seen (from Figs. 8.3, 8.5 and 8.8) that the effect of the focused pore-fluid flow on the localized temperature distribution within the upper crust decreases considerably with decrease of the fault dip angle, especially in the early stage of the warming up process. At a time of 40,000 years, the temperature differences relative to the ambient temperature vary from about 100 °C above a vertical fault with a lithostatic pore-fluid pressure gradient, to a maximum of about 25 °C above a fault dipping at 30 degrees. Since a fault of any dip angle draws the pore-fluid from the bottom of the fault and expels the pore-fluid on the upper side of the fault, there are some areas where the transport of the pore-fluid flow is relatively strong, and other areas where there is relatively little pore-fluid movement near the fault. For a vertical fault, the areas of relatively slow movement of the pore-fluid are located on either side of the fault, while for the dipping faults, the areas of relatively slow movement of the pore-fluid are located near both the bottom of the fault within the hanging wall and near the top of the fault within the footwall. Thus, the dip angle of a geological fault can significantly affect the pore-fluid flow and transient heat transfer patterns around the fault.

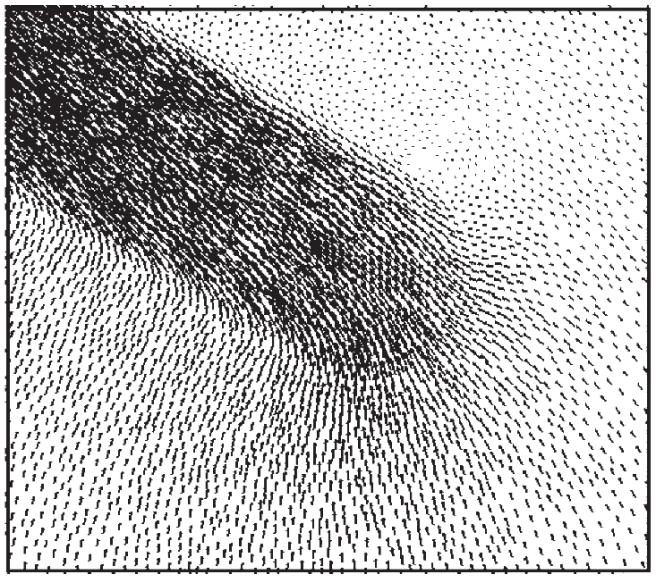

(Zoom-in view at the inlet of the fault, maximum velocity = 1.46×10^{-8} *m/s*)

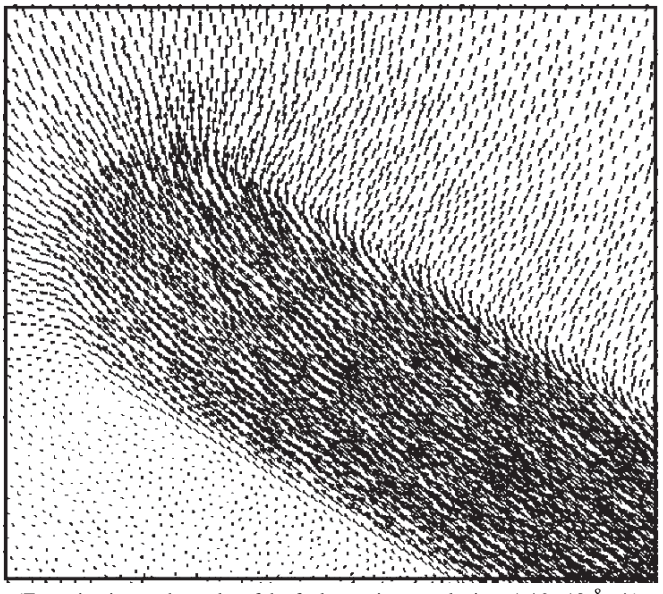

(Zoom-in view at the outlet of the fault, maximum velocity = 1.46×10^{-8} *m/s*)

Fig. 8.7 Pore-fluid flow velocity distributions due to an inclined fault of 30 degrees dip

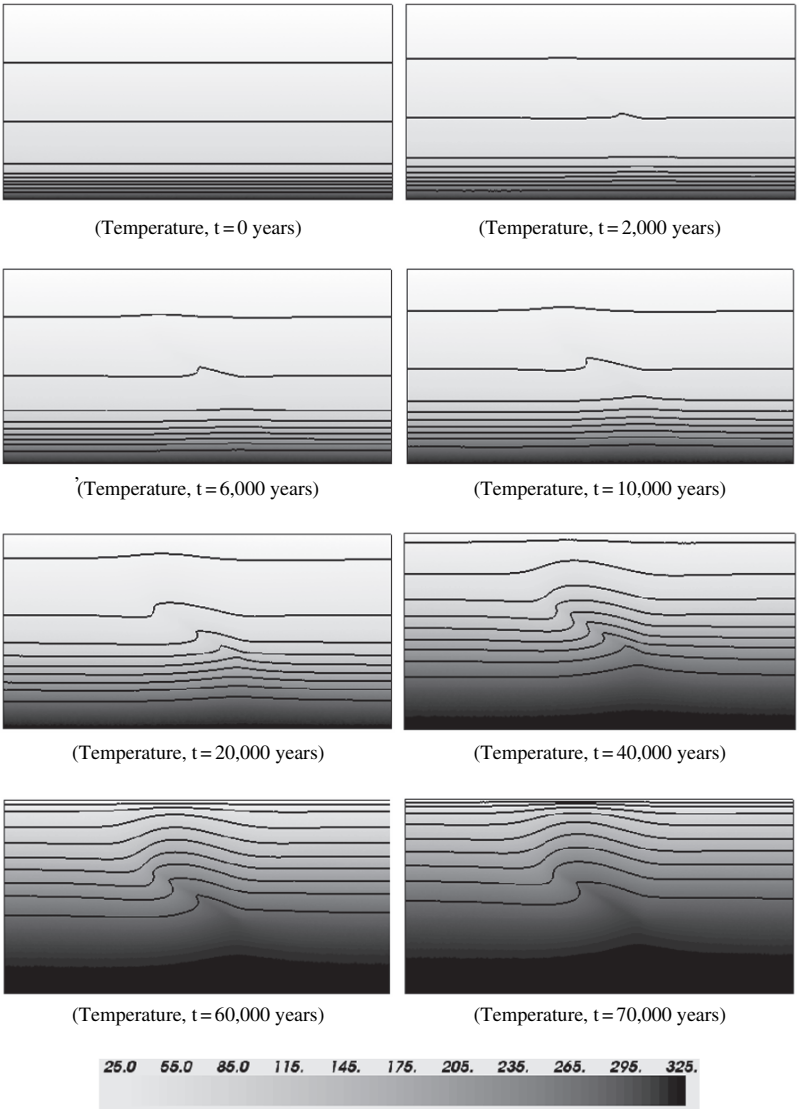

Fig. 8.8 Temperature evolution due to pore-fluid flow in an inclined fault of 30 degrees dip

Chapter 9
Convective Heat Transfer within Three-Dimensional Vertical Faults Heated from Below

Over the past decade, great efforts have been made to understand the basic physical and chemical processes behind ore body formation and mineralization in hydrothermal systems. On the scientific development side, analytical solutions have been developed to answer the following scientific questions (Zhao et al. 1998b, 1999a):

(1) Can the pore-fluid pressure gradient be maintained at the value of the lithostatic pressure gradient in the upper crust of the Earth?
(2) Can convective pore-fluid flow take place in the upper crust of the Earth if there is fluid/mass leakage from the mantle to the upper crust of the Earth?

On the modeling development side, numerical methods have been developed to model the following problems: (1) convective pore-fluid flow in hydrothermal systems (Zhao et al. 1997); (2) coupled reactive pore-fluid flow and multiple species transport in porous media (Zhao et al. 1999d); (3) precipitation and dissolution of minerals and rock alteration in the upper crust of the Earth (Zhao et al. 1998a); (4) double-diffusion driven reactive flow transport in deformable fluid-saturated porous media with particular consideration of temperature-dependent chemical reaction rates (Zhao et al. 2000c); (5) pore-fluid flow patterns near geological lenses in hydrodynamic and hydrothermal systems (Zhao et al. 1999b); (6) dissipative structure of non-equilibrium chemical reactions in fluid-saturated porous media (Zhao et al. 2000d); (7) convective pore-fluid flow and related mineralization in three-dimensional hydrothermal systems (Zhao et al. 2001a), and (8) fluid-rock interaction problems associated with rock alteration and metamorphic process in fluid-saturated hydrothermal/sedimentary basins (Zhao et al. 2001c). Rice and Cleary (1976) as well as McTigue (1986) amongst others have also studied different aspects of this problem. In addition, we have developed numerical methods to model various aspects of the fully coupled problem involving material deformation, pore-fluid flow, heat transfer and species transport/chemical reactions in pore-fluid saturated porous rock masses. The above-mentioned work has significantly enriched our knowledge of the physical and chemical processes related to ore body formation and mineralization in the upper crust of the Earth. However, convective instability of three-dimensional geological fault zone systems has not been well studied so far. Since geological fault zones and their surrounding rocks are favorable locations for ore body formation and mineralization to take place, it is important to gain a theoretical

C. Zhao et al., *Convective and Advective Heat Transfer in Geological Systems*,

© Springer-Verlag Berlin Heidelberg 2008

insight into convective flow structures in three-dimensional geological fault zones when they are heated uniformly from below.

The study of convective instability in fluid-saturated porous media was initiated by Horton and Rogers (1945) as well as Lapwood (1948) about one-half century ago. Since then, a large number of publications have been produced on this particular research topic. Nield and Bejan (1992) as well as Phillips (1991) have summarized the related research results in their books. Although research on the general aspects of the topic is extensive, it is very limited with respect to convective instability within three-dimensional geological fault zones when they are heated uniformly from below. In this regard, a geological fault zone is usually represented by a vertically oriented thin finite slab, which is comprised of fluid-saturated porous media. The large and small vertical surfaces of the slab are called the sidewalls and end walls, respectively. Beck (1972) and Zebib and Kassoy (1977) first solved the problem without considering the sidewall heat loss, so their solution is of little value for a vertically oriented geological fault. Considering the sidewall heat loss, Lowell and Shyu (1978) as well as Murphy (1979) used the Galerkin and simplified methods to obtain approximate solutions, which may only be used to qualitatively judge some kinds of convective flow structures in the system. To overcome the shortcomings of the approximate solutions presented by Lowell and Shyu (1978) as well as Murphy (1979), Kassoy and Cotte (1985) used the linear stability approach to produce asymptotic solutions for the above system. Since the asymptotic solutions are only valid when the thickness of the fault approaches zero, it is impossible to use such asymptotic solutions to predict the different critical Rayleigh numbers, under which different convective flow structures, such as two-dimensional slender-circle convective flow, three-dimensional standard convective flow and three-dimensional finger-like convective flow, may occur because the critical Rayleigh numbers of these flows are very close to each other, especially when the fault thickness to height ratio is very small. Therefore, exact solutions for the system must be developed so that different convective flow structures can be predicted exactly in a three-dimensional fluid-saturated geological fault zone system. The main purpose of this chapter is to develop these solutions for different critical Rayleigh numbers. This then enables different convective flow structures to be predicted based on the Rayleigh number of the fault system.

9.1 Statement of the Problem

We consider a three-dimensional fluid-saturated geological fault zone where the thickness is much smaller than both its length and height, as shown in Fig. 9.1. *The fault zone is assumed to be much more permeable than the surrounding rocks*. Numerical simulations (Zhao et al. 2006c) have demonstrated that if the permeability of the fault zone is three orders of magnitude higher than that of the surrounding rocks, the resulting convective pore-fluid flow in the surrounding rocks is much smaller than that in the fault zone, so that the interaction between the fault zone and

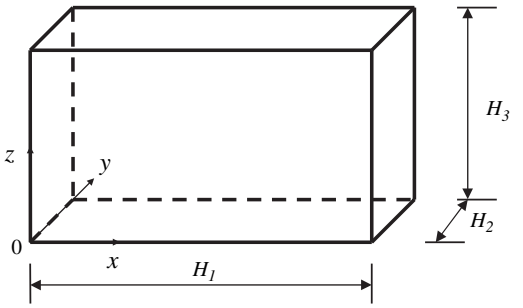

Fig. 9.1 Geometry of the problem

the surrounding rocks is negligible, from a theoretical analysis point of view. Thus, the fault zone is separated from the surrounding rocks in the following theoretical analysis. The length of the fault may be infinite in the x direction, but we consider the size of convection cells as H_1 in this direction so that insulated and impermeable boundary conditions can be added at both $x = 0$ and $x = H_1$. In the thickness direction, both the geothermal gradient and a hydrostatic pore-fluid pressure gradient are considered and, therefore, both these gradient conditions need to be added at both $y = 0$ and $y = H_2$. This means that any perturbation due to temperature within the geological fault zone has little influence on the initial thermal and flow pattern distributions of the surrounding rocks. It is assumed that the fault zone is uniformly heated from below so that constant temperature and impermeable boundary conditions are added at both $y = 0$ and $y = H_3$. In order to facilitate the following theoretical analysis, the material of the fault zone is assumed to be a homogeneous and isotropic porous medium. If Darcy's Law is used to describe pore-fluid flow and the Oberbeck-Boussinesq approximation is employed to describe a change in pore-fluid density due to a change in pore-fluid temperature, the governing equations of natural convection for incompressible fluid in a steady state can be expressed as

$$\frac{\partial u}{\partial x} + \frac{\partial v}{\partial y} + \frac{\partial w}{\partial z} = 0, \tag{9.1}$$

$$u = \frac{K_x}{\mu}\left(-\frac{\partial P}{\partial x} + \rho_f g_x\right), \tag{9.2}$$

$$v = \frac{K_y}{\mu}\left(-\frac{\partial P}{\partial y} + \rho_f g_y\right), \tag{9.3}$$

$$w = \frac{K_z}{\mu}\left(-\frac{\partial P}{\partial z} + \rho_f g_z\right), \tag{9.4}$$

$$\rho_{f0} c_p \left(u\frac{\partial T}{\partial x} + v\frac{\partial T}{\partial y} + w\frac{\partial T}{\partial z}\right) = \lambda_{ex}\frac{\partial^2 T}{\partial x^2} + \lambda_{ey}\frac{\partial^2 T}{\partial y^2} + \lambda_{ez}\frac{\partial^2 T}{\partial z^2}, \tag{9.5}$$

$$\rho_f = \rho_{f0}[1 - \beta_T(T - T_0)], \tag{9.6}$$

$$\lambda_{ex} = \phi\lambda_{fx} + (1-\phi)\lambda_{sx}, \quad \lambda_{ey} = \phi\lambda_{fy} + (1-\phi)\lambda_{sy}, \quad \lambda_{ez} = \phi\lambda_{fz} + (1-\phi)\lambda_{sz}, \tag{9.7}$$

where u, v and w are the velocity components of the pore-fluid in the x, y and z directions, respectively; P is the pore-fluid pressure; T is the temperature of the crustal material; K_x, K_y and K_z are the permeabilities of the porous material in the x, y and z directions, respectively; μ is the dynamic viscosity of the pore-fluid; ρ_f is the density of the pore-fluid; ρ_{f0} and T_0 are the reference density and temperature; λ_{fx} and λ_{sx} are the thermal conductivities of the pore-fluid and rock mass in the x direction; λ_{fy} and λ_{sy} are the thermal conductivities of the pore-fluid and rock mass in the y direction; λ_{fz} and λ_{sz} are the thermal conductivities of the pore-fluid and rock mass in the z direction; c_p is the specific heat of the pore-fluid; g_x, g_y and g_z are the gravity acceleration components in the x, y and z directions, and ϕ and β_T are the porosity of the crustal material and the thermal volume expansion coefficient of the pore-fluid.

For a homogeneous and isotropic porous medium, the following expressions exist:

$$K_x = K_y = K_z = K_0, \tag{9.8}$$

$$\lambda_{ex} = \lambda_{ey} = \lambda_{ez} = \lambda_{e0}, \tag{9.9}$$

where K_0 is the permeability of the porous medium, and λ_{e0} is the thermal conductivity coefficient of the porous medium.

The corresponding boundary conditions of the problem are as follows:

$$u = 0, \quad \frac{\partial T}{\partial x} = 0 \qquad (x = 0 \text{ and } x = H_1), \tag{9.10}$$

$$P = \rho_0 g_z (H_3 - z), \quad T = \frac{T_b - T_o}{H_3}(H_3 - z) + T_0 \quad (y = 0 \text{ and } y = H_2), \tag{9.11}$$

$$w = 0, \quad T = T_b \quad (z = 0), \tag{9.12}$$

$$w = 0, \quad T = T_0 \quad (z = H_3). \tag{9.13}$$

Since the perturbed temperature is much smaller than the base temperature on the two vertical surfaces (i.e., $y = 0$ and $y = H_2$), it is neglected in (9.11). However, the effect of this small perturbed temperature due to convective flow can be offset by using the effective thickness of the fault zone. Generally, the effective thickness of the fault zone should be a little larger than the physical thickness of the fault zone.

In order to simplify (9.1), (9.2), (9.3), (9.4) and (9.5), the following dimensionless variables are defined:

$$x^* = \frac{x}{H}, \quad y^* = \frac{y}{H}, \quad z^* = \frac{z}{H}, \tag{9.14}$$

$$H_1^* = \frac{H_1}{H}, \quad H_2^* = \frac{H_2}{H}, \quad H_3^* = \frac{H_3}{H}, \tag{9.15}$$

$$u^* = \frac{H\rho_{f0}c_p}{\lambda_{e0}}u, \quad v^* = \frac{H\rho_{f0}c_p}{\lambda_{e0}}v, \quad w^* = \frac{H\rho_{f0}c_p}{\lambda_{e0}}w, \tag{9.16}$$

$$T^* = \frac{T - T_0}{\Delta T}, \quad P^* = \frac{K_0\rho_{f0}c_p}{\mu\lambda_{e0}}(P - P_0), \tag{9.17}$$

where x^*, y^* and z^* are the dimensionless coordinates; u^*, v^* and w^* are the dimensionless velocity components in the x, y and z directions, respectively; H_1^*, H_2^* and H_3^* are the dimensionless length, thickness and height of the fault zone; P^* and T^* are the dimensionless excess pressure and temperature; K_0 is the reference medium permeability coefficient in the horizontal direction; λ_{e0} is the reference conductivity coefficient of the porous medium; $\Delta T = T_b - T_0$ is the temperature difference between the bottom and top boundaries of the porous medium; H is the reference length, and P_0 is the static pore-fluid pressure. In the following analysis, H_3 is chosen as the reference length (i.e., $H = H_3$).

Substituting the above dimensionless variables into (9.1), (9.2), (9.3), (9.4) and (9.5) yields:

$$\frac{\partial u^*}{\partial x^*} + \frac{\partial v^*}{\partial y^*} + \frac{\partial w^*}{\partial z^*} = 0, \tag{9.18}$$

$$u^* = -\frac{\partial P^*}{\partial x^*} + Ra_T T^* e_1, \tag{9.19}$$

$$v^* = -\frac{\partial P^*}{\partial y^*} + Ra_T T^* e_2, \tag{9.20}$$

$$w^* = -\frac{\partial P^*}{\partial z^*} + Ra_T T^* e_3, \tag{9.21}$$

$$u^* \frac{\partial T^*}{\partial x^*} + v^* \frac{\partial T^*}{\partial y^*} + w^* \frac{\partial T^*}{\partial z^*} = \frac{\partial^2 T^*}{\partial x^{*2}} + \frac{\partial^2 T^*}{\partial y^{*2}} + \frac{\partial^2 T^*}{\partial z^{*2}}, \tag{9.22}$$

where $\boldsymbol{e}$ is a unit vector, and $\boldsymbol{e} = e_1\boldsymbol{i} + e_2\boldsymbol{j} + e_3\boldsymbol{k}$ for a general three-dimensional problem. For the particular problem considered in this chapter, $e_1 = e_2 = 0$ and $e_3 = 1$ since the acceleration due to gravity is only exerted on the vertical direction. Ra_T is the Rayleigh number, defined as

$$Ra_T = \frac{(\rho_{f0} c_p)\rho_{f0} g \beta \Delta T K_0 H}{\mu \lambda_{e0}}. \tag{9.23}$$

Using the dimensionless variables, the corresponding boundary conditions can be expressed as

$$u^* = 0, \quad \frac{\partial T^*}{\partial x^*} = 0 \quad (x^* = 0 \text{ and } x^* = H_1^*), \tag{9.24}$$

$$P^* = 0, \quad T^* = (1 - z^*) \quad (y^* = 0 \text{ and } y^* = H_2^*), \tag{9.25}$$

$$w^* = 0, \quad T^* = 1 \quad (z^* = 0), \tag{9.26}$$

$$w^* = 0, \quad T = T_0 \quad (z^* = 1), \tag{9.27}$$

The linear stability theory has been used to deal with the convective instability problem in fluid-saturated porous media for many years (Horton and Rogers 1945; Lapwood 1948; Nield and Bejan 1992; Phillips 1991), but an analytical solution to the convective instability problem in three-dimensional geological fault zones is seldom considered. Although Kassoy and Cotte (1985) used the linear stability approach to produce asymptotic solutions for a problem similar to that stated here,

their solutions are only valid when the thickness of the fault zone tends to zero. Therefore, it is desirable to develop exact analytical solutions for this problem so that the onset conditions of the convective flow in the three-dimensional fault zones can be rigorously investigated.

From the mathematical point of view, the study of convective instability in a three-dimensional fault zone, in essence, involves finding nontrivial solutions for the partial differential equations expressed in (9.18), (9.19), (9.20), (9.21) and (9.22), with the given boundary conditions in (9.24), (9.25), (9.26) and (9.27). The conditions, under which the nontrivial solutions for the partial differential equations can exist, are the onset conditions for pore-fluid convective flow in the fault zone, while the nontrivial solutions are the convective flow modes of the fault zone. These onset conditions are often expressed as non-dimensional parameters, that is, the critical Rayleigh numbers, of the system. The nontrivial solution corresponding to the minimum critical Rayleigh number is called the fundamental convective flow mode of the system. Keeping this in mind, conventional linear stability theory is used, in this chapter, to deal with convective instability in a three-dimensional fault zone in a much more flexible, but logical manner. However, the linear stability analysis is only valid in determining the onset of the convective instability because, once the convective instability occurs, the perturbation approach fails and the nonlinear terms in the governing equations cannot be neglected. In this regard, if only the linear stability theory is used the first triggered convective flow mode of the system is meaningful. Since the geometric characteristics of a three-dimensional fault zone are that the lengths of the fault zone in both the thickness and the height directions (i.e., H_2 and H_3) are finite, and that the ratio of fault thickness to height (i.e., H_2/H_3) is very small, convective flow structure is mainly controlled by the fault height to thickness ratio. As a result, several different convective flow structures may have the same chance to occur, even if the linear stability theory is used. This means that linear stability theory can be used to predict several different convective flow structures because the differences in the critical Rayleigh numbers are very small, as will be demonstrated in the next section.

9.2 Analysis of Convective Instability of the Fault Zone System

This section investigates the condition under which three-dimensional convective flow can take place in the fault zone system defined in the previous section. Specifically, the main purpose is to determine the critical Rayleigh number, for which convective instability within the fault zone system can be initiated. This can be achieved using the linear stability analysis below.

If the hydrothermal system is subjected to a small disturbance, then the total solutions for the dimensionless velocities, temperature and pressure of the system can be expressed as

$$u_t^* = u^* + \hat{u}^*, \quad v_t^* = v^* + \hat{v}^*, \quad w_t^* = w^* + \hat{w}^*, \tag{9.28}$$

$$T_t^* = T^* + \hat{T}^*, \quad P_t^* = P^* + \hat{P}^*, \tag{9.29}$$

where u_t^*, v_t^*, w_t^*, T_t^* and P_t^* are the total solutions of the problem; u^*, v^*, w^*, T^* and P^* are the base solutions prior to the onset of the convective pore-fluid flow, and $\hat{u}^*$, $\hat{v}^*$, $\hat{w}^*$, $\hat{T}^*$ and $\hat{P}^*$ are the corresponding perturbation solutions due to the small disturbance.

From the linear stability theory point of view, if and only if all these perturbation solutions are zero, then the base solutions of the problem are stable. This implies that the stability of the base solutions for the hydrothermal system considered here can be judged by examining the existence of the non-zero solutions for $\hat{u}^*$, $\hat{v}^*$, $\hat{w}^*$, $\hat{T}^*$ and $\hat{P}^*$.

Note that the small disturbance may be caused by a small tremor of the Earth. From the classical perturbation theory, we can introduce a small parameter, ε, to express the consequence of this small disturbance. For example, using this small parameter, it is possible to express the resulting perturbation velocity, temperature and pressure of a system in the following form:

$$\hat{u}^* = \varepsilon(\hat{u}^{*(0)} + \varepsilon\hat{u}^{*(1)} + \varepsilon^2\hat{u}^{*(2)} + \ldots\ldots), \tag{9.30}$$

$$\hat{v}^* = \varepsilon(\hat{v}^{*(0)} + \varepsilon\hat{v}^{*(1)} + \varepsilon^2\hat{v}^{*(2)} + \ldots\ldots), \tag{9.31}$$

$$\hat{w}^* = \varepsilon(\hat{w}^{*(0)} + \varepsilon\hat{w}^{*(1)} + \varepsilon^2\hat{w}^{*(2)} + \ldots\ldots), \tag{9.32}$$

$$\hat{P}^* = \varepsilon(\hat{P}^{*(0)} + \varepsilon\hat{P}^{*(1)} + \varepsilon^2\hat{P}^{*(2)} + \ldots\ldots), \tag{9.33}$$

$$\hat{T}^* = \varepsilon(\hat{T}^{*(0)} + \varepsilon\hat{T}^{*(1)} + \varepsilon^2\hat{T}^{*(2)} + \ldots\ldots). \tag{9.34}$$

Substituting (9.28), (9.29), (9.30), (9.31), (9.32), (9.33) and (9.34) into (9.18), (9.19), (9.20), (9.21) and (9.22), considering the linear perturbation terms only (i.e., ε terms only) and then dropping the unnecessary superscripts, we obtain the following eigenvalue problem:

$$\frac{\partial\hat{u}^*}{\partial x^*} + \frac{\partial\hat{v}^*}{\partial y^*} + \frac{\partial\hat{w}^*}{\partial z^*} = 0, \tag{9.35}$$

$$\hat{u}^* = -\frac{\partial\hat{P}^*}{\partial x^*} + Ra_T\hat{T}^*e_1, \tag{9.36}$$

$$\hat{v}^* = -\frac{\partial\hat{P}^*}{\partial y^*} + Ra_T\hat{T}^*e_2, \tag{9.37}$$

$$\hat{w}^* = -\frac{\partial\hat{P}^*}{\partial z^*} + Ra_T\hat{T}^*e_3, \tag{9.38}$$

$$\hat{u}^*\frac{\partial T^*}{\partial x^*} + \hat{v}^*\frac{\partial T^*}{\partial y^*} + \hat{w}^*\frac{\partial T^*}{\partial z^*} = \frac{\partial^2\hat{T}^*}{\partial x^{*2}} + \frac{\partial^2\hat{T}^*}{\partial y^{*2}} + \frac{\partial^2\hat{T}^*}{\partial z^{*2}}. \tag{9.39}$$

The corresponding boundary conditions for the perturbation variables can be expressed as

$$\hat{u}^* = 0, \quad \frac{\partial\hat{T}^*}{\partial x^*} = 0 \quad (x^* = 0 \text{ and } x^* = H_1^*), \tag{9.40}$$

$$\hat{P}^* = 0, \quad \hat{T}^* = 0 \quad (y^* = 0 \text{ and } y^* = H_2^*), \tag{9.41}$$

$$\hat{w}^* = 0, \quad \hat{T}^* = 0 \quad (z^* = 0 \text{ and } z^* = 1). \tag{9.42}$$

Inserting (9.36), (9.37) and (9.38) into (9.35) yields the following equation:

$$\frac{\partial^2 \hat{P}^*}{\partial x^{*2}} + \frac{\partial^2 \hat{P}^*}{\partial y^{*2}} + \frac{\partial^2 \hat{P}^*}{\partial z^{*2}} - Ra_T \frac{\partial \hat{T}^*}{\partial z^*} = 0. \tag{9.43}$$

Substituting (9.36), (9.37) and (9.38) into (9.39) yields another equation as follows:

$$\frac{\partial \hat{P}^*}{\partial z^*} - Ra_T \hat{T}^* = \frac{\partial^2 \hat{T}^*}{\partial x^{*2}} + \frac{\partial^2 \hat{T}^*}{\partial y^{*2}} + \frac{\partial^2 \hat{T}^*}{\partial z^{*2}}. \tag{9.44}$$

For the given fault zone configuration shown in Fig. 9.1, since the lengths of the fault zone in all three directions are finite, the well-known separation of variables method in mathematics is useful to solve this problem. As we mentioned before, the study of convective instability in a three-dimensional fault zone involves finding nontrivial solutions for the partial differential equations expressed in (9.43) and (9.44), with the prescribed boundary conditions in (9.40), (9.41) and (9.42). The conditions, under which the nontrivial solutions for the partial differential equations can exist, are the onset conditions of the pore-fluid convective flow in the fault zone, and the nontrivial solutions are the convective flow structures of the fault zone. This means that any useful mathematical method can be used to solve the convective instability problem considered in this study as long as the onset conditions of the pore-fluid convective flow can be found. From the general expression of the derived onset conditions, we need to find the most possible onset condition, which corresponds to the minimum critical Rayleigh number of the system in the conventional linear stability analysis sense. For the above reasons, the solutions that satisfy the boundary conditions in the x^* and y^* directions are expressed as follows:

$$\hat{P}^* = f(z^*)\cos(k_1^* x^*)\sin(k_2^* y^*), \tag{9.45}$$

$$\hat{T}^* = \theta(z^*)\cos(k_1^* x^*)\sin(k_2^* y^*), \tag{9.46}$$

where k_1^* and k_2^* are the dimensionless wave numbers in the x^* and y^* directions, respectively:

$$k_1^* = \frac{m\pi}{H_1^*} \quad (m = 1, 2, 3, \ldots\ldots), \tag{9.47}$$

$$k_2^* = \frac{n\pi}{H_2^*} \quad (n = 1, 2, 3, \ldots\ldots). \tag{9.48}$$

Using (9.45) and (9.46), the boundary conditions in the z^* direction can be expressed as

$$Ra_T \theta(z^*) - f'(z^*) = 0 \quad (z^* = 0 \text{ and } z^* = 1), \tag{9.49}$$

$$\theta(z^*) = 0 \quad (z^* = 0 \text{ and } z^* = 1). \tag{9.50}$$

Substituting (9.45) and (9.46) into (9.43) yields the following equation:

$$-(k_1^{*2}+k_2^{*2})f(z^*)+f''(z^*)-Ra_T\theta'(z^*)=0. \tag{9.51}$$

Inserting (9.45) and (9.46) into (9.44) yields another equation as follows:

$$f'(z^*)=(Ra_T-k_1^{*2}-k_2^{*2})\theta(z^*)+\theta''(z^*). \tag{9.52}$$

Differentiating (9.52) with respect to z^* twice yields the following equation:

$$f'''(z^*)=(Ra_T-k_1^{*2}-k_2^{*2})\theta''(z^*)+\theta^{(IV)}(z^*). \tag{9.53}$$

Differentiating (9.51) with respect to z^* once yields another equation as follows:

$$-(k_1^{*2}+k_2^{*2})f'(z^*)+f'''(z^*)-Ra_T\theta''(z^*)=0. \tag{9.54}$$

Substituting (9.52) and (9.53) into (9.54) yields the following equation:

$$\theta^{(IV)}(z^*)-2(k_1^{*2}+k_2^{*2})\theta''(z^*)-(k_1^{*2}+k_2^{*2})(Ra_T-k_1^{*2}-k_2^{*2})\theta(z^*)=0. \tag{9.55}$$

Inserting (9.52) into (9.49) yields the boundary conditions depending on θ only:

$$(k_1^{*2}+k_2^{*2})\theta(z^*)-\theta''(z^*)=0 \quad (z^*=0 \text{ and } z^*=1), \tag{9.56}$$

The following function satisfies the boundary conditions expressed in (9.50) and (9.56).

$$\theta(z^*)=\sin(k_3^*z^*), \tag{9.57}$$

where k_3^* is the dimensionless wave number in the x_3^* direction:

$$k_3^*=q\pi \quad (q=1,2,3,\ldots\ldots). \tag{9.58}$$

Substituting (9.57) into (9.55) yields the critical Rayleigh numbers for different convection modes as follows:

$$Ra_T=\frac{(k_1^{*2}+k_2^{*2}+k_3^{*2})^2}{k_1^{*2}+k_2^{*2}}. \tag{9.59}$$

Substituting the dimensionless wave number into (9.59) yields the following equation:

$$Ra_T=\frac{\left[\left(\frac{mH_3}{H_1}\right)^2+\left(\frac{nH_3}{H_2}\right)^2+q^2\right]^2\pi^2}{\left(\frac{mH_3}{H_1}\right)^2+\left(\frac{nH_3}{H_2}\right)^2}. \tag{9.60}$$

Note that (9.60) is a general expression for the critical Rayleigh numbers of the three-dimensional fault zone. These critical Rayleigh numbers describe the onset conditions of the convective flows in the system. Since the linear stability concept is used in the analysis, it is important to find the minimum critical Rayleigh number,

which corresponds to the most possible convective flow structure in the system. For the given fault zone configuration shown in Fig. 9.1, since the lengths of the fault zone in all three directions are finite, we can set $m = n = q = 1$ and allow H_1 to vary in the fault length direction. This means that both the height and the thickness of the fault zone are fixed as constants, but the length of the fault zone can change as a variable of the system. Through selecting the appropriate value of H_1, the minimum critical Rayleigh number of the system can be determined. For this purpose, the critical Rayleigh number for three-dimensional convection flow to take place can be expressed as

$$Ra_{Tcritical}^{3D} = \frac{\left[\left(\frac{H_3}{H_1}\right)^2 + (\frac{H_3}{H_2})^2 + 1\right]^2 \pi^2}{\left(\frac{H_3}{H_1}\right)^2 + \left(\frac{H_3}{H_2}\right)^2}. \tag{9.61}$$

Differentiating (9.61) with respect to H_1 yields the following equation:

$$\frac{dRa_{Tcritical}^{3D}}{dH_1} = -2\pi^2 \frac{H_3^2 \left\{\left[\left(\frac{H_3}{H_1}\right)^2 + (\frac{H_3}{H_2})^2\right]^2 - 1\right\}}{H_1^3 \left[\left(\frac{H_3}{H_1}\right)^2 + (\frac{H_3}{H_2})^2\right]^2} \approx -2\pi^2 \frac{H_3^2}{H_1^3}. \tag{9.62}$$

Note that (9.62) is valid when $H_3/H_2 >> 1$ and $H_1/H_2 >> 1$, which are true for the fault zone considered in this study. Equation (9.62) indicates that the minimum critical Rayleigh number of the system is obtained only when H_1 tends to infinity. In such a case, the wave number in the x direction is zero and convective flow is essentially two-dimensional convective flow, which is the degenerated case of three-dimensional convective flow. We call this kind of convective flow two-dimensional slender-circle convective flow with the following minimum critical Rayleigh number:

$$Ra_{Tcritical}^{2D} = \frac{\left[\left(1 + \left(\frac{H_3}{H_2}\right)^2\right]^2 \pi^2}{\left(\frac{H_3}{H_2}\right)^2}. \tag{9.63}$$

Equation (9.62) also indicates that when $H_3/H_1 << 1$, the critical Rayleigh number of the system changes very slowly so that the differences between the corresponding critical Rayleigh numbers and the minimum critical Rayleigh number of the system are very small. This means that several convective flow structures may have almost the same chance to take place in the system. Since the three-dimensional standard convective flow structures are only of interest here, we consider the case of $H_3 = H_1$ and determine the corresponding critical Rayleigh number below. If $H_3 = H_1$, we have the following equation:

$$Ra_{Tcritical}^{3D} = \frac{\left[\left(2 + \left(\frac{H_3}{H_2}\right)^2\right]^2 \pi^2}{1 + \left(\frac{H_3}{H_2}\right)^2}. \tag{9.64}$$

Thus, the critical Rayleigh number for three-dimensional standard convective flow to occur is proportional to the ratio of the fault height to thickness.

The relative difference between $Ra^{3D}_{Tcritical}$ and $Ra^{2D}_{Tcritical}$ can be expressed from (9.63) and (9.64) as follows:

$$\bar{\Delta}_1 = \frac{Ra^{3D}_{Tcritical} - Ra^{2D}_{Tcritical}}{Ra^{2D}_{Tcritical}} = \frac{(\frac{H_3}{H_2})^4 + (\frac{H_3}{H_2})^2 - 1}{\left[\left(\frac{H_3}{H_2}\right)^2 + 1\right]^3}. \tag{9.65}$$

Since $H_3/H_2 >> 1$, (9.65) can be approximately written as

$$\bar{\Delta}_1 \approx \left(\frac{H_2}{H_3}\right)^2. \tag{9.66}$$

Equation (9.66) indicates that the relative difference between $Ra^{3D}_{Tcritical}$ and $Ra^{2D}_{Tcritical}$ is a second-order small quantity, provided that H_2/H_3 is very small, just as considered in this study. For example, if $H_2/H_3 = 0.01$, the relative difference between $Ra^{3D}_{Tcritical}$ and $Ra^{2D}_{Tcritical}$ is about 0.0001, which is a very small number indeed. In this case, $Ra^{3D}_{Tcritical} \approx 98716.2$, while $Ra^{2D}_{Tcritical} \approx 98726.1$. The relative difference between $Ra^{3D}_{Tcritical}$ and $Ra^{2D}_{Tcritical}$ approaches zero as H_2/H_3 tends to zero.

Similarly, for the three-dimensional finger-like convective structure, the corresponding critical Rayleigh number can be expressed as

$$Ra^{3D-finger}_{Tcritical} = \frac{\left[(m^2 + \left(\frac{H_3}{H_2}\right)^2 + 1\right]^2 \pi^2}{m^2 + \left(\frac{H_3}{H_2}\right)^2} \quad (m \geq 2). \tag{9.67}$$

In the case of $m = 3$ and $H_2/H_3 = 0.01$, the corresponding $Ra^{3D-finger}_{Tcritical} \approx 98805$. Again, this value is also very close to the minimum critical Rayleigh number of the system, $Ra^{2D}_{Tcritical} \approx 98726.1$, indicating that three-dimensional finger-like convective flow can also take place in three-dimensional fault zones. As a recent numerical simulation of convective flow in a vertically oriented geological fault zone has demonstrated, three-dimensional finger-like convective flow does occur in such systems (Rabinowicz et al. 1999).

The occurrence of three-dimensional finger-like convective flow has a significant geological implication for ore body formation and mineralization within three-dimensional geological fault zones. Since down-temperature convective flow may result in mineral precipitation and up-temperature convective flow may result in mineral dissolution, periodic mineral zonation can be produced within three-dimensional geological fault zones. Such a quasiperiodic distribution of mineralization phenomenon has been observed in the Yilgarn ore deposits, Western Australia (Zhao et al. 2008).

It is noted that the following relation exists:

$$k_i^* = k_i H \quad (i = 1,2,3), \tag{9.68}$$

where k_i is the dimensional wave number in the real physical system.

For the three-dimensional fault zone considered in this study, the dimensional wave numbers are as follows:

$$k_1 = \frac{m\pi}{H_1}, \quad k_2 = \frac{n\pi}{H_2}, \quad k_3 = \frac{q\pi}{H_3}. \tag{9.69}$$

Finally, the dimensionless perturbation solutions for pore-fluid velocity, temperature and pressure can be derived and expressed as

$$\hat{u}_1^* = -\frac{k_1^* k_3^* (k_1^{*2} + k_2^{*2} + k_3^{*2})}{k_1^{*2} + k_2^{*2}} \sin(k_1^* x^*) \sin(k_2^* y^*) \cos(k_3^* z^*), \tag{9.70}$$

$$\hat{u}_2^* = \frac{k_2^* k_3^* (k_1^{*2} + k_2^{*2} + k_3^{*2})}{k_1^{*2} + k_2^{*2}} \cos(k_1^* x^*) \cos(k_2^* y^*) \cos(k_3^* z^*), \tag{9.71}$$

$$\hat{u}_3^* = (k_1^{*2} + k_2^{*2} + k_3^{*2}) \cos(k_1^* x^*) \sin(k_2^* y^*) \sin(k_3^* z^*), \tag{9.72}$$

$$\hat{T}^* = \cos(k_1^* x^*) \sin(k_2^* y^*) \sin(k_3^* z^*), \tag{9.73}$$

$$\hat{P}^* = \cos(k_1^* x^*) \sin(k_2^* y^*) f(z^*), \tag{9.74}$$

where $f(z^*)$ can be determined by integrating (9.52) with respect to z^* as follows:

$$f(z^*) = -\frac{Ra_T - (k_1^{*2} + k_2^{*2} + k_3^{*2})}{k_3^*} \cos(k_3^* z^*). \tag{9.75}$$

9.3 Possibility of Convective Flow in Geological Fault Zone Systems

In this section, the analytical solution derived in the previous section is used to investigate the possibility of convective flow in geological fault zones. Using an idealized geological fault zone as an illustrative example, the following parameters are used in the subsequent analysis. For pore-fluid, dynamic viscosity is $10^{-3}\,\mathrm{N\cdot s/m^2}$; reference density is $1000\,\mathrm{kg/m^3}$; volumetric thermal expansion coefficient is $2.07 \times 10^{-4}(1/\mathrm{K})$; specific heat is $4185\,\mathrm{J/(kg\cdot K)}$, and thermal conductivity coefficient is $0.6\,\mathrm{W/(m\cdot K)}$. For the porous matrix, porosity is 0.1; thermal conductivity coefficient is $3.35\,\mathrm{W/(m\cdot K)}$; specific heat is $815\,\mathrm{J/(kg\cdot K)}$; permeability is $10^{-12}\mathrm{m}^2$, which is assumed as a representative value for a fractured environment (Berryman and Wang 1995); height and thickness of the fault are 10 km and 0.5 km, respectively, and temperature at the top and bottom is 25 °C and 225 °C, respectively.

Substituting the related parameters into (9.23) yields the Rayleigh number for the system:

$$\begin{aligned} Ra_T &= \frac{(\rho_{f0}c_p)\rho_{f0}g\beta\Delta T K_0 H}{\mu\lambda_{e0}} \\ &= \frac{1000\times 4185\times 1000\times 9.8\times 2\times 10^{-4}\times 200\times 10^{-12}\times 10^4}{10^{-3}\times 3} \approx 5380. \end{aligned} \tag{9.76}$$

The corresponding minimum critical Rayleigh number of the fault zone of infinite length is

$$Ra_{Tcritical}^{2D} = \frac{\left[\left(1+\left(\frac{H_3}{H_2}\right)^2\right]^2\pi^2}{\left(\frac{H_3}{H_2}\right)^2} = \frac{(1+20^2)^2\pi^2}{20^2} \approx 3967.6. \tag{9.77}$$

The corresponding critical Rayleigh number for three-dimensional standard convective flow is

$$Ra_{Tcritical}^{3D} = \frac{\left[\left(2+\left(\frac{H_3}{H_2}\right)^2\right]^2\pi^2}{1+\left(\frac{H_3}{H_2}\right)^2} = \frac{(2+20^2)^2\pi^2}{1+20^2} \approx 3977.5. \tag{9.78}$$

In the case of $m = 3$, the corresponding critical Rayleigh number for three-dimensional convective flow is

$$Ra_{Tcritical}^{3D-finger} = \frac{\left[\left(m^2+\left(\frac{H_3}{H_2}\right)^2+1\right]^2\pi^2}{m^2+\left(\frac{H_3}{H_2}\right)^2} = \frac{(10+20^2)^2\pi^2}{9+20^2} \approx 4056.5. \tag{9.79}$$

Because the three critical Rayleigh numbers described above are very close to each other and $Ra_T > Ra_{Tcritical}^{3D-finger}$, the three kinds of convective flow have very similar possibilities of occurring in the geological fault zone considered here.

The two-dimensional slender-circle structure of convection cells can only take place when the length of the fault zone is infinite (i.e., H_1 approaches infinite). This means that no convection cell takes place in the x direction and the two-dimensional slender-circle flow structure is obtained in the plane perpendicular to the x axis. However, if the length of the fault zone is finite, the corresponding convective flow must be three-dimensional. Even if the length of the fault zone is infinite, since the minimum critical Rayleigh number of the system (i.e., 3967.6) for the two-dimensional slender-circle flow structure is so close to the critical Rayleigh number (i.e., 3977.5) for three-dimensional standard convective flow structure, the system may have a high probability of developing a three-dimensional convective flow structure. Since the convection modes are so close for three-dimensional convective

flow structures, convective flow may also evolve into the three-dimensional finger-like structure (i.e., $m \geq 2$). These conclusions demonstrate the beautiful aspects of the present analytical solution for convective instability within three-dimensional geological fault zones, because this analytical solution is valid for any value of the ratio of the fault height to thickness. Using the present analytical solution, the conditions, under which different convective flow structures may occur in a three-dimensional fault zone, can be easily determined.

Figures 9.2 and 9.3 show the theoretical fundamental mode ($m = 1$) and finger-like mode ($m = 3$) for the perturbed pore-fluid velocity on three particular cross sections in a pore-fluid saturated geological fault zone. The length and height of the fault zone are 10 km, while the thickness of the fault zone is 1 km. Convective

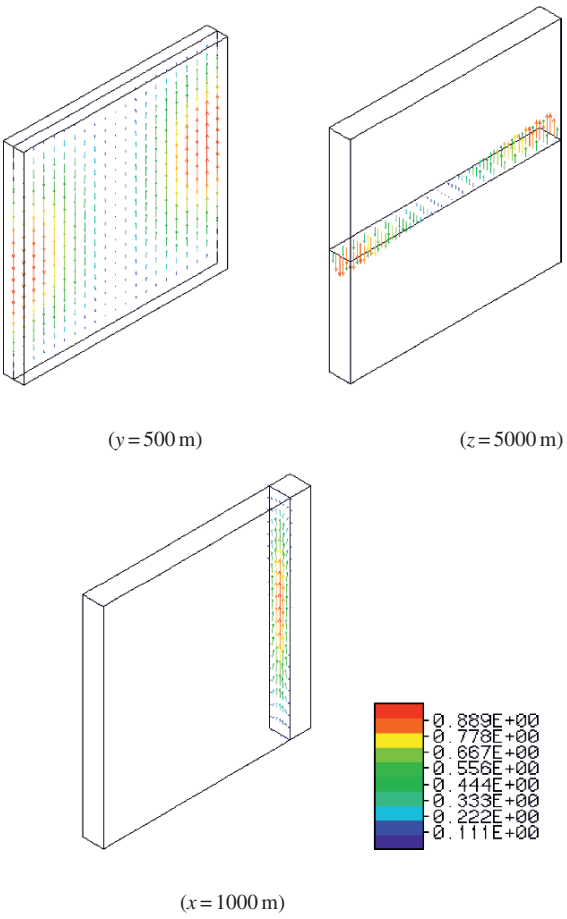

Fig. 9.2 Convective flow mode in a three-dimensional fault (theoretical fundamental mode)

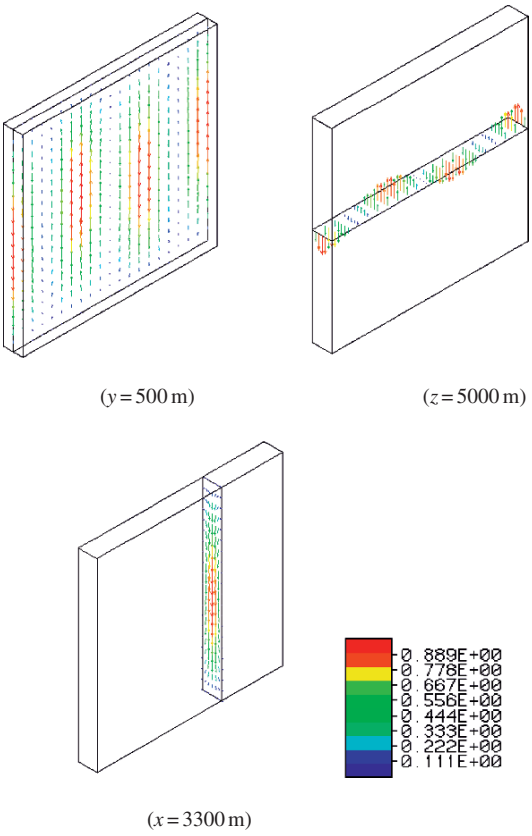

Fig. 9.3 Convective flow mode in a three-dimensional fault (theoretical finger-like mode)

pore-fluid flow takes place strongly in the vertical direction. Indeed, the horizontal pore-fluid velocity is negligible on both the sidewalls (i.e., $y = 0$ and $y = H_2$) of the fault zone, although a hydrostatic pore-fluid pressure gradient condition is used in the analysis. In the case of the finger-like mode, the pore-fluid flow channeling can be clearly observed. This pore-fluid flow channeling phenomenon can significantly influence ore body formation and mineralization patterns within geological fault zones.

Chapter 10
Convective Heat Transfer within Three-Dimensional Inclined Faults Heated from Below

Extensive studies on the governing processes behind ore body formation and mineralization in hydrothermal systems (Walther and Orville 1982; Etheridge et al. 1983; Garven and Freeze 1984; Bjorlykke et al. 1988; England and Thompson 1989; Deming and Nunn 1991; Hoisch 1991; Hanson 1992; Yardley and Bottrell 1992; Zhao et al. 1998a, 2000c, 2002b; Gow et al. 2002; Ord et al. 2002; Schaubs and Zhao 2002) have demonstrated that pore-fluid flow in permeable rocks in the upper crust of the Earth is a very complicated phenomenon, from both physical and chemical points of view. Generally, pore-fluid flow can be generated by the following main processes: mechanical process, thermal process, chemical process, or any combination thereof. In the case of mechanical process, pore-fluid flow is mainly caused by a pressure gradient in the porous basin and is, therefore, called pressure gradient driven flow. Pore-fluid flow induced by uneven topography of a basin and pore-fluid flow squeezed out of a sedimentary basin by shortening of the upper crust of the Earth are typical examples of pressure gradient driven flow. In the case of thermal process, pore-fluid flow is dominantly caused by the temperature gradient in porous rocks. Thus, it is often called temperature gradient driven flow (Horton and Rogers 1945; Lapwood 1948; Phillips 1991; Nield and Bejan 1992; Zhao et al. 1997, 1999a, 2001a; Lin et al. 2003). Note that, in order to generate temperature gradient driven flow in the upper crust with a flat top and bottom to the system, the temperature gradient of the hydrothermal system must be equal to or greater than a critical temperature gradient. Pore-fluid flow driven by the critical or supercritical temperature gradient in a hydrothermal system is often called convective pore-fluid flow (Horton and Rogers 1945; Lapwood 1948; Phillips 1991; Nield and Bejan 1992; Zhao et al. 1997, 1999a, 2001a; Lin et al. 2003). This kind of convective pore-fluid flow is significant for ore body formation and mineralization in hydrothermal systems from the following three points of view.

(1) Since the pore-fluid flows circularly within hydrothermal systems, the consumption of the pore-fluid is a minimum within the system.
(2) Since convective pore-fluid flow comprises a circular flow regime, it is an effective and efficient tool for mixing different chemical species within the hydrothermal system.

C. Zhao et al., *Convective and Advective Heat Transfer in Geological Systems*,

© Springer-Verlag Berlin Heidelberg 2008

(3) Convective pore-fluid flow may result in the highly localized distribution of temperature in a hydrothermal system. This provides a favorable condition under which highly localized, high-grade, giant ore deposits may be formed.

For these reasons, the study of convective pore-fluid flow instability in geological systems has attracted ever-increasing attention in recent years. In the case of chemical process, a chemical species concentration gradient can be the main driven force to trigger pore-fluid flow. This kind of pore-fluid flow is called chemical species concentration gradient driven flow.

The study of convective instability of pore-fluid flow in fluid-saturated porous media was initiated by Horton and Rogers (1945) as well as Lapwood (1948) about one-half century ago. Since then, a large number of publications have been produced on this particular research topic. Nield and Bejan (1992) as well as Phillips (1991) have summarized the related research results in their books. Although research on the general aspects of the topic is extensive, it is very limited with respect to convective instability of pore-fluid flow in three-dimensional geological fault zones when they are heated uniformly from below (Beck 1972; Zebib and Kassoy 1977; Shyu 1978; Murphy 1979; Kassoy and Cotte 1985). In particular, Tournier et al. (2000) used a numerical method, which considers pore-fluid convection in the fault plane and the heat conduction in the rocks surrounding the fault zone using two-dimensional and three-dimensional computational models, respectively, to investigate the onset of natural convection of pore-fluid in vertical fault planes. In order to couple the two-dimensional convection simulation with the three-dimensional heat conduction simulation, they assumed that the fault zone is very thin and that the pore-fluid flow is slow within the fault plane, so that the temperature field within the fault zone is smooth enough to be correctly described by their computational model. It is well-known that, compared with analytical solutions, numerical solutions usually have the following intrinsic drawbacks. Since it is often impossible to use numerical solutions to investigate the behaviors of a system within the whole parameter space, which is usually of infinite nature, numerical solutions can only produce some kind of specific solution and conclusion for a particular problem. Therefore, in order to draw general conclusions for a problem, analytical solutions, if possible and available, are always superior to numerical solutions. More importantly, since numerical solutions always involve approximations, numerical solutions are often of doubtable value unless they are well validated and verified. On the other hand, analytical solutions to benchmark problems provide an important, and often unique, tool for validating and verifying the numerical methods and algorithms, which may then be extended to solve the same kind of problem, but with complicated geometries and complex material properties. For the above reasons, an analytical solution is always preferred for investigating the onset condition of natural convective pore-fluid flow in three-dimensional geological fault zones. Since the asymptotic solutions presented by Kassoy and Cotte (1985) are only valid when the thickness of the fault zone approaches zero, it is impossible to use such asymptotic solutions to predict the different critical Rayleigh numbers, under which different convective flow structures can take place in the system. Keeping this in mind, Zhao et al. (2003a, b) have recently derived exact solutions for different critical Rayleigh

numbers. Using these exact solutions, different convective flow structures can be accurately defined in vertically oriented geological fault zones that contain geothermal gradients at both sidewalls.

Although significant achievements have been made in the study of convective flow instabilities in pore-fluid saturated porous media, theoretical work to study the onset condition of convective flow in an *inclined* three-dimensional geological fault zone that is heated uniformly from below has yet to be done. Since inclined three-dimensional geological fault zones are much more common than their vertically oriented counterpart, the main purpose of this chapter is to derive the exact critical conditions which can be used to examine convective flow instability in such inclined three-dimensional geological fault zones. However, from the mathematical analysis point of view, considering *inclined* three-dimensional fault zones with any arbitrary values of the dip angle results in some serious difficulties in deriving the critical onset condition for convective pore-fluid flow. Compared with the previous study (Zhao et al. 2003a), a combination of the variable separation method and the integration elimination method has been used, in logical and flexible ways, to derive the critical onset condition for convective pore-fluid flow in such a system (Zhao et al. 2004).

10.1 Governing Equations of the Problem

Consider an inclined and fluid-saturated three-dimensional geological fault zone; its thickness is much smaller than both its length and height, as shown in Fig. 10.1. *The fault zone with dip angle, φ, is assumed to be much more permeable than the surrounding rocks*. Numerical simulations (Zhao et al. 2006c) have demonstrated that if the permeability of the fault zone is three orders of magnitude higher than that

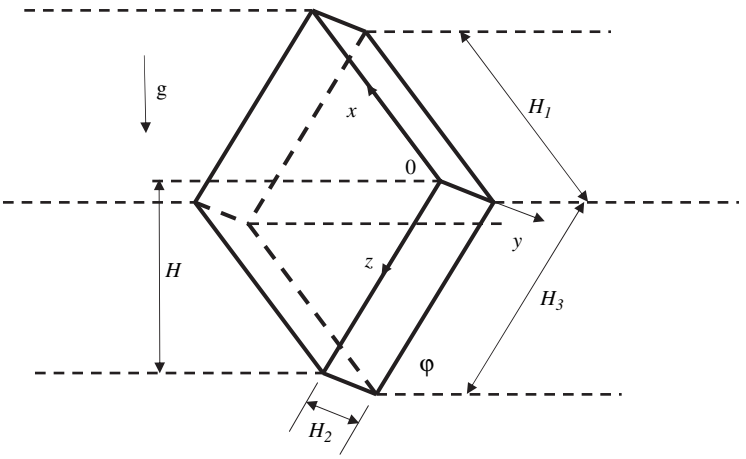

Fig. 10.1 Geometry of the problem

of the surrounding rocks, the resulting convective pore-fluid flow in the surrounding rocks is much smaller than that in the fault zone, indicating that the interaction between the fault zone and its surrounding rocks is negligible. Thus, from a theoretical analysis point of view, the fault zone can be separated from the surrounding rocks in the following theoretical analysis. Under this assumption, only the fault zone with appropriate boundary conditions is considered to derive the analytical solutions. Hence, the global rotation with respect to the different far fields does not affect the theoretical analysis carried out in this investigation.

The length of the inclined fault zone may be infinite in the x direction, but we consider a finite length for the fault zone of H_1 in this direction so that insulated and impermeable boundary conditions can be applied at both $x = 0$ and $x = H_1$. In the thickness direction, both the geothermal and background pore-fluid pressure gradients are considered and, therefore, the geothermal gradient and the background pore-fluid pressure gradient before convection need to be applied at both $y = 0$ and $y = H_2$. This means that any perturbation of the temperature within the geological fault zone has little influence on the initial thermal and pore-fluid pressure distributions of the surrounding rocks. It is assumed that the inclined fault zone is uniformly heated from below so that constant temperature and impermeable boundary conditions are applied at both $z = 0$ and $z = H_3$. In order to facilitate the forthcoming theoretical analysis, the material of the inclined fault zone is assumed to be homogeneous and isotropic. If Darcy's Law is used to describe pore-fluid flow and the Oberbeck-Boussinesq approximation is employed to describe a change in pore-fluid density due to a change in pore-fluid temperature, the governing equations of natural convection for incompressible fluid in a steady state can be expressed as

$$\frac{\partial u}{\partial x} + \frac{\partial v}{\partial y} + \frac{\partial w}{\partial z} = 0, \tag{10.1}$$

$$u = \frac{K_0}{\mu}\left(-\frac{\partial P}{\partial x} + \rho_f g_x\right), \tag{10.2}$$

$$v = \frac{K_0}{\mu}\left(-\frac{\partial P}{\partial y} + \rho_f g_y\right), \tag{10.3}$$

$$w = \frac{K_0}{\mu}\left(-\frac{\partial P}{\partial z} + \rho_f g_z\right), \tag{10.4}$$

$$\rho_{f0} c_p \left(u\frac{\partial T}{\partial x} + v\frac{\partial T}{\partial y} + w\frac{\partial T}{\partial z}\right) = \lambda_{e0}\left(\frac{\partial^2 T}{\partial x^2} + \frac{\partial^2 T}{\partial y^2} + \frac{\partial^2 T}{\partial z^2}\right), \tag{10.5}$$

$$\rho_f = \rho_{f0}[1 - \beta_T (T - T_0)], \tag{10.6}$$

$$\lambda_{e0} = \phi\lambda_{f0} + (1 - \phi)\lambda_{s0}, \tag{10.7}$$

where u, v and w are the velocity components of the pore-fluid in the x, y and z directions, respectively; P and T are pressure and temperature of the porous material; ρ_{f0} and T_0 are the reference density of pore-fluid and the reference temperature of the inclined fault zone; μ and c_p are the dynamic viscosity and specific heat of the pore-fluid; λ_{f0} and λ_{s0} are the thermal conductivity coefficients for the pore-fluid

and solid matrix in the inclined fault zone; ϕ and β are the porosity of the inclined fault zone and the thermal volume expansion coefficient of the pore-fluid; K_0 is the permeability of the inclined fault zone, and and g_x, g_y and g_z are the gravity acceleration components in the x, y and z directions.

The corresponding boundary conditions of the problem to be considered are as follows:

$$u = 0, \qquad \frac{\partial T}{\partial x} = 0 \qquad (x = 0 \text{ and } x = H_1), \quad (10.8)$$

$$P = P_b, \qquad T = \frac{T_b - T_0}{H}(z \sin \varphi) + T_0 \qquad (y = 0 \text{ and } y = H_2), \quad (10.9)$$

$$w = 0, \qquad T = T_0 \qquad (z = 0), \quad (10.10)$$

$$w = 0, \qquad T = T_b \qquad (z = H_3), \quad (10.11)$$

where P_b is the background pore-fluid pressure before convection occurs.

Although the onset of natural convective flow in a thin layer of the similar geometry as that considered in this chapter has been theoretically investigated in previous studies (Caltagirone 1975 and 1976; Caltagirone and Bories 1985; Ormond and Genthon 1993; Chevalier et al. 1999), the boundary conditions of the problem considered here are different from those in these previous studies. Since both the critical Rayleigh number and the corresponding pore-fluid convective mode are strongly dependent on the boundary conditions of a problem, the solutions for these two characteristics can be different for a problem with the same geometry, but with different boundary conditions. Nield and Bejan (1992) presented a useful comparison for the onset conditions of natural convective flow in a horizontal layer with different boundary conditions. For example, for a horizontal layer with constant temperature and impermeable boundary conditions at both the top and the bottom of the layer, the critical Rayleigh number of the system is $4\pi^2$ and the corresponding convective flow mode is of a closed cellular shape. However, for a horizontal layer with constant temperature and impermeable boundary conditions at the bottom of the layer, but with constant temperature and permeable boundary conditions at the top of the layer, the critical Rayleigh number of the system is reduced to 27.1 and the corresponding convective flow mode is of an open U-shape. Since the temperature at the sidewalls (i.e., at both $y = 0$ and $y = H_2$) of the fault zone was assumed to be constant, the related previous results (Caltagirone 1975, 1976; Caltagirone and Bories 1985; Ormond and Genthon 1993; Chevalier et al. 1999 and the references therein) have extensively demonstrated that the predominant convective flow modes can only take place in the planes perpendicular to the fault plane. Although some preliminary analytical results (Lowell and Shyu 1978; Murphy 1979; Kassoy and Cotte 1985; Tournier et al. 2000) indicated possible predominant convective flow modes occurring in the fault plane, theoretical work has recently studied the onset condition of convective flow in an *inclined* three-dimensional geological fault zone that is a pore-fluid saturated porous medium and has been heated uniformly from below (Zhao et al. 2004).

Another important characteristic of this study is that the thickness of the fault zone is finite. This means that variations of both the temperature and the pore-fluid

velocity in the thickness direction (i.e., in the y direction) are considered in deriving the analytical solutions for the onset condition of convective flow in the *inclined* fault zone. Indeed, as demonstrated later in this chapter, both the temperature and the pore-fluid velocity vary in the thickness direction of the fault zone, even though the predominant convective flow modes occur in the fault plane. This new recognition, again, sets this study apart from the previous studies (Lowell and Shyu 1978; Murphy 1979; Kassoy and Cotte 1985; Tournier et al. 2000).

The assumption of a geothermal gradient at the sidewalls (i.e., at both $y = 0$ and $y = H_2$) of the fault zone implies that the perturbed temperature within the fault zone is much smaller than the initial temperature at the sidewalls and, therefore, the effect of the perturbed temperature within the fault zone on the initial temperature at the sidewalls can be neglected. Nevertheless, the above-mentioned effect can be considered by using the effective thickness of the fault zone. The effective thickness of the fault zone should be a little larger than the physical thickness of the fault zone. This may be considered as a limitation of the analytical solutions presented in this study.

In order to simplify (10.1), (10.2), (10.3), (10.4) and (10.5), the following dimensionless variables are defined:

$$x^* = \frac{x}{H_r}, \qquad y^* = \frac{y}{H_r}, \qquad z^* = \frac{z}{H_r}, \tag{10.12}$$

$$H_1^* = \frac{H_1}{H_r}, \qquad H_2^* = \frac{H_2}{H_r}, \qquad H_3^* = \frac{H_3}{H_r}, \tag{10.13}$$

$$u^* = \frac{H\rho_{f0}c_p}{\lambda_{e0}}u, \qquad v^* = \frac{H\rho_{f0}c_p}{\lambda_{e0}}v, \qquad w^* = \frac{H\rho_{f0}c_p}{\lambda_{e0}}w, \tag{10.14}$$

$$T^* = \frac{T - T_0}{\Delta T}, \qquad P^* = \frac{K_0\rho_{f0}c_p}{\mu\lambda_{e0}}(P - P_b), \tag{10.15}$$

where x^*, y^* and z^* are the dimensionless coordinates; u^*, v^* and w^* are the dimensionless velocity components in the x, y and z directions, respectively; H_1^*, H_2^* and H_3^* are the dimensionless length, thickness and height of the fault zone; P^* and T^* are the dimensionless excess pressure and temperature; ΔT is the temperature difference between the bottom and top boundaries of the porous medium; H_r is a reference length and p_b is the background pore-fluid pressure before the occurrence of convection. In the following analysis, H_3 is chosen as the reference length (i.e., $H_r = H_3$).

Substituting the above dimensionless variables into (10.1), (10.2), (10.3), (10.4) and (10.5) yields

$$\frac{\partial u^*}{\partial x^*} + \frac{\partial v^*}{\partial y^*} + \frac{\partial w^*}{\partial z^*} = 0, \tag{10.16}$$

$$u^* = -\frac{\partial P^*}{\partial x^*} + Ra_T T^* e_1, \tag{10.17}$$

$$v^* = -\frac{\partial P^*}{\partial y^*} + Ra_T T^* e_2, \tag{10.18}$$

$$w^* = -\frac{\partial P^*}{\partial z^*} + Ra_T T^* e_3, \tag{10.19}$$

$$u^* \frac{\partial T^*}{\partial x^*} + v^* \frac{\partial T^*}{\partial y^*} + w^* \frac{\partial T^*}{\partial z^*} = \frac{\partial^2 T^*}{\partial x^{*2}} + \frac{\partial^2 T^*}{\partial y^{*2}} + \frac{\partial^2 T^*}{\partial z^{*2}}, \tag{10.20}$$

where $\boldsymbol{e}$ is a unit vector and $\boldsymbol{e} = e_1\boldsymbol{i} + e_2\boldsymbol{j} + e_3\boldsymbol{k}$ for a general three-dimensional problem. For the particular problem considered in this chapter, $e_1 = 0$, $e_2 = \cos\varphi$ and $e_3 = \sin\varphi$ since the acceleration due to gravity is only exerted on the vertical direction that is not parallel to either the y or z axis (see Fig. 10.1). Ra_T is the Rayleigh number, defined as

$$Ra_T = \frac{(\rho_{f0} c_p)\rho_{f0} g \beta \Delta T K_0 H_r}{\mu \lambda_{e0}}. \tag{10.21}$$

Using the dimensionless variables, the corresponding boundary conditions can be expressed as

$$u^* = 0, \quad \frac{\partial T^*}{\partial x^*} = 0 \quad (x^* = 0 \text{ and } x^* = H_1^*), \tag{10.22}$$

$$P^* = 0, \quad T^* = z^* \quad (y^* = 0 \text{ and } y^* = H_2^*), \tag{10.23}$$

$$w^* = 0, \quad T^* = 1 \quad (z^* = 0), \tag{10.24}$$

$$w^* = 0, \quad T^* = 0 \quad (z^* = 1). \tag{10.25}$$

10.2 Analysis of Convective Instability of Pore-Fluid Flow in an Inclined Three-Dimensional Fault Zone System

This section investigates the condition under which three-dimensional convective flow can take place in the inclined fault zone system defined in the previous section. Specifically, the main purpose is to determine the critical Rayleigh number, with which convective instability can be explored. From linear stability theory, the first-order perturbation equations of the hydrothermal system considered here can be expressed as follows:

$$\frac{\partial \hat{u}^*}{\partial x^*} + \frac{\partial \hat{v}^*}{\partial y^*} + \frac{\partial \hat{w}^*}{\partial z^*} = 0, \tag{10.26}$$

$$\hat{u}^* = -\frac{\partial \hat{P}^*}{\partial x^*} + Ra_T \hat{T}^* e_1, \tag{10.27}$$

$$\hat{v}^* = -\frac{\partial \hat{P}^*}{\partial y^*} + Ra_T \hat{T}^* e_2, \tag{10.28}$$

$$\hat{w}^* = -\frac{\partial \hat{P}^*}{\partial z^*} + Ra_T \hat{T}^* e_3, \tag{10.29}$$

$$\hat{w}^* \frac{\partial T^*}{\partial z^*} = \frac{\partial^2 \hat{T}^*}{\partial x^{*2}} + \frac{\partial^2 \hat{T}^*}{\partial y^{*2}} + \frac{\partial^2 \hat{T}^*}{\partial z^{*2}}, \tag{10.30}$$

where $\hat{u}^*$, $\hat{v}^*$ and $\hat{w}^*$ are the dimensionless perturbation velocity components (i.e., dimensionless convective velocity components), and $\hat{P}^*$ and $\hat{T}^*$ are the dimensionless perturbation pressure and temperature. Note that $\partial T^* \big/ \partial z^* = 1$ in (10.30).

The corresponding boundary conditions for the perturbation variables can be expressed as

$$\hat{u}^* = 0, \qquad \frac{\partial \hat{T}^*}{\partial x^*} = 0 \qquad (x^* = 0 \text{ and } x^* = H_1^*), \tag{10.31}$$

$$\hat{P}^* = 0, \qquad \hat{T}^* = 0 \qquad (y^* = 0 \text{ and } y^* = H_2^*), \tag{10.32}$$

$$\hat{w}^* = 0, \qquad \hat{T}^* = 0 \qquad (z^* = 0 \text{ and } z^* = 1). \tag{10.33}$$

Inserting (10.27), (10.28) and (10.29) into (10.26) yields the following equation:

$$\frac{\partial^2 \hat{P}^*}{\partial x^{*2}} + \frac{\partial^2 \hat{P}^*}{\partial y^{*2}} + \frac{\partial^2 \hat{P}^*}{\partial z^{*2}} + Ra_T \frac{\partial \hat{T}^*}{\partial y^*} \cos\varphi + Ra_T \frac{\partial \hat{T}^*}{\partial z^*} \sin\varphi = 0. \tag{10.34}$$

Substituting (10.27), (10.28) and (10.29) into (10.30) yields another equation as follows:

$$-\frac{\partial \hat{P}^*}{\partial z^*} - Ra_T \hat{T}^* \sin\varphi = \frac{\partial^2 \hat{T}^*}{\partial x^{*2}} + \frac{\partial^2 \hat{T}^*}{\partial y^{*2}} + \frac{\partial^2 \hat{T}^*}{\partial z^{*2}}. \tag{10.35}$$

Given the fault zone configuration shown in Fig.10.1, since the lengths of the fault zone in all three directions are finite, the well-known variable separation method in mathematics is useful to solve this problem. The aim of this analysis of convective instability in an inclined three-dimensional fault zone is, in essence, to find the existence conditions of nontrivial solutions for the partial differential equations expressed in (10.34) and (10.35), with the prescribed boundary conditions in (10.31), (10.32) and (10.33). The conditions under which such nontrivial solutions for the partial differential equations can exist are the onset conditions for pore-fluid convective flow in the inclined fault zone; the nontrivial solutions represent the convective flow structures of the fault zone. From the general expression of the onset conditions, we need to find the most probable onset condition, which corresponds to the minimum critical Rayleigh number of the system in the conventional linear stability analysis sense. For the above reasons, a combination of the variable separation method and the integration elimination method is used to derive the onset conditions of pore-fluid convective flow. Using the variable separation method, the solutions that satisfy the boundary conditions in the x^* and y^* directions are expressed as follows:

$$\hat{P}^* = A_1 f(z^*) \cos(k_1^* x^*) \sin(k_2^* y^*), \tag{10.36}$$

$$\hat{T}^* = A_1 \theta(z^*) \cos(k_1^* x^*) \sin(k_2^* y^*), \tag{10.37}$$

where A_1 is an arbitrary non-zero constant and k_1^* and k_2^* are the dimensionless wave numbers in the x^* and y^* directions, respectively.

$$k_1^* = \frac{m\pi}{H_1^*} \qquad (m = 1,2,3,\ldots\ldots), \tag{10.38}$$

$$k_2^* = \frac{n\pi}{H_2^*} \qquad (n = 1,2,3,\ldots\ldots). \tag{10.39}$$

Note that since the main purpose of this chapter is to investigate the critical condition under which three-dimensional fundamental convective flow may take place in the inclined geological fault zone, the case of $m = 1$ and $n = 1$ is only considered in the following analysis.

Using (10.36) and (10.37), the boundary conditions in the z^* direction can be expressed as

$$Ra_T\theta(z^*)\sin\varphi + f'(z^*) = 0 \qquad (z^* = 0 \text{ and } z^* = 1), \tag{10.40}$$

$$\theta(z^*) = 0 \qquad (z^* = 0 \text{ and } z^* = 1). \tag{10.41}$$

Substituting (10.36) and (10.37) into (10.34) yields the following equation:

$$A_1[-(k_1^{*2} + k_2^{*2})\sin(k_2^* y^*) f(z^*) + \sin(k_2^* y^*) f''(z^*) + k_2^* Ra_T \cos\varphi \cos(k_2^* y^*)\theta(z^*) + Ra_T \sin\varphi \sin(k_2^* y^*)\theta'(z^*)] = 0. \tag{10.42}$$

Inserting (10.36) and (10.37) into (10.35) yields another equation as follows:

$$A_1[f'(z^*) + (Ra_T \sin\varphi - k_1^{*2} - k_2^{*2})\theta(z^*) + \theta''(z^*)] = 0. \tag{10.43}$$

Differentiating (10.43) with respect to z^* twice yields the following equation:

$$A_1[f'''(z^*) + (Ra_T \sin\varphi - k_1^{*2} - k_2^{*2})\theta''(z^*) + \theta^{(IV)}(z^*)] = 0. \tag{10.44}$$

Differentiating (10.42) with respect to z^* once yields another equation as follows:

$$A_1[-(k_1^{*2} + k_2^{*2})\sin(k_2^* y^*) f'(z^*) + \sin(k_2^* y^*) f'''(z^*) + k_2^* Ra_T \cos\varphi \cos(k_2^* y^*)\theta'(z^*) + Ra_T \sin\varphi \sin(k_2^* y^*)\theta''(z^*)] = 0. \tag{10.45}$$

Substituting (10.43) and (10.44) into (10.45) yields the following equation:

$$A_1\{[\theta^{(IV)}(z^*) - 2(k_1^{*2} + k_2^{*2})\theta''(z^*) - (k_1^{*2} + k_2^{*2})(Ra_T \sin\varphi - k_1^{*2} - k_2^{*2})\theta(z^*)]\sin(k_2^* y^*) - k_2^* Ra_T \cos\varphi \theta'(z^*)\cos(k_2^* y^*)\} = 0. \tag{10.46}$$

Note that if the dip angle is equal to 90°, then the last term involving the first derivative with respect to z^* in (10.46) vanishes. In this special case, the onset condition for convective pore-fluid flow in a vertically oriented three-dimensional geological fault zone can be directly obtained using the variable separation method alone. However, if the dip angle of the fault zone is not equal to 90°, it is troublesome

to directly obtain the onset condition for convective pore-fluid flow from (10.46) alone. In this case, the integration elimination method needs to be used further. For this purpose, another set of the solutions that satisfy the boundary conditions in the x^* and y^* directions are expressed as follows:

$$\hat{P}^* = A_2 f(z^*)\cos(k_1^* x^*)\sin(2k_2^* y^*), \tag{10.47}$$

$$\hat{T}^* = A_2 \theta(z^*)\cos(k_1^* x^*)\sin(2k_2^* y^*), \tag{10.48}$$

where A_2 is another arbitrary non-zero constant.

Substituting (10.47) and (10.48) into (10.34) and (10.35) and repeating the same procedures as used above yields the following equation:

$$\begin{aligned} A_2\{[\theta^{(IV)}(z^*) - 2(k_1^{*2} + 4k_2^{*2})\theta''(z^*) - (k_1^{*2} + 4k_2^{*2})(Ra_T \sin\varphi - k_1^{*2} \\ - 4k_2^{*2})\theta(z^*)]\sin(2k_2^* y^*) - 2k_2^* Ra_T \cos\varphi\theta'(z^*)\cos(2k_2^* y^*)\} = 0. \end{aligned} \tag{10.49}$$

Joining (10.46) and (10.49) together leads to the following equation:

$$\begin{aligned} \sum_{r=1}^{2} A_r\{[\theta^{(IV)}(z^*) - 2(k_1^{*2} + r^2 k_2^{*2})\theta''(z^*) - (k_1^{*2} + r^2 k_2^{*2})(Ra_T \sin\varphi - k_1^{*2} \\ - r^2 k_2^{*2})\theta(z^*)]\sin(rk_2^* y^*) - rk_2^* Ra_T \cos\varphi\theta'(x_3^*)\cos(rk_2^* y^*)\} = 0. \end{aligned} \tag{10.50}$$

Inserting (10.36), (10.37), (10.47) and (10.48) into (10.40) yields the boundary conditions depending on θ only:

$$\sum_{r=1}^{2} A_r[(k_1^{*2} + r^2 k_2^{*2})\theta(z^*) - \theta''(z^*)] = 0 \qquad (z^* = 0 \text{ and } z^* = 1). \tag{10.51}$$

Multiplying (10.50) by $\sin(k_2^* y^*)$ and then integrating with respect to y^* yields the following equation:

$$\begin{aligned} \sum_{r=1}^{2} A_r \int_0^{H_2^*} \{[\theta^{(IV)}(z^*) - 2(k_1^{*2} + r^2 k_2^{*2})\theta''(z^*) - (k_1^{*2} + r^2 k_2^{*2})(Ra_T \sin\varphi - k_1^{*2} \\ - r^2 k_2^{*2})\theta(z^*)]\sin(rk_2^* y^*) - rk_2^* Ra_T \cos\varphi\theta'(z^*)\cos(rk_2^* y^*)\}\sin(k_2^* y^*)dy^* = 0. \end{aligned} \tag{10.52}$$

Similarly, multiplying (10.50) by $\sin(2k_2^* y^*)$ and then integrating with respect to y^* yields another equation as follows:

$$\begin{aligned} \sum_{r=1}^{2} A_r \int_0^{H_2^*} \{[\theta^{(IV)}(z^*) - 2(k_1^{*2} + r^2 k_2^{*2})\theta''(z^*) - (k_1^{*2} + r^2 k_2^{*2})(Ra_T \sin\varphi - k_1^{*2} \\ - r^2 k_2^{*2})\theta(z^*)]\sin(rk_2^* y^*) - rk_2^* Ra_T \cos\varphi\theta'(z^*)\cos(rk_2^* y^*)\}\sin(2k_2^* y^*)dy^* = 0 \end{aligned} \tag{10.53}$$

Equations (10.52) and (10.53) can be rewritten in a matrix form as

$$\begin{bmatrix} a_{11} & a_{12} \\ a_{21} & a_{22} \end{bmatrix} \begin{Bmatrix} A_1 \\ A_2 \end{Bmatrix} = \begin{Bmatrix} 0 \\ 0 \end{Bmatrix}, \tag{10.54}$$

where

$$a_{11} = \frac{H_2^*}{2}\Big[\theta^{(IV)}(z^*) - 2(k_1^{*2} + k_2^{*2})\theta''(z^*) - (k_1^{*2} + k_2^{*2}) (Ra_T \sin\varphi - k_1^{*2} - k_2^{*2})\theta(z^*)\Big], \tag{10.55}$$

$$a_{12} = \frac{4}{3} Ra_T \cos\varphi \theta'(z^*), \tag{10.56}$$

$$a_{21} = -\frac{4}{3} Ra_T \cos\varphi \theta'(z^*), \tag{10.57}$$

$$a_{22} = \frac{H_2^*}{2}\Big[\theta^{(IV)}(z^*) - 2(k_1^{*2} + 4k_2^{*2})\theta''(z^*) - (k_1^{*2} + 4k_2^{*2})(Ra_T \sin\varphi - k_1^{*2} - 4k_2^{*2})\theta(z^*)\Big]. \tag{10.58}$$

The condition, under which (10.54) has non-zero solutions (i.e., A_1 and A_2), requires that the determinant of the matrix in the left-hand side of the equation be equal to zero. This results in the following equation:

$$a_{11}a_{22} - a_{12}a_{21} = 0. \tag{10.59}$$

Substituting (10.55), (10.56), (10.57) and (10.58) into (10.59) yields the following equation:

$$\frac{H_2^{*2}}{4}[\theta^{(IV)}(z^*) - 2(k_1^{*2} + k_2^{*2})\theta''(z^*) - (k_1^{*2} + k_2^{*2})(Ra_T \sin\varphi - k_1^{*2} - k_2^{*2})\theta(z^*)] [\theta^{(IV)}(z^*) - 2(k_1^{*2} + 4k_2^{*2})\theta''(z^*) - (k_1^{*2} + 4k_2^{*2})(Ra_T \sin\varphi - k_1^{*2} - 4k_2^{*2})\theta(z^*)] + \frac{16}{9} Ra_T^2 \cos^2\varphi \theta'(z^*) = 0. \tag{10.60}$$

Note that the condition, under which convective pore-fluid flow just begins in the inclined three-dimensional geological fault zone, is called the onset condition for convective pore-fluid flow. From a mathematical point of view, the condition mentioned above is exactly the same as the condition under which (10.60) with the related boundary conditions has non-zero solutions. Based on this recognition, we can use the inverse method to derive the condition under which (10.60) with the related boundary conditions has non-zero solution. In other words, we need to find a non-zero solution to (10.60) first and then substitute this non-zero solution into

(10.60) to find the expected condition. In the context of investigating convective instability of pore-fluid in the fluid-saturated porous medium, the onset condition of convective pore-fluid flow is often expressed using the critical Rayleigh number of the system.

A pair of the functions, $\theta(z^*)$, that satisfy the boundary conditions expressed in (10.41) and (10.51) are expressed as follows:

$$\theta(z^*) = B_1 \sin(k_3^* z^*), \qquad \theta(z^*) = B_2 \sin(2k_3^* z^*), \tag{10.61}$$

where B_1 and B_2 are two arbitrary non-zero constants.

Clearly, (10.61) can be written into the following form:

$$\theta(z^*) = \sum_{s=1}^{2} B_s \sin(s k_3^* z^*), \tag{10.62}$$

where k_3^* is the dimensionless wave number in the x_3^* direction:

$$k_3^* = q\pi \qquad (q = 1,\ 2,\ 3,\ \ldots..). \tag{10.63}$$

Again, since the main purpose of this chapter is to investigate the critical condition under which three-dimensional fundamental convective flow may take place in the inclined geological fault zone, the case of $q = 1$ is only considered in the following analysis.

Inserting (10.62) into (10.60) yields the following equation:

$$\sum_{s=1}^{2} B_s [G_1(sz^*) \sin^2(s k_3^* z^*) + G_2(sz^*) \cos^2(s k_3^* z^*)] = 0, \tag{10.64}$$

where

$$\begin{aligned} G_1(z^*) = {} & \frac{H_2^{*2}}{4} [k_3^{*4} + 2(k_1^{*2} + k_2^{*2}) k_3^{*2} - (k_1^{*2} + k_2^{*2})(Ra_T \sin\varphi - k_1^{*2} - k_2^{*2})] \\ & [k_3^{*4} + 2(k_1^{*2} + 4k_2^{*2}) k_3^{*2} - (k_1^{*2} + 4k_2^{*2})(Ra_T \sin\varphi - k_1^{*2} - 4k_2^{*2})], \end{aligned} \tag{10.65}$$

$$G_2(z^*) = \frac{16}{9} k_3^{*2} Ra_T^2 \cos^2\varphi, \tag{10.66}$$

$$\begin{aligned} G_1(2z^*) = {} & \frac{H_2^{*2}}{4} [16k_3^{*4} + 8(k_1^{*2} + k_2^{*2}) k_3^{*2} - (k_1^{*2} + k_2^{*2})(Ra_T \sin\varphi - k_1^{*2} - k_2^{*2})] \\ & [16k_3^{*4} + 8(k_1^{*2} + 4k_2^{*2}) k_3^{*2} - (k_1^{*2} + 4k_2^{*2})(Ra_T \sin\varphi - k_1^{*2} - 4k_2^{*2})], \end{aligned} \tag{10.67}$$

$$G_2(2z^*) = \frac{64}{9} k_3^{*2} Ra_T^2 \cos^2\varphi. \tag{10.68}$$

Multiplying (10.64) by $\sin^2(k_3^* z^*)$ and then integrating with respect to z^* yields the following equation:

$$\sum_{s=1}^{2} B_s \int_0^1 \{[G_1(sz^*)\sin^2(sk_3^* z^*) + G_2(sz^*)\cos^2(sk_3^* z^*)]\}\sin^2(k_3^* z^*)dz^* = 0. \quad (10.69)$$

Similarly, multiplying (10.69) by $\sin^2(2k_3^* z^*)$ and then integrating with respect to z^* yields:

$$\sum_{s=1}^{2} B_s \int_0^1 \{[G_1(sz^*)\sin^2(sk_3^* z^*) + G_2(sz^*)\cos^2(sk_3^* z^*)]\}\sin^2(2k_3^* z^*)dz^* = 0. \quad (10.70)$$

Equations (10.69) and (10.70) can be rewritten in a matrix form as

$$\begin{bmatrix} b_{11} & b_{12} \\ b_{21} & b_{22} \end{bmatrix} \begin{Bmatrix} B_1 \\ B_2 \end{Bmatrix} = \begin{Bmatrix} 0 \\ 0 \end{Bmatrix}, \quad (10.71)$$

where

$$b_{11} = \frac{1}{8}[G_1(z^*) + 3G_2(z^*)], \quad (10.72)$$

$$b_{12} = \frac{1}{4}[G_1(2z^*) + G_2(2z^*)], \quad (10.73)$$

$$b_{21} = \frac{1}{4}[G_1(z^*) + G_2(z^*)], \quad (10.74)$$

$$b_{22} = \frac{1}{8}[G_1(2z^*) + 3G_2(2z^*)]. \quad (10.75)$$

Considering the existence condition of non-zero solutions to (10.71) yields the following equation:

$$F(Ra_T, \varphi) = 3G_1(z^*)G_1(2z^*) + G_2(z^*)G_1(2z^*) + G_1(z^*)G_2(2z^*) - 5G_2(z^*)G_2(2z^*) = 0. \quad (10.76)$$

Note that (10.76) is the characteristic equation of the Rayleigh number and the dip angle of the three-dimensional fault zone. If $\varphi = 90^\circ$ (i.e., in the case of a vertically oriented three-dimensional geological fault zone), the critical Rayleigh number associated with a different convective mode can be derived from (10.76) exactly as follows:

$$Ra_{T\,critical} = \frac{(k_1^{*2} + k_2^{*2} + k_3^{*2})^2}{k_1^{*2} + k_2^{*2}}. \quad (10.77)$$

As expected, the resulting critical Rayleigh number (i.e., the one expressed in (10.77)), which is directly derived using the variable separation method combined with the integration elimination method in this analysis, is exactly the same as that previously derived for a vertically oriented three-dimensional geological zone (Zhao

et al. 2003a). This indicates that the characteristic equation of the Rayleigh number and the dip angle of the inclined three-dimensional fault zone, as expressed in (10.76), is correct and useful for investigating convective instability of pore-fluid flow in *inclined* three-dimensional geological fault systems. Since the main purpose of this study is to derive the minimum critical Rayleigh number that is associated with the first modal function of the system, only the first two modal functions, instead of the entire Fourier series expansion, are used. Even though only the first two exact modal functions are used, the resulting minimum critical Rayleigh number is very accurate, as demonstrated in the case of $\varphi = 90^\circ$. However, if the critical Rayleigh numbers associated with higher modes are of interest, more modal functions or even the entire Fourier series expansion needs to be used in the theoretical analysis.

Note that if H_2 tends to infinity, the problem degenerates into a two-dimensional one. Thus, the theoretical solution for the critical Rayleigh number in a horizontal isotropic porous layer (Phillips 1991; Nield and Bejan 1992) can be used to validate the current solution for this degenerated case. Substituting $H_2 \to \infty$ into (10.77) yields the critical Rayleigh number of a value of $4\pi^2$, which is exactly the same as the theoretical solution previously presented (Phillips 1991; Nield and Bejan 1992).

In terms of the Rayleigh number expression, the height of the fault zone (i.e., H_3 in Fig. 10.1) is used as the characteristic length of the system in the above analysis. If the thickness of the stratum (i.e., H in Fig. 10.1) is used as the characteristic length of the system, the corresponding Rayleigh number of the system is expressed as

$$Ra_T^{H-reference} = \frac{(\rho_{f0} c_p)\rho_0 g \beta \Delta T K_0 H}{\mu \lambda_{e0}}. \tag{10.78}$$

Obviously, the following equation exists between the two Rayleigh numbers defined by using different characteristic lengths for the system:

$$Ra_T^{H-reference} = Ra_T \sin\varphi. \tag{10.79}$$

10.3 Effect of the Dip Angle on Convective Instability of an Inclined Three-Dimensional Geological Fault Zone

In this section, (10.76) is used to investigate the effect of the dip angle on convective instability of the inclined three-dimensional geological fault zone. Except for a vertically oriented three-dimensional fault zone (i.e., $\varphi = 90^\circ$), it is difficult to obtain an explicit expression for the critical Rayleigh number for an inclined three-dimensional geological fault zone. Alternatively, (10.76) is solved numerically to obtain the critical Rayleigh number for three-dimensional fundamental convective flow in an inclined geological fault zone system. For this purpose, $m = n = q = 1$, $H_2^* = 0.1$ and different values of H_3/H_1 are used in the related calculations. Equation (10.76) is valid for any of the fault thickness to height ratio values (i.e., any values of H_2^*); the selection of $H_2^* = 0.1$ here is only for the purpose

of demonstrating that (10.76) can be used to obtain the critical Rayleigh number for three-dimensional fundamental convective flow in inclined geological fault zones. It is also noted that from a mathematical point of view, (10.76) is valid for any values of the dip angle of the fault zone, if the boundary conditions of the problem are unchanged. However, for small values of the dip angle of the fault zone in geological reality, the boundary conditions considered in this study may be violated and, in this case, further detailed study is needed to investigate the possible onset conditions for natural convective flow.

Figure 10.2 shows the distribution of the normalized function, $F^*\ (Ra, \varphi)$, for several different groups of dip angles for the geological fault zone. The normalized function in this figure is defined as the ratio of the function, $F(Ra, \varphi)$, to the corresponding value, $F(0,\ 90^\circ)$, in the case of $Ra = 0$ and $\varphi = 90^\circ$. It can be seen from Fig. 10.2 that, for a given dip angle, there are at least two real roots for the related normalized function. This indicates that three-dimensional fundamental convective flow does exist in the inclined three-dimensional geological fault zone system. Since the main purpose of this chapter is to investigate the effect of dip angle on the onset of three-dimensional fundamental convective flow in an inclined geological fault zone system, only the smallest real root of the normalized function is of interest. For a given dip angle, the smallest real root of the normalized function is defined as the critical Rayleigh number for three-dimensional fundamental convective flow to occur in the inclined three-dimensional geological fault zone.

Figure 10.3 shows the effect of the dip angle on the critical Rayleigh number for three-dimensional fundamental convective flow structure (i.e., $H_3/H_1 = 1$) in the inclined three-dimensional geological fault zone. Obviously, if the height of the fault zone (i.e., H_3 in Fig. 10.1) is used as the characteristic length of the system, with the decrease of the dip angle, the critical Rayleigh number for three-dimensional fundamental convective flow to take place increases considerably (see the corresponding results marked as H3-constant in Fig. 10.3). For example, the critical Rayleigh number for three-dimensional fundamental convective flow to take place is equal to 1016.7 in the case of $\varphi = 90^\circ$, while it increases to 1543.8 in the case of $\varphi = 30^\circ$. In this case it indicates that a decrease in the dip angle stabilizes the fundamental convective system. The geological significance of this observation is that if the height of the inclined fault zone (i.e., H_3 in Fig. 10.1) is kept constant, a decrease in the dip angle of the fault zone results in a decrease in the thickness of the stratum (i.e., H in Fig. 10.1). Since the temperature at the bottom of the inclined fault zone system is directly proportional to the thickness of the stratum, a decrease in the thickness of the stratum results in a decrease in the geothermal temperature at the bottom of the inclined fault zone so that the total temperature difference between the top and bottom of the inclined fault system decreases. Since the total temperature difference between the top and bottom of the inclined fault system is the main driving force to trigger convective pore-fluid flow in the system, a decrease in the total temperature difference between the top and bottom of the system reduces the possibility for the convective pore-fluid flow to take place in the system. In other words, a decrease in the dip angle of the inclined fault zone stabilizes three-dimensional fundamental convective flow.

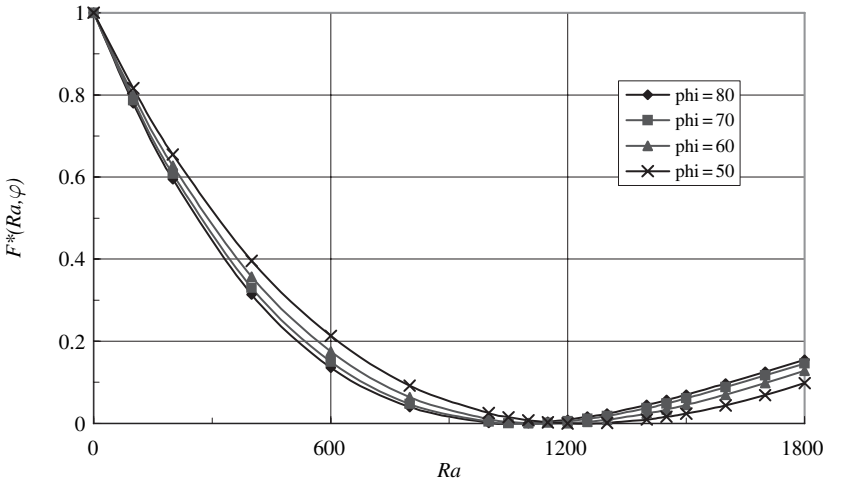

(A) Overall distribution pattern

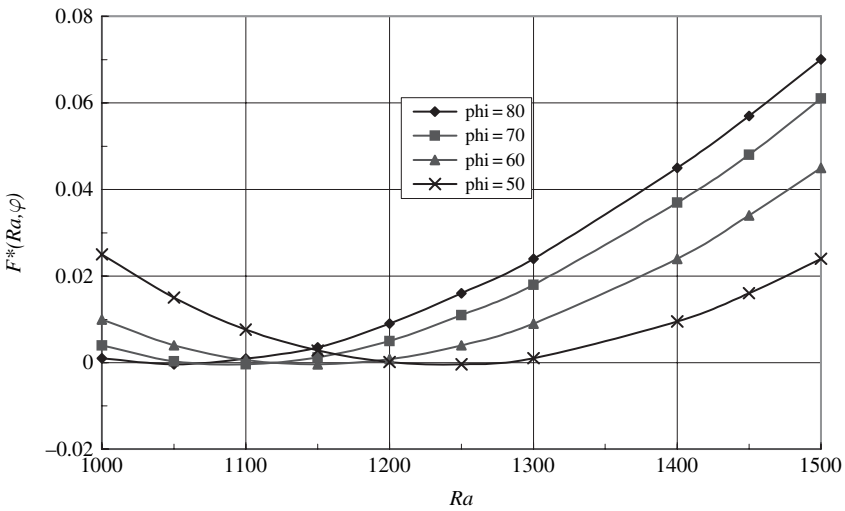

(B) Enlargement of part of the curves in (A)

Fig. 10.2 Distribution of the dimensionless function

However, if the thickness of the stratum (i.e., H in Fig. 10.1) is kept constant, a decrease in the dip angle destabilizes three-dimensional fundamental convective flow in inclined three-dimensional geological fault zones (see the corresponding results marked as H-constant in Fig. 10.3). For instance, the critical Rayleigh number for three-dimensional fundamental convective flow to take place is equal to 1016.7 in the case of $\varphi = 90^\circ$, while it decreases to 771.9 in the case of $\varphi = 30^\circ$. In this case, a decrease in the dip angle of the fault zone has the following two significant effects. First, it results in an increase in the height of the fault zone, indicating that

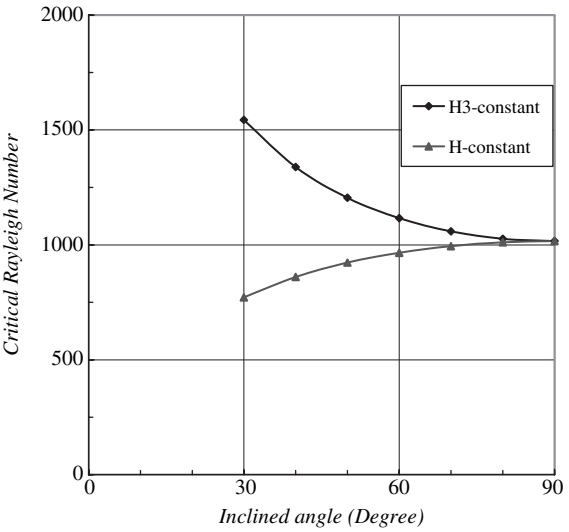

Fig. 10.3 Effect of the dip angle on the critical Rayleigh number for three-dimensional fundamental convective flow ($H_3/H_1 = 1$)

the space for the convective pore-fluid flow to take place becomes larger. Secondly, it results in a decrease of the gravity component in the fault height direction (i.e., in the z direction), indicating that the gravity effect becomes less important in this particular direction. Due to these two significant effects, a decrease in the dip angle of the inclined fault zone destabilizes three-dimensional fundamental convective flow in the inclined three-dimensional geological fault zone.

If we define $HR = H_3/H_1$ and set HR equal to 3, 5 and 7, respectively, the effect of the dip angle on the critical Rayleigh number for three-dimensional convective flow to take place in each of the different shapes for the inclined three-dimensional geological fault zone may also be examined using (10.76). Figure 10.4 shows the results when the height of the fault zone (i.e., H_3 in Fig. 10.1) is used as the characteristic length of the system. It is clear that with an increase in the dip angle, the corresponding critical Rayleigh number for convective flow to take place decreases for the three different shaped geological fault zones. This further confirms that if the height of the fault zone (i.e., H_3 in Fig. 10.1) is used as the characteristic length of the system, a decrease in the dip angle stabilizes convective flow in inclined three-dimensional geological fault zones, even though the inclined three-dimensional geological fault zone may have different shapes (i.e., different values of H_3/H_1). Another important phenomenon, which can be derived from the results in Fig. 10.4, is that for a given dip angle, the value of the critical Rayleigh number increases as the value of H_3/H_1 increases. This means that a slender shape for the inclined fault zone relatively reduces the possibility for convective pore-fluid flow to take place in the system, compared with inclined three-dimensional geological fault zones with more equant shapes (i.e., $H_3/H_1 = 1$).

With an inclined geological fault zone taken as an illustrative example, we can examine the possibility of convective flow. These parameters were used in the following examples. For the pore-fluid, dynamic viscosity is $10^{-3}\,\mathrm{N}\cdot\mathrm{s/m^2}$;

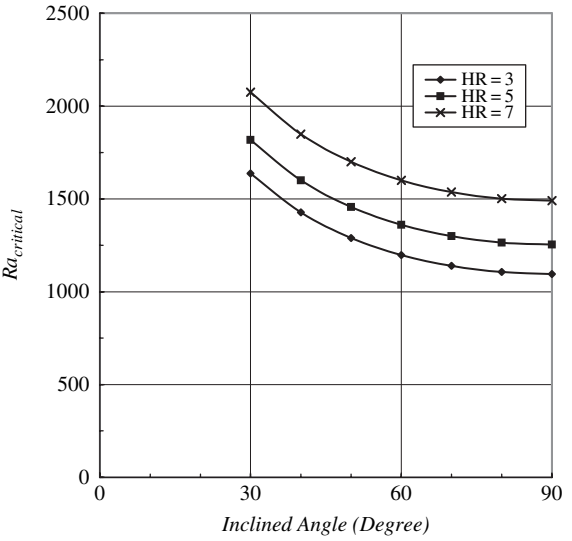

Fig. 10.4 Effect of the dip angle on the critical Rayleigh number arising from different values of $HR = H_3/H_1$

reference density is $1000\,\mathrm{kg/m^3}$; volumetric thermal expansion coefficient is $2.07 \times 10^{-4}(1/\mathrm{K})$; specific heat is $4185\,\mathrm{J/(kg \cdot K)}$, and thermal conductivity coefficient is $0.6\,\mathrm{W/(m \cdot K)}$. For the porous matrix, porosity is 0.1; thermal conductivity coefficient is $3.35\,\mathrm{W/(m \cdot K)}$; specific heat is $815\,\mathrm{J/(kg \cdot K)}$; permeability is $2 \times 10^{-12}\,\mathrm{m^2}$; height and thickness of the inclined fault zone are 5 km and 0.5 km, respectively; temperature at the top and bottom is 25 °C and 125 °C, respectively, and the dip angle of the fault zone is 50°.

Substituting the related parameters into (10.21) yields the Rayleigh number for the system:

$$Ra_T = \frac{(\rho_{f0}c_p)\rho_{f0}g\beta\Delta T K_0 H_r}{\mu\lambda_{e0}} = \frac{1000^2 \times 4185 \times 9.8 \times 2.07 \times 10^{-4} \times 200 \times 10^{-12} \times 5 \times 10^3}{10^{-3} \times 3.08} \approx 2756.5. \tag{10.80}$$

As can be seen from Figs. 10.3 and 10.4, in the case of $\varphi = 50°$, the corresponding critical Rayleigh numbers are 1204.8, 1289.7, 1456.5 and 1699.9 for $H_3/H_1 = 1$, 3, 5 and 7, respectively. Because $Ra_T > Ra_{T\,critical}$ for all four of these cases, three-dimensional fundamental convection flow can take place in the inclined three-dimensional geological fault zone for the four different shapes considered here.

Chapter 11
Double-Diffusion Driven Convective Heat Transfer within Three-Dimensional Vertical Faults Heated from Below

In a fluid-saturated porous medium with stagnant pore-fluid, heat can be transferred in both the pore-fluid and the matrix through thermal diffusion, while chemical species can only be transported in the pore-fluid through chemical species diffusion. Since at least the upper part of the Earth's crust is usually considered as a fluid-saturated porous medium, the onset of convective flow of stagnant pore-fluid within the Earth's crust has been an important topic in the field of geoscience for many years (Horton and Rogers 1945; Lapwood 1948; Phillips 1991; Nield and Bejan 1992; Zhao et al. 1997, 1999a). If the onset of convective flow of the stagnant pore-fluid is driven by either thermal diffusion or chemical species diffusion separately, the resulting convective flow is referred to as either thermal diffusion driven convective flow or chemical species diffusion driven convective flow. However, if the onset of convective flow of stagnant pore-fluid depends on both thermal diffusion and chemical species diffusion simultaneously, the resulting convective flow is referred to as double-diffusion driven convective flow. In the case of double-diffusion driven convective flow, the diffusion of chemical species can have two important, but different effects: namely stabilization or destabilization of the convective flow, when compared with thermal diffusion driven convective flow alone. If the concentration of dense chemical species at the top of the system is greater than that at the bottom (i.e., cold saline fluid is located above relatively hot fresh water), diffusion of chemical species enhances the possibility of thermal diffusion driven convective flow alone and, therefore, destabilizes the resulting convective flow. However, if the concentration of dense chemical species at the top of the system is smaller than that at the bottom (i.e., hot saline fluid is located under relatively cold fresh water), diffusion of chemical species reduces the possibility of thermal diffusion driven convective flow alone and, therefore, stabilizes the resulting convective flow.

The double-diffusion driven convective flow problem, in which the density of pore-fluid varies with both temperature and chemical species concentrations, eventually belongs to a class of variable density flow problems in pore-fluid saturated porous media. This kind of problem has been encountered in many scientific and engineering fields. For example, in geoenvironmental engineering, the diffusion and dispersion of buried industrial waste and nuclear waste in soil and/or rock masses are typical problems of this kind. In exploration geosciences, ore body formation and mineralization in the upper crust of the Earth can also be closely associated

C. Zhao et al., *Convective and Advective Heat Transfer in Geological Systems*,

© Springer-Verlag Berlin Heidelberg 2008

with this kind of problem. Although a considerable amount of research has been carried out on double-diffusion driven convective flow instability problems in a large block of pore-fluid saturated porous medium with similar dimensions in two or three dimensions (Nield and Bejan 1992; Alavyoon 1993; Gobin and Bennacer 1994; Nguyen et al. 1994; Nithiarasu et al. 1996; Goyeau et al. 1996; Mamou et al. 1998; Zhao et al. 2000c), little, if any, research exists on double-diffusion driven convective flow instability problems in a three-dimensional pore-fluid saturated geological fault zone. Since there is clear evidence that many ore deposits are located around and within geological fault zones, there is a clear need to investigate double-diffusion driven convective instability in a three-dimensional fault zone, so that the basic physical process behind ore body formation and mineralization can be further understood. Thus, the main purpose of the present study is to gain theoretical insight into double-diffusion driven convective flow instability in three-dimensional geological fault zones when they are heated uniformly from below.

In terms of convective instability in three-dimensional fluid-saturated geological fault zones, previous research in this particular field has concentrated mainly on thermal diffusion driven convective flow problems (Beck 1972; Zebib and Kassoy 1977; Lowell and Shyu 1978; Murphy 1979; Kassoy and Cotte 1985). In addition, Zhao et al. (2003b) have recently presented the exact solutions for the same system so that the onset of *thermal diffusion driven convective flow* can be predicted exactly in a three-dimensional fluid-saturated geological fault zone system. The main purpose of this chapter is to develop the exact solutions for critical Rayleigh numbers, so that the onset of *double-diffusion driven convective flow* can be accurately identified in three-dimensional fault systems (Zhao et al. 2005b).

11.1 Governing Equations of the Problem

Consider a three-dimensional fluid-saturated geological fault zone; its thickness is much smaller than both its length and height, as shown in Fig. 11.1. *The fault zone is assumed to be much more permeable than the surrounding rocks*. Through numerical simulations (Zhao et al. 2006c), it has been demonstrated that if the permeability

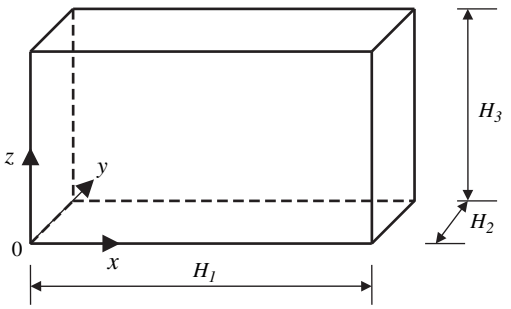

Fig. 11.1 Geometry of the problem

of the fault zone is three orders of magnitude higher than that of the surrounding rocks, then the resulting convective pore-fluid flow in the surrounding rocks is much smaller than that in the fault zone, indicating that the interaction between the fault zone and its surrounding rocks is negligible. Thus, the fault zone can be separated from the surrounding rocks in the following theoretical analysis.

The length of the fault may be infinite in the x direction, but we consider the size of convection cells as H_1 in this direction so that insulated and impermeable boundary conditions can be added at both $x = 0$ and $x = H_1$. In the thickness direction the following conditions exist: a geothermal gradient, a chemical species concentration gradient and the baselevel pore-fluid pressure gradient that is very close to a hydrostatic pore-fluid pressure gradient before convection develops. Therefore, these conditions need to be added at both $y = 0$ and $y = H_2$. This means that any perturbation due to both temperature and chemical species concentration within the geological fault zone has little influence on the initial thermal, chemical species and pore-fluid pressure distributions of the surrounding rocks. It is assumed that the fault zone is uniformly heated from below so that constant temperature and impermeable boundary conditions are added at both $z = 0$ and $z = H_3$. In addition, a constant chemical species concentration boundary condition is applied at both $z = 0$ and $z = H_3$.

In conventional analyses of convective flow instability problems, the system is assumed to be in a steady state. The basic characteristic of the steady state is that all the variables in the system do not evolve with time and, therefore, they are time-independent. In order to investigate the stability of a steady state system, the conventional method used in stability analysis is to perturb the system slightly and discover its stability characteristics in a time evolution frame. Because of this consideration of perturbation evolution with time, the conventional method can be called the transient state perturbation method. The slightly perturbed system must have one of the following three reactions. If the system returns to the initial steady state, the system is said to be stable. If it remains in the slightly perturbed state, the system is said to be neutral or marginal. However, if the disturbance is amplified and the slightly perturbed system evolves into some different state, the system loses its initial steady state and, therefore, is said to be unstable. It is important to note that *the neutral or marginal state of a system belongs to a steady state so that all the variables do not evolve with time in the system*. Thus, if the onset of convective flow is the only issue of interest, we can use the neutral steady state of a system directly to derive the onset condition under which the system starts to lose its initial steady state condition.

From a mathematical point of view, the study of convective instability, in essence, consists of finding a nontrivial bifurcation solution for an initial steady state system. The state of the initial system is usually described by simultaneous partial differential equations and appropriate boundary conditions. The condition under which a nontrivial bifurcation solution for the partial differential equations can exist is the onset condition of the convective pore-fluid flow in the initial steady state system. This onset condition is often expressed by a non-dimensional parameter, namely the critical Rayleigh number of the system. The nontrivial solution corresponding to the minimum critical Rayleigh number is called the fundamental convective flow mode of the system. This means that any useful mathematical methods can be used to

solve the convective instability problem as long as the onset condition for pore-fluid convective flow can be found. Keeping this in mind, the steady state perturbation method in which the neutral steady state system is considered can be used in a very flexible, but logical way to derive the onset condition for convective pore-fluid flow in hydrothermal systems (Zhao et al. 1997, 1999a). This allows the onset condition for convective pore-fluid flow in a hydrothermal system to be directly derived without considering time-dependent terms in the governing partial differential equations of the system. The use of the steady state perturbation method in deriving the onset condition for convective pore-fluid flow can be justified as follows. Since the neutral or marginal state of a system is a steady state, not only does the total steady state solution of the system exist, but such a solution can also be divided into the following two parts: first, the original steady state solution before convection initiates and, secondly, the slightly perturbed steady state solution due to the initiation of convection. From a mathematical point of view, no matter how small the slight perturbation is, it gives a nontrivial steady state bifurcation solution for the system in the neutral steady state. This shows that we can use the neutral steady state of a system to derive the onset condition, under which a slight perturbation can be maintained in the neutral steady state of the system. Mathematically, previous studies (Zhao et al. 1997) have shown that the transient state perturbation method and the steady state perturbation method result in identical solutions for the onset condition of convective pore-fluid flow in a hydrothermal system.

In order to facilitate the following theoretical analysis, the material comprising the fault zone is assumed to be homogeneous and isotropic. If Darcy's Law is used to describe pore-fluid flow and the Oberbeck-Boussinesq approximation is employed to describe a change in pore-fluid density arising from a change in both the pore-fluid temperature and chemical species concentration, the governing equations for the natural convection of incompressible fluid in a neutral steady state can be expressed as

$$\frac{\partial u}{\partial x}+\frac{\partial v}{\partial y}+\frac{\partial w}{\partial z}=0, \tag{11.1}$$

$$u=\frac{K_0}{\mu}\left(-\frac{\partial P}{\partial x}+\rho_f g_x\right), \tag{11.2}$$

$$v=\frac{K_0}{\mu}\left(-\frac{\partial P}{\partial y}+\rho_f g_y\right), \tag{11.3}$$

$$w=\frac{K_0}{\mu}\left(-\frac{\partial P}{\partial z}+\rho_f g_z\right), \tag{11.4}$$

$$\rho_{f0}c_p\left(u\frac{\partial T}{\partial x}+v\frac{\partial T}{\partial y}+w\frac{\partial T}{\partial z}\right)=\lambda_{e0}\left(\frac{\partial^2 T}{\partial x^2}+\frac{\partial^2 T}{\partial y^2}+\frac{\partial^2 T}{\partial z^2}\right), \tag{11.5}$$

$$u\frac{\partial C}{\partial x}+v\frac{\partial C}{\partial y}+w\frac{\partial C}{\partial z}=D_{e0}\left(\frac{\partial^2 C}{\partial x^2}+\frac{\partial^2 C}{\partial y^2}+\frac{\partial^2 C}{\partial z^2}\right), \tag{11.6}$$

$$\rho_f = \rho_{f0}[1 - \beta_T(T - T_0) + \beta_C(C - C_0)], \tag{11.7}$$

$$\lambda_{e0} = \phi\lambda_{f0} + (1 - \phi)\lambda_{s0}, \tag{11.8}$$

$$D_{e0} = \phi D_0, \tag{11.9}$$

where u, v and w are the velocity components of the pore-fluid in the x, y and z directions, respectively; P, T and C are pressure, temperature and chemical species concentration; ρ_{f0}, T_0 and C_0 are the reference density of pore-fluid, reference temperature of the medium and reference concentration of the chemical species; μ and c_p are the dynamic viscosity and specific heat of the pore-fluid; λ_{f0} and λ_{s0} are the thermal conductivity coefficients for the pore-fluid and solid matrix in the fault zone; ϕ and β_T are the porosity of the porous rock and the thermal volume expansion coefficient of the pore-fluid; D_0 is the diffusivity of the chemical species; β_C is the concentration expansion coefficient of the chemical species; K_0 is the permeability of the fault zone, and g_x, g_y and g_z are the gravity acceleration components in the x, y and z directions.

The corresponding boundary conditions are as follows:

$$u = 0, \qquad \frac{\partial T}{\partial x} = 0, \qquad \frac{\partial C}{\partial x} = 0 \qquad (x = 0 \text{ and } x = H_1), \tag{11.10}$$

$$P = P_{base}, \qquad T = \frac{T_b - T_o}{H_3}(H_3 - z) + T_0, \qquad C = \frac{C_b - C_o}{H_3}(H_3 - z) + C_0 \quad (y = 0 \text{ and } y = H_2), \tag{11.11}$$

$$w = 0, \qquad T = T_b, \qquad C = C_b \qquad (z = 0), \tag{11.12}$$

$$w = 0, \qquad T = T_0, \qquad C = C_0 \qquad (z = H_3). \tag{11.13}$$

$C_0 > C_b$ indicates that the concentration of chemical species is relatively high at the top surface of the system. On the contrary, $C_0 < C_b$ indicates that the concentration of chemical species is relatively low at the top surface of the system.

The base solutions for the above steady state system before convection is initiated can be derived and expressed as follows:

$$u_{base} = v_{base} = w_{base} = 0, \tag{11.14}$$

$$T_{base} = \frac{T_b - T_o}{H_3}(H_3 - z) + T_0, \tag{11.15}$$

$$P_{base} = \rho_{f0} g(H_3 - z) - \frac{1}{2}\left(\frac{T_b - T_0}{H_3}\beta_T - \frac{C_b - C_o}{H_3}\beta_C\right)\rho_{f0} g(H_3 - z)^2, \tag{11.16}$$

$$C_{base} = \frac{C_b - C_o}{H_3}(H_3 - z) + C_0, \tag{11.17}$$

where u_{base}, v_{base} and w_{base} are the base solutions for the Darcy velocity component in the x, y and z directions before convection is initiated; P_{base}, T_{base} and C_{base} are the base solutions for the pressure, temperature and chemical species concentration before convection is initiated, respectively, and g is the acceleration due to gravity in the vertical direction. Since the positive direction of the gravity acceleration (g) is in the downward direction, $g_z = -g$ in the derivation of the above base solutions.

In order to simplify (11.1), (11.2), (11.3), (11.4), (11.5) and (11.6), the following dimensionless variables are defined:

$$x^* = \frac{x}{H}, \qquad y^* = \frac{y}{H}, \qquad z^* = \frac{z}{H}, \tag{11.18}$$

$$H_1^* = \frac{H_1}{H}, \qquad H_2^* = \frac{H_2}{H}, \qquad H_3^* = \frac{H_3}{H}, \tag{11.19}$$

$$u^* = \frac{H\rho_{f0}c_p}{\lambda_{e0}}u, \qquad v^* = \frac{H\rho_{f0}c_p}{\lambda_{e0}}v, \qquad w^* = \frac{H\rho_{f0}c_p}{\lambda_{e0}}w, \tag{11.20}$$

$$T^* = \frac{T - T_0}{\Delta T}, \qquad C^* = \frac{C - C_0}{\Delta C}, \tag{11.21}$$

$$P^* = \frac{K_0\rho_{f0}c_p}{\mu\lambda_{e0}}(P - P_0), \tag{11.22}$$

where x^*, y^* and z^* are the dimensionless coordinates; u^*, v^* and w^* are the dimensionless velocity components in the x, y and z directions, respectively; H_1^*, H_2^* and H_3^* are the dimensionless length, thickness and height of the fault zone; P^*, T^* and C^* are the dimensionless pressure, temperature and chemical species concentration; ΔT and ΔC are the temperature and chemical species concentration differences between the bottom and top boundaries of the porous medium, respectively; H_1, H_2 and H_3 are the length, thickness and height of the fault zone; H is a reference length; P_0 is the reference static pore-fluid pressure and this reference pressure in the porous medium has a hydrostatic pressure gradient. This means that $P - P_0$ is the excessive pore-fluid pressure of the system. In the following analysis, H_3 is chosen as the reference length (i.e., $H = H_3$).

Substituting the above dimensionless variables into (11.1), (11.2), (11.3), (11.4), (11.5) and (11.6) yields

$$\frac{\partial u^*}{\partial x^*} + \frac{\partial v^*}{\partial y^*} + \frac{\partial w^*}{\partial z^*} = 0, \tag{11.23}$$

$$u^* = -\frac{\partial P^*}{\partial x^*} + Ra_T T^* e_1 - NRa_T C^* e_1, \tag{11.24}$$

$$v^* = -\frac{\partial P^*}{\partial y^*} + Ra_T T^* e_2 - NRa_T C^* e_2, \tag{11.25}$$

$$w^* = -\frac{\partial P^*}{\partial z^*} + Ra_T T^* e_3 - NRa_T C^* e_3, \tag{11.26}$$

$$u^* \frac{\partial T^*}{\partial x^*} + v^* \frac{\partial T^*}{\partial y^*} + w^* \frac{\partial T^*}{\partial z^*} = \frac{\partial^2 T^*}{\partial x^{*2}} + \frac{\partial^2 T^*}{\partial y^{*2}} + \frac{\partial^2 T^*}{\partial z^{*2}}, \tag{11.27}$$

$$u^* \frac{\partial C^*}{\partial x^*} + v^* \frac{\partial C^*}{\partial y^*} + w^* \frac{\partial C^*}{\partial z^*} = \frac{1}{Le}\left(\frac{\partial^2 C^*}{\partial x^{*2}} + \frac{\partial^2 C^*}{\partial y^{*2}} + \frac{\partial^2 C^*}{\partial z^{*2}}\right), \tag{11.28}$$

where $\boldsymbol{e}$ is a unit vector and $\boldsymbol{e} = e_1\boldsymbol{i} + e_2\boldsymbol{j} + e_3\boldsymbol{k}$ for a general three-dimensional problem. For the particular problem considered in this chapter, $e_1 = e_2 = 0$ and $e_3 = 1$ since the gravity acceleration is only exerted on the vertical direction. Ra_T is the Rayleigh number due to thermal diffusion only and N is the buoyancy ratio of the chemical species concentration to the temperature. Le is the Lewis number of the system. These dimensionless numbers are defined as

$$Ra_T = \frac{(\rho_{f0} c_p)\rho_{f0} g \beta_T \Delta T K_0 H}{\mu \lambda_{e0}}, \quad N = \frac{\beta_C \Delta C}{\beta_T \Delta T}, \quad Le = \frac{\lambda_{e0}}{D_{e0}\rho_{f0} c_p}. \tag{11.29}$$

In some hydrothermal systems within the upper crust of the Earth the thermal diffusion scale is much larger than the chemical species diffusion scale so the Lewis number of the system is a large one in this analysis. This may result in some problems in the numerical analysis of the double-diffusion driven convective instability problem. From the physical point of view, this problem belongs to a multi-scale physical problem. Although numerical analysis may often meet some difficulty in dealing with a multi-scale physical problem, theoretical analysis can avoid the difficulty because it is the parameters rather than the specific numbers that are considered in such a purely theoretical analysis. This is the well-known advantage of using the analytical method and the reason why an analytical solution is always superior to a numerical solution for a given problem.

Using the dimensionless variables, the corresponding boundary conditions can be expressed as

$$u^* = 0, \qquad \frac{\partial T^*}{\partial x^*} = 0, \qquad \frac{\partial C^*}{\partial x^*} = 0 \qquad (x^* = 0 \text{ and } x^* = H_1^*), \tag{11.30}$$

$$P^* = P^*_{base}, \qquad T^* = (1 - z^*), \qquad C^* = (1 - z^*) \qquad (y^* = 0 \text{ and } y^* = H_2^*), \tag{11.31}$$

$$w^* = 0, \qquad T^* = 1, \qquad C^* = 1 \qquad (z^* = 0), \tag{11.32}$$

$$w^* = 0, \qquad T^* = 0, \qquad C^* = 0 \qquad (z^* = 1). \tag{11.33}$$

It is noted that from a mathematical point of view, the study of double-diffusion driven convective instability in three-dimensional fault zones is, in essence, an exercise to find nontrivial solutions for the partial differential equations expressed

in (11.23), (11.24), (11.25), (11.26), (11.27) and (11.28), with the given boundary conditions in (11.30), (11.31), (11.32) and (11.33). The conditions, under which the nontrivial solutions for the partial differential equations can exist, are the onset conditions of convective pore-fluid flow in a fault zone, while the nontrivial solutions are the convective flow modes of the fault zone. These onset conditions are often expressed by non-dimensional parameters, such as the critical Rayleigh numbers of the system. The nontrivial solution corresponding to the minimum critical Rayleigh number is labeled the fundamental convective flow mode of the system. Keeping this in mind, the steady state perturbation method, which is based on the conventional linear stability theory, is used to deal with double-diffusion driven convective instability in three-dimensional fault zones.

11.2 Analysis of Double-Diffusion Driven Convective Instability for Three-Dimensional Fault Zones

This section will investigate the conditions under which three-dimensional double-diffusion driven convective flow can take place in the fault zone system defined in the previous section. Specifically, the main purpose is to determine the critical Rayleigh number. This enables the exploration of the double-diffusion driven convective instability of the fault zone system. From linear stability theory, the first-order perturbation equations of the hydrothermal system in the marginal steady state can be expressed as follows:

$$\frac{\partial \hat{u}^*}{\partial x^*} + \frac{\partial \hat{v}^*}{\partial y^*} + \frac{\partial \hat{w}^*}{\partial z^*} = 0, \tag{11.34}$$

$$\hat{u}^* = -\frac{\partial \hat{P}^*}{\partial x^*} + Ra_T \hat{T}^* e_1 - NRa_T \hat{C}^* e_1, \tag{11.35}$$

$$\hat{v}^* = -\frac{\partial \hat{P}^*}{\partial y^*} + Ra_T \hat{T}^* e_2 - NRa_T \hat{C}^* e_2, \tag{11.36}$$

$$\hat{w}^* = -\frac{\partial \hat{P}^*}{\partial z^*} + Ra_T \hat{T}^* e_3 - NRa_T \hat{C}^* e_3, \tag{11.37}$$

$$-\hat{w}^* = \frac{\partial^2 \hat{T}^*}{\partial x^{*2}} + \frac{\partial^2 \hat{T}^*}{\partial y^{*2}} + \frac{\partial^2 \hat{T}^*}{\partial z^{*2}}, \tag{11.38}$$

$$-\hat{w}^* = \frac{1}{Le}\left(\frac{\partial^2 \hat{C}^*}{\partial x^{*2}} + \frac{\partial^2 \hat{C}^*}{\partial y^{*2}} + \frac{\partial^2 \hat{C}^*}{\partial z^{*2}}\right), \tag{11.39}$$

where $\hat{u}^*$, $\hat{v}^*$ and $\hat{w}^*$ are the dimensionless perturbation velocity components (i.e., dimensionless convective velocity components), and $\hat{P}^*$, $\hat{T}^*$ and $\hat{C}^*$ are the dimensionless perturbation pressure, temperature and chemical species concentration.

The corresponding boundary conditions for the perturbation variables can be expressed as

$$\hat{u}^* = 0, \qquad \frac{\partial \hat{T}^*}{\partial x^*} = 0, \qquad \frac{\partial \hat{C}^*}{\partial x^*} = 0 \qquad (x^* = 0 \text{ and } x^* = H_1^*), \tag{11.40}$$

$$\hat{p}^* = 0, \qquad \hat{T}^* = 0, \qquad \hat{C}^* = 0 \qquad (y^* = 0 \text{ and } y^* = H_2^*), \tag{11.41}$$

$$\hat{w}^* = 0, \qquad \hat{T}^* = 0, \qquad \hat{C}^* = 0 \qquad (z^* = 0 \text{ and } z^* = 1). \tag{11.42}$$

Inserting (11.35), (11.36) and (11.37) into (11.34) yields the following equation:

$$\frac{\partial^2 \hat{P}^*}{\partial x^{*2}} + \frac{\partial^2 \hat{P}^*}{\partial y^{*2}} + \frac{\partial^2 \hat{P}^*}{\partial z^{*2}} - Ra_T \frac{\partial \hat{T}^*}{\partial z^*} + NRa_T \frac{\partial \hat{C}^*}{\partial z^*} = 0. \tag{11.43}$$

Substituting (11.35), (11.36) and (11.37) into (11.38) yields another equation as follows:

$$\frac{\partial P^*}{\partial z^*} - Ra_T \hat{T}^* + NRa_T \hat{C}^* = \frac{\partial^2 \hat{T}^*}{\partial x^{*2}} + \frac{\partial^2 \hat{T}^*}{\partial y^{*2}} + \frac{\partial^2 \hat{T}^*}{\partial z^{*2}}. \tag{11.44}$$

Substituting (11.35), (11.36) and (11.37) into (11.39) yields the following equation:

$$\frac{\partial \hat{P}^*}{\partial z^*} - Ra_T \hat{T}^* + NRa_T \hat{C}^* = \frac{1}{Le}\left(\frac{\partial^2 \hat{C}^*}{\partial x^{*2}} + \frac{\partial^2 \hat{C}^*}{\partial y^{*2}} + \frac{\partial^2 \hat{C}^*}{\partial z^{*2}}\right). \tag{11.45}$$

Comparing (10.44) with (10.45) yields the following equation:

$$\hat{C}^* = Le\hat{T}^*. \tag{11.46}$$

In Fig. 11.1, since the lengths of the fault zone in all three directions is finite, the well-known variable separation method in mathematics is useful to solve this problem. As we mentioned before, the study of double-diffusion driven convective instability in three-dimensional fault zones is, in essence, an attempt to find nontrivial solutions for the partial differential equations expressed in (11.43), (11.44) and (11.45), with the prescribed boundary conditions in (11.40), (11.41) and (11.42). The conditions under which these nontrivial solutions can exist are the onset conditions for double-diffusion driven convective pore-fluid flow in the fault zone, and the nontrivial solutions correspond to double-diffusion driven convective flow structures of the fault zone. This means that any useful mathematical method can be used to solve the double-diffusion driven convective instability problem considered in this study as long as the onset conditions of the double-diffusion driven convective pore-fluid flow can be found. From the general expression of the derived onset conditions, we need to find the minimum critical Rayleigh number of the system in the conventional linear stability analysis sense. For the these reasons, the solutions that satisfy the boundary conditions in the x^* and y^* directions are expressed as follows:

$$\hat{P}^* = f(z^*)\cos(k_1^* x^*)\sin(k_2^* y^*), \tag{11.47}$$

$$\hat{T}^* = \theta(z^*)\cos(k_1^* x^*)\sin(k_2^* y^*), \tag{11.48}$$

$$\hat{C}^* = \gamma(z^*)\cos(k_1^* x^*)\sin(k_2^* y^*), \tag{11.49}$$

where k_1^* and k_2^* are the dimensionless wave numbers in the x^* and y^* directions, respectively.

$$k_1^* = \frac{m\pi}{H_1^*} \qquad (m = 1,2,3,\ldots\ldots), \tag{11.50}$$

$$k_2^* = \frac{n\pi}{H_2^*} \qquad (n = 1,2,3,\ldots\ldots). \tag{11.51}$$

Using (11.46), (11.47), (11.48) and (11.49), the boundary conditions in the z^* direction can be expressed as

$$Ra_T\theta(z^*) - NRa_T Le\theta(z^*) - f'(z^*) = 0 \qquad (z^* = 0 \text{ and } z^* = 1), \tag{11.52}$$

$$\theta(z^*) = 0 \qquad (z^* = 0 \text{ and } z^* = 1). \tag{11.53}$$

Substituting (11.46), (11.47), (11.48) and (11.49) into (11.43) yields the following equation:

$$-(k_1^{*2} + k_2^{*2})f(z^*) + f''(z^*) - Ra_T\theta'(z^*) + NRa_T Le\theta'(z^*) = 0. \tag{11.54}$$

Inserting (11.46), (11.47), (11.48) and (11.49) into (11.44) yields:

$$f'(z^*) = (Ra_T - NRa_T Le - k_1^{*2} - k_2^{*2})\theta(z^*) + \theta''(z^*). \tag{11.55}$$

Differentiating (11.55) with respect to z^* twice yields the following equation:

$$f'''(z^*) = (Ra_T - NRa_T Le - k_1^{*2} - k_2^{*2})\theta''(z^*) + \theta^{(IV)}(z^*). \tag{11.56}$$

Differentiating (11.54) with respect to z^* once yields:

$$-(k_1^{*2} + k_2^{*2})f'(z^*) + f'''(z^*) - (Ra_T - NRa_T Le)\theta''(z^*) = 0. \tag{11.57}$$

Substituting (11.55) and (11.56) into (11.57) yields the following equation:

$$\theta^{(IV)}(z^*) - 2(k_1^{*2} + k_2^{*2})\theta''(z^*) - (k_1^{*2} + k_2^{*2})(Ra_T - NRa_T Le - k_1^{*2} - k_2^{*2})\theta(z^*) = 0. \tag{11.58}$$

Inserting (11.55) into (11.52) yields the boundary conditions depending on θ only:

$$(k_1^{*2} + k_2^{*2})\theta(z^*) - \theta''(z^*) = 0 \qquad (z^* = 0 \text{ and } z^* = 1). \tag{11.59}$$

The following function satisfies the boundary conditions expressed in (11.53) and (11.59):

$$\theta(z^*) = A\sin(k_3^* z^*), \tag{11.60}$$

where k_3^* is the dimensionless wave number in the z^* direction, and A is an arbitrary constant to be determined.

$$k_3^* = q\pi \qquad (q = 1, 2, 3, \ldots\ldots). \tag{11.61}$$

Using the sinusoidal perturbation solutions expressed by (11.47), (11.48), (11.49) and (11.60), the original differential equations (i.e., (11.34), (11.35), (11.36), (11.37), (11.38) and (11.39)) with the corresponding boundary conditions (i.e., (11.40), (11.41) and (11.42)) have been converted into the following linear homogeneous algebraic equation:

$$[k_3^{*4} + 2(k_1^{*2} + k_2^{*2})k_3^{*2} - (k_1^{*2} + k_2^{*2})(Ra_T - NRa_T Le - k_1^{*2} - k_2^{*2})]A = 0. \tag{11.62}$$

It is well-known from an elementary theorem in linear algebra that (11.62) only has a zero solution for the arbitrary constant A, if and only if this linear homogeneous algebraic equation is nonsingular. However, if and only if (11.62) is singular, this elementary theorem in linear algebra also says that this linear homogeneous algebraic equation has non-zero solutions for the arbitrary constant A. In the latter case, the perturbation solutions can be maintained so that the system under consideration is in a neutral steady state. As a result, the total critical Rayleigh numbers for different convection modes due to the double-diffusion can be derived and expressed as follows:

$$Ra_{critical} = (Ra_T + Ra_C)_{critical} = \frac{(k_1^{*2} + k_2^{*2} + k_3^{*2})^2}{k_1^{*2} + k_2^{*2}}, \tag{11.63}$$

where $Ra_{critical}$ is the total critical Rayleigh number of the system. This is the sum of the critical Rayleigh numbers arising from thermal diffusion and chemical species diffusion of the system. Ra_C is the Rayleigh number due to chemical species diffusion of the system and is expressed as

$$Ra_C = -NRa_T Le = -\frac{\rho_{f0} g \beta_C \Delta C K_0 H}{\mu D_{e0}}. \tag{11.64}$$

Substituting the dimensionless wave number into (11.63) yields the following equation:

$$Ra_{critical} = \frac{\left[\left(\frac{mH_3}{H_1}\right)^2 + \left(\frac{nH_3}{H_2}\right)^2 + q^2\right]^2 \pi^2}{\left(\frac{mH_3}{H_1}\right)^2 + \left(\frac{nH_3}{H_2}\right)^2}. \tag{11.65}$$

Note that (11.65) is a general expression for the total critical Rayleigh number of the three-dimensional fault zone. If $m = n = q = 1$, the critical Rayleigh number for three-dimensional standard convection flow to take place can be expressed as

$$Ra_{critical}^{3D} = \frac{\left[\left(\frac{H_3}{H_1}\right)^2 + \left(\frac{H_3}{H_2}\right)^2 + 1\right]^2 \pi^2}{\left(\frac{H_3}{H_1}\right)^2 + \left(\frac{H_3}{H_2}\right)^2}. \tag{11.66}$$

If $H_3 = H_1$, (10.66) can be rewritten as

$$Ra_{critical}^{3D} = \frac{\left[2 + \left(\frac{H_3}{H_2}\right)^2\right]^2 \pi^2}{1 + \left(\frac{H_3}{H_2}\right)^2}. \tag{11.67}$$

It is clear that the critical Rayleigh number for three-dimensional standard convective flow to occur is proportional to the ratio of the fault height to thickness.

Similarly, if m is considered as a variable, the corresponding critical Rayleigh number for three-dimensional finger-like convective structure due to double-diffusion can be expressed as

$$Ra_{critical}^{3D-finger} = \frac{\left[m^2 + \left(\frac{H_3}{H_2}\right)^2 + 1\right]^2 \pi^2}{m^2 + (\frac{H_3}{H_2})^2} \qquad (m \geq 2). \tag{11.68}$$

Figure 11.2 shows the variation of the critical Rayleigh number expressed by (11.68) with the fault height to thickness ratio H_3/H_2. With an increase of the fault height to thickness ratio, the critical Rayleigh number increases significantly. This means that, for a given fault height, a decrease in the fault thickness stabilizes convective flow in three-dimensional fault zones so that convective flow becomes more and more difficult as the fault thickness becomes smaller and smaller. Although the value of m may have some influence on the critical Rayleigh number, its overall influence is not significant within the scope of this investigation.

The total critical Rayleigh number of the system due to double-diffusion expressed by (11.63) is dependent only on the geometry and boundary conditions of the system, while the total Rayleigh number (i.e., $Ra = Ra_T + Ra_C$) of the system due to double-diffusion expressed by (11.29) and (11.64) is mainly dependent on the thermal dynamic properties and characteristic length of the system. Once the total Rayleigh number of the system is equal to or greater than the corresponding total critical Rayleigh number of the system, double-diffusion driven convective flow can take place in three-dimensional fluid-saturated geological faults. Since the total Rayleigh number of the system is the sum of the Rayleigh numbers due to thermal diffusion and chemical species diffusion of the system, the effect of chemical species diffusion on the onset of double-diffusion driven convective flow in three-dimensional fluid-saturated geological fault zones can be straightforwardly investigated through the relationship, $Ra = Ra_T + Ra_C$. If the chemical species concentration at the top surface of the system is greater than that at the bottom surface (i.e., $\Delta C = C_b - C_0 < 0$), then $Ra_C > 0$, so the total Rayleigh number of the system

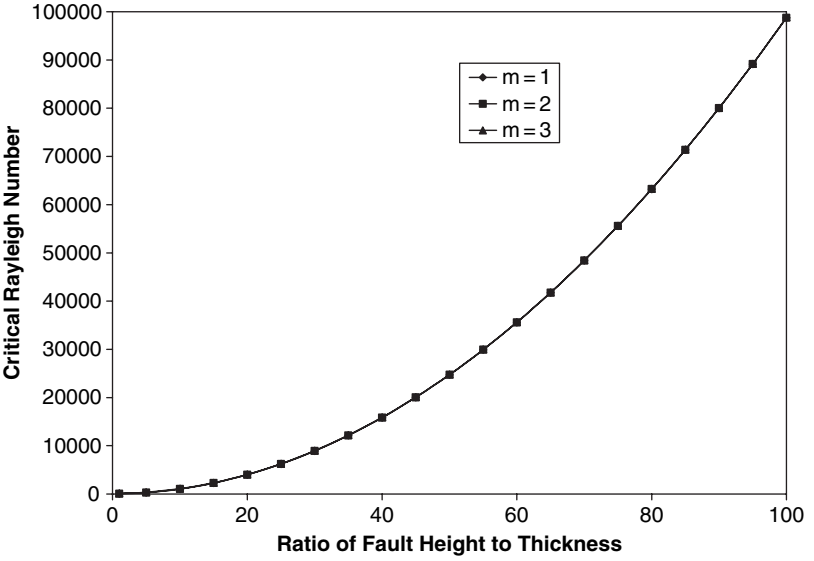

(Large scale view)

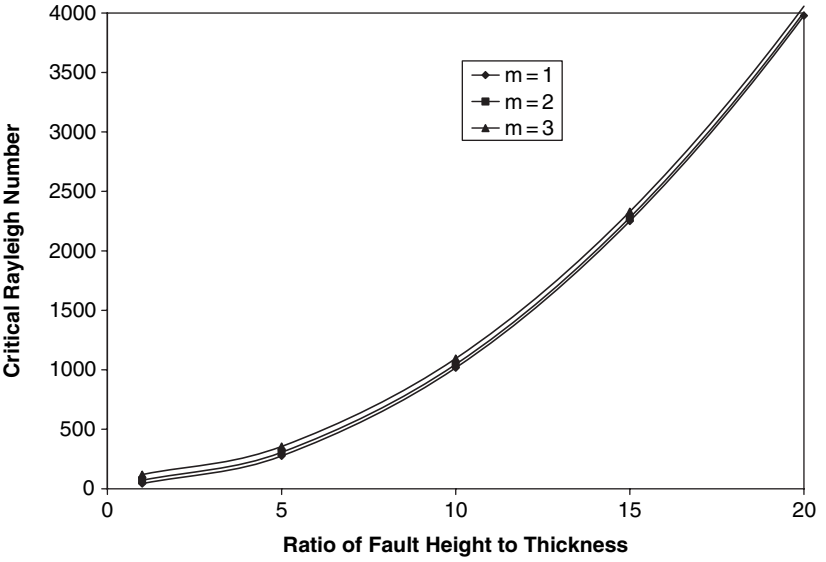

(Small scale view)

Fig. 11.2 Distributions of critical Rayleigh number versus fault height to thickness ratio

increases. In this case, chemical species diffusion destabilizes the convective instability of the system, compared to thermal diffusion driven convective flow alone. However, if the chemical species concentration at the top surface of the system is smaller than that at the bottom surface of the system (i.e., $\Delta C = C_b - C_0 > 0$), then $Ra_C < 0$, so that the total Rayleigh number of the system decreases. This means that chemical species diffusion stabilizes the convective instability of the system, compared with thermal diffusion driven convective flow alone.

An important characteristic of three-dimensional geological fault zones is that the total critical Rayleigh number expressed by (11.68) varies very slightly with the convection cell number, m, in the x direction. For example, with $H_2/H_3 = 0.01$ the corresponding total critical Rayleigh numbers of the system are 98726.2, 98755.7, 98805.0 for $m = 1$, 2 and 3, respectively. Compared with the total critical Rayleigh number of the system in the case of $m = 1$, the relative differences between the total critical Rayleigh numbers of the system are 0.04 percent and 0.09 percent for $m = 2$ and 3, respectively. Such a relative difference between the total critical Rayleigh numbers of the system diminishes with decrease in the ratio, H_2/H_3, of the three-dimensional geological fault zone. This indicates that double-diffusion driven convective flow modes of three-dimensional geological fault zones are very close to each other and, as a result, the system has similar chances to pick up different double-diffusion driven convective flow modes, especially in the case of H_2/H_3 approaching zero.

11.3 The Possibility of Double-Diffusion Driven Convective Flow in Three-Dimensional Geological Fault Zones

In this section, the analytical solution derived in the previous section is used to investigate the possibility of double-diffusion driven convective flow in geological fault zones. Using an idealized geological fault zone as an illustrative example, these parameters are used in the following analysis. For pore-fluid, dynamic viscosity is $10^{-3}\,\mathrm{N\cdot s/m^2}$; reference density is $1000\,\mathrm{kg/m^3}$; volumetric thermal expansion coefficient is $2.1\times10^{-4}(1/\mathrm{K})$; concentration expansion coefficient is $0.001\,\mathrm{m^3/kg}$; specific heat is $4185\,\mathrm{J/(kg\cdot K)}$; thermal conductivity coefficient is $0.6\,\mathrm{W/(m\cdot K)}$, and diffusivity of the chemical species is $0.736\times10^{-6}\,\mathrm{m^2/s}$. For the porous matrix, porosity is 0.1; thermal conductivity coefficient is $3.35\,\mathrm{W/(m\cdot K)}$; specific heat is $815\,\mathrm{J/(kg\cdot K)}$; permeability is $10^{-12}\,\mathrm{m^2}$; height and thickness of the fault zone are 1 km and 0.05 km, respectively, and temperature at the top and bottom is 20°C and 50°C, respectively. The approximate concentrations of the brine (*NaCl*) in seawater at the top and bottom are 0.5 mol/l (i.e. $29.25\,\mathrm{kg/m^3}$) and zero.

Substituting the related parameters into (11.29) yields the Rayleigh number of the system due to thermal diffusion only:

$$Ra_T = \frac{(\rho_{f0}c_p)\rho_{f0}g\beta_T\Delta T K_0 H}{\mu\lambda_{e0}} = \frac{1000\times 4185\times 1000\times 9.8\times 2.1\times 10^{-4}\times 30\times 10^{-12}\times 10^3}{10^{-3}\times 3.08} \approx 83.89. \tag{11.69}$$

Similarly, substituting the related parameters into (11.64) yields the Rayleigh number of the system due to chemical species diffusion only:

$$Ra_C = -\frac{\rho_{f0}g\beta_C\Delta C K_0 H}{\mu D_{e0}} = \frac{1000\times 9.8\times 10^{-3}\times 29.25\times 10^{-12}\times 10^3}{10^{-3}\times 0.1\times 0.736\times 10^{-6}} \approx 3894.7. \tag{11.70}$$

Adding (11.69) and (11.70) together yields the total Rayleigh number of the system due to double-diffusion:

$$Ra = Ra_T + Ra_C = 83.89 + 3894.7 = 3978.59. \tag{11.71}$$

The corresponding total critical Rayleigh number for the three-dimensional standard convective flow is

$$Ra^{3D}_{critical} = \frac{\left[\left(2+\left(\frac{H_3}{H_2}\right)^2\right]^2\pi^2}{1+\left(\frac{H_3}{H_2}\right)^2} = \frac{\left(2+20^2\right)^2\pi^2}{1+20^2} \approx 3977.5. \tag{11.72}$$

Because $Ra > Ra^{3D}_{critical}$, double-diffusion driven convective flow may take place in the three-dimensional geological fault zone considered here. However, if we considered either thermal diffusion or chemical species diffusion alone, convective flow cannot take place. Since $Ra_C > Ra_T$, chemical species diffusion plays a more important role in double-diffusion driven convective instability of a shallow three-dimensional geological fault zone. If we increase the concentration of the brine ($NaCl$) at the top of the system from 0.5 mol/l to 0.6 mol/l, the Rayleigh number of the system due to chemical species diffusion only becomes 4673.64, which is greater than the corresponding total critical Rayleigh number of the three-dimensional standard convective. This implies that seawater intrusion into the surface waters of the Earth is a potential mechanism to trigger convective flow in shallow three-dimensional geological fault zones.

In summary, this theoretical analysis demonstrates that:

(1) Higher concentrations of chemical species at the top of three-dimensional geological fault zones can destabilize convective flow of the system, while lower concentrations of chemical species at the top of three-dimensional geological fault zones can stabilize convective flow of the system.
(2) The double-diffusion driven convective flow modes of three-dimensional geological fault zones are very close to each other and, therefore, the system may

have similar chances to pick up different double-diffusion driven convective flow modes, especially in the case where the fault thickness to height ratio approaches zero.

(3) The significant influence of chemical species diffusion on convective instability of three-dimensional geological fault zones implies that seawater intrusion into the surface waters of the Earth is a potential mechanism to trigger convective flow in shallow three-dimensional geological fault zones.

Chapter 12
Convection Induced Ore Body Formation and Mineralization within the Upper Crust of the Earth

Convective pore-fluid flow can efficiently mix reactive fluids containing metal species in solution within hydrothermal systems and, therefore, plays an important role in ore body formation and mineralization in the Earth's upper crust. Generally, pore-fluid is the sole agent carrying metals in solution from one part of the Earth's crust to another. Once two or more different compositions of reactive metal carrying fluids meet under appropriate temperature and pressure conditions, chemical reactions may take place and an appropriate environment for ore body formation and mineralization is created. For instance, when fluids containing reduced sulfur (H_2S, HS^-, $S^=$, etc.) and sulfates ($SO_4^=$, HSO_4^-, $NaSO_4^-$, etc.) meet, an appropriate pH/redox environment may be created to favor the precipitation of several minerals such as those containing zinc, lead and iron. Therefore, numerical modeling of convection induced mixing processes between reactive metal carrying fluids is very important in understanding mechanisms of ore body formation and mineralization in hydrothermal systems in the upper crust of the Earth. From a thermodynamic point of view, the equilibrium concentration of an aqueous metal species is a function of temperature, pressure, space variables and other relevant aqueous species concentrations. Thus, it is necessary to solve a fully coupled problem between pore-fluid flow, heat transfer, species transport and chemical reactions (including dissolution and precipitation) in fluid-saturated hydrothermal systems in order to understand the mineralization process.

On the geochemical modeling front, it is commonly assumed that the reactive mineral of interest constitutes only a small fraction of the whole rock matrix and that the solutions of aqueous metal species are in an equilibrium state, or near an equilibrium state (Phillips 1991). Under these assumptions, the main task of conventional geochemical modeling is to analyze the constituents of minerals in a rock matrix, without directly considering fluid flow within or through the rock matrix. That is to say, in conventional geochemical modeling, the distribution of minerals in porous rocks is determined from an equilibrium point of view. Thus, conventional geochemical modeling is usually referred to as equilibrium geochemical modeling. Although geochemical modeling can be used to approximately determine the constituents of minerals in a rock matrix, it cannot be used to answer the following fundamental question regarding the mineralization process: Why and how

C. Zhao et al., *Convective and Advective Heat Transfer in Geological Systems*,

© Springer-Verlag Berlin Heidelberg 2008

are metals transported, precipitated and dissolved in porous rocks? To answer this fundamental question, pore-fluid flow within and/or through permeable rocks must be considered. It is pore-fluid flow that carries metals from one place to another in permeable rocks. This means that the precipitation and dissolution of minerals in hydrothermal/sedimentary basins should be considered from a dynamic, not an equilibrium, point of view. Towards this goal, the rock alteration index (RAI), which is defined as the dot product of the pore-fluid velocity and the temperature gradient (Phillips 1991; Zhao et al. 1998a), has been presented to predict possible precipitation and dissolution regions in hydrothermal systems. Predicting mineral precipitation and dissolution regions using the RAI is both approximate and qualitative because only the temperature gradient (i.e., the influence of temperature) is considered to determine the region of ore body formation and mineralization. In order to improve the accuracy of predicting mineral precipitation and dissolution regions, an improved rock alteration index (IRAI) is presented to consider the dependence of mineralization on temperature and the equilibrium concentration variation with temperature for a particular kind of metal. The IRAI is defined as the product of the RAI and the first derivative of the equilibrium concentration of a metal species with respect to temperature (Zhao et al. 2000a). Although the IRAI can be used to predict the most possible regions of precipitation and dissolution for a specific mineral, the prediction result is still approximate and qualitative. The reason for this is that the kinetics of the chemical reactions related to the mineral assemblage were neglected in the development of the IRAI. For the purpose of quantitatively predicting the mineralization regions in hydrothermal systems, there is a need to further develop mineralization theory by including the kinetics of the relevant chemical reactions.

The mixing of reactive fluids is by no means relevant only to ore body formation and mineralization. There are a large number of reactive fluid mixing problems in other scientific and engineering fields. For example, in geoenviromental engineering, the reclamation and rehabilitation of polluted soils by injecting a reactive acid and/or base into the polluted soil site is an example of reactive fluid mixing problems (Zhao et al. 1999d). In chemical engineering, the mixing of reactive fluids is often used as an effective tool to produce new substances. Thus, the general ideas and discussions presented in this chapter may be helpful in solving reactive fluid mixing problems within other scientific and engineering fields.

The finite element method (Zienkiewicz 1977; Zhao et al. 1994c) is used in this section to solve reactive fluid mixing and related ore body formation and mineralization problems. After stating the problem the related governing equations are given, and the concept of the mineralization rate is presented and discussed. Particular attention is paid to considering the kinetics of the reactions between reduced and oxidized sulfur bearing fluids mixing in hydrothermal systems. Using the present theory of the mineralized rate, the precipitation and dissolution of several metals such as zinc, lead and iron under conditions of the mixing of sulfide and sulfate bearing fluids in permeable rocks is considered.

12.1 Statement of the Problem and the Concept of Mineralization Rate

Pore-fluid flow in permeable rocks in the Earth's upper crust is a complicated phenomenon, from both the physical and chemical points of view. Although pore-fluid flow can be generated by mechanical process, thermal process, chemical process, or a combination of these, convective pore-fluid flow is significant for ore body formation and mineralization in hydrothermal systems from the following three points of view.

(1) Since pore-fluid flows circularly within hydrothermal systems, consumption of the pore-fluid is a minimum within the system. This enables the convective flow to last for relatively long periods of time, provided that the high temperature at the base of the system is maintained.
(2) Since convective pore-fluid flow comprises a circular flow regime, it is an effective and efficient tool to mix different species within a hydrothermal system.
(3) Convective pore-fluid flow may result in the highly localized distribution of temperature in a hydrothermal system. This provides a favorite condition under which highly localized, high-grade, giant ore deposits may be formed.

For these reasons, the mixing of reactive metal carrying fluids is considered below within a convective pore-fluid flow regime. This means that a fully coupled problem between pore-fluid flow, heat transfer, species transport and chemical reactions needs to be solved.

For the modeling of pore-fluid flow at a hydrothermal system scale, the governing equations for the problem involve the following. Darcy's Law is used to describe pore-fluid flow in porous rocks. Fourier's Law and Fick's Law are used to describe heat transfer and mass (chemical species) transport, respectively. In addition, the Oberbeck-Boussinesq approximation is employed to describe changes in pore-fluid density arising from changes in pore-fluid temperature. Using these laws, the corresponding governing equations for steady state pore-fluid flow, heat transfer and mass (chemical species) transport in two-dimensional porous rocks can be expressed as

$$\frac{\partial u}{\partial x}+\frac{\partial v}{\partial y}=0, \tag{12.1}$$

$$u=\frac{K_0}{\mu}\left(-\frac{\partial P}{\partial x}+\rho_f g_x\right), \tag{12.2}$$

$$v=\frac{K_0}{\mu}\left(-\frac{\partial P}{\partial y}+\rho_f g_y\right), \tag{12.3}$$

$$\rho_{f0}c_p(u\frac{\partial T}{\partial x}+v\frac{\partial T}{\partial y})=\lambda_{e0}\left(\frac{\partial^2 T}{\partial x^2}+\frac{\partial^2 T}{\partial y^2}\right), \tag{12.4}$$

$$u\frac{\partial C_k}{\partial x}+v\frac{\partial C_k}{\partial y}=D_{e0}\left(\frac{\partial^2 C_k}{\partial x^2}+\frac{\partial^2 C_k}{\partial y^2}\right)+\phi R_k,\quad (k=1,2,\ldots n), \tag{12.5}$$

$$\rho_f=\rho_{f0}[1-\beta_T(T-T_0)], \tag{12.6}$$

$$\lambda_{e0}=\phi\lambda_{f0}+(1-\phi)\lambda_{s0}, \tag{12.7}$$

$$D_{e0}=\phi D_0, \tag{12.8}$$

where u and v are the velocity components of the pore-fluid in the x and y directions, respectively; P and T are pressure and temperature; C_k is the concentration of chemical species k; ρ_{f0} and T_0 are the reference density of pore-fluid and the reference temperature of the porous rock; μ and c_p are the dynamic viscosity and specific heat of the pore-fluid; λ_{f0} and λ_{s0} are the thermal conductivity coefficients for the pore-fluid and solid matrix; ϕ and β_T are the porosity of the porous rock and the thermal volume expansion coefficient of the pore-fluid; D_0 is the diffusivity of the chemical species; K_0 is the permeability of the porous rock; g_x and g_y are the gravity acceleration components in the x and y directions, and n is the total number of chemical species in the system.

Note that a positive value of R_k means that a certain amount of chemical species k is added into the system due to the relevant chemical reactions, while a negative value of R_k means that a certain amount of chemical species k is taken away from the system due to the relevant chemical reactions. In the former case, R_k is referred to as a source term and, in the latter case, R_k is referred to as a sink term. The specific value of R_k is determined by the chemical reactions considered in the hydrothermal system.

For the mixing of reactive sulfide- and sulfate-bearing fluids, the corresponding chemical formula can be expressed, in an ionic form, as

$$H_2S+2O_2\overset{k_R}{\Leftrightarrow}SO_4^{=}+2H^+ \tag{12.9}$$

where k_R is the overall reaction rate constant, which is strongly dependent on temperature.

For the mixing of sulfide- and sulfate-bearing fluids, the experimental rate law has the following form (Ohmoto and Lasaga 1982):

$$R=k_R C_{H_2S}C_{SO_4^{=}} \tag{12.10}$$

where R is the experimental reaction rate of the mixing between the sulfide and sulfate fluids, and C_{H_2S} and $C_{SO_4^{=}}$ are the concentrations of the sulfide and sulfate, respectively.

In the geochemical modeling of ore body formation and mineralization, it is common practice to assume that the solutions of aqueous minerals are in a chemical equilibrium state or near a chemical equilibrium state (Phillips 1991). This is true for most hydrothermal systems because the process of mineralization may last

millions of years. Even though the reaction rates between the pore-fluid and rocks are very small, an equilibrium concentration of a mineral can be reached during such long periods of time. If there is no pore-fluid flow in a hydrothermal system, one can calculate the unknown concentration of a mineral using the concentrations of the other relevant minerals and the equilibrium constant of the particular chemical reaction under consideration. This is commonly called the equilibrium method of geochemical modeling in the geoscience. However, if there is pore-fluid flow in a hydrothermal system, the flow can transport solutions containing aqueous metal species either from a high temperature region to a low temperature region or vice versa. To maintain the equilibrium state of a mineral, precipitation and/or dissolution of minerals must take place in the hydrothermal system. In the following, we will deduce the mineralization rate of a mineral in a hydrothermal system. The mineralization rate of a mineral is defined as the variation in the mineral weight per unit volume rock per unit time during mineralization. Using this definition, a positive value of the mineralization rate of a mineral means the dissolution of the mineral in the hydrothermal system, while a negative value of the mineralization rate means the precipitation of the mineral.

The mineralization rate of a metal can be derived from a mass conservation point of view. For this purpose, a particular metal species (i.e., species q) is considered in an equilibrium state and a pore-fluid flow regime. The mass (chemical species) transport equation for this particular species reads:

$$u\frac{\partial C_q^e}{\partial x}+v\frac{\partial C_q^e}{\partial y}=D_{e0}\left(\frac{\partial^2 C_q^e}{\partial x^2}+\frac{\partial^2 C_q^e}{\partial y^2}\right)+\phi R_q, \tag{12.11}$$

where C_q^e is the equilibrium concentration of species q, and R_q is the source/sink term. Other quantities have the same meaning as defined in (12.5).

In ore body formation and mineralization problems, the diffusion term on the right-hand side of (12.11) is usually much smaller than the advection term. Thus, (12.11) can be approximately expressed as

$$MR_q=\phi R_q=u\frac{\partial C_q^e}{\partial x}+v\frac{\partial C_q^e}{\partial y}, \tag{12.12}$$

where MR_q is the mineralization rate associated with species q.

Generally, the equilibrium concentration of a particular metal species is a function of temperature, pressure and other relevant chemical species as follows:

$$C_q^e=f(T,P,C_1,C_2\cdots,C_n), \tag{12.13}$$

where n is the number of the relevant chemical species needed to determine the equilibrium concentration of chemical species q in the chemical reaction. Substituting (12.13) into (12.12) yields the following equation:

$$MR_q=\frac{\partial C_q^e}{\partial T}\left(u\frac{\partial T}{\partial x}+v\frac{\partial T}{\partial y}\right)+\frac{\partial C_q^e}{\partial P}\left(u\frac{\partial P}{\partial x}+v\frac{\partial P}{\partial y}\right)+\sum_{r=1}^{n}\frac{\partial C_q^e}{\partial C_r}\left(u\frac{\partial C_r}{\partial x}+v\frac{\partial C_r}{\partial y}\right). \tag{12.14}$$

The influence of temperature on the mineralization rate expressed in (12.12) can be explained as follows. Since the equilibrium concentration of a chemical species is strongly dependent on the local temperature, a temperature variation in a hydrothermal system may provide a favorite environment for mineralization to take place. For example, the equilibrium concentration of NaCl increases with an increase in temperature because NaCl's solubility in water is dependent on temperature. Thus, if a saturated NaCl solution is transported from a high temperature region into a low temperature region by advection/convection in a hydrothermal system, the NaCl solution will become supersaturated and, therefore, NaCl will be precipitated in the porous rock. On the contrary, if a saturated NaCl solution is transported from a low temperature region into a high temperature region, it will become undersaturated and, therefore, NaCl will be dissolved from the porous rock. The precipitation/dissolution of NaCl due to a variation in temperature can be better demonstrated by the following experiment. Suppose we have two beakers filled with water of different temperatures, one at a temperature of 20 °C, and the other 100 °C. First, we add NaCl to these two beakers until the NaCl solution becomes saturated in both beakers. This step is equivalent to a NaCl solution becoming saturated in porous rocks after an extended period of time. Secondly, we cool the saturated NaCl solution in the beaker of the higher temperature from 100 °C to 20 °C. As a result, NaCl is precipitated gradually as the temperature of the saturated NaCl solution is decreased. This step is equivalent to that when a saturated NaCl solution is transported from a high temperature region into a low temperature region by convection/advection of pore-fluid: NaCl is precipitated in the low temperature region within the hydrothermal system. Thirdly, we heat the saturated NaCl solution in the beaker at the lower temperature from 20 °C to 100 °C. Then NaCl is added to the beaker to keep the NaCl solution saturated. This step is equivalent to when a saturated NaCl solution is transported from a low temperature region to a high temperature region: NaCl is dissolved from the surrounding rocks in the hydrothermal system. Equation (12.12) clearly indicates that convective pore-fluid flow also plays an important role in ore body formation and mineralization. Without pore-fluid flow, the velocity of pore-fluid is zero and so is the mineralization rate of the mineral in a hydrothermal system. In order to maintain the equilibrium state of a metal species in a pore-fluid flow regime, precipitation and/or dissolution of minerals must take place in the hydrothermal system. Similar discussions follow for the influence of pressure and of other chemical species upon the mineralization rate.

It is also important to note that the derivatives $\partial C_q^e/\partial T$, $\partial C_q^e/\partial P$, $\partial C_q^e/\partial C_r$ in (12.14) are not constants and are strongly dependent on the variables T, P and C_r. These derivatives can be positive for some ranges of these variables, and zero or negative for other ranges. Examples of the NaCl concentration's influence, temperature and fluid pressure upon the equilibrium concentration of Zn at a fixed pH and redox condition are given in Murphy et al. (2008). We will return to this issue in the examples of this chapter.

12.2 Precipitation and Dissolution of Zinc, Lead and Iron in Hydrothermal Systems

As application examples of the present mineralization theory, the precipitation and dissolution of zinc, lead and iron in hydrothermal systems is considered in this section. In the following, convection is the driver for pore-fluid flow as the carrier of aqueous metal species in hydrothermal systems.This means that the temperature gradient in the system must be high enough to trigger convective pore-fluid flow. On the other hand, mixing reduced (H_2S) and oxidized $(SO_4^=)$ fluids is assumed to create an appropriate environment for the mineralization of zinc, lead and iron within the hydrothermal systems.

The relevant chemical reactions describing the deposition of zinc, lead and iron minerals can be expressed as follows:

$$Zn^{2+} + H_2S \Leftrightarrow ZnS + 2H^+, \tag{12.15}$$

$$Pb^{2+} + H_2S \Leftrightarrow PbS + 2H^+, \tag{12.16}$$

$$Fe^{2+} + H_2S \Leftrightarrow FeS + 2H^+. \tag{12.17}$$

Using the related chemical equilibrium reaction constants of these equations, the equilibrium concentration of the corresponding metals in solution can be expressed as:

$$C^e_{Zn^{2+}} = \frac{C^2_{H^+}}{K_{Zn}C_{H_2S}}, \tag{12.18}$$

$$C^e_{Pb^{2+}} = \frac{C^2_{H^+}}{K_{Pb}C_{H_2S}}, \tag{12.19}$$

$$C^e_{Fe^{2+}} = \frac{C^2_{H^+}}{K_{Fe}C_{H_2S}}, \tag{12.20}$$

where $C^e_{Zn^{2+}}$, $C^e_{Pb^{2+}}$ and $C^e_{Fe^{2+}}$ are the equilibrium concentrations of zinc, lead and iron in the solution, respectively; K_{Zn}, K_{Pb} and K_{Fe} are the chemical equilibrium reaction constants for the chemical reactions expressed by (12.15), (12.16) and (12.17), and C_{H^+} and C_{H_2S} are the concentrations of H^+ and H_2S in the hydrothermal system. Note that the equilibrium constants for chemical reactions are dependent on both temperature and pressure. Their values can be determined from a relevant thermodynamic database.

The first example (i.e., Case 1) considered is a square box measuring 10×10 km. The box is filled with porous rock and modeled by 2,500 four-node quadrilateral elements. As shown in Fig. 12.1, a reduced fluid (i.e., H_2S) and an oxidized fluid (i.e., $SO_4^=$) are injected at the left quarter and right quarter of the bottom of the computational domain. The concentrations in solution of the injected H_2S and $SO_4^=$

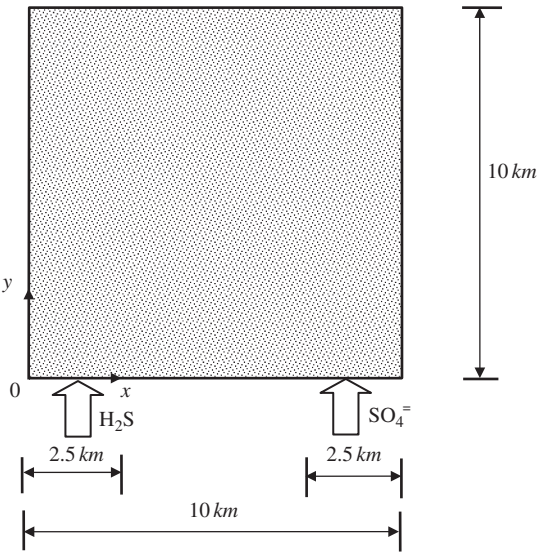

Fig. 12.1 Geometry of the pore-fluid mixing problem (Case 1)

are $0.1\,\mathrm{kmol/m^3}$. The temperatures at the top and bottom boundaries are $25\,^{\circ}\mathrm{C}$ and $325\,^{\circ}\mathrm{C}$, respectively. This means that the hydrothermal system is uniformly heated from below. The following parameters are used in the computations. The dynamic viscosity of pore-fluid is $10^{-3}\,\mathrm{N\cdot s/m^2}$; the reference density of pore-fluid is $1,000\,\mathrm{kg/m^3}$; the specific heat of pore-fluid is $4,185\,\mathrm{J/(kg\cdot^{\circ}C)}$; the thermal conductivity coefficient of pore-fluid is $0.6\,\mathrm{W/(m\cdot^{\circ}C)}$; the volumetric thermal expansion coefficient of pore-fluid is $2.07\times10^{-4}(1/^{\circ}\mathrm{C})$; the diffusivity of chemical species in the porous medium is $3\times10^{-7}\,\mathrm{m^2/s}$; the porosity of the porous medium is 0.1; the specific heat of the porous rock is $815\,\mathrm{J/(kg\cdot^{\circ}C)}$; the thermal conductivity coefficient of the porous rock is $3.35\,\mathrm{W/(m\cdot^{\circ}C)}$, and the permeability of the porous medium is $10^{-13}\,\mathrm{m^2}$.

Figure 12.2 shows the distributions of the pore-fluid velocity, streamlines and temperature in the hydrothermal system. Since the Rayleigh number of the hydrothermal system is supercritical, convective pore-fluid flow takes place. This convective pore-fluid flow can be clearly observed from the distributions of the pore-fluid velocity and streamlines, as shown in Fig. 12.2. Due to this convective pore-fluid flow, the distribution of temperature is highly localized in the system. The localization of temperature may provide one of the appropriate conditions for ore body formation and mineralization in some regions of the system.

Figure 12.3 shows the concentration distributions of H_2S, $SO_4^{=}$ and H^+ in the hydrothermal system. Again, the localization of these chemical species is clearly shown in this figure. This indicates that convective pore-fluid flow can result in highly localized distributions of chemical species in a hydrothermal system.

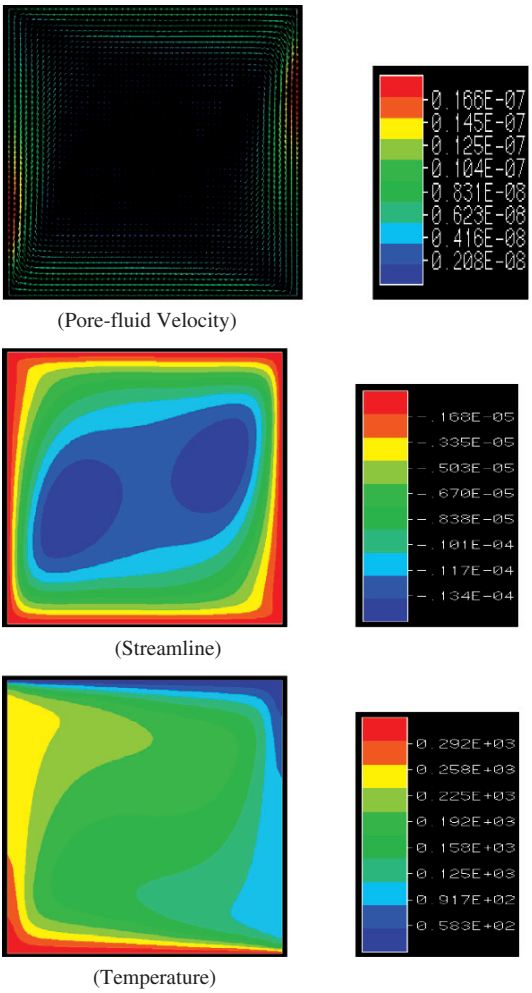

Fig. 12.2 Distributions of pore-fluid velocity, streamlines and temperature (Case 1)

Figure 12.4 shows the mineralization rate distributions of lead, zinc and iron in the hydrothermal system. Both the minimum negative value and maximum positive value of the mineralization rate are shown in this figure. Since a negative value of the mineralization rate of a mineral reflects the precipitation of the mineral and a positive value of the mineralization rate reflects the dissolution of the mineral, the precipitation and dissolution regions of lead, zinc and iron in the hydrothermal system are clearly shown here although it should be noted that the regions delineated as dissolution areas would only act in that manner if lead, zinc or iron were actually present in the pore spaces. The precipitation pattern for lead is very similar to that for zinc. However, the precipitation pattern for iron is quite different. This indicates that chemical kinetics may influence the zonation of minerals in a hydrothermal system.

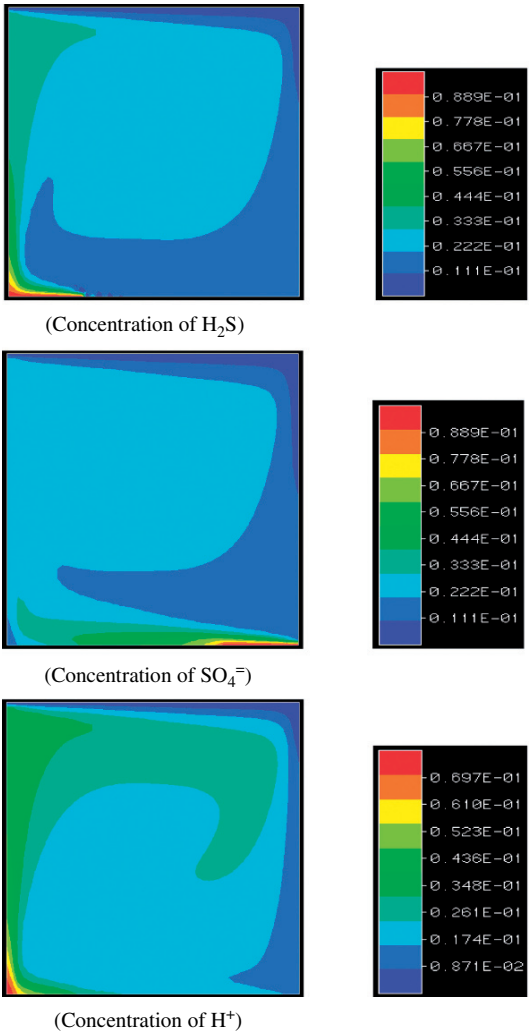

Fig. 12.3 Distributions of concentrations of H_2S, $SO_4^{=}$ and H^+ (Case 1)

At this point we need to reconsider the derivatives $\partial C_q^e/\partial T$, $\partial C_q^e/\partial P$, $\partial C_q^e/\partial C_r$ in (12.14). For temperatures above approximately 200 °C, derivatives such as $\partial C_{Pb}^e/\partial T$ and $\partial C_{Zn}^e/\partial T$ may be small so that even though large regions of precipitation for Pb and Zn are delineated within Fig. 12.4, only the low temperature regions may show appreciable mineralization for these metals. This same issue needs to be considered in the next two examples presented in this section.

Equation (12.12) states that the mineralization rate is directly proportional to the porosity. This means that as precipitation in the initial pore space proceeds during mineralization the porosity is continuously decreased. This process has not been built into these models, but in nature (12.14) would describe a process where the porosity and, hence, the permeability of the porous medium, continuously decreased

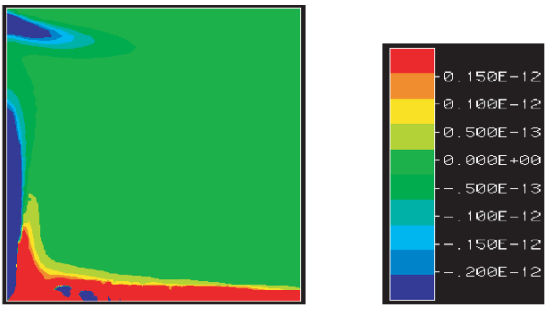

(Precipitation of Lead)

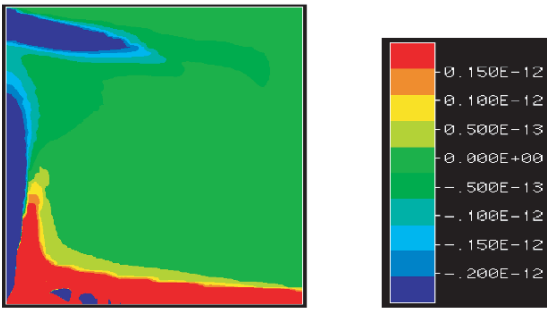

(Precipitation of Zinc)

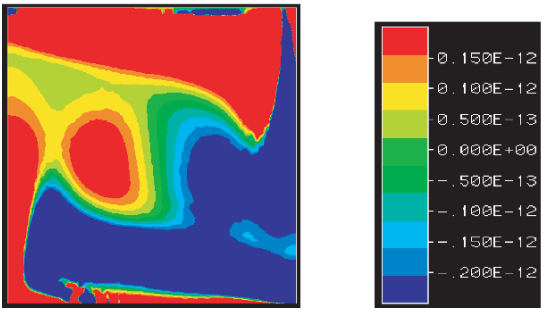

(Precipitation of Iron)

Fig. 12.4 Distributions of precipitation rates of lead, zinc and iron (Case 1)

as the mineralization proceeded. This means that the Darcy fluid velocity would also decrease leading to a decrease in the mineralization rate. Thus (12.14) describes potential mineralization sites only. In order to generate a high-grade deposit through this process porosity must be continuously generated at the mineralization site by other mechanical or chemical processes. These processes would include deformation enhanced dilation and chemical dissolution. Such processes have not been included here.

The second example (i.e., Case 2) considered is a layered hydrothermal system, the geometry of which is shown in Fig. 12.5. The main purpose of this example is to investigate the effects of geological structures on ore body formation and

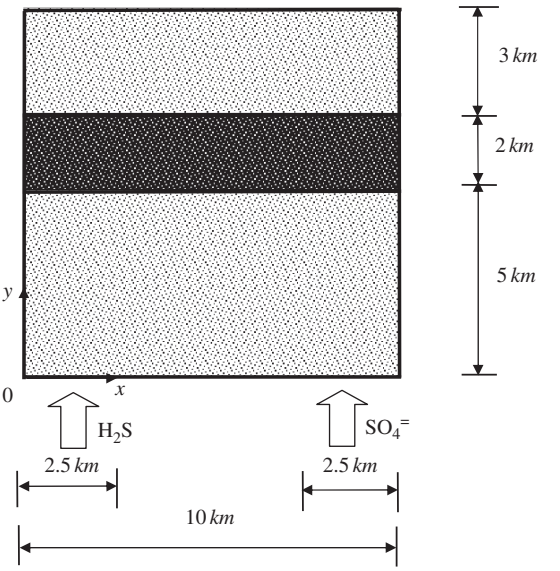

Fig. 12.5 Geometry of the pore-fluid mixing problem (Case 2)

mineralization in hydrothermal systems. For this purpose, the parameters used in Case 2 are exactly the same as those used in Case 1, except that the middle layer is less permeable than the upper and lower layers. The permeability of the middle layer is $10^{-14}\,\mathrm{m}^2$. Thus, by comparing the results from Case 2 with the results from Case 1, the effects of geological structures can be examined.

Figure 12.6 shows the distribution of the pore-fluid velocity, streamlines and temperature in the layered hydrothermal system. Due to the influence of the middle layer, the distributions of the pore-fluid velocity, streamlines and temperature in the layered hydrothermal system (i.e., Case 2) are different from those in Case 1. The existence of the middle layer clearly influences the concentration distributions of chemical species in the hydrothermal system as shown in Fig. 12.7 which illustrates the concentration distributions of H_2S, $SO_4^=$ and H^+. The difference in the zonation of lead, zinc and iron minerals can be seen by comparing the results in Fig. 12.8 (i.e., Case 2) with those in Fig. 12.4 (i.e., Case 1). This indicates that geological structures may influence the precipitation and dissolution patterns of minerals in hydrothermal systems.

The third example (i.e., Case 3) considered is a simplified example of a magma intrusion problem in hydrothermal systems. Figure 12.9 shows the geometry of the problem. The central part at the base of the system is modeled as an intruded magma measuring $2 \times 4\,\mathrm{km}$. The temperature within the whole magma body is the same as that at the bottom of the system. The reduced (H_2S) fluid is injected at the middle part of the base, while the oxidized $(SO_4^=)$ fluid is injected at the left and right parts of the base, except for the injected region of the reduced fluid. The temperatures at the top and base are fixed at 25°C and 325°C, respectively. Other parameters used in this example are exactly the same as those used in the first two examples.

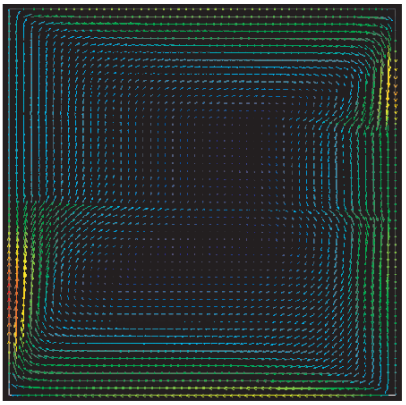

(Pore-fluid Velocity)

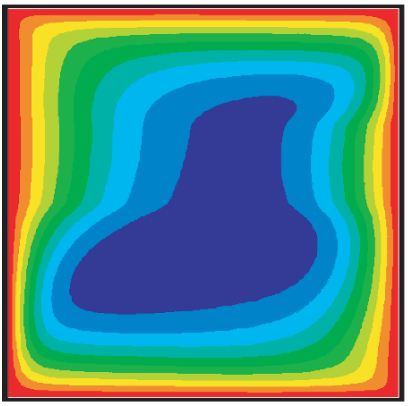

(Streamline)

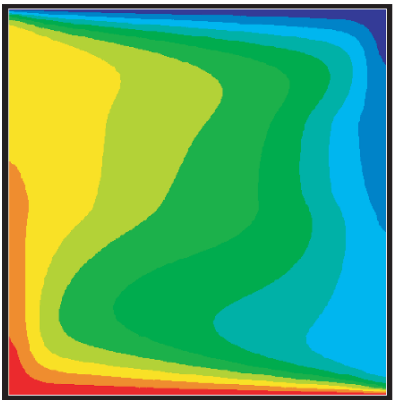

(Temperature)

Fig. 12.6 Distributions of pore-fluid velocity, streamlines and temperature (Case 2)

(Concentration of H_2S)

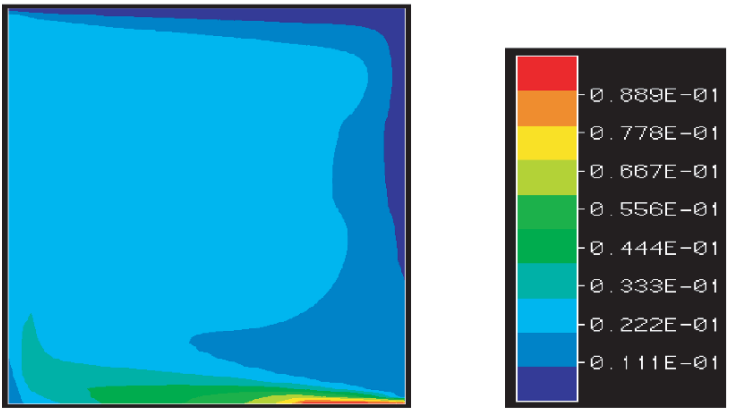

(Concentration of $SO_4^{=}$)

(Concentration of H^+)

Fig. 12.7 Distributions of concentrations of H_2S, $SO_4^{=}$ and H^+ (Case 2)

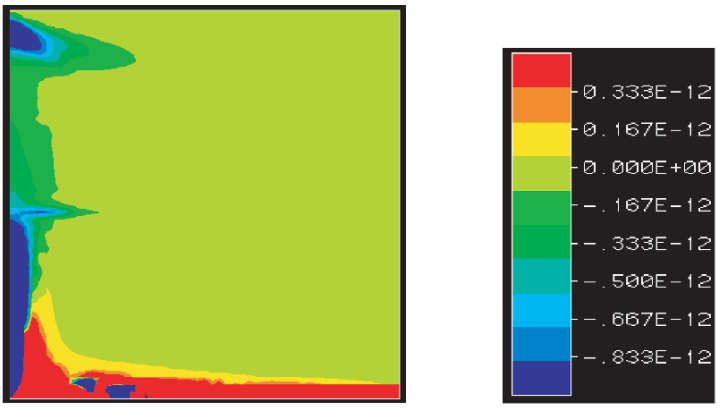

(Precipitation of Lead)

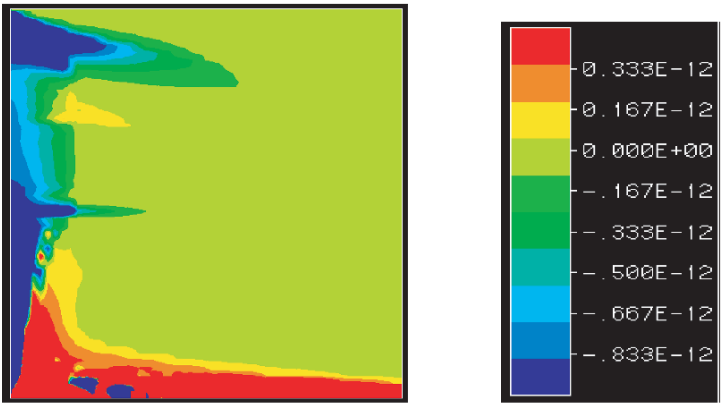

(Precipitation of Zinc)

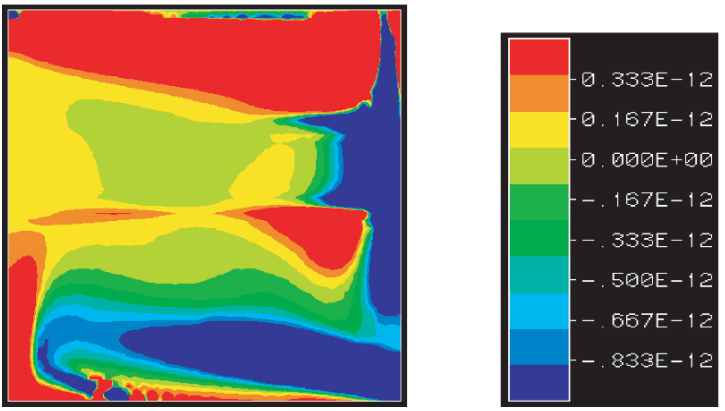

(Precipitation of Iron)

Fig. 12.8 Distributions of precipitation rates of lead, zinc and iron (Case 2)

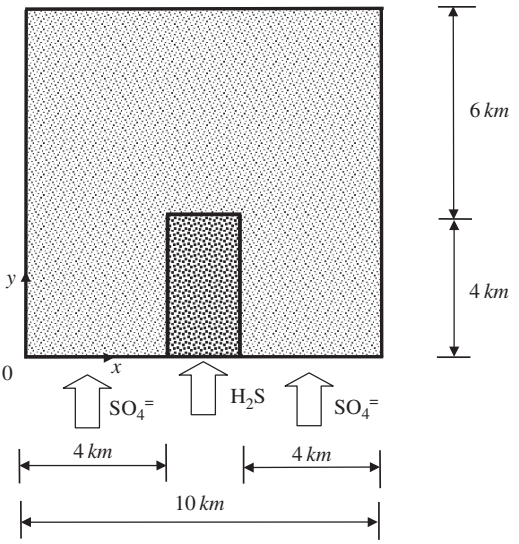

Fig. 12.9 Geometry of the pore-fluid mixing problem (Case 3)

The main purpose of this example is to investigate how the locations of the injected reactive fluid sources and geological structures influence ore body formation and mineralization in this hydrothermal system.

Figure 12.10 shows the distributions of the pore-fluid velocity, streamlines and temperature in the hydrothermal system. Clearly, all distribution patterns are different from those shown in Fig. 12.2 (Case 1) and Fig. 12.6 (Case 2). Not surprisingly, the concentration distribution patterns of H_2S, $SO_4^=$ and H^+, as shown in Fig. 12.11, are also different from those in the former two examples (see Figs. 12.3 and 12.7).

Figure 12.12 shows the mineralization rate distributions of lead, zinc and iron in the hydrothermal system. As expected, the precipitation regions of these three metals shown in Fig. 12.12 (i.e., Case 3) are also different from those shown in Fig. 12.4 (i.e., Case 1) and Fig. 12.8 (i.e., Case 2). Therefore, not only can the locations of both the injected reactive fluids and geological structures influence pore-fluid flow and temperature distributions, but they can also influence the zonation of minerals within hydrothermal systems.

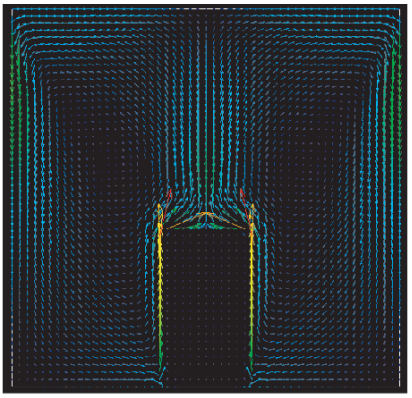

(Pore-fluid Velocity)

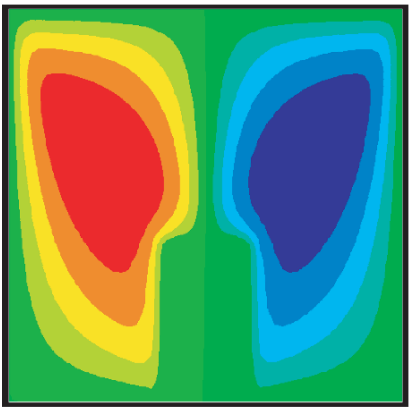

(Streamline)

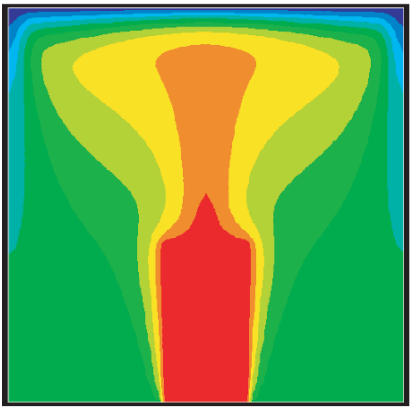

(Temperature)

Fig. 12.10 Distributions of pore-fluid velocity, streamlines and temperature (Case 3)

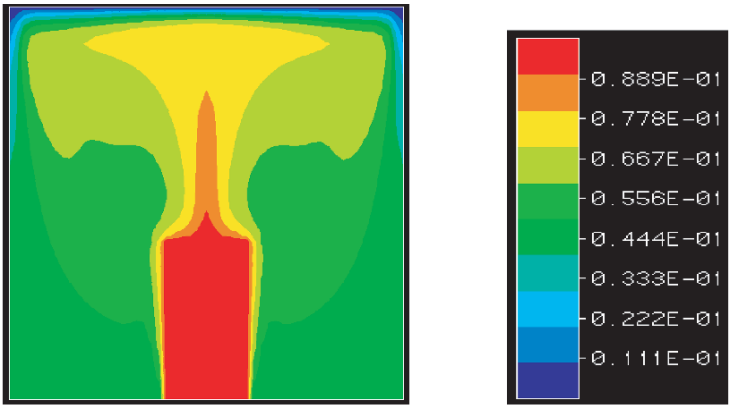

(Concentration of H_2S)

(Concentration of $SO_4^{=}$)

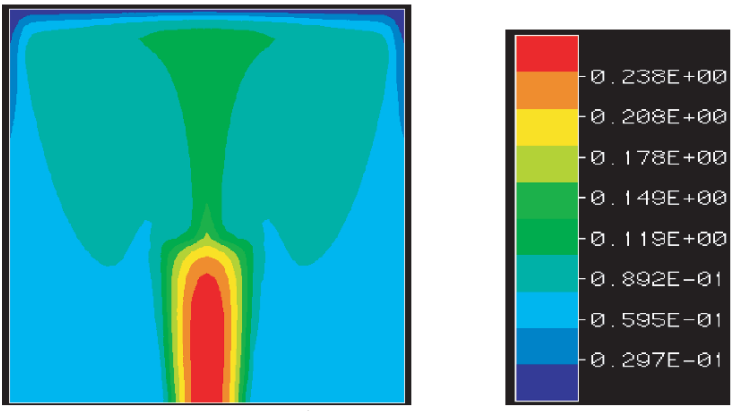

(Concentration of H^+)

Fig. 12.11 Distributions of concentrations of H_2S, $SO_4^{=}$ and H^+ (Case 3)

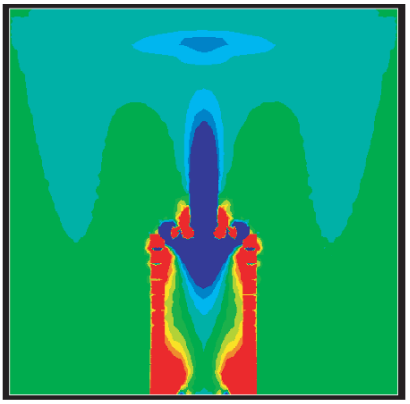

(Precipitation of Lead)

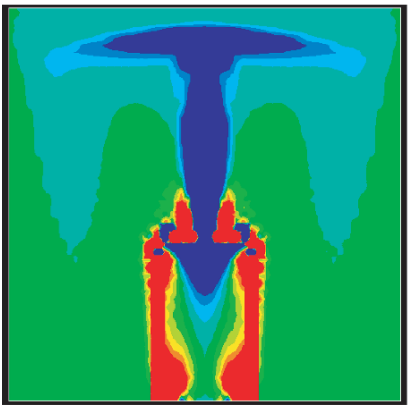

(Precipitation of Zinc)

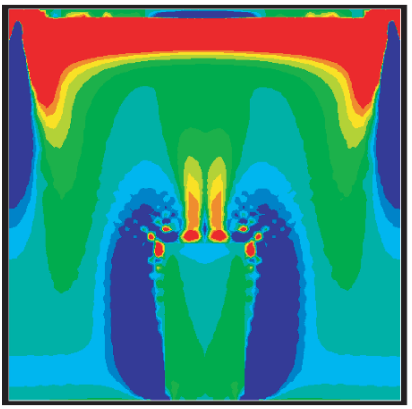

(Precipitation of Iron)

Fig. 12.12 Distributions of precipitation rates of lead, zinc and iron (Case 3)

Summary Statements

In this monograph, convective and advective heat transfer phenomena in geological systems of crustal scales are investigated in a systematic manner. Using both theoretical and numerical methods, the detailed physical mechanisms related to pore-fluid pressure gradient distributions, the critical conditions required to trigger convective pore-fluid flow and the effects of geological heterogeneities on advective and convective heat transfer in the crust of the Earth are thoroughly examined. The following conclusions have been drawn from the theoretical and numerical results.

(1) For a stable (that is, non-deforming) continental crust, although the entrapped pore-fluid pressure may reach or exceed the lithostatic pressure in an overpressured system consisting of a permeable layer and two adjacent impermeable layers, the pore-fluid pressure gradient cannot be maintained at or exceed the lithostatic pressure gradient, even if thermal effects are neglected in the crust.

(2) Pure heat conduction may have some influence on the distribution of pore-fluid pressure in the lower part of the crust, but it has little influence on the distribution of pore-fluid pressure in the upper part of the crust. Thus, for a fluid-saturated crust with motionless pore-fluid, the pore-fluid pressure gradient is very close to the hydrostatic pressure gradient resulting from a constant density of the pore-fluid.

(3) In the case of a thin crust, the thermal effect of heat advection on the distribution of pore-fluid pressure gradient is very limited, but in the case of a thick crust, the thermal effect of heat advection is significant. Generally, the thermal effect of heat advection on the distribution of pore-fluid pressure gradient becomes more significant with an increase in the conductive thermal flux at the base of the system. For a thin crustal model with an impermeable seal at the top, the pore-fluid pressure gradient is very close to a lithostatic pressure gradient. However, for a similar thick crustal model, the pore-fluid pressure gradient is less than a lithostatic pressure gradient, especially in the situation where a high basal heat flux exists.

(4) If the Rayleigh number of the system is either critical or supercritical, convective pore-fluid flow can take place in the crust where the pore-fluid pressure gradient is close to the hydrostatic pressure gradient. The resulting convective pore-fluid flow has a significant effect on heat transfer and can result in temperature localization within the crust. This kind of convective pore-fluid flow is significant for

ore body formation and mineralization in hydrothermal systems from the following three points of view.

- Since the pore-fluid flows circularly within hydrothermal systems, the consumption of the pore-fluid is minimal within the system.
- Since convective pore-fluid flow comprises a circular flow regime, it is an effective and efficient tool to mix different chemical species within the hydrothermal system.
- Convective pore-fluid flow may result in highly localized temperature distributions in a hydrothermal system. This provides a favorable condition under which highly localized, high-grade, giant ore deposits may be formed.

(5) If the pore-fluid pressure gradient is close to a lithostatic pressure gradient, convective pore-fluid flow cannot take place in a crust that has constant temperature and impermeable boundary conditions at both the top and the bottom of the system, but it can take place if the crust has a permeable top with constant pressure and temperature, and a base with constant upward pore-fluid velocity and conductive heat flux.

(6) The heterogeneity of either the medium permeability or the thermal conductivity has a significant effect on convective heat transfer within a system. Material thermoelasticity may also affect the heat transfer, depending on the elastic hardness of the rock masses within the crust. In addition, the effect of temperature-dependent pore-fluid viscosity is to destabilize convective flow in the crust. In other words, convective flow takes place more easily when temperature-dependent pore-fluid viscosity is considered within the Earth's crust.

(7) In the case of strong pore-fluid inflow from the far field in the surrounding rock, the inflow is highly focused within existing geological faults. The focused pore-fluid flow can result in significant advective heat transfer within and around these faults. The strength of pore-fluid focusing can be measured by the pore-fluid focusing factor, which depends on the dip of the fault, the aspect ratio of the fault and the permeability ratio of the fault to the surrounding rock. For the first time, the theoretical solution has shown that the pore-fluid pressure gradient is exactly equal to hydrostatic pressure gradient within a fault if the fault is perfectly permeable. However, even if a fault is not perfectly permeable, the pore-fluid pressure gradient is close to the hydrostatic pressure gradient within a permeable fault of finite size. This is true even if the surrounding rocks contain fluid with a lithostatic pressure gradient.

(8) Under certain boundary conditions, convective pore-fluid flow is possible within both vertical and inclined three-dimensional fault zones. This conclusion is also valid when double-diffusion driven convective instability of pore-fluid flow is considered. If the length of a fault zone is infinite, the critical Rayleigh number has a minimum value, which corresponds to a two-dimensional slender-circle convective flow geometry. This slender-circle convective geometry develops in the plane perpendicular to the strike of the fault. However, if the length of a fault zone is finite, the corresponding convective flow structure must be three-dimensional. Even if the length of a fault zone is infinite, since the minimum critical Rayleigh numbers of

the system are very close to each other, several three-dimensional convective flow geometries may have similar probabilities of existing, especially when the ratio of fault thickness to height is very small.

(9) Convective pore-fluid flow is very efficient for mixing reactive mineral carrying fluids and, therefore, plays an important role in ore body formation and mineralization within the upper crust of the Earth. A key issue associated with ore body formation and mineralization is to predict the precipitation and dissolution regions in hydrothermal systems. This can be addressed using the concept of the mineralization rate of a mineral. The mineralization rate can be used to predict the precipitation and dissolution regions of a mineral in hydrothermal systems. The locations of both injected reactive fluids and geological structures can significantly affect the distributions of pore-fluid flow and temperature as well as the zonation of minerals within the upper crust of the Earth.

(10) One of the important values of this monograph is that the derived theoretical solutions are useful, as benchmark solutions, to verify and validate numerical methods and models that can be used to simulate more complicated and complex situations within the Earth's crust. Because of their intrinsic approximate nature, numerical methods need to be verified and validated before they are used to solve geoscience problems. In this aspect, theoretical solutions play an important role in ensuring the accuracy and reliability of numerical solutions obtained from numerical simulation of geoscience problems.

References

Aidun CK (1987) Stability of convection rolls in porous media. ASME HTD 94:31–36

Alavyoon F (1993) On natural convection in vertical porous enclosures due to prescribed fluxes of heat and mass at the vertical boundaries. International Journal of Heat and Mass Transfer 36: 2479–2498

Bau HH and Torrance K E (1982) Low Rayleigh number thermal convection in a vertical cylinder filled with porous materials and heated from below. ASME Journal of Heat Transfer 104: 166–172

Bear J (1972) Dynamics of Fluids in Porous Media. American Elsevier Publishing Company, New York

Bear J and Bachmat Y (1990) Introduction to Modelling of Transport Phenomena in Porous Fractured Media. Kluwer Academic Press

Beck JL (1972) Convection in a box of porous material saturated with fluid. Physical Fluids 15: 1377–1383

Berryman JG and Wang HF (1995) The elastic coefficients of double-porosity models for fluid transport in jointed rock. Journal of Geophysical Research 100:24611–24627

Beukema KJ and Bruin S (1983) Three-dimensional natural convection in a confined porous medium with internal heat generation. International Journal of Heat and Mass Transfer 26: 451–458

Bickle MJ and McKenzie D (1987) The transport of heat and matter by fluids during metamorphism. Contributions to Mineralogy and Petrology 95:384–392

Bjorlykke K, Mo A and Palm E (1988) Modelling of thermal convection in sedimentary basins and its relevance to diagenetic reactions. Marine and Petroleum Geology 5: 338–351

Booker JR and Savvidou C (1985) Consolidation around a heat source. International Journal for Numerical and Analytical Methods in Geomechanics 9:173–184

Bories SA and Combarnous MA (1973) Natural convection in a sloping porous layer. Journal of Fluid Mechanics 57:63–79

Bower KM and Zyvoloski G (1997) A numerical model for thermo-hydro-mechanical coupling in fractured rock. International Journal of Rock Mechanics and Mining Science 34:1201–1211

Brady J (1988) The role of volatiles in the thermal history of metamorphic terrains. Journal of Petrology 29:1187–1213

Buretta RJ and Berman AS (1976) Convective heat transfer in a liquid saturated porous layer. ASME Journal of Applied Mechanics 43:249–253

Caltagirone JP (1975) Thermoconvective instabilities in a horizontal layer. Journal of Fluid Mechanics 72:269–287

Caltagirone JP (1976) Thermoconvective instabilities in a porous medium bounded by two concentric horizontal cylinders. Journal of Fluid Mechanics 76:337–362

Caltagirone JP and Bories S (1985) Solutions and stability criteria of natural convective flow in an inclined porous layer. Journal of Fluid Mechanics 155:267–287

Carslaw HS and Jaeger JC (1959) Conduction of Heat in Solids. Clarendon Press, Oxford

Chan YT and Banerjee S (1981) Analysis of transient three-dimensional natural convection in porous media. ASME Journal of Heat Transfer 103:242–248

Chen F and Chen CF (1989) Experimental investigation of convective stability in a superposed fluid and porous layer when heated from below. Journal of Fluid Mechanics 207:311–321

Chevalier S, Bernard D and Joly N (1999) Natural convection in a porous layer bounded by impervious domains: from numerical approaches to experimental realization. International Journal of Heat and Mass Transfer 42:581–597

Combarnous MA and Bories SA (1975) Hydrothermal convection in saturated porous media. Advanced Hydroscience 10:231–307

Connolly JAD and Ko SC (1995) Development of excess fluid pressure during dehydration of the lower crust. Terra Abstracts 7:312

Connolly JAD (1997) Mid-crustal focused fluid movements: thermal consequences and silica transport. In: Fluid flow and transport in rocks: mechanics and effects. Editors: Jamtveit B and Yardley BWD. Chapman and Hall, London

Deming D and Nunn JA (1991) Numerical simulations of brine migration by topographically driven recharge. Journal of Geophysical Research. 96: 2485–2499

Elder JW (1967) Transient convection in a porous medium. Journal of Fluid Mechanics 27: 609–623

England WA, Mackenzie AS, Mann DM and Quigley TM (1987) The movement and entrapment of petroleum fluids in the subsurface. Journal of the Geological Society, London 144:327–347

England PC and Thompson AB (1989) Pressure-temperature-time paths of regional metamorphism: heat transfer during the evolution of regions of thickened crust. Journal of Metamorphic Petrology 83:205–226

Etheridge MA, Wall VA and Vernon RH (1983) The role of the fluid phase during regional metamorphism and deformation. Journal of Metamorphic Petrology 83:205–226

Fisher DM and Brantley SL (1992) Models of quartz overgrowth and vein formation: deformation and episodic fluid flow in an ancient subduction zone. Journal of Geophysical Research 97:20043–20061

Flemings PB, Stump BB, Finkbeiner T and Zoback M (2002) Flow focusing in overpressured sandstones: theory, observations and applications. American Journal of Science 302:827–855

Fluid Dynamics International (1997) Fluid Dynamics Analysis Package: FIDAP. Fluid Dynamics International Inc., Illinois

Fyfe WS, Price NJM and Thompson AB (1978) Fluids in the Earth's Crust. Elsevier, Amsterdam

Garven G and Freeze RA (1984) Theoretical analysis of the role of groundwater flow in the genesis of stratabound ore deposits: mathematical and numerical model. American Journal of Science 284:1085–1124

Gasser RD and Kazimi MS (1976) Onset of convection in a porous medium with internal heat generation. ASME Journal of Heat Transfer 98:49–54

Garg SK and Nur A (1973) Effective stress laws for fluid-saturated porous media. Journal of Geophysical Research 78:5911–5921

Genuchten M van and Alvel WJ (1982) Analytical solutions of the one-dimensional convection-dispersion solute transport equation. Tech. Bull., U.S. Dept. Agric

Gerhart PM, Gross RJ and Hochstein JI (1993) Fundamentals of Fluid Mechanics. Addison-Wesley Publishing Company, New York

Gobin D and Bennacer R (1994) Double diffusion convection in a vertical fluid layer: onset of the convection regime. Physical Fluids 6:59–67.

Gow P, Upton P, Zhao C and Hill K (2002) Copper-Gold mineralization in the New Guinea: numerical modeling of collision, fluid flow and intrusion-related hydrothermal systems. Australian Journal of Earth Sciences 49:753–771

Goyeau B, Songbe JP and Gobin D (1996) Numerical study of double-diffusive convection in a porous cavity using Darcy-Brinkman formulation. International Journal of Heat and Mass Transfer 39:1363–1378
Hanson RB (1992) Effects of fluid production on fluid flow during regional and contact metamorphism. Journal of Metamorphic Geology 10:87–97
Hetenyi M (1980) Beams on Elastic Foundation. The University of Michigan Press
Hoaglund JR and Pollard D (2003) Dip and anisotropy effects on flow using a vertically skewed model grid. Ground Water 41:841–846
Hoisch TD (1991) The thermal effects of pervasive and channelized fluid flow in the deep crust. Journal of Geology 99:69–80
Horne RN and Caltagirone JP (1980) On the evaluation of thermal disturbances during natural convection in a porous medium. Journal of Fluid Mechanics 100:385–395
Horton CW and Rogers FT (1945) Convection currents in a porous medium Journal of Applied Physics 16:367–370
Impey MD, Riley DS and Winters KH (1990) The effect of sidewall imperfections on pattern formation in Lapwood convection. Nonlinearity 3:197–230
Islam MR and Nandakumar K (1990) Transient convection in saturated porous layers. International Journal of Heat and Mass Transfer 33:151–161
Itasca Consulting Group (1995) Fast Lagrangian Analysis of Continua (FLAC), Itasca Consulting Group, Inc., Minnesota
Jamtveit B and Yardley BWD (1997) Fluid flow and transport in rocks: mechanisms and effects, Chapman and Hall, London
Jiao Y and Hudson JA (1995) The fully-coupled model for rock engineering systems. International Journal of Rock Mechanics and Mining Scence 32:491–512
Jones MC and Persichetti JM (1986) Convective instability in packed beds with throughflow. AIChE Journal 32:1555–1557
Kassoy DR and Cotte B (1985) The effects of sidewall heat loss on convection in a saturated porous vertical slab. Journal of Fluid Mechanics 152:361–378
Kaviany M (1984) Thermal convective instabilities in a porous medium. ASME Journal of Heat Transfer 106:137–142
Kladias N and Prasad V (1990) Flow transitions in buoyancy-induced non-Darcy convection in a porous medium heated from below. ASME Journal of Heat Transfer 112:675–684
Korsch RJ, Goleby BR, Leven JH and Drummond BJ (1998) Crustal architecture of central Australia based on deep seismic reflection profiling. Tectonophysics 288:57–69
Kulacki FA and Freeman RG (1979) A note on thermal convection in a saturated, heat generating porous layer. ASME Journal of Heat Transfer 101:169–171
Kvernvold O and Tyvand PA (1980) Dispersion effects on thermal convection in porous media. Journal of Fluid Mechanics 99:673–686
Lamb H (1975) Hydrodynamics. Cambridge University Press, London
Lapwood ER (1948) Convection of a fluid in a porous medium. Proc. Camb. Phil. Soc. 44:508–521
Lebon G and Cloot A (1986) A thermodynamical modeling of fluid flows through porous media: application to natural convection. International Journal of Heat and Mass Transfer 29:381–390
Lewis RW and Schrefler BA (1998) The finite element method in the static and dynamic deformation and consolidation of porous media. John Wiley & Sons, New York
Lin G, Zhao C, Hobbs BE, Ord A and Muhlhaus HB (2003) Theoretical and numerical analyses of convective instability in porous media with temperature-dependent viscosity. Communications in Numerical Methods in Engineering 19:787–799
Lowell RP and Shyu CT (1978) On the onset of convection in a water-saturated porous box: effect of conducting walls. Letters of Heat and Mass Transfer 5:371–378
Mamou M, Vasseur P and Bilgen E (1998) Double-diffusive convection instability in a vertical porous enclosure. Journal of Fluid Mechanics 368:263–289
Matthai SK (2003) Fluid flow and reactive transport in fractured and faulted rock. Journal of Geochemical Exploration 78:179–182

McKibbin R and O'Sullivan MJ (1980) Onset of convection in a layered porous medium heated from below. Journal of Fluid Mechanics 96:375–393
McTigue DF (1986) Thermoelastic response of fluid-saturated porous rock. Journal of Geophysical Research 91:29533–29542
Morse PM and Feshbach H (1953) Methods of theoretical physics. vol. 2. McGraw-Hill, New York
Murphy HD (1979) Convective instabilities in vertical fractures and faults. Journal of Geoghysical Research 84:6121–6130
Murphy FC, Ord A, Hobbs BE, Willetts G and Barnicoat AC (2008) Targeting stratiform Zn-Pb-Ag massive sulfide deposits in Ireland through coupled deformation/thermal transport/fluid flow numerical modeling. Economic Geology (in review)
Nguyen HD, Pack S and Douglass RW (1994) Study of double diffusive convection in a layered anisotropic porous medium. Numerical Heat Transfer 26:489–505
Nield DA (1968) Onset of thermohaline convection in a porous medium. Water Resources Research 11:553–560
Nield DA and Bejan A (1992) Convection in porous media. Springer-Verlag, New York
Nithiarasu P, Seetharamu KN and Sundararajan T (1996) Double-diffusive natural convection in an enclosure filled with fluid-saturated porous medium: a generalized non-Darcy approach. Numerical Heat Transfer 30:430–436
Norton D and Knapp R (1970) Transport phenomena in hydrothermal systems: nature of porosity. American Journal of Sciences 277:913–936
Obdam ANM and Veling EJM (1987) Elliptical inhomogeneities in groundwater flow: an analytical description. Journal of Hydrology 95:87–96
Ohmoto H and Lasage AC (1982) Kinetics of reactions between aqueous sulfates and sulfides in hydrothermal systems. Geochemica et Cosmochimica Acta 46:1727–1745
Ohnishi Y, Shibata H and Kobayashi A (1985) Development of finite element code for the analysis of coupled thermo-hydro-mechanical behaviour of saturated-unsaturated medium. Proceedings of International Symposium on Coupled Process Affecting the Performance of a Nuclear Waste Repositor, Berkeley, California
Ord A, Hobbs BE, Zhang Y, Broadbent GC, Brown M, Willetts G, Sorjonen-Ward P, Walshe J and Zhao C (2002) Geodynamic modelling of the Century deposit, Mt Isa Province, Queensland.Australian Journal of Earth Sciences 49:1011–1039
Ormond A and Genthon P (1993) 3-D thermoconvection in an anisotropic inclined sedimentary layer. Geophysical Journal International 112:257–263
Palm E, Weber JE and Kvernvold O (1972) On steady convection in a porous medium. Journal of Fluid Mechanics 54:153–161
Peacock SM (1989) Numerical constraints on rates of metamorphism, fluid production and fluid flux during regional metamorphism. Geological Society of America Bulletin 101:476–485
Person M and Baumgartner L (1995) New evidence for long-distance fluid migration within the Eath's crust. Reviews of Geophysics 33 (Supplement):1083–1091
Person M, Raffensperger JP Ge S and Garven G (1996) Basin-scale hydrogeologic modeling. Reviews of Geophysics 34:1083–1091
Phillips OM (1991) Flow and reactions in permeable rocks. Cambridge University Press, Cambridge
Pillatsis G, Taslim ME and Narusawa U (1987) Thermal instability of a fluid-saturated porous medium bounded by thin fluid layers. ASME Journal of Heat Transfer 109:677–682
Poulikakos D (1987) Thermal instability in a horizontal fluid layer superposed on a heat-generating porous bed. Numerical Heat Transfer 12:83–100
Powley DE (1990) Pressures and hydrogeology in petroleum basins. Earth Science Reviewers 29: 215–226
Prasad V and Kulacki FA (1987) Natural convection in horizontal fluid layers with localized heating from below. ASME Journal of Heat Transfer 109, 795–706
Rabinowicz M, Sempere JC and Genthon P (1999) Thermal convection in a vertical permeable slot: implications for hydrothermal circulation along mid-ocean ridges. Journal of Geophysical Research 104:29275–29292

Rice JR and Cleary MP (1976) Some basic stress diffusion solutions for fluid-saturated elastic porous media with compressible constituents. Reviews of Geophysics and Space Physics 14:227–241

Riley DS and Winters KH (1989) Modal exchange mechanisms in Lapwood convection. Journal of Fluid Mechanics 204:325–358

Roberts SJ, Nunn JA, Cathles L and Cipriani FD (1996) Expulsion of abnormally pressured fluids along faults. Journal of Geophysical Research 101:28,231–28,252

Salt H (1988) Heat transfer across a convecting porous layer with flux boundaries. Transport in Porous Media 3:325–341

Schaubs P and Zhao C (2002) Numerical modelling of gold-deposit formation in the Bendigo-Ballarat zone, Victoria. Australian Journal of Earth Sciences 49:1077–1096

Scheidegger AE (1974) The physics of flow through porous media. University of Toronto Press, Toronto

Sorjonen-Ward P, Zhang Y and Zhao C (2002) Numerical modelling of orogenic processes and mineralization in the south eastern part of the Yilgarn Craton, Western Australia. Australian Journal of Earth Sciences 49:935–964

Stratton JA (1941) Electromagnetic theory. McGraw-Hill, New York

Terzaghi K (1925) Erdbaumechanik auf Bodenphysikalischer Grundlage. Deuticke, Leipzig

Terzaghi K (1943) Theoretical soil mechanics. Wiley, New York

Terzaghi K (1960) From theory to practice in soil mechanics. Wiley, New York

Thomas HR, He Y and Onofrei C (1998) An examination of the validation of engineered clay barriers. International Journal for Numerical and Analytical Methods in Geomechanics 22: 49–71

Toth J (1962) A theory of groundwater motion in small drainage basins in central Alberta, Canada. Journal of Geophysical Research 67:4375–4387

Tournier C, Genthon P and Rabinowicz M (2000) The onset of natural convection in vertical fault planes: consequences for the thermal regime in crystalline basements and for heat recovery experiments. Geophysical Journal International 140:500–508

Walther JV and Orville PM (1982) Volatile production and transport in regional metamorphism. Contributions to Mineralogy and Petrology 79:252–257

Wallstrom TC, Christie MA, Durlofsky LJ and Sharp DH (2002) Effective flux boundary conditions for upscaling porous media equations. Transport in Porous Media 46:139–153

Webster AG (1897) The theory of electricity and magnetism. Macmillan, New York

Wieck J, Person M and Strayer L (1995) A finite element method for simulating fault block motion and hydrothermal fluid flow within rifting basins. Water Resources Research 31:3241–3258

Yardley BWD and Bottrell SH (1992) Silica mobility and fluid movement during metamorphism of the Connemara schists, Ireland. Journal of Metamorphic Geology. 10:453–464

Yardley BWD and Lloyd GE (1995) Why metasomatic fronts are really sides. Geology 23:53–56

Yardley BWD (1997) The evolution of fluids through the metamorphic cycle. In: Fluid flow and transport in rocks: mechanics and effects (eds: B Jamtveit and BWD. Yardley), Chapman & Hall

Yen YC (1974) Effects of density inversion on free convective heat transfer in porous layer heated from below. International Journal of Heat and Mass Transfer 17:1349–1356

Zebib A and Kassoy DR (1977) Onset of natural convection in a box of water-saturated porous media with large temperature variation. Physical Fluids 20:4–9

Zhao C and Valliappan S (1994a) Numerical modelling of transient contaminant migration problems in infinite porous fractured media using finite/infinite element technique: theory. International Journal for Numerical and Analytical Methods in Geomechanics 18:523–541

Zhao C and Valliappan S (1994b) Numerical modelling of transient contaminant migration problems in infinite porous fractured media using finite/infinite element technique: parametric study. International Journal for Numerical and Analytical Methods in Geomechanics 18:543–564

Zhao C, Xu TP and Valliappan S (1994c) Numerical modelling of mass transport problems in porous media: a review. International Journal of Computers and Structures 53:849–860

Zhao C and Steven GP (1996) Analytical solutions for transient diffusion problems in infinite media. Computer Methods in Applied Mechanics and Engineering 129:29–42

Zhao C, Mühlhaus HB and Hobbs BE (1997) Finite element analysis of steady-state natural convection problems in fluid-saturated porous media heated from below. International Journal for Numerical and Analytical Methods in Geomechanics 21:863–881

Zhao C, Hobbs BE and Mühlhaus HB (1998a) Finite element modelling of temperature gradient driven rock alteration and mineralization in porous rock masses. Computer Methods in Applied Mechanics and Engineering 165:175–187

Zhao C, Hobbs BE and Mühlhaus HB (1998b) Analysis of pore-fluid pressure gradient and effective vertical-stress gradient distribution in layered hydrodynamic systems. Geophysical Journal International 134:519–526

Zhao C, Mühlhaus HB and Hobbs BE (1998c) Effects of geological inhomogeneity on high Rayleigh number steady-state heat and mass transfer in fluid-saturated porous media heated from below. Internal Journal of Computation and Methodology: Numerical Heat Transfer 33:415–431

Zhao C, Hobbs BE and Mühlhaus HB (1999a) Theoretical and numerical analyses of convective instability in porous media with upward throughflow. International Journal for Numerical and Analytical Methods in Geomechanics 23:629–646

Zhao C, Hobbs BE. Mühlhaus HB and Ord A (1999b) Finite element analysis of flow patterns near geological lenses in hydrodynamic and hydrothermal systems. Geophysical Journal International 138:146–158

Zhao C, Hobbs BE, Mühlhaus HB and Ord A (1999c) A consistent point-searching algorithm for solution interpolation in unstructured meshes consisting of 4-node bilinear quadrilateral elements. International Journal for Numerical Methods in Engineering 45:1509–1526

Zhao C, Hobbs BE and Mühlhaus HB (1999d) Finite element modelling of reactive mass transport problems in fluid-saturated porous media. Communications in Numerical Methods in Engineering 15:501–513

Zhao C, Hobbs BE and Mühlhaus HB (1999e) Effects of medium thermoelasticity on high Rayleigh number steady-state heat transfer and mineralization in deformable fluid-saturated porous media heated from below. Computer Methods in Applied Mechanics and Engineering 173:41–54

Zhao C, Hobbs BE and Mühlhaus HB (2000a) Finite element analysis of heat transfer and mineralization in layered hydrothermal systems with upward throughflow. Computer Methods in Applied Mechanics and Engineering 186:49–64

Zhao C, Hebblewhite BK and Galvin JM (2000b) Analytical solutions for mining induced horizontal stress in floors of coal mining panels. Computer Methods in Applied Mechanics and Engineering 184:125–142

Zhao C, Hobbs BE, Mühlhaus HB, Ord A and Lin G (2000c) Numerical modelling of double diffusion driven reactive flow transport in deformable fluid-saturated porous media with particular consideration of temperature-dependent chemical reaction rates. International Journal for Computer-aided Engineering and Software: Engineering Computations 17:367–385.

Zhao C, Hobbs BE, Mühlhaus HB and Ord A (2000d) Finite element modelling of dissipative structures for nonequilibrium chemical reactions in fluid-saturated porous media. Computer Methods in Applied Mechanics and Engineering 184:1–14

Zhao C, Hobbs BE, Mühlhaus HB, Ord A and Lin G (2001a) Finite element modelling of three-dimensional convection problems in pore-fluid saturated porous media heated from below. Communications in Numerical Methods in Engineering 17:101–114

Zhao C, Lin G, Hobbs BE, Mühlhaus HB, Ord A and Wang Y (2001b) Finite element modelling of heat transfer through permeable cracks in hydrothermal systems with upward throughflow. International Journal for Computer-Aided Engineering and Software: Engineering Computations 18:996–1011

Zhao C, Hobbs BE, Walshe JL, Mühlhaus HB and Ord A (2001c) Finite element modeling of fluid-rock interaction problems in pore-fluid saturated hydrothermal/sedimentary basins. Computer Methods in Applied Mechanics and Engineering 190:2277–2293

Zhao C, Hobbs BE, Mühlhaus HB, Ord A and Lin G (2002a) Analysis of steady-state heat transfer through mid-crustal vertical cracks with upward throughflow in hydrothermal systems. International Journal for Numerical and Analytical Methods in Geomechanics 26:1477–1491

Zhao C, Lin G, Hobbs BE, Wang Y, Mühlhaus HB and Ord A (2002b) Finite element modelling of reactive fluids mixing and mineralization in pore-fluid saturated hydrothermal/sedimentary basins. International Journal for Computer-Aided Engineering and Software: Engineering Computations 19:364–387

Zhao C, Hobbs BE, Mühlhaus HB, Ord A and Lin G (2003a) Convective instability of three-dimensional fluid-saturated geological fault zones heated from below. Geophysical Journal International 155:213–220

Zhao C, Hobbs BE, Ord A, Mühlhaus HB and Lin G (2003b) Effect of material anisotropy on the onset of convective flow in three-dimensional fluid-saturated faults. Mathematical Geology 35:141–154

Zhao C, Hobbs BE, Ord A, Peng S, Mühlhaus HB and Liu L (2004) Theoretical investigation of convective instability in inclined and fluid-saturated three-dimensional fault zones. Tectonophysics 387:47–64

Zhao C, Hobbs BE, Ord A, Lin G and Mühlhaus HB (2005a) Theoretical and numerical analysis of large-scale heat transfer problems with temperature-dependent pore-fluid densities. International Journal for CAE and Software: Engineering Computations 22:232–252

Zhao C, Hobbs BE, Ord A, Peng S, Mühlhaus HB and Liu L (2005b) Double diffusion-driven convective instability of three-dimensional fluid-saturated geological fault zones heated from below. Mathematical Geology. 37:373–391

Zhao C, Hobbs BE, Ord A, Hornby P, Peng S and Liu L (2006a) Theoretical and numerical analyses of pore-fluid flow patterns around and within inclined large cracks and faults. Geophysical Journal International 166:970–988

Zhao C, Hobbs BE, Ord A, Peng S, Liu L and Mühlhaus HB (2006b) Analytical solutions for pore-fluid flow focusing within inclined elliptical inclusions in pore-fluid saturated porous rocks: solutions derived in an elliptical coordinate system. Mathematical Geology 38:987–1010

Zhao C, Hobbs BE, Ord A, Kuhn M, Mühlhaus HB and Peng S (2006c) Numerical simulation of double-diffusion driven convective flow and rock alteration in three-dimensional fluid-saturated geological fault zones. Computer Methods in Applied Mechanics and Engineering 195: 2816–2840

Zhao C, Hobbs BE and Ord A (2008) Investigating dynamic mechanisms of geological phenomena using methodology of computational geosciences: an example of equal-distant mineralization in a fault. Science in China Series D: Earth Sciences 51:947–954

Zienkiewicz OC (1977) The finite element method. McGraw-Hill, London

Zimmerman RW (1996) Effective conductivity of a two-dimensional medium containing elliptical inhomogeneities. Proceedings of the Royal Society of London A 452:1713–1727

Index